Structure-reactivity relationships in Cu/TEMPO catalyzed aerobic alcohol oxidation

Mechanistic assessment by (coupled) *operando* spectroscopic tools

Dissertation

Zur Erlangung des akademischen Grades
doctor rerum naturalium (Dr. rer. nat.)

der mathematisch-naturwissenschaftlichen Fakultät
der Universität Rostock

vorgelegt von
M.Sc. Sven Adomeit
geboren am 21.10.1988 in Hamburg
Rostock, 22.02.2019

https://doi.org/10.18453/rosdok_id00002740

Gutachter:

Prof. Dr Angelika Brückner, Leibniz-Institut für Katalyse e.V. an der Universität Rostock.

Prof. Dr. Felix Tuczek, Institut für Anorganische Chemie an der Christian-Albrechts-Universität zu Kiel

Datum der Einreichung: 22.02.2019

Datum der Verteidigung: 28.05.2019

EIDESSTATTLICHE ERKLÄRUNG

Ich versichere hiermit an Eides statt, dass ich die vorliegende Arbeit selbstständig angefertigt und ohne fremde Hilfe verfasst habe. Dazu habe ich keine außer den von mir angegebenen Hilfsmitteln und Quellen verwendet. Inhaltlich und wörtlich entnommene Textstellen sowie Abbildungen habe ich als solche kenntlich gemacht.

Rostock, den 22.02.2019

Sven Adomeit

ZUSAMMENFASSUNG

Die Cu/TEMPO katalysierte, aerobe Alkoholoxidation ist eine umweltfreundliche, alternative Syntheseroute zur Generierung von Carbonylverbindungen, das heißt, Aldehyden und Ketonen, aus primären oder sekundären Alkoholen. Allerdings sind sowohl der Reaktionsmechanismus als auch etwaige Intermediate im Detail nicht bekannt. Stand der Forschung ist lediglich, dass Cu-Komplexe *in-situ* gebildet werden, die während der Reaktion zwischen den Oxidationsstufen I und II alternieren. Ziel dieser Arbeit ist es daher mittels (gekoppelter) spektroskopischer *in-situ* und *operando* Methoden detaillierteren Einblick in die Funktionsweise verschiedener Cu-Komplexe zu erhalten.

In einem ersten Schritt wurde die *in-situ* Bildung von Cu^I-Komplexen aus dem Cu^IOTf Präkatalysator in Gegenwart verschiedener Liganden, 2,2-Bipyridin (bpy) und 1-Methyl-imidazol (NMI) in unterschiedlichen molarer Konzentrationen mittels UV-vis Spektroskopie und Cyclovoltammetrie eingehend untersucht, wobei festgestellt werden konnte, dass sich nicht ein aktiver Cu^I-Komplex sondern mehrere aktive Spezies ausbilden.

Im nächsten Schritt wurde das Oxidations- und Reduktionsverhalten dieser Spezies genauer untersucht, indem beide Teilschritte voneinander separiert wurden. Eine 3-in-1 Kopplung bestehend aus EPR-, UV-vis- und ATR-IR-Spektroskopie ermöglichte die Identifizierung von Cu^I und Cu^{II} Spezies mit der Zeit. Ein ausgeprägter Ligandeneffekt durch NMI auf den Oxidationsschritt wurde festgestellt. Hiernach wurde die Variation des Grundgerüstes der Imidazol-Liganden tiefergehend betrachtet. Es konnte nachgewiesen werden, dass Substituenten mit einem +*I*-Effekt die höchste katalytische Aktivität aufweisen, welches auf niedrigeres Redoxpotential zurückgeführt werden konnte.

Neben bpy und NMI wurden auch Pyridin-Derivate u.a. 4-Dimethylaminopyridin (4-DMAP) als Liganden in der Alkoholoxidation verwendet. Ein deutlicher Effekt der molaren Konzentration von 4-DMAP auf die katalytische Aktivität konnte ermittelt werden, der auf die Bildung von aktiven $Cu^{I/II}N_4$ Komplexen zurückgeht, welche durch EPR Untersuchungen nachgewiesen werden konnten. Eine ebenfalls durchgeführte Variation der Substituenten des Pyridin-Gerüstes führte erstaunlicherweise zu dem Schluss, dass die höchste katalytische Aktivität von Cu-Komplexen mit Liganden erreicht wird, die in *para* Position eine Amingruppe aufweisen. Andere Substitutionsmuster weisen hingegen eine sehr niedrige Aktivität auf, was auf veränderte Redoxparameter dieser Cu-Komplexe zurückgeführt wurde.

Im letzten Kapitel wurde die bestehende 3-in-1 Kopplung um Röntgenabsorptionsspektroskopie (XAS) erweitert, welche am Synchrotron SOLEIL weltweit zum ersten Mal installiert und im weiteren Verlauf zum Patent angemeldet wurde. Mittels dieser neuen Methodik konnten auch bisher nicht zugängliche Spezies, wie z.B. EPR-inaktive Cu^{II}-Dimere, nachgewiesen werden. Hierin wurde beobachtet, dass sich während des Oxidationsschrittes bis-µ-hydroxy Cu^{II} Dimere ausbilden, die ebenfalls katalytisch aktiv sind, jedoch während der Reaktion in Cu^{II} Monomere umgewandelt werden. Gleichzeitig sinkt jedoch die katalytische Aktivität. Es wurde ein Mechanismus erarbeitet, der diese Deaktivierungsroute beinhaltet.

ABSTRACT

The Cu/TEMPO catalyzed aerobic alcohol oxidation is a green, alternative pathway for the transformation of alcohols into carbonyl compounds, *e.g.* aldehydes and ketones, respectively. However, several open questions remain regarding the *precise* reaction mechanism and possible intermediates occurring during those mechanistic steps. It is well-known, that the active Cu complexes are formed *in-situ* during the reaction and subsequently alternate between the valence states I and II. The main aim of this thesis is to obtain deeper insight into the reaction mechanism and the mode of action of those Cu complexes by using (coupled) *in-situ* and *operando* spectroscopic techniques.

In the first chapter the *in-situ* formation of Cu^I complexes from the Cu^IOTf starting material in the presence of different molar ratios of 2,2-bipyridine (bpy) and 1-methylimidazole (NMI) was studied extensively by UV-vis spectroscopy as well as cyclovoltammetry. By using these methods we could evidence the formation of several active Cu species contrary to previous reports of only one Cu species. In the following the oxidation and reduction processes of those Cu species were investigated in detail by separating those steps. The recently developed 3-in-1 coupling consisting of EPR, UV-vis and ATR-IR spectroscopy enabled us to monitor the Cu^I and Cu^{II} species with time during the fundamental mechanistic steps. NMI was found to exhibit a pronounced ligand effect upon the oxidation step.

Afterwards the substituents at the imidazole scaffold were varied systematically showing the highest catalytic activity for substituents with an *+I* effect. This was found to be related to lowered redox potentials when using such imidazole ligands. Besides bpy and NMI, Pyridine-type ligands were also employed as ligands, *e.g.* 4-dimethylaminopyridine (4-DMAP) within the aerobic alcohol oxidation. Pronounced effects of the molar concentration on the catalytic activity were observed. These findings are directly related to the formation of active $Cu^{I/II}N_4$ complexes which were confirmed by *in-situ* EPR studies. Again, systematic variation of the substituents of the pyridine scaffold showed Cu complexes having ligands with an amine moiety in *para* position to be most active. Interestingly, all other substituents or substitution patterns do not show significant catalytic activity. This was shown to be directly related to altered redox properties of those Cu complexes compared to the most active ones.

In the last chapter the existing 3-in-1 coupling had been extended by X-ray absorptions spectroscopy (XAS) at SOLEIL synchrotron facility. This was the first time that such a simultaneous coupling was developed and afterwards patented. By using this new technique it was possible to monitor previously inaccessible species *e.g.* EPR-inactive Cu^{II} dimers. It could be shown that during the oxidation steps bis-μ-hydroxy Cu^{II} dimers are formed which exhibited catalytic activity. The ratio of those Cu^{II} dimers, however, decreases throughout the reaction whereas the amount of Cu^{II} monomers increases evidencing transformation of the former species into the latter. It was also found, that the activity of the catalytic system decreases with time. A new reaction mechanism was proposed based on the new spectroscopic findings including a deactivation pathway.

It's me.

I'm alive.

Am I?

(Yoko Ono)

ACKNOWLEDGEMENTS

First of all, I would like to express my deepest gratitude to you, ***Prof. Angelika Brückner***, for the possibility of writing my PhD thesis under your supervision and being a member of your excellent research group. I would like to thank you for your detailed discussions, encouragement and motivation throughout this journey.

This thesis would not have been possible without your tremendous support, ***Dr. Ursula Bentrup***. Over the course of this thesis we had innumerable meetings where we discussed everything, starting in the deepest vaults of IR spectroscopy and finishing in the realms of Cu chemistry. I credit you with the development of my analytical skills. Thank you so much!

I would like to thank ***Dr. Jabor Rabeah*** for his helpful guidance, ideas and numerous discussions during this time. I highly appreciate his opinion.

My special thanks go out to my office mates ***Dr. Huyen Vuong***, ***Dr. Denise Heyl***, ***Cristina Cerdá Moreno***, ***Romina Bassi*** and ***Dr. Jana Weiß*** for the good vibes, the fun we had during this time and the support.

Next, I would like to thank *all* my other colleagues. Particularly, I would like to mention ***Reni Grauke*** and ***Dr. Andrea Bellmann*** for all their help & support during the good and the bad times, for the talks, the coffee breaks and all the other events we participated in our free time. I also thank ***Christine Rautenberg***, ***Sonja Keller***, ***Anja Simmula***, ***Dr. Nils Rockstroh*** and ***Dr. Dirk Hollmann*** for their warm welcome and their support.

I am also grateful for having had the opportunity to meet so many kind colleagues at LIKAT, *i.a.* ***Dr. Marie-Luis Schirmer***, ***Christoph Wulf***, ***Dr. Saskia Möller*** and ***Dr. habil. Thomas Werner***.

Cordial thanks go out to my fellow researchers, in particular, ***Dr. Annette-Enrica Surkus***, ***Dr. Valerie Briois & the team of the ROCK beamline*** at SOLEIL synchrotron, the analytical team of the LIKAT (***PD Wolfgang Baumann***, ***Dr. Christine Fischer and their team***), the ***LIKAT workshop*** and ***IT department*** and ***all the other colleagues*** I might have forgotten.

Of course, this thesis would not have been possible without the support and love of my family, *i.e.* ***my mother***, ***my grandparents***, ***my aunt*** and ***my niece*** throughout my life. Very special places are reserved for ***my friends*** – you brighten my days bringing so much joy to my life, every moment.

CONTENT

LIST OF FIGURES

LIST OF FIGURES APPENDIX

LIST OF SCHEMES

LIST OF TABLES

LIST OF ABBREVIATIONS

°C	Degrees Celsius
λ_{max}	Highest absorbance of a wavelength (in nm) in a spectrum
σ	Sigma (used *i.a.* for Debye-Weller factor)
3-AmP	3-aminopyridine
4,4-MeO-bpy	4-4'-Dimethoxy-2-2'-bipyridine
4-AmP	4-aminopyridine
4-DMAP	4-dimethylaminopyridine
Å	Ångström ($1x10^{-10}$ m)
A	Hyperfine splitting constant (in Gauss)
ABNO	9-Azabicyclo[3.3.1]nonane N-Oxyl
ALS	Alternating least squares
ATR	Attenuated total reflexion
BA	Benzaldehyde
bpy	2,2'-bipyridine
BzOH	Benzyl alcohol
BzOOH	Benzoic acid
cf.	confer
cm^{-1}	Reziprocal centimeter = wavenumber
CT	Charge transfer
CV	Cyclovoltammetry
DBU	1,8-Diazabicyclo[5.4.0]undec-7-en
DFT	Density functional theory
DMF	Dimethylformamide
DMSO	Dimethyl sulfoxide
DPV	Differential pulse voltammetry
EPR	Electron paramagnetic resonance spectroscopy
equiv/s.	Equivalent/s
eV	Electronvolt
EXAFS	Extended X-ray Absorption Fine Structure
g	g-factor
G	Gauss
Hfs	Hyperfine splitting
Hz	Hertz

I	nuclear spin
$+I$	Inductive effects
IL	Intraligand
IR	Infrared spectroscopy
K	Kelvin
kHz	Kilohertz = 1x10^3 Hz
L	Ligand
LMCT	Ligand to metal charge transfer
m_l	Magnetic quantum number
$+M$	Mesomeric effect
MCR	Multivariate curve resolution
MeCN	Methyl cyanide = acetonitrile
MLCT	Metal to ligand charge transfer
mol%	molar percentage
nm	nanometer = 10^{-8} m
N	N-donor ligand
NMI	1- or N-methylimidazole
OTf/OTf$_2$	Triflouromethanesulfonate anion
pKa	Negative decadic logarithm of acid dissociation constant
PTFE	Polytetrafluoroethylene
R	Atomic distance in Ångström
R_f	R-factor (representing the relative error of the fit vs data)
S	Spin
Shfs	super hyperfine splitting
t-BuOK	Potassium tert-butanolate
TEMPO	2,2,6,6-tetramethylpiperidinyloxyl radical
UV-vis	Ultra-violett visible spectroscopy
V	Volt
XANES	X-ray Absorption Near Edge Structure
XAS	X-ray absorption spectroscopy

1. MOTIVATION AND OBJECTIVES

Selective oxidation of hydroxyl moieties to carbonyl compounds is one of the most fundamental transformations in organic chemistry and for the synthesis of fine chemicals.[1-3] Various heterogeneous as well as homogeneous pathways exist.[1, 4] However, their signify-cance crucially depends on catalyst activity and selectivity, reaction conditions and environmental impact, especially if harmful oxidants are used *e.g.* Cr^{VI} or Mn^{VII} compounds.[2-3] Another important factor is the economic feasibility of a synthetic route in terms of large-scale applications.[5-6] Development of processes that use environmentally friendly reactants as terminal oxidants *e.g.* air or O_2 is one of the main research fields in chemical sciences.[7-9]

One well-known transition metal that is able to activate molecular O_2 by electron transfer (*oxygen activation*) and to reversibly cycle between two oxidation states is Cu.[10-12]

Thus, aerobic alcohol oxidation utilizing Cu catalysts is an alternative to harsh routes, enabling oxidation of varied substrates.[13] Some type of reactions[14-16] are able to proceed at room temperature and under atmospheric pressure, reaching full conversion of substrates within minutes.[17]

In one of those reactions Cu precursors are utilized in addition to the stable 2,2,6,6-tetramethylpiperidinyloxyl radical (TEMPO) in liquid-phase media.[18] In the most widely used protocol complexes consisting of $Cu^{I}OTf$, 2,2-bpyridine (bpy) and 1-methylimidazole (NMI) are formed *in-situ* in acetonitrile (MeCN) as solvent.[16] The Cu centers engage in an intricate way with the TEMPO radical.[19-20] **Scheme 1** depicts the concurrent redox processes of the Cu centers.

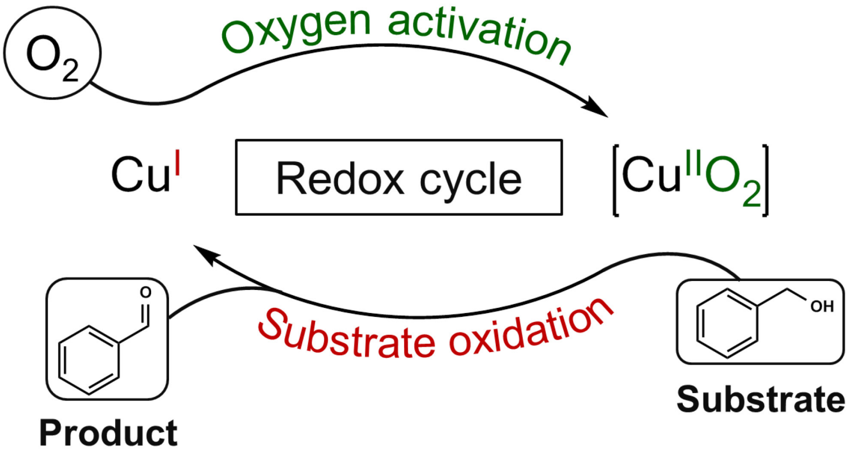

Scheme 1. The two fundamental, concurrent processes during Cu/TEMPO catalyzed aerobic alcohol oxidation.

Although the reaction has been investigated since the 1960s[21-23] open questions remain, in particular, relating to the nature and role of the active Cu species and its additives - notably NMI and TEMPO - during the catalytic cycle. Moreover, even the fundamental steps of the catalytic cycle are still not completely understood and under debate.

However, knowledge concerning precise catalyst mode of action is necessary for designing specifically tailored catalysts and hence optimizing chemical reactions. In-depth and detailed mechanistic knowledge can only be obtained by *in-situ* and *operando* spectroscopic techniques. *In-situ* measurements mean *under reaction conditions*, in this case, measuring directly within the reaction solution. Thus, alterations of the sample when taking aliquots (*ex-situ* measurements), are avoided. *Operando* spectroscopy on the other hand refers to a concept incorporating *in-situ* spectroscopy alongside real-time product detection providing useful information about the catalytic system under *working conditions*.

In the Brückner group various set-ups incorporating coupled spectroscopic techniques have been developed over the past 15 years, mainly in the field of heterogeneous catalysis[24-26] but also few homogeneous reactions in liquid phase media.[17, 27] Especially, the novel, triple coupled *operando* EPR/UV-vis/ATR-IR spectroscopy in one reaction set-up attracted considerable attention.[17]

Brückner et al. used that coupling technique to study mechanistic aspects of Cu/TEMPO catalyzed aerobic alcohol oxidation step-wise.[17] Previous extensive investigations by the Stahl group[19-20] left lots of issues unexplained *e.g.* the exact nature of the active Cu^{II} species (*monomer* or *dimer* ?) and the precise role of the TEMPO radical, since the catalytic reaction does not proceed in the absence of this additive. In literature[28-31] often peculiar redox couples between the TEMPO radical and Cu^{I} or Cu^{II} species are discussed without presenting any spectroscopic evidence for the change of the TEMPO oxidation state. The spectroscopic methods used by Brückner et al[17] have been chosen according to their different modes of action, complementarity to each other and their ability to analyze distinct components within the reaction solution. For instance, UV-vis spectroscopy as an analytical method providing knowledge about the electronic state is able to yield information about the current oxidation state of the $Cu^{I/II}$ complex during the redox processes and its coordination sphere. Thereby, this method supports EPR spectroscopy which detects paramagnetic species *e.g.* the Cu^{II} valence state and the TEMPO radical. Lastly, ATR-IR spectroscopy reveals information in terms of vibrations of characteristic functional groups making it useful in tracking substrate or product related bands.

Using the operando EPR/UV-vis/ATR-IR approach,[17] the investigations revealed clear evidence for a completely different pathway as described by Stahl et al.[19-20] Their findings rather suggest that no redox couple is formed between the TEMPO radical and $Cu^{I/II}$ species. Instead, the radical interacts most likely dipolarly with the superoxide intermediate Cu^{II}-$O_2^{\bullet-}$ and hence fixes and stabilizes that species to facilitate electron transfer from the substrate and speed up H_2O_2 formation.

However, still open questions remained requiring further detailed investigations. Most notably, the *exact* nature of the active Cu^{I} complex and its oxidation to one or more Cu^{II} species remained unclear. In addition, tentative evidence for ligand effects was found during previous studies.[16, 29, 32] These findings have widespread implications *e.g.* for selecting the highest performing ligands within the aerobic alcohol oxidation. Highly active catalytic systems utilizing pyridine-type ligands *e.g.* 4-dimethylaminopyridine (4-DMAP) for *in-situ* formation of corresponding Cu^{I} complexes have also been described in subsequent literature.[14, 33] Therefore, further investigations are needed, especially with regard to ligand variation and ligand substituent effects.

One essential drawback of the EPR/UV-vis/ATR-IR coupling, however, lies in the inability to give *precise* information about the coordination sphere of involved transition metal species, in this case $Cu^{I/II}$. Other spectroscopic methods such as X-ray absorption spectroscopy (XAS), on the other hand, are able to determine the *exact* structural arrangement around the metal center and the number of coordinated ligands regardless of valence state. XAS itself can be divided into **E**xtended **X**-ray **A**bsorption **F**ine **S**tructure (EXAFS) and **X**-ray **A**bsorption **N**ear **E**dge **S**tructure (XANES) features that examine different aspects of the X-ray absorption spectrum. To get deeper mechanistic insight extension of the current EPR/ATR-IR/UV-vis triple coupling by EXAFS/XANES techniques would be beneficial.

Which are the aims of this thesis?

Against this background and motivated by the results obtained from the existing EPR/UV-vis/ATR-IR coupling, in the first part of this thesis that particular method coupling is used to study the effect of ligands and additives on the formation of active $Cu^{I/II}$ complexes using following conditions established by the Stahl group[16]:

Cu^{I}OTf/bpy/NMI/TEMPO.

Applying this catalytic system, the oxidation and reduction behavior of the $Cu^{I/II}$ complexes within this framework shall be investigated separately in a step-wise approach. Moreover, the catalytic activity of those complexes within aerobic alcohol oxidation is studied and discussed systematically in dependence on the molar ratios of bpy and NMI. Finally, the differently substituted imidazoles have been used as additives to investigate electronic and steric effects upon the catalytic reaction.

In the second part of this thesis, a different class of ligands – pyridine-type ligands – is used to generate complexes according to conditions established by the Zhang group[14]:

$Cu^IOTf/(bpy)/4$-DMAP/TEMPO.

Likewise, coupled EPR/UV-vis/ATR-IR spectroscopy shall be used to study *in-situ* formation of Cu^I/4-DMAP complex species and their redox properties using the same step-wise approach used prior. The additional usage of bpy is discussed as well as modifications of the pyridine scaffold substituents regarding redox behavior and catalytic properties of Cu complexes composed of those compounds.

New spectroscopic coupling: EPR/UV-vis/ATR-IR/XAS

In the third part an extension of the present triple method coupling by X-ray absorption techniques shall be applied to elucidate key mechanistic aspects *e.g.* the precise structural arrangement of the $Cu^{I/II}$ redox shuttle and deactivation processes when using Stahl's[16] conditions. The existing 3-in-1 coupling is hereby extended for the first time into a 4-in-1 spectroscopic coupling involving XAS (EXAFS and XANES) measurements.

Auxiliary *ex-situ* methods have also been employed to complete the characterization of used $Cu^{I/II}$ complexes *e.g.* electrochemical measurements (CV and DPV) and low-temperature EPR and IR investigations.

2. STATE OF THE ART

2.1. Cu/TEMPO catalyzed aerobic alcohol oxidation

Alcohol oxidation in general

Selective transformation of compounds containing hydroxyl moieties (*e.g.* alcohols, sugars) to aldehydes and ketones is one of the most important chemical conversion processes in chemical and pharmaceutical industry.[1-2, 4] Historically, oxidation of alcohols in large scale quantities has been accomplished by using homogeneous as well as heterogeneous catalyst. In homogeneously catalyzed reactions, frequently toxic or non-green substances are used, *e.g.* Cr^{VI} compounds or the Swern reagent which contains toxic and odorous sulfur compounds.[1, 4] The widely distributed heterogeneously catalyzed oxidations proceed over catalysts, in which a wide range of metals, supports and solvents are utilized *e.g.* active Pd^{II} sites on PdO surfaces, Ru/Al_2O_3 and Fe_2O_3/SiO_2.[34] Often, however, heterogeneous routes require elevated temperatures or high pressure reactors, *e.g.* when utilizing supercritical CO_2 as an environmentally friendly solvent, posing technical limitations.[34] Another, heterogeneously catalyzed, but mild route employs the Fétizon reagent. Herein, the oxidation of a substrate alcohol into its corresponding aldehyde is catalyzed by Ag_2O_3 adsorbed on kieselgur as support.[35] By using these methods, a variety of primary and secondary alcohols can be converted into the corresponding carbonyl compounds, however with varying degrees of activity as well as chemo- and regioselectivity. In the following, we focus on homogeneous methods because they are object of this thesis.

Homogeneous and aerobic alcohol oxidation

Homogenous methods in the past often used toxic substances like Mn^{VII}, PCC (pyridinium chlorochromate), Ru^{IV}, hypervalent iodine compounds *e.g.* the Dess-Martin reagent or DMSO used in Swern oxidation processes.[1, 4] However, mild reaction conditions and environmentally friendly and benign reagents are commonly used within the Oppenauer oxidation and its modifications.[36] Herein, $Al(O^iPr)_3$ selectively catalyzes the oxidation of secondary alcohol substrates into ketones in the presence of excess acetone as oxidizing agent.[36] Before the development of TEMPO-catalyzed methods those were main methods for selectively transforming alcohols into carbonyl compounds.

Oxidations mediated by nitroxide radicals: TEMPO & related compounds

TEMPO belongs to a class of compounds known as nitroxide radicals which are noteworthy for their radical persistency as they are stable and isolable radicals at ambient conditions.[37-38] The reason for this stability can be attributed to two main factors[37-38]:

1) Delocalization of the free electron over the N–O bond gives rise to two resonance structures (**Scheme 2**).

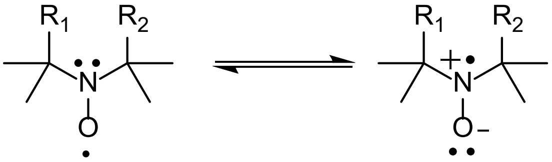

Scheme 2. Resonance structures of nitroxide free radicals

2) Steric hindrance of the N–O bond and electron density donation provided by hyper conjugation of the four methyl substituents in α-position to the nitrogen atom stabilize the radical. The former prevents the recombination of radicals such as polymerization or adduct formation. By electron density donation the oxoammonium-like resonance structure is stabilized.

Stable nitroxide radicals have been known since the 1840's when potassium nitrosodisulfonate, known as Frémy's salt,[39] was first synthesized by Edmond Frémy being still in use today, *e.g.* as EPR reference and standard for spin quantification.[40] Oxidative properties of Frémy's salt were discovered in 1951 by Teuber et al. They found that organic compounds could be oxidized by using stoichiometric amounts of that radical.[41] The stable, piperidine-type TEMPO radical was first described in 1960 by Lebedev et al.[42] and is of relevance due to its air and moisture resistance.[43] TEMPO can easily change its oxidation state by either one electron reduction or one electron oxidation processes as seen in **Scheme 3**. Oxidation yields the oxoammonium salt (TEMPO$^+$) whereas reduction yields the hydroxylamine (TEMPOH).

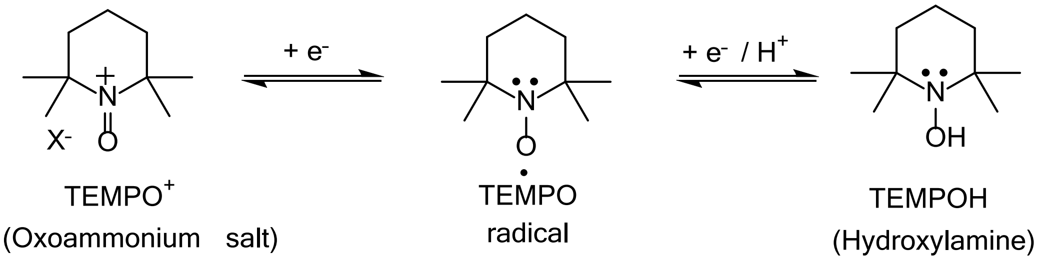

Scheme 3. Oxidation states of TEMPO

Early reports about the utilization of TEMPO regarding oxidation of alcohols were published in 1965 by Golubev et al.[44] describing the formation of acetaldehyde when stoichiometric amounts of TEMPO$^+$ are treated with ethanol.

Pioneering work in TEMPO mediated oxidation reactions has been made by Anelli and co-workers in 1987.[45] They utilized TEMPO or its derivatives in catalytic quantities combined with stoichiometric amounts of sodium hypochlorite (NaOCl) as the terminal oxidant in the oxidation of alcohols to aldehydes using a biphasic system (**Scheme 4**).

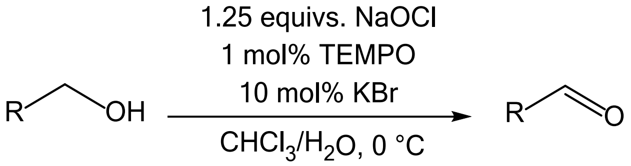

Scheme 4. Alcohol oxidaztion utilizing Anelli's procedure.[45]

Thereby they could show that the oxidation of primary and secondary alcohols can be achieved selectively (> 95%) for saturated alkyl and aryl substrates as well as different protecting groups are tolerated. Selectivity of primary alcohols over secondary alcohols is observed, which is attributed to steric hindrance imposed by TEMPO$^+$.[4]

Mechanistic investigations revealed the involvement of several species in an intricate coupled system.[4, 18, 45] TEMPO$^+$ was found to be the main catalytically active species (primary oxidant) transforming the alcohol into the aldehyde simultaneously being reduced to TEMPOH. That species is re-oxidized by a secondary, stoichiometric oxidant, *e.g.* NaOCl, to TEMPO$^+$. The oxidation of the substrate mediated by TEMPO$^+$ most likely proceeds via a five-membered transition state (**Scheme 5**) during which a bond between the hydroxyl oxygen atom of the substrate and the nitrogen atom of TEMPO$^+$ is formed.[4]

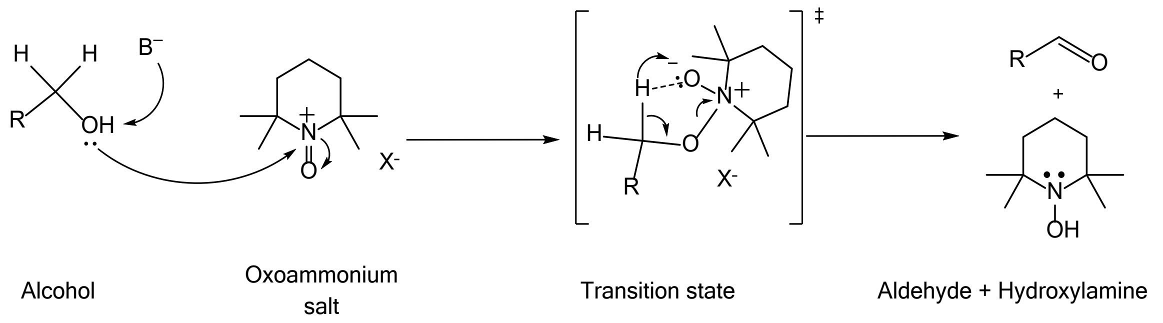

Scheme 5. Proposed transition state during the oxoammonium-catalyzed alcohol oxidation.[4]

TEMPO catalyzed aerobic alcohol oxidation

Based on observations from "*Anelli's protocol*", considerable efforts had been made to utilize molecular oxygen under ambient conditions, *e.g.* air, as a secondary or terminal (stoichiometric) oxidant within the oxidation of alcohols.[18] Under ambient conditions dioxygen (O_2) is not able to promote the direct oxidation of either TEMPOH or TEMPO radical to $TEMPO^+$ required for the oxidation of the substrate.[46] The reason for this lies in the potential required for the oxidation of TEMPO to $TEMPO^+$ at +0.76 V being too high to directly reduce O_2 to O_2^- which is at +0.11 V.[47-48] Therefore, coupled systems were developed utilizing TEMPO in addition to *e.g.* NO/NO_2 shuttles, similar to "*Anelli's protocol* ", which in turn are oxidized by O_2.[49] However, one disadvantage is the need for relatively high temperatures (80 °C–100 °C).[49]

Copper/TEMPO-catalyzed aerobic alcohol oxidation

One alternative to elude those obstacles is incorporation of transition metal ions as catalytic species. Often, activation of small molecules *e.g.* O_2 (*oxygen activation*) or N_2 can be catalyzed by transition metal ions since the activation barrier is lowered[9, 50] as occurring in ubiquitous biochemical processes necessary to sustain life.[51] Moreover, different valence states of a metal center enable (coupled) cycles similar to those participating in "*Anelli's protocol*". Besides, coordination effects by different ligands as well as substrates to metal centers are known to tune activity and selectivity of catalytic reactions being a well–known phenomenon in naturally occurring enzymes.[52-54] Especially substrate coordination is an important factor in enhancing its reactivity as the metal center serves as a template, thus, facilitating reactions with other components present in solution.[31]

In biochemistry, Cu plays a pivotal role in promoting chemical reactions within many classes of proteins and enzymes.[55-56] Various reactions are catalyzed by Cu containing enzymes *e.g.*

redox reactions by *cytochrome c oxidases* (active in respiratory electron chain, necessary to drive ATP synthesis) or disproportionation reactions in *Cu/Zn superoxide dismutase* (catalyzing decomposition of highly reactive $O_2^{\bullet -}$ species into less reactive O_2 and H_2O_2).[55] Most Cu containing enzymes, *e.g.* cytochrome c oxidases are essential for life and therefore have been studied extensively.[12, 55] One particular enzyme known as *galactose oxidase* attracts interest of catalytic scientists, since the active Cu site is well characterized and known for containing a free radical ligand.[52, 54, 57-58] The role of the enzyme, which is found in fungal organisms from *e.g.* the *Fusarium* and *Aspergillus* genera, is to activate molecular O_2 to oxidize substrates *e.g.* alcohols and sugars to their corresponding carbonyl compounds.[58-59] As a byproduct H_2O_2 is formed which can also be utilized by these organisms and might be of even greater importance than the carbohydrate derivatives being a bacteriostatic agent.[60] Thus, the enzyme mode of action makes it a viable candidate for biomimetic approaches.[58]

First reactions that make use of similar catalytic systems, *i.e.* Cu centers in combination with stable free radicals, have been reported by Brackman and Gaasbeek in 1966.[21-23, 61] They described a catalytic system consisting of $Cu^{II}(NO_3)_2$, 1,10-phenanthroline, (*t*-butyl)$_2$NO$^\bullet$ free radical and $NaOCH_3$ in methanol being both, the solvent and the substrate (**Table 1**, entry 1). The reaction was typically carried out at elevated temperatures between 30-45 °C and formaldehyde could be detected as oxidation product upon O_2 bubbling.[22-23] They reported reduction of Cu^{II}-methanol complexes by nitroxide radicals even in absence of oxygen. Introducing oxygen led to reoxidation of formed Cu^{I} species.[22]

In 1984 Semmelhack et al. published a pioneering paper about a catalytic system being able to efficiently convert aromatic and allylic alcohols into aldehydes by using catalytic amounts of TEMPO, $Cu^{I}Cl$ in DMF while bubbling O_2 into the solutions (**Table 1**, entry 2).[30] Curiously, despite the similarities in their catalytic systems, the authors were obviously *not aware* of the previous studies conducted by Brackman and Gaasbeek. Most substrates – primary aromatic and allylic alcohols – could be converted into their corresponding aldehydes within 1-4 hours.[30] The conversion of aliphatic alcohols, however, required more demanding conditions, since the use of stoichiometric amounts of TEMPO, $Cu^{II}Cl_2$ in combination with a strong base, CaH_2, was necessary to obtain significant conversion. Improvements of *Semmelhack's protocol* or additional contributions regarding this topic had been sparsely made during the mid-late 1980s and 1990s. In 1985, Tretyakov et al. reported about the use of Cu^{II} precursors in combination with 1,10-phenanthroline as catalytic systems. The authors studied the oxidation of isopropanol to aceton in basic aqueous media as model reactions.[62] Early mechanistic investigations were conducted which highlighted the importance of Cu^{2+} reduction to maintain the catalytic cycle.

However, significant improvements regarding aerobic alcohol oxidation began to develop in 2000 with studies by Knochel et al.[63] They described a biphasic system consisting of Cu^{I} precursors, perfluoroalkylated 2,2-bpyridine and the TEMPO radical using perfluorooctane/chlorobenzene as solvent in the oxidation of primary and secondary alcohols to their corresponding carbonyl compounds (**Table 1**, entry 3).[63] The Cu^{I}/bpy complex is formed *in-situ* from its individual components and is soluble in perfluorooctane whereas the aldehyde product is only soluble within the chlorobenzene layer. Thereby, separation between the product and the catalyst is facilitated and the catalyst can be used for further catalytic runs. For this reaction a temperature of 90° C were needed. That system also showed high activity in the conversion of primary or secondary aliphatic alcohols. The conversion time for the model substrate *p*-nitrobenzylalcohol was 4 h whereas for secondary alcohols reaction times between 8 and 17 h were required. In a following paper they described extended substrate scopes of aliphatic as well as aromatic substrates showing that aromatic substrates are more easily converted.[64] Main disadvantages of their approach are the need for relatively high reaction temperatures and the usage of chlorobenzene as solvent. Interestingly, Knochel et al.[64] described the main active species as $TEMPO^{+}$ in a very similar mechanistic approach compared to Semmelhack et al.[30, 65] (*vide infra*).

Aerobic alcohol oxidation attracted even more widespread attention after the works of Sheldon et al. beginning in 2002.[29, 66-67] They utilized a Cu^{II} precursor, $CuBr_2$, in addition to bpy, TEMPO and potassium tert-butoxide (*t*-BuOK) as a strong base in the conversion of primary aromatic and aliphatic alcohols in aqueous MeCN solution (**Table 1**, entry 4).[66] In a model reaction benzyl alcohol (BzOH) as the substrate was transformed into benzaldehyde (BA) in full conversion within 2.5 h. Other activated allylic alcohols were also completely converted, but longer reaction times were required. Secondary aromatic/aliphatic alcohols did not show any reactivity under these reaction conditions. Sheldon et al. also carried out extensive optimization studies.[66] They utilized different Cu^{II} salts as precursors for the *in-situ* active complex formation. Thereby they could reveal that salts with weakly (*e.g.* Br^{-}) or non-coordinating anions (ClO_4^{-}) show highest activity compared to stronger coordinating Cl^{-} or NO_3^{-} counterions. This was attributed to a facilitated dissociation of the Cu^{II} precursor and complexation by the bpy ligand. They found that, without the potassium *tert*-butoxide base, the activity is lowered but conversion still reaches 27% after 1.5 h within the model reaction. Curiously, *no activity* of the catalytic system was observed when solely using MeCN as solvent; only addition of H_2O led to significant conversion.[29] However, if the amount of H_2O was too high, the activity of the system decreased markedly. These effects were attributed to the increased solubility of *t*-BuOK in aqueous media and the solubility of BzOH within the solvent and precipitation of Cu-OH species. Interestingly, replacement of bpy with 4,4-MeO-bpy showed significantly higher activity, as full conversion of BzOH is achieved within 1 h.[29]

Koskinen et al. in 2009 made significant improvements towards Sheldon's system.[32] Instead of inorganic bases such as *t*-BuOK and CaH_2 they tested organic bases *e.g.* NMI or DBU in combination with lower amounts of $Cu^{II}Br_2$, 2,2-bpy and TEMPO simultaneously replacing aqueous media with organic solvents (**Table 1**, entry 5).[32] In this way they were able to transform aromatic and allylic alcohols into their corresponding aldehydes in good yields within 0.5 – 2 h. Aliphatic alcohols typically showed low activity depending on the used base. Only a combination of 3 mol% NMI and 3 mol% DBU lead to nearly 50% conversion of those substrates after 20 h. Moreover, increased reactivity for aliphatic alcohols was found when $Cu^{I}Br$, as a Cu precursor and NMI as the sole base, were used. Similar to the work of Sheldon et al.[66] they focused on the influence of the Cu counterions on the catalytic activity as they assumed that coordinating anions, especially halogenides, could lead to precipitation of Cu-OH species which were postulated to form during the catalytic cycle. By replacing $Cu^{II}Br_2$ with $Cu^{II}OTf_2$ as the Cu source they were able to oxidize aliphatic substrates in nearly full conversion. Additional use of 3 Å molecular sieves to absorb formed traces of H_2O during catalytic cycle caused dramatically improved activity. Thereby, reactivity towards aliphatic alcohols increased significantly by tolerating also various protecting groups and other functional groups.[18, 32] Secondary alcohols, however, required elevated temperatures of 40 °C and significantly prolonged reaction times to yield the corresponding ketones.

Further advances, sophisticated and elaborate substrate optimization and mechanistic studies were achieved by the Stahl group beginning in 2011.[16] They dedicted increased attention to this green alternative oxidation route[18] establishing it as a benchmark reaction for practical courses[68] and scientific studies[69] as well as possessing potential for large–scale industrial application.[6, 70] The major advancement made by Stahl et al. was the replacement of Cu^{II} precursors by Cu^{I} salts while in general maintaining Koskinen's conditions (**Table 1**, entry 6).[16] They identified the most efficient reaction parameters enabling fast conversion of activated, primary alcohols into their corresponding aldehydes in less than 20 min using O_2 from ambient air as terminal oxidant. A variety of substrates including primary aromatic as well as aliphatic alcohols and substrates possessing heteroatoms (*e.g.* heterocycles) or functional groups (*e.g.* aryl halides, esters, ethers, thioethers) could be converted into the desired carbonyl compounds in yields typically greater than 85%. However, aliphatic and non-activated alcohols expectedly showed lower activity and required significantly longer reaction times. By using Cu^I precursors for the formation of active Cu complexes they found the reactivity of the system to increase dramatically omitting the need for stronger bases[71] *e.g.* *t*-BuOK or DBU as used in previous studies.[32, 66] Cu^I precursors having non-coordinating anions *e.g.* OTf^- or PF_6^- showed improved activity compared to halide counterions. Secondary alcohols showed only poor reactivity towards Stahl's initial reaction conditions.[16] In 2013, Stahl et al. published an updated protocol, enabling the oxidation of primary *and* secondary aromatic *as well as* aliphatic alcohols with nearly equal efficacy. The main reason for improved reactivity was the replacement of TEMPO with ABNO, a similar nitroxide free radical, but sterically less hindered due to a bicyclic backbone (**Scheme 6**).[15] They found that utilizing ABNO lead to similar reaction rates for all classes of alcohol substrates.[15, 18] Remarkably, by optimizing the reaction conditions, it turned out that the amount of free radical could be reduced from 5 mol% to 1 mol% without significant decrease in reaction rates. Introduction of 4,4-MeO-bpy further improved catalytic activity.

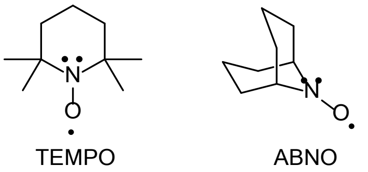

Scheme 6. Comparison of TEMPO and ABNO radical structures.

Subsequent studies by Stahl et al. mainly focused on mechanistic issues, in particular to the intricate interaction between the $Cu^{I/II}$ shuttle and the nitroxide free radical (*vide infra*).[19-20, 28, 68, 71] In 2014 Zhang et al.[14, 33] could show that catalytic systems consisting of a $Cu^{I/II}$ precursor in combination with pyridine-type ligands *e.g.* 4-DMAP in addition to TEMPO possess high activity towards primary aromatic alcohols (**Table1**, entry 7) using H_2O as solvent.[14, 33] They found that the catalyst is active in aqueous media being a major advantage to previous catalytic systems using organic solvents. A ratio of at least 1:2 Cu^ICl/4-DMAP was necessary for the reaction to proceed smoothly. Optimization studies similar to Stahl et al.[16] regarding the oxidation state of the Cu precursor, revealed that Cu^I salts exhibited higher activity; however, Cu^{II} precursors still possessed catalytic activity in contrast to Stahl's system using bpy/NMI.[14] Contrary to other reports, Zhang et al. found that Cu^I halides were superior to other counterions when H_2O is used as solvent. Primary aromatic and heteroaromatic alcohols could be converted into their corresponding aldehydes using reaction conditions shown in **Table1**, entry 7 within 5 h. However, aliphatic alcohols only showed low reactivity using this catalytic approach. Activity towards secondary alcohols was less compared to primary ones, unless TEMPO is substituted for ABNO facilitating their conversion at similar reaction rates. In a subsequent paper from 2015 Zhang et al. described the formation and precipitation of several Cu complexes *e.g.* tetranuclear Cu^{II} clusters bearing a $Cu_4(\mu\text{-}O)Cl_6$ unit and chlorido bridged $Cu_2(4\text{-}DMAP)_4Cl_2$ complexes within reaction solutions under catalytic conditions.[33] Those complexes were found to be catalytically active reaching full conversion of BzOH using methanol as solvent.[33]

Table 1. Short historical overview about the development of Cu/TEMPO catalyzed aerobic alcohol oxidation.

Entry	Reference	Year	Substrate alcohol	Cu precursor	Ligand	Additive	Base	Free radical	Solvent	Notes
1	Brackmann, Gaasbeek	1966[21-23, 61]	Methanol	0.007-0.02 mol% $Cu^{II}(NO_3)_2$	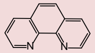 2.0 equivs. relative to Cu	–	0.03 mol% $NaOCH_3$ or KOH	0.01-0.03 mol% 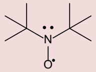	MeOH	30–45 °C, O_2
2	Semmelhack et al.	1984[30]	Primary aromatic, allylic	10 mol% $Cu^{I}Cl$	–	–	–	10 mol% 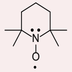	DMF	r.t., O_2
			Primary aliphatic	stoichiometric $Cu^{II}Cl_2/Cu^{II}Br_2$	–	–	CaH_2	Stoichiometric 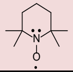	DMF	r.t., O_2
3	Knochel et al.	2000[63]	Primary aromatic & aliphatic	2 mol% $Cu^{I}Br(Me_2S)$	2 mol% 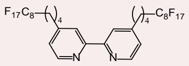	–	–	3.5 mol% 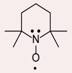	C_8F_{18}/ PhCl	90 °C, O_2
		2002[64]	Secondary aromatic & aliphatic (lower activity)							
4	Sheldon et al.	2002[67] 2003[72]	Primary aromatic & aliphatic	5 mol% $Cu^{II}Br_2$	5 mol% 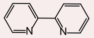	–	5 mol% *t*-BuOK	5 mol% 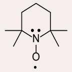	MeCN/ H_2O (2:1)	r.t., air
		2004[29]			5 mol% 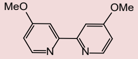					
5	Koskinen et al.	2009[32]	Primary aromatic & aliphatic	3 mol% $Cu^{II}Br_2$ or $Cu^{II}(OTf)_2$	3 mol% 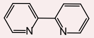	3 mol% 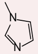 and/or 3 mol% 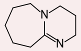		3 mol% 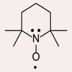	MeCN	r.t., O_2 balloon, 3 Å mole sieve
6	Stahl et al.	2011[16]	Primary aromatic & aliphatic	5 mol% $Cu^{I}OTf$	5 mol% 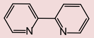	5 mol% 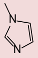	–	5 mol% 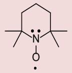	MeCN	r.t., air
		2013[15]	Primary & secondary aromatic and aliphatic	5 mol% $Cu^{I}OTf$	5 mol% 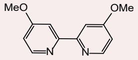	5 mol% 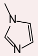	–	1 mol% 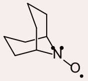	MeCN	r.t., air
7	Zhang et al.	2014[14, 33]	Primary aromatic	5 mol% $Cu^{I}Cl$	10 mol% 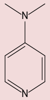	–	–	5 mol% 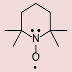	H_2O	r.t., air
			Secondary aromatic					5 mol% 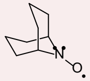		

Proposed reaction mechanisms for Cu/TEMPO-catalyzed aerobic alcohol oxidation

Based on the literature three prevailing reaction mechanisms shall be discussed. Semmelhack et al. presented an early mechanistic proposal[30] which, however, is not based on spectroscopic evidence or kinetics but rather borrows concepts from solely TEMPO$^+$ catalyzed alcohol oxidations.[65]

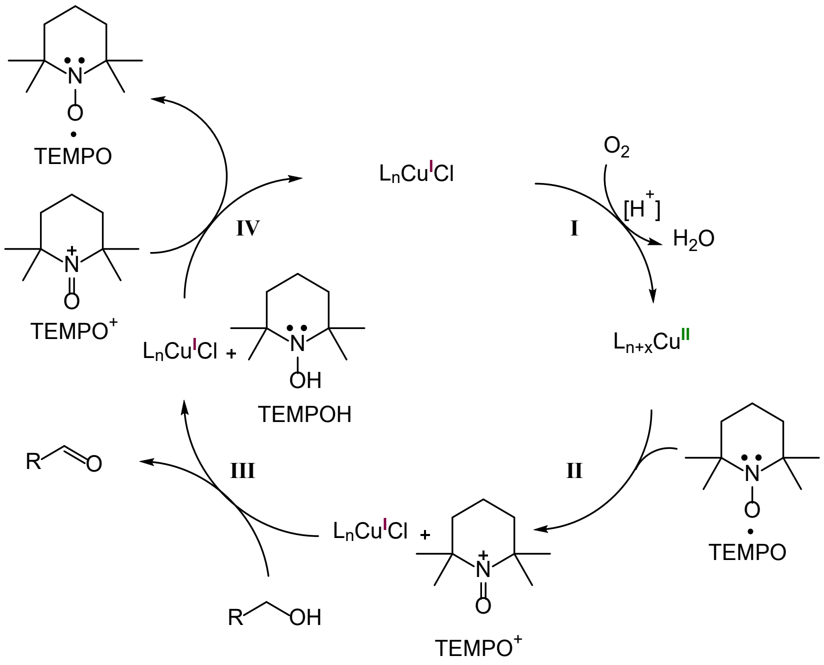

Scheme 7. Mechanism for aerobic alcohol oxidation produced from a scheme of catalytic sequences by Semmelhack et al.[30] L_n in this case being used to denominate the coordinating solvent.

The catalytic sequences presented in **Scheme 7** are based on empirical evidence from the screening of reaction parameters as well as previous electrochemical studies[73-74] and studies about the redox behavior of nitroxide radicals.[44]

Originally, they formulated the sequences starting with Cu^{II} valence state. However, since a Cu^I precursor (Cu^ICl) was used within their studies and the Cu species are regenerated during the cycle, for the sake of clarity, the Cu^I oxidation state was chosen as the starting point. Starting with Cu^ICl, in **step I** O_2 is activated, forming H_2O as a byproduct, simultaneously oxidizing Cu^I to Cu^{II}. Subsequently, the TEMPO radical reacts during **step II** with the formed Cu^{II} species to yield the TEMPO$^+$ oxoammonium species. Moreover, regeneration of the Cu^I starting material takes place. In step **III** the substrate alcohol is oxidized by TEMPO$^+$ leading to formation of the TEMPOH hydroxylamine state and the aldehyde product. Step **IV** concerns the regeneration of the TEMPO radical by synproportionation of TEMPOH and TEMPO$^+$. However, several open questions remain as their research does not take into account *e.g.* solvent and ligand effects of DMF on the redox properties of the $Cu^{I/II}$ shuttle.[75-78] Furthermore, no direct spectroscopic evidence for the formation of TEMPO or TEMPOH and their catalytic activity was provided. However, evidence for the involvement of such species is derived from their previous research in the TEMPO-mediated electrocatalytic oxidation of alcohols to aldehydes.[73-74] They could show that during electrocatalytic oxidation $TEMPO^+$ is formed, evidenced by the appearance of distinct redox features. The $TEMPO^+$ species leads to oxidation of the substrate as consumption of the alcohol could only be detected after generation of $TEMPO^+$. However, because the reaction could be carried out at an oxidation potential of +0.4 V vs $Ag/AgNO_3$, being considerably lower than needed for direct oxidation of TEMPOH (requiring a potential of +0.8 V in MeCN vs $Ag/AgNO_3$), another process must be involved. Thus, they proposed synproportionation between $TEMPO^+$ and TEMPOH to occur as it was found that two $TEMPO^+$ or TEMPO species are needed for conversion of one substrate molecule .[30, 73]

The most prominent mechanistic proposals were made by the Stahl group.[15, 18-20, 28, 31] Borrowing many aspects from Koskinen et al.[32] and Sheldon et al.[29] as well as previous concepts about oxygen activation in Cu systems (*e.g.* Stack et al.[12, 57] and Tolman et al.[10-11, 79]). Stahl et al. combined these findings with their own vast amount of spectroscopic results formulating a reaction cycle comprising four main steps (**Scheme 8**).[15, 18-20, 28, 68]

However, Stahl's proposed mechanisms differ significantly from Semmelhack's proposal in terms of involved species and their redox processes. Complex **1** is formed *in-situ* by adding bpy and NMI to a solution of $Cu^{I}OTf$ in MeCN. Complexation of Cu^I by bpy was evidenced from *in-situ* UV-vis studies which show appearance of broad MLCT bands at approx. 550 nm.[20] However, additional coordination of NMI was not further discussed, since the components had not been added successively and bpy is known to yield broad absorptions in UV-vis leading to overlapping bands.[80-82] When in step **I** O_2 is introduced into the solution, a color change from brown to deep green can be observed accompanied by appearance of a broad band centered around 650 nm increasing with time. That feature is highly indicative of a d-d transition band of Cu^{II} since the characteristic broad MLCT absorption band for Cu^I-bpy complexes around 550 nm disappears simultaneously. The nature of the formed Cu^{II} species, however, is still unclear. Kinetic studies show a 1st order dependence on $[O_2]$ and a mixed 1st order/2nd order dependence on [Cu], therefore the authors proposed a two-step process with the initial formation of a Cu^{II}-superoxide mononuclear species reacting with another unit **1** to yield the peroxo-bridged Cu^{II} dimer **2** $(Cu^{II})_2O_2$.[11, 20] Such processes are known to occur in biological as well as biomimetic Cu^I containing systems.[11, 83] Then, the cleaving of such Cu^{II} dimers by TEMPOH is proposed leading to complex **3**. However, no spectroscopic evidence for the formation of that species is presented.

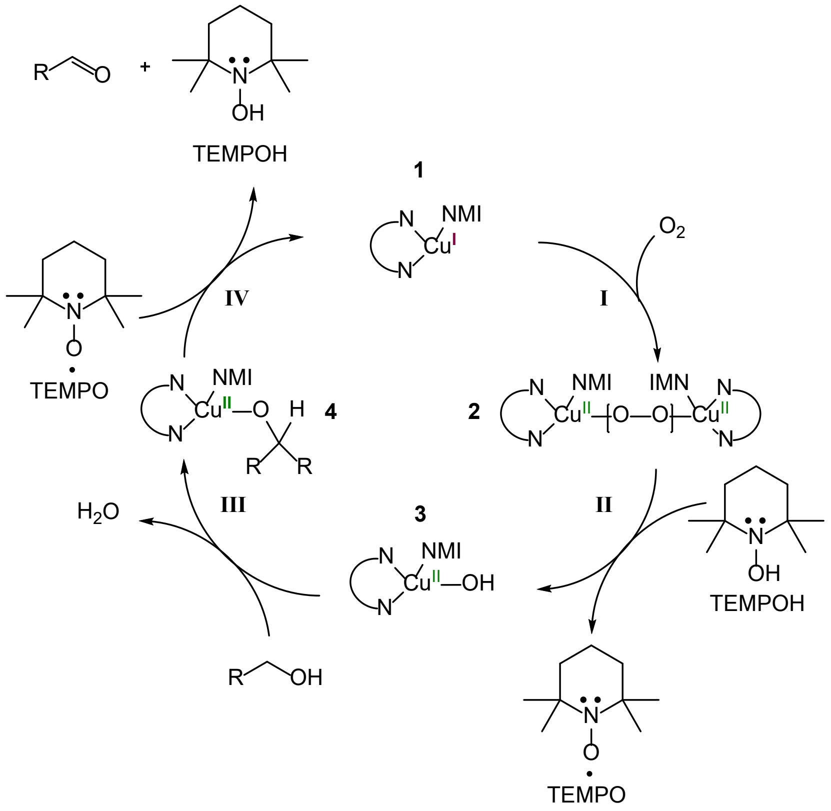

Scheme 8. Reaction mechanism proposed by Stahl et al. in 2013.[20]

Furthermore, TEMPOH is not present in the reaction solution at the beginning as only TEMPO *radical* is added. But how is TEMPOH formation possible under such conditions? Stahl et al. proposed the idea,[19-20] stemming from Koskinen et al.,[32] that a Cu^{II} species stoichiometrically reacts with the substrate in presence of TEMPO generating TEMPOH during an initiation step. Even if TEMPOH may be pre-formed by a stoichiometric reaction, a simultaneous decrease of the Cu^{II} species should be observed, which was not reported. If TEMPOH supposedly cleaves such peroxo Cu^{II} dimers to yield Cu^{II} monomeric hydroxy species in step **II,** an increasing amount of Cu^{II} species should be expected. Simultaneous EPR-investigations were carried out, however, only under *ex-situ* conditions. Over the course of the reaction the Cu^{II} signal only emerged when O_2 was introduced. Since the rise of the Cu^{II} signal indicates paramagnetic species (most Cu^{II} dimers are EPR-inactive[83]) and displays typical characteristics of a mononuclear species[84-85] it is unlikely that an EPR-active dimer is responsible for this signal. Likewise, an increase of the TEMPO EPR signal intensity has not been reported, which is expected to occur, as EPR-silent TEMPOH is oxidized to paramagnetic TEMPO radical when those dimers are broken up. Both, the formed (bpy)Cu^{II}-OH complex **3** as well as their corresponding dimeric species, the bis-μ-hydroxy (bpy)Cu^{II} dimer, were proposed as an active and resting species by kinetic isotope effect (KIE) studies and DFT calculations.[19-20, 28] The authors speculated that the bis-μ-hydroxy dimer is in equilibrium with the Cu^{II}-OH monomeric species and that formation might be facilitated by high concentration of H_2O. However, they could show, that those Cu^{II} dimers can be precipitated out of the reaction solution and are catalytically active, in fact possessing similar reaction rates after an induction period.[19]

In separate EPR and electrochemical studies Stahl et al. showed that TEMPO neither significantly influences the Cu^{II} EPR signal nor the redox potential of the Cu^{I}/Cu^{II} shuttle.[20] During step **III** the substrate is supposed to be deprotonated by Cu-OH species, acting as a pre-formed base, and in turn coordinates at the Cu^{II} center while 1.0 equivalent H_2O is released and species **4** is formed. During the last step **IV**, coordinated alcohol at species **4** is oxidized by TEMPO radical to the corresponding aldehyde with simultaneous reduction of TEMPO to TEMPOH and regeneration of starting material **1**. For this step, too, no direct spectroscopic evidence has been presented substantiating the formation of TEMPOH. Significant decrease in TEMPO EPR signal intensity, which would confirm this mechanistic step was not reported.[19-20]

In summary, Stahl's reaction mechanism reflects reasonable concepts (*e.g.* activation of O_2) but the authors fail to provide pivotal evidence for other conclusions *e.g.* the interaction of the formed Cu^{II} complex with TEMPO. However, they could show that a direct redox interaction between Cu centers and TEMPO radical, previously suggested by Semmelhack et al.,[30] is highly unlikely meaning a paradigm shift.

In addition, Stahl et al. performed KIE studies to further elucidate the reaction mechanism. They could show that a KIE of ~ 1 is derived for aromatic alcohol substrates, meaning that C-H cleaving is not rate limiting in this case. However, if aliphatic alcohols are used, a distinct KIE is observed implying that aliphatic and aromatic alcohols differ in their turnover limiting steps. This was attributed to a higher bond dissociation energy of the C-H bond for aliphatic alcohols.[20, 86-87] This corresponds well to the kinetic profil of the reaction as, in addition to the first and mixed-order dependence on [O_2] and [Cu], respectively, 0th order dependence was found for [BzOH] and [TEMPO] evidencing the rate-determining step to be Cu^{I} oxidation but not substrate oxidation.[15, 18-20]

In subsequent papers, Stahl et al. again discussed the possibility of direct coordination of the TEMPO radical replacing NMI in the coordination sphere of the Cu^{II} active site.[28] By DFT calculations and the utilization of radical probe substrates they could reveal that the electron transfer during the substrate oxidation (**step IV**) most likely does not appear to proceed via radical intermediates (*e.g.* homolytic α-C-H bond dissociation) but rather in a concerted fashion with simultaneous electron transfer.[28] Such transition state was also proposed by Sheldon et al., similar to the radical of the active *galactose oxidase* site, in which TEMPO is coordinated in a η^2 fashion to the Cu^{II} species.[72] Stahl et al. discussed several transition states and α-hydrogen transfer mechanisms based on DFT calculations, where the η^1 coordinated nitroxyl radical proved to be the most stable one, being similar to the transition state encountered within the Oppenauer alcohol oxidation (**Scheme 9**).[28, 36]

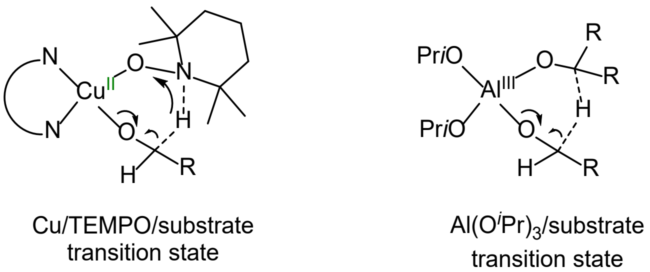

Scheme 9. Transition state during Cu/TEMPO catalyzed aerobic alcohol oxidation proposed by Stahl et al.[28] compared to the transition state occurring during the Oppenauer alcohol oxidation.[36]

However, no experimental evidence for the coordination of TEMPO – neither in η^1 nor in η^2-mode – has been reported by the authors. These statements seem questionable, since the proposed Cu^{II}-TEMPO adduct during the transition state should also form in the absence of the substrate, which would be easier to detect due to less interference. Even more, since replacement of one ligand of the Cu^{II} complex in favor of TEMPO coordination was calculated to be energetically unfavorable.[28] In 2017 Stahl et al. reported about XANES/EXAFS studies of solid Cu^{II}-nitroxyl complexes, precipitated from reaction solutions, combined with DFT calculations revealing a distinct *oxoammonium character* of coordinated nitroxyl species and hence Cu^{II} oxidation states that *tend* to be more reduced.[31] Yet, it was revealed that Cu^{II} is not able to *fully* oxidize TEMPO to $TEMPO^+$ but provides an "*activation*" making it prone to reduction by the substrate while the Cu^{II} center merely serves as a *template* for the coordination of the substrate.[31]

The third and most recent mechanistic cycle was suggested by the Brückner group in 2015.[17] The authors studied the reaction mechanism (proposed by Stahl et al.[20]) systematically using a coupled 3-in-1 *in-situ* spectroscopic approach.[17] For their detailed spectroscopic investigations they implemented a specifically built reactor enabling simultaneous *operando* EPR/UV-vis/ATR-IR measurements. Based on their findings they proposed a new mechanism (**Scheme 10**). At first, oxygen activation (**step I**) in Stahl's mechanism was studied. *In-situ* UV-vis and EPR measurements revealed that oxidation of Cu^I to Cu^{II} only occurs in the presence of NMI. Without NMI the characteristic MLCT bands of the Cu^I-bpy complex around 450/550 nm only slightly decreased during O_2 bubbling and no significant d-d transition band in the region of 650 nm could be observed. Simultaneously, the EPR spectra only showed a very small Cu^{II} signal. However, upon addition of NMI to this aerated solution, the Cu^I MLCT bands immediately decreased with concurrent appearance of a well-pronounced band around 650 nm attributed to a d-d transition of Cu^{II} species.[17] Similar conclusions could be drawn from EPR spectra which show a rapidly increasing, isotropic Cu^{II} signal. From *ex-situ* measurements a coordination of NMI to a Cu^{II} complex could be veryfied. These findings underline the significance of NMI coordination to the Cu^I species in facilitating one electron transfer to the O_2 molecule while simultaneously oxidizing Cu^I to Cu^{II}. Hence, Brückner et al. proposed the formation of an end-on superoxide **2**, Cu^{II}-$O_2^{-\bullet}$ which in turn is stabilized by the TEMPO radical present in solution (step **II**) yielding species **3**. Addition of the model substrate BzOH did not lead to significant changes in both the UV-vis and the EPR spectra in the *absence* of TEMPO. However, when TEMPO was added, immediate decrease of the Cu^{II} EPR signal could be observed which was paralleled by increase in MLCT bands of Cu^I and decrease of the d-d transition band. These results suggest that reduction of Cu^{II} to Cu^I only takes place in the presence of the TEMPO radical (step **IV**). By simultaneous *operando* IR measurements the conversion of BzOH to BA could be evidenced by the evolution of a band around 1702 cm^{-1} which is related to the ν(C=O) vibration of BA.

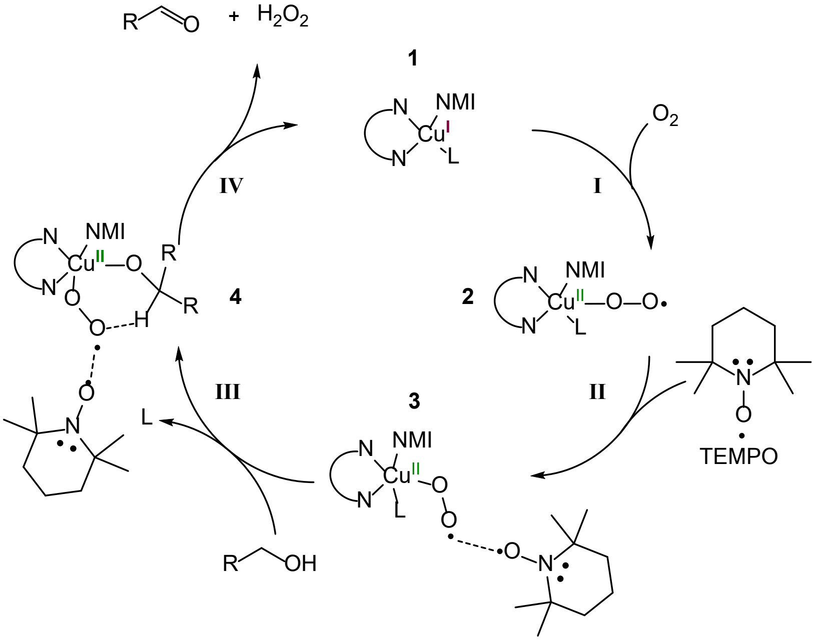

Scheme 10. Simplified reaction mechanism based on *in-situ* studies by the Brückner group.[17]

A six-membered transition state **4** between Cu^{II}-$O_2^{-\bullet}$-TEMPO and the alcohol via concerted electron transfer was proposed when the substrate is added (step **III**). Nevertheless, some assumptions remain challenging such as the lack of evidence for the formation and stability of intermediate species being well-known as highly unstable *e.g.* Cu^{II}-superoxide[88-89] or Cu^{II}-hydroperoxide.[90-91] The existence of a weak dipolar interaction between a superoxide and TEMPO radical also seems troublesome. Such interaction should be strong enough to fixate and activate the superoxide[17] but similar structural motifs (*e.g.* "*ozonide-like* ") are unstable under ambient conditions.[92-93] Moreover, neither experimental evidence nor DFT calculations were provided for the occurrence of a six-membered transition state involving superoxide/TEMPO interaction. However, later DFT studies by Li et al regarding Brückner's mechanistic proposal showed that such a pathway is not possible under ambient conditions since it involves energetically unfavorable transition states.[94]

The Brückner group specifically studied the intricate interaction between TEMPO and the Cu centers as well as O_2[17] apart from the previously mentioned step-wise approach. When TEMPO is added to a pre-oxidized solution of Cu^{I}/bpy/NMI no significant changes in the EPR signal of Cu^{II} are observed. In separate experiments, TEMPO was added to Cu^{II} precursors, *e.g.* $Cu^{II}OTf_2$, under inert atmosphere which also did not lead to significant changes in the EPR signal of either Cu^{II} *or* TEMPO. The authors conclude that no *direct* interaction between TEMPO and Cu^{II} occurs regardless if a Cu^{I} or Cu^{II} precursor is used to generate Cu^{II}/bpy/NMI complexes.[17] Regarding the TEMPO signal they found that the radical signal *does* undergo changes: Thus, dipolar interaction of O_2 introduced into Cu^{I}/bpy/NMI/TEMPO containing solutions broadens the TEMPO EPR signal considerably.[95] Interestingly, this feature is completely reversible when the same solution is flushed with N_2 or Ar. Even in *absence* of $Cu^{I/II}$ complexes or *other* reaction components the TEMPO signal displays the same behavior. Based on these results, the structure of intermediate **3** was justified, which is a weakly interacting adduct between Cu^{II}-$O_2^{-\bullet}$ and TEMPO radical. The proposed function of this species is said to "*fixate and activate*" Cu^{II}-$O_2^{-\bullet}$ making it more prone to oxidize the substrate alcohol in **step IV** by simultaneous generation of H_2O_2.

Further spectroscopic investigations revealed the broadening of the TEMPO signal, caused by formation of the Cu^{II}-$O_2^{-\bullet}$-TEMPO adduct, to be reversible when adding BzOH *despite* continuous O_2 flow. These findings suggest the cleaving of the weakly interacting adduct as long as substrate is present in oxygenated solutions.[17]

2.2. Coupling of *in-situ* methods in homogeneous systems

As demonstrated above, it is important to combine several *in-situ* spectroscopic methods in *one* set-up to answer those intricate mechanistic questions. Especially, the *operando* concept – addressing *in-situ* measurements under real catalytic reaction conditions (the term coined by Bañares in 2002[96-97]) – enables the analytical chemist to differentiate between active and inactive Cu^{II} complexes under working conditions. Compared to *ex-situ* measurements, the coupled ap-proach provides in-depth characterization in real-time and simultaneously, allowing for one-to-one data comparison of involved techniques. *Ex-situ* analyses on the other hand often cannot be directly compared to real-time conditions due to *e.g.* time delay and unstable intermediate species, in this case the Cu^{II}-$O_2^{-\bullet}$-TEMPO adduct. Consequently, pro-found mechanistic insight can only be obtained by coupled *in-situ* spectroscopic methods.

Ideally, those coupled techniques are complementary, meaning that one spectroscopy compensates for the disadvantages of other methods, *e.g.* UV-vis in combination with EPR spectroscopy, since the latter inherently measures paramagnetic compounds only. Another example is the implementation of IR alongside Raman spectroscopy, as they have different selection rules regarding excitation of vibrational states.[27] Implementation of spectroscopic techniques in homogeneous, liquid-phase media is often achieved by using fiber-optical immersion probes *e.g.* for UV-vis, ATR-IR and Raman spectroscopy gaining more widespread prominence in the early 2000s due to advances in fabrication of efficient optical fibers, in particular for the mid-infrared region.

Combinations of *in-situ* UV-vis, IR and/or Raman spectroscopy are widely used in liquid-phase media as shown by Grabow and Bentrup.[27] Thus, the benefit of those coupled spectroscopies for elucidating distinct mechanistic aspects within catalytic reactions was demonstrated.[27]

The advantage of using combined *in-situ* UV-vis and IR spectroscopy was nicely shown in a study by Das et al.[98] concerning the *n*-Bu_4NF (TBAF) catalyzed reduction of phtalimides to the corresponding indolinone using diphenylsilane as reducing agents. Since indolinones are interesting building blocks in pharmaceutical industry, detailed mechanistic understanding of that reaction is necessary.[99] Activation of the silane by the additive TBAF could be proven by monitoring the particular IR bands while product and byproduct formation was monitored by the corresponding UV-vis absorbances as well as intensity of the C=O moiety by

IR spectroscopy. Evidence for five- and six-coordinated reactive silicon species, formed during reaction, was collected.

As an add-on, Mellmann et al.[100] implemented Raman spectroscopy alongside *in-situ* UV-vis and IR spectroscopy in a triple method coupling. Therefore, a specially designed five-neck reactor was used, enabling the implementation of spectroscopic probes, for studying the Fe-catalyzed decomposition of HCOOH. Because that reaction could be a sustainable route to produce H_2 and CO_2, detailed studies had been conducted. The $Fe/P(PPh_2)_3$ catalyst was found to be activated by coordination of formic acid evidenced by distinct bands in the UV-vis range. In the corresponding Raman spectra coordination of the solvent (THF) and replacement by formic acid could also be observed, as well as the interaction with chloride ions by appearance of distinct Fe-Cl bands in the Raman spectra. That was further substantiated by the simultaneously acquired IR spectra and gas analytics showing the detrimental effects of NaCl on the activity of the catalytic system.

Other interesting and more sophisticated coupling techniques *e.g.* involve the coupling of *in-situ* UV-vis and energy dispersive X-ray absorption spectroscopy (ED-XAFS). Such an approach has been used by Tromp et al.[101-103] to investigate *i.a.* the Cu^{II} catalyzed N-arylation of imidazole. The advantage of ED-XAFS compared to conventional scanning methods lies in the possibility to acquire the total spectrum at once providing a millisecond time-resolution scale. Moreover, this technique proved to be favorable as the energy output of the X-ray beam is very stable which produces a higher sensitivity and only requires a very small sample size compared to quick EXAFS. During the start of the reaction the dimeric nature of the Cu^{II} starting material being a Cu^{II}-bis-μ-hydroxy dimer chelated by two tetramethylenediamine units was confirmed by characteristic EXAFS fitting parameters and distinct LMCT and d-d bands in the UV-vis range. During the reaction disappearance of the dimeric Cu^{II} species could be evidenced by ED-XAFS and UV-vis spectroscopy when both imidazole and the phenyl-donor (phenylboronic acid) are introduced into the reaction solution simultaneously. The Cu^{II} species start to disappear which was evident from a drop in the d-d transition band as well as appearance of a distinct pre-edge peak at approx. 8982 eV indicating formation of Cu^{I} species. When the desired product, phenylimidazole, has been formed (monitored by *ex-situ* NMR) the specific features for Cu^{II} species are found to re-appear indicating reversibly cycling $Cu^{I/II}$ shuttle very similar in nature to the present catalytic system discussed in this thesis.

EPR/UV-vis/ATR-IR coupling

Recently, the already mentioned *operando* triple coupling of EPR/UV-vis/ATR-IR spectroscopies for usage in liquid-phase media received considerable attention.[17] The main innovation was the simultaneous coupling of EPR in addition to the commonly used combination of UV-vis and ATR-IR spectroscopy. This was achieved by using an electrochemical flat cell as a reactor for insertion into an EPR resonator. In the top part, two openings allow the implementation of both the UV-vis and ATR-IR fiber-optical probe as well as the gas inlet, while the flat section itself is located within the cavity of the EPR spectrometer. The flat cell was needed as the high dielectric constant of the solvent (MeCN) requires minimization of the total volume inside the EPR cavity. Circulation was achieved by connecting the lower end with the top part using a syringe pump. Using this set-up several open question concerning mechanistic aspects of the Cu/TEMPO catalyzed aerobic alcohol oxidation could be answered, since the reaction cycle was investigated step-wise without the limitations posed by taking *ex-situ* EPR samples. UV–vis and EPR spectroscopies enabled investigation of the change of the Cu oxidation state depending on addition of different components *e.g.* TEMPO, NMI and the introduction of O_2 while ATR-IR allowed to monitor the catalytic activity by analyzing intensities of related carbonyl bands of the product. Only by combining these techniques the intricate interaction of the Cu^{II}-$O_2^{-\bullet}$ species with TEMPO radical could be proved and distinguished between active and inactive Cu precursors. Furthermore, the findings suggest that the major catalytically active species are mononuclear Cu^{II} complexes in contrast to earlier proposed intermediates. Thus, it was shown that coupled spectroscopies and magnetic resonance techniques were complementary to each other with each method being an important piece in revealing key mechanistic aspects. However, there are still several open issues such as the formation of the active $Cu^{I/II}$ sites, their oxidation and reduction behavior as well as the performance within catalytic systems. Elucidation of these aspects using either the Cu^{I}OTf/bpy/NMI[16] or the Cu^{I}OTf/(bpy)/4-DMAP[14] system was the aim of this thesis. In addition, an extension of that triple coupling by X-ray absorption spectroscopy has been developed and applied on a catalytic system using similar conditions as in the Cu^{I}OTf/bpy/NMI system.[16]

3. EXPERIMENTAL PROCEDURES

3.1. Coupled *operando* EPR/UV-vis/ATR-IR set-up

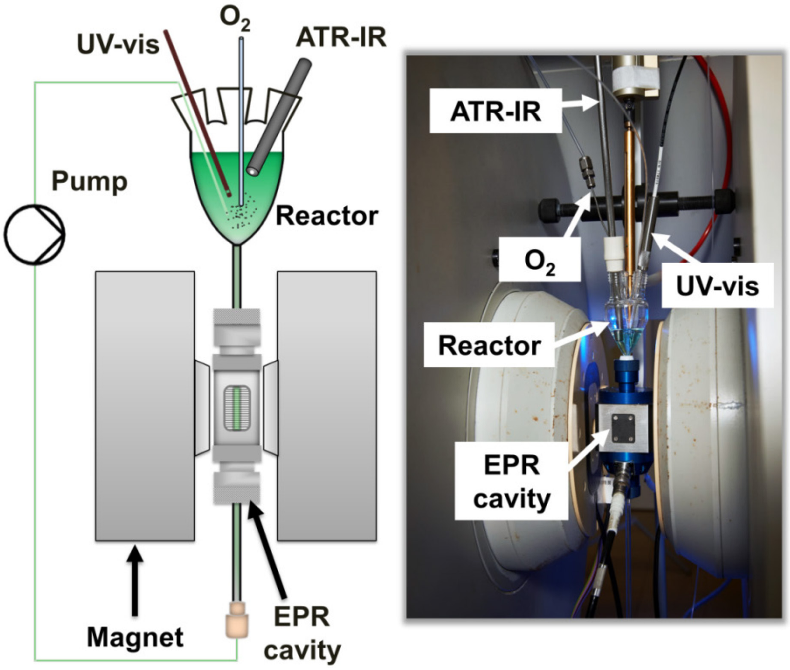

Figure 1. Schematic representation of the experimental set-up (left) and close-up image of the set-up in *operando* mode (right).

Coupled *operando* EPR/UV-vis/ATR-IR measurements for testing the activity of *in-situ* formed $Cu^{I}(L)_{X}$/TEMPO catalytic systems as well as their redox behavior the aerobic alcohol oxidation have been carried out using a specially designed quartz glass reactor (QSIL GmbH Quarzschmelze Ilmenau) (**Figure 1**). In previous investigations, Brückner et al. implemented a two-neck flat cell within the EPR cavity.[17] However, a new reactor was developed increasing the size of the upper part, thus enabling better positioning of the fiber-optical probes. The upper part of the new reactor consists of a three-neck, oval shaped reservoir possessing a volume of approx. 20 ml. It is connected at the bottom to a cylindrical tube, which is approx. 25 cm in length, having an internal diameter of approx. 1 mm and a wall thickness of approx. 2 mm, thus limiting the volume residing inside the EPR cavity. Another advantage compared to commercially available reaction cells is the possibility to use reaction volumes in ranges between approx. 4 and 20 ml. Both ATR-IR and UV-vis fiber-optical probe heads are located at the bottom of the reservoir in the upper part of the reactor. Circulation of the reaction solution through the reactor at a rate of 2.5 ml/min was achieved using a rotary piston pump (Reglo-CPF-Digital with RH00 pumphead, ISMATEC/Cole-Palmer GmbH). The pump was connected to the reaction cell using 1/16” OD PTFE lines. Time lack between the location of the probe heads and the center of the EPR cavity was calculated to be approx. 2.4 s at the used circulation speed. Gases were introduced by single-use stainless steel cannula (Sterican® Ø 0.8 mm x 120 mm, BRAUN) connected to an 1/8” OD PTFE line via SWAGELOK adapters. The PTFE tubing was connected to a digital mass flow controller (MFC) (EL-FLOW® Select, Bronkhorst) which in turn has been attached to gas supply. The MFC had been calibrated to O_2 and Ar flow prior to use. A constant flow rate of 25 ml/min was set for each gas, if not stated otherwise. O_2 and Ar have been purified before, using the Gas Clean Filter System by Agilent removing H_2O and O_2/H_2O, respectively.

In-situ UV-vis measurements

In-situ UV-vis spectra were recorded by an Avantes Avaspec 2048 and collected using Avasoft proprietary software in a range from 300-1000 nm at intervals between 1-60 s. Solvent subtraction has been performed prior to measuring by using acetonitrile as reference; the dark reference was recorded with closed shutter prior to the measurement. A fiber-optical SiO_2 micro immersion probe (WPI Dip Tip™, World Precision Instruments) with a fixed 10 mm gap (optical path length 2.0 mm) was used. For separate measurements a fiber-optical immersion probe with an adjustable beam path (Avantes) was used. This is necessary when higher or lower concentrated solutions need to be analyzed being either too saturated or too low to be visualized.

In-situ IR measurements

In-situ IR spectra were recorded by ReactIR 15 spectrometer system from Mettler Toledo using iCIR proprietary software in a range from 650-1900 cm^{-1} at intervals between 1-5 min. A fiber-optical AgX ATR probe with a diamond reflection element at the tip was used. The ATR-IR probe was inserted into the solution at the beginning of the reaction and its resolution was set to 4 cm^{-1} while using *Happ-Genzel* algorithm as apodization method. Prior to measurement a background was collected in ambient air; solvent subtraction was not performed.

In-situ EPR measurements

In-situ EPR spectra were recorded on an ELEXYS 500 continuous wave EPR spectrometer by Bruker using the rectangular shqe1062 resonator. The measurements have been performed applying microwave energy in the X-band range (~ 9.7 GHz) with a MW power of 6.3 mW. Spectra were recorded with a sweep time of 60 s, a modulation frequency of 100 kHz and modulation amplitude of up to 5 G. During measurements the EPR cavity was continuously flushed with N_2 to prevent H_2O condensation.

Ex-situ EPR

Separate, *ex-situ* measurements at different temperatures (77 K – 300 K) were carried out on an EMX continuous wave EPR spectrometer by Bruker using the rectangular ER4102ST resonator connected to a variable temperature controlling unit including liquid N_2 cryostate to adjust the temperature. The measurements have been performed applying microwave energy in the X-band range. Spectra were recorded with a sweep time of 60 s, a modulation frequency of 100 kHz and modulation amplitude of up to 5 G. During measurements the EPR cavity had been continuously flushed with N_2 to prevent H_2O condensation.

Electrochemical investigations: Cyclic Voltammetry (CV) and Differential Pulse Voltammetry (DPV)

All electrochemical studies were performed at room temperature in anhydrous MeCN p.A. (VWR Chemicals) under Ar atmosphere with 0.1 mol/L NBu_4PF_6 (Fluka) as conducting salt using an Autolab potentiostat/galvanostat (PGSTAT 302N, Metrohm). A glassy carbon disk (d=2 mm) working electrode, a Pt counter electrode and an Ag/AgCl/LiClsat./EtOH reference electrode (all electrodes: Metrohm) were used. Potentials measured with respect to this reference were checked by using the ferrocenium/ferrocene internal reference system (potential of Fc^+/Fc vs. Ag/AgCl/$LiCl_{sat.}$ in EtOH: 0.505 V). Cyclic voltammetry (CV) scans were recorded three times at a scan rate of 100 mV/s. The initial measurement was performed with 0.05 mmol Cu^IOTf dissolved within 5 ml of the electrolyte, [Cu]=0.01 M under Ar atmosphere. Afterwards, as indicated, 0-1.0 equiv. bpy (0-0.05 mmol) and 0-20 equivs. (0-1.0 mmol) ligand/additive (*e.g.* NMI, 4-DMAP or other imidazole/pyridine derivatives) were introduced subsequently under Ar atmosphere and CVs were recorded. The differential pulse voltammograms (DPVs) of the same solutions were acquired in anodic direction with a scan rate of 5 mV/s (step potential 2.5 mV , modulation amplitude 25 mV, modulation time 0.05 s, interval time 0.5 s) immediately after the CVs have been recorded. In addition, CVs and DPVs of the individual ligands/additives in the absence of Cu salts have been performed, typically using 1.0-3.0 equivs (0.05-0.15 mmol), as indicated, to differentiate redox events of coordinated species from the free compound.

General procedure for Cu/TEMPO-catalyzed aerobic alcohol oxidation

All chemicals have been purchased in purity > 99% from Sigma® (Sigma-Aldrich Chemie GmbH), if not otherwise stated. Purification of the gases from basic supply (Ar and O_2) has been carried out in advance (*vide supra*). Liquid compounds were degassed using at least three freeze-pump-thaw cycles and traces of H_2O were removed by adding 3 Å mole sieves. All components were stored in the glove box under Ar atmosphere shielded from light. The reaction cell was inserted and secured within the EPR cavity and flushed with Ar for 15 min at a rate of 50 ml/min prior to addition of solvent to remove gaseous O_2 while the pump was set at a rate of 2.5 ml/min. The three openings on top were secured with screw caps equipped with silicon septa. Two of those openings are fitted with the fiber-optical probes while one opening was provided with the gas inlet in addition to a small cannula for pressure release. The lower end of the reaction cell has been connected to the pumping unit using Precision Seal® rubber septa. For this purpose, a Sterican® Ø 0.8 mm x 120 mm cannula was fixed within 1/16” PTFE tubing and pierced through the rubber septum to serve as connector.

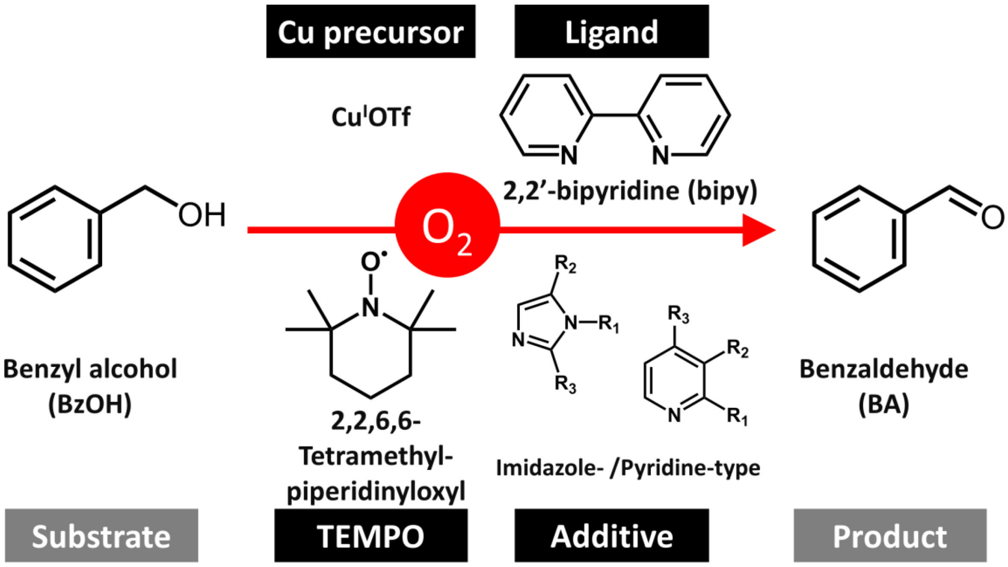

Scheme 11. General conditions of Cu^I/TEMPO catalyzed aerobic alcohol oxidation.

In general, catalytic investigations were performed according to **Scheme 11** at a concentration of 0.01 M Cu catalyst, if not stated otherwise. For the catalytic reaction 5 ml of previously degassed and anhydrous MeCN (99,8 %, spectroscopic grade) were introduced into the upper part of the reaction cell by using a syringe using one of the three openings. Subsequently, 0.05 mmol Cu^{I}OTf, 0-2.0 equivs. bpy (0-0.1 mmol), 1.0 equiv. TEMPO (0.05 mmol) and 0-6.0 equivs. (0-0.3 mmol) ligand/additive (*e.g.* NMI, 4-DMAP or other imidazole/pyridine derivatives) were transferred into the flask while continuously introducing Ar at a flow rate of 25 ml/min to prevent oxidation. Complexation was confirmed by UV-vis measurements as Cu^I species are diamagnetic and thus EPR-inactive. As soon as the reaction solution was stable, 1.0 mmol (20.0 equivs.) of BzOH was added to this mixture via a syringe. Gases were switched from Ar to O_2 and dosing was continued at a rate of 25 ml/min afterwards to initiate the reaction. The reaction was terminated once the integrated area of the ν(C=O) band equilibrated. Additional experiments have been performed with a coupled *in-situ* IR/UV-vis set-up using a 10 ml Schlenk flask equipped with a stirrer using a protocol similar to that discussed prior.

General procedure for investigating the redox properties of $Cu^{I/II}$ species

For investigating the influence of nature and amount of ligand/additive on the redox properties of the $Cu^{I/II}$ shuttle the individual reactions, being oxidation and reduction, were studied separately. First, $[Cu^I]$ between 0.01–0.02 M (0.05 mmol or 0.1 mmol Cu^IOTf in 5 ml MeCN used as Cu precursor) was introduced into the reaction cell under Ar atmosphere. Afterwards, this solution was oxidized in the presence of either 0-1.0 equiv. of bpy (0-0.1 mmol) and 0-3.0 equivs. (0-0.2 mmol) of ligand/additive (*e.g.* NMI, 4-DMAP or other imidazole/pyridine derivatives) as well as 1.0 equiv. (0.05-0.1 mmol) TEMPO by dosing O_2 at a rate of 25 ml/min. The O_2 dosing was stopped after approx. 30 min, when the Cu^{II} signal in the UV-vis and EPR spectra equilibrated and broadening of TEMPO EPR signal remained stable. Then, Ar flow was started at a rate of 25 ml/min for approx. 15 min to remove solved O_2 from the solution until the TEMPO EPR signal lines narrowed.[95] Afterwards, either 1.0 equiv. (0.1 mmol) or 20.0 equivs. (1-2 mmol) of BzOH were added to reduce the formed Cu^{II} species in absence of O_2 under continuous Ar dosing. The term *equivalents* is used in relation to the initial Cu precursor concentration.

3.2. Coupled *operando* EPR/XANES/EXAFS/UV-vis/ATR-IR investigations

Coupled *operando* EPR/XANES/EXAFS/UV-vis/ATR-IR measurements for studying the structural arrangement and reaction kinetics of $Cu^{I/II}$ species in the Cu/TEMPO catalyzed aerobic alcohol oxidation have been carried out at the ROCK Quick-EXAFS beamline at SOLEIL synchrotron facility in Saint-Aubin, France.[104]

The combination between XAS, EPR and optical spectroscopy in general, and XAS and EPR in particular, in this specific set-up is a newly developed, coupled spectroscopy. This set-up can be easily assembled at different X-ray beamlines according to experimental requirements which is achieved by using a portable EPR spectrometer (Bruker EMXnano) (**Figure 2**). The main part of this set-up is a modified EPR cavity containing a grid in the front and a small opening in the wave guide (~ 4 mm) on the opposite side allowing the X-ray beam to pass through upon the X-ray detector (**Figure 3**). XAS measurements are performed in transmission mode when using that set-up.

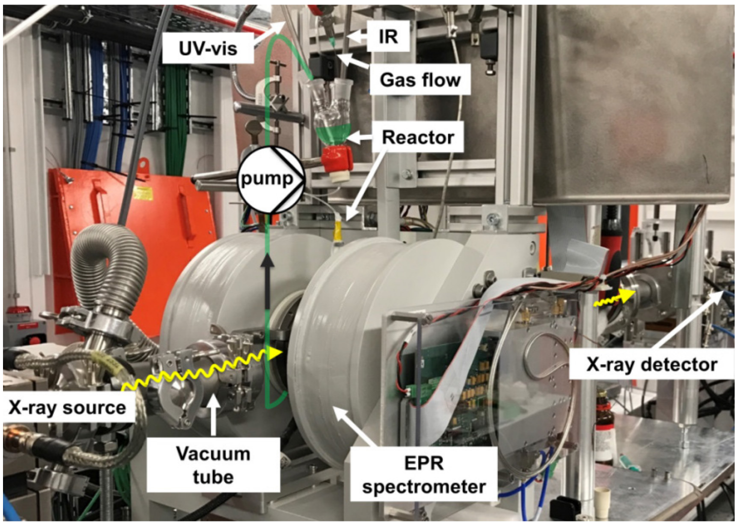

Figure 2. Coupled *operando* EPR/XANES/EXAFS/UV-vis/ATR-IR set-up assembled at the Quick-EXAFS ROCK beamline at SOLEIL synchrotron facility in Saint-Aubin, France.[104]

Moreover, this coupling requires significant changes of the reactor inserted within the EPR cavity. Briefly, a quartz tube being approx. 20 cm in length, having an inner diameter of approx. 1.5 mm and a wall thickness of approx. 1.0 mm was equipped with a Kapton® tube (Polyimide; 1.0 mm inner diameter and a wall thickness of approx. 0.025 mm) and fixed within the resonator. The quartz glass serves as a support tube possessing two small holes of approx. 2 mm in diameter in the front/back exposing only the Kapton® tube, thus allowing the X-ray beam to pass through. Kapton® tubes are necessary as they possess high transmittance to X-rays. In addition, Kapton® is less sensitive towards radiation damage and retains structural stability despite relatively high mechanical stress. ATR-IR and UV-vis probe heads (using a Varian Cary50 and a ReactIR 15 spectrometer, respectively) are located at the bottom of a three neck reservoir, having a volume of approx. 25 ml, located slightly above the quartz tube. Both parts are connected by a 1/16" PTFE line with a length of approx. 10 cm. The upper part of this new reactor is similar to that used within the coupled *operando* EPR/UV-vis/ATR-IR spectroscopy.

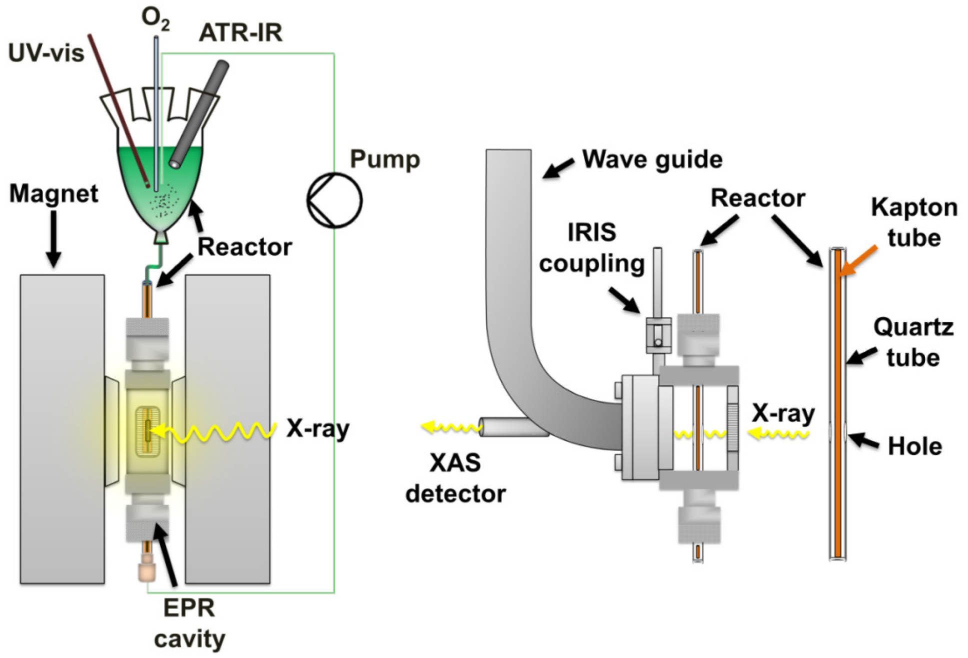

Figure 3. Front view of the coupled operando EPR/XANES/EXAFS/UV-vis/ATR-IR set-up (left) and side view of the modified EPR cavity with the reactor in place (right).

The lower end of the quartz tube is connected to a rotary piston pump (Reglo-CPF-Digital with RH00 pumphead, ISMATEC/Cole-Palmer GmbH) for circulation of the reaction solution at a rate of 2.5 ml/min. The average time lack between the lower part of the reservoir and the center of the EPR cavity is approx. 2.3 s. A gas inlet for dosing Ar and O_2 is located in the reservoir which is connected to a mass flow controller introducing those gases at a constant rate of 25 ml/min. XAS measurements often require higher concentrated solutions and therefore [Cu] of 0.025 M was used (2.5 x higher than [Cu] used within catalytic reaction monitored by coupled *operando* EPR/UV-vis/ATR-IR spectroscopy) (*vide infra*). This novelty, coupled spectroscopic set–up has been filed for patent.[105]

In-situ EPR

In-situ and *operando* EPR spectra were recorded on a portable continuous wave EPR spectrometer (Bruker EMXnano) using the X-band MW range. MW power of 6.9 mW, a modulation frequency of 100 kHz and modulation amplitude up to 5G were used as parameters. The EPR half-wave resonator was modified accordingly (**Figure 3**).

In-situ X-ray absorption spectroscopy (XAS)

XANES and EXAFS spectra were measured at the ROCK Quick-EXAFS beamline at

SOLEIL[104] in transmission mode using two ionization chambers filled with N_2 under a pressure of 1 bar. A Si(111) channel-cut crystal was used as a monochromator with an oscillation amplitude of 2.1° and an oscillation frequency of 2 Hz. During monochromator oscillation, two 250 ms spectra were recorded, one with increasing Bragg angles, one with decreasing Bragg angles. During data processing, only spectra recorded with upward Bragg angles have been considered. Harmonic rejection was done using 2 mirrors surrounding the monochromator both coated with B4C, accepting the pink beam and monochromatized beam at 2.75 mrad of incidence, respectively. The beam size at the sample position was 0.4 mm (H) x 0.2 mm (V) (full width at half maximum). A Cu metal foil was recorded permanently during data acquisition using a third ionization chamber.

XAS data normalization was performed using the Python "normal_gui" graphical interface developed at SOLEIL for the fast handling of Quick-XAS data.[106] Energy calibration was done by using first derivative maximum of the spectrum of the Cu metal foil (8979 eV). 20 spectra recorded with increasing angles were averaged in order to improve the signal to noise ratio. Thereby, a time resolution of 10 s between two consecutive spectra has been achieved.

In-situ UV-vis spectroscopy

UV-vis spectra in the range of 200–800 nm were recorded using a Varian Cary 50 dual beam spectrometer. This apparatus was fitted with a fiber-optical Hellma immersion probe with an optical path length of 1.0 mm used for collecting the data. Spectra were measured with a scan rate of 4800 nm/min and a cycle time of 10 s, corresponding to the time between two consecutive spectra. UV-vis spectra were recorded without baseline correction and only a subtraction of the spectrum of the acetonitrile solvent recorded under the same conditions is carried out as post-treatment.

In-situ IR measurements were carried out using the same parameters as described before.

General procedure for coupled *operando* EPR/XANES/EXAFS/UV-vis/ATR-IR investigations of Cu/TEMPO-catalyzed aerobic alcohol oxidation

For monitoring the catalytic reaction a slightly different approach compared to the *operando* EPR/UV-vis/ATR-IR spectroscopy was chosen. Due to partial oxidation of the Cu^I precursor when transferring the solution from the glove box to the beamline, the Cu containing solutions were pre-oxidized until the Cu^{II} concentration equilibrated which was set as starting point. Prior to measuring the reactor and lines were vigorously flushed with dry N_2. In principal, 0.015 mmol Cu^IOTf (0.025 M) and 1.0 equiv. bpy (0.15 mmol, 0.025 M) were suspended in 6 ml MeCN inside the glove box and added to the reservoir via syringe. Subsequently, 1.0 equiv. TEMPO (0.15 mmol, 0.025 M) and 2.0 equivs. NMI (0.3 mmol, 0.05 M) were added to this solution under continuous N_2 flow. Afterwards, coupled measurements were started and O_2 flow initiated remotely. Cu^{II} concentrations were monitored by UV-vis, XAS and EPR spectroscopy until the corresponding signals stabilized (~ 20 min). Then, 5.0 equivs. of benzyl alcohol were added while continuing O_2 flow. Thus, reduction of Cu^{I} and subsequent reoxidation to Cu^{II} take place. This cycling was performed four times, corresponding to 20 equivs. of benzyl alcohol in total (which is the amount used within the previous investigations).

3.3. Data treatment

IR spectra

For *in-situ* IR measurements a background spectrum has been recorded at ambient air prior to the measurement. Quantification of formed BA was done in the following way: The concentration of benzaldehyde (BA) was determined by using a calibration series shown in **Figure 4**. The ν(C=O) band at approx. 1702 cm^{-1} was analyzed by full area integration without baseline subtraction or other mathematical operations. The spectral range of integration was determined manually according to band width as bands broaden with higher concentration.

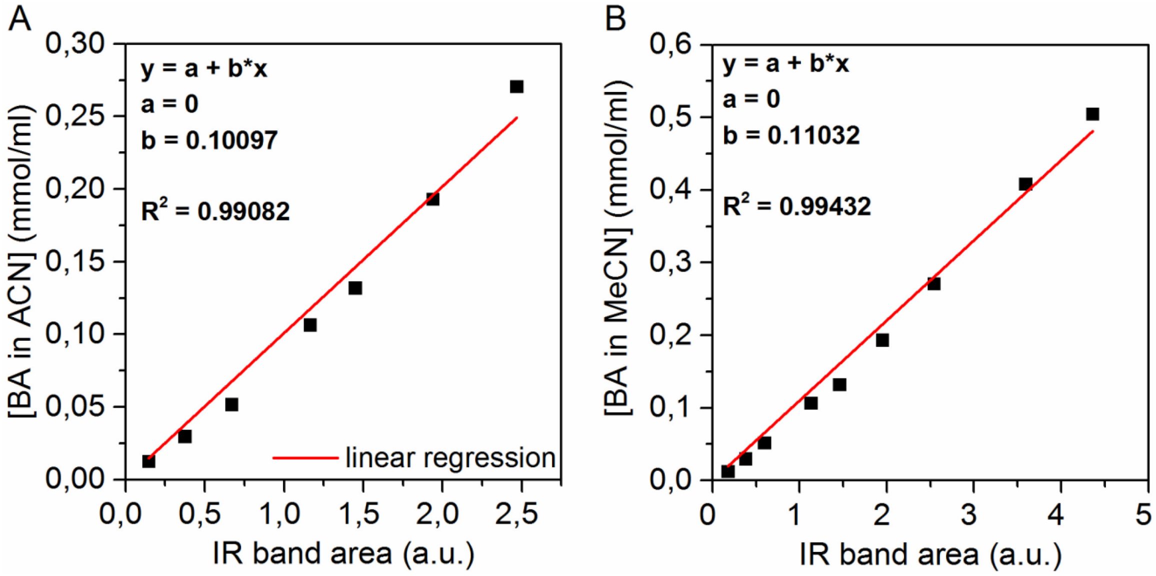

Figure 4. Calibration of BA: [BA] in MeCN plotted against 1702 cm^{-1} IR signal intensity (obtained by integration) for lower [BA] used for *operando* EPR/UV-vis/ATR-IR coupling (**A**) and higher [BA] used for *operando* EPR/XANES/EXAFS/UV-vis/ATR-IR coupling (**B**).

One calibration series for lower [BA] used for *operando* EPR/UV-vis/ATR-IR investigations (**Figure 4A**) and an additional series for higher [BA] needed for *operando* EPR/XANES/EXAFS/UV-vis/ATR-IR spectroscopy (**Figure 4B**) have been recorded and subjected to linear regression analysis. As expected, both calibration series nicely obey *Lambert-Beer* law. Subsequently, formation of BA (in percent) has been determined according and related to the amount of added BzOH. Relative comparison of BA conversion (without calculating the actual BA concentration) was done when indicated. No calibration series for the alcohol substrate has been recorded.

UV-vis

Bands from UV-vis spectra were not subjected to quantification. Spectra displayed from different experiments are baseline-offset corrected and only normalized when indicated. For selected purposes specific absorptions were followed with time. Comparison of different experiments was achieved by normalization to maximum with prior subtraction of the starting value.

EPR

Quantification of EPR spectra has not been conducted. For selected purposes it was necessary to monitor the Cu^{II} as well as the TEMPO radical EPR signal. Since the reaction solution contains both species, significant interference between EPR signals of TEMPO and Cu^{II} occurs; both species having similar g_{iso} values. This often leads to overlapping of signals, mostly due to broad lines of TEMPO. Therefore, it is not possible to determine the Cu^{II} signal area by double integration. However, relative tracking of the Cu^{II} signal is possible as the low field peak $m_I=+\ 3/2$ is not affected by overlap with the TEMPO radical hence its amplitude serves as a measure. Normalization to maximum with prior subtraction of the starting value yields a relative trend for comparing different experiments. In the absence of TEMPO radical, double integration of Cu^{II} EPR signal area was performed for relative comparison as indicated. Monitoring of TEMPO radical with time, however, could be performed by double integration since this area is only insignificantly affected by the Cu^{II} signal. The normalization procedure is the same as described before.

XAS

Analyses of XANES, EXAFS and UV-vis data of the 4-in-1 coupling has been performed by the team of the ROCK beamline at SOLEIL synchrotron facility (Saint-Aubin, France), in particular, Valerie Briois and Camille La Fontaine. For example, the extraction of the individual components from XAS/UV-vis and the determination of the local geometry from EXAFS has been conducted by Valerie Briois.

Briefly, EXAFS analysis of components extracted by MCR-ALS (*vide infra*) was performed using the Athena software bundle.[107] After specific background correction EXAFS spectra were Fourier-transformed (k^3-weighting and a Kaiser-Bessel window (in the k range 3.0-10.5 $Å^{-1}$ with dk=2 was applied).

EXAFS fitting of structural parameters such as the atomic distances R, the coordination number N, and the Debye-Weller factor σ was performed with the Artemis interface to IfeFFIT.[108] The amplitude reduction parameter and the energy shift e_{not} were first calibrated by fitting EXAFS spectra of crystalline CuO and Cu_2O as references. The obtained values were then used in the simulation of MCR components as fixed values (S_0^2 = 0.716) and constrained variable parameters (E_0+e_{not}= 8989.2 ± 1.5 eV). Feff paths required for the simulation of components were calculated from crystallographic structures of bpy,[19] NMI[109] and MeCN[110] containing Cu^{II} complexes. Crystallographic structures of dimeric Cu^{II} complexes exhibiting ferromagnetic coupling were also taken into account for calculating relevant Feff paths in dinuclear complexes.[111]

Due to very similar electronic properties of O, N and C atoms, the resulting backscattering is indistinguishable by EXAFS fitting. However, the presence of NMI or bpy moieties around Cu was confirmed by other methods *e.g.* UV-vis and furthermore, identified SS and MS paths which contribute to the second FT, led us to the assumption that those ligands surround the Cu complexes. The coordination number of the different Cu species was fixed during the fitting process. For some of the paths required for the simulation of the mononuclear Cu^I and Cu^{II} species, common Debye-Waller factors were used.

Multivariate Data Analysis

Multivariate-Curve Resolution by Alternative-Least Squares (MCR-ALS) processing[112-117] was used to isolate the pure $Cu^{I/II}$ components present in reaction solution by separately analyzing the spectra from XAS and UV-vis spectroscopy. That operation is based on bilinear decomposition of the recorded spectra with ongoing reaction time into a matrix, D, according to the relation: D = CxST + E where C corresponds to the matrix concentration profiles of pure species occurring during the reaction, ST is the transposed matrix of the spectra of pure species and E is the matrix of residuals. Moreover, Principal Component

Analysis by Singular Value Decomposition (PCA-SVD) was utilized to estimate the number of relevant components participating within the reaction being necessary to explain the variance of the experimental data. A scree plot test has been used to determine the least number of components. Calculations were performed using the Matlab platform with the free MCR-ALS 2.0 Graphical User Interface developed by Tauler et al.[118]

4. RESULTS AND DISCUSSION

4.1. Catalytic system formed *in-situ* from CuOTf, bpy and (un-)substituted imidazoles

4.1.1. Effect of NMI: *Ligand or Base?*

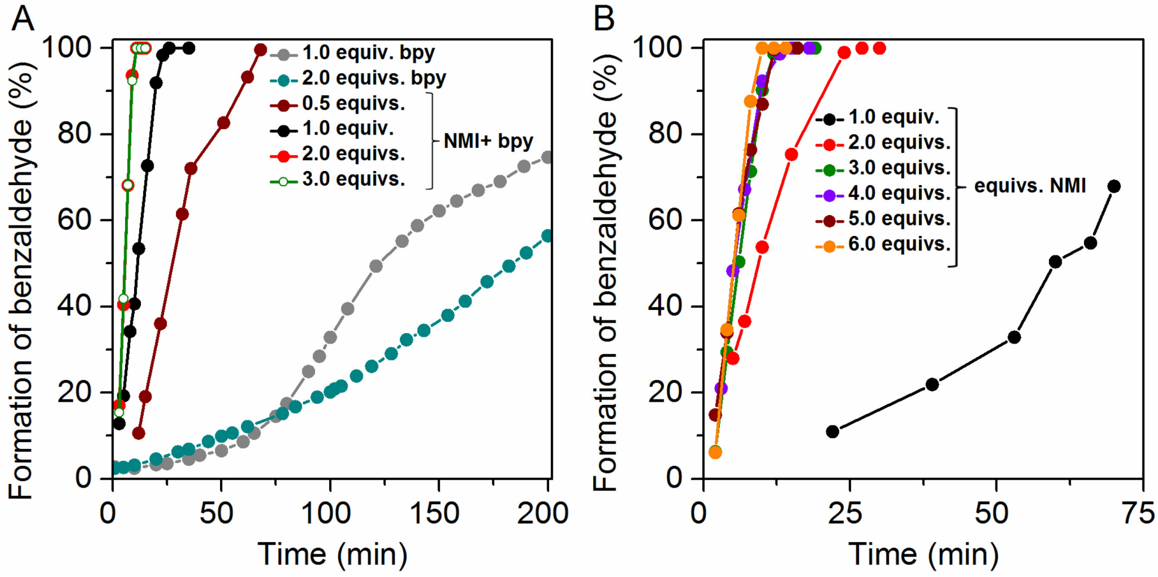

Figure 5. Formation of BA as a function of time (monitored by ATR-IR) presence of either 1.0 or 2.0 equivs. of bpy or 1.0 equiv. of bpy and 1.0-3.0 equivs of NMI (**A**) and sole implementation of NMI in 1.0-3.0 equivs. (**B**). Adapted with permission from reference119.

As mentioned previously, while optimizing reaction parameters of the aerobic alcohol oxidation, Stahl et al. found the reaction to proceed more efficiently when more than 1.0 equivalent of additive/base (either NMI or a combination of KOtBu/NMI) was added.[16] However, detailed screenings regarding the nature of the base or the number of bpy and NMI equivalents were not performed during the course of those studies. However, it is known *e.g.* from the previous works of Sheldon et al.[29, 66] that full conversion of BzOH as a model substrate can be also achieved within 24 h even in the absence of NMI, *i.e.* only in the presence of bpy.

It has been evidenced that the Cu^{I} starting species is oxidized to Cu^{II} by O_2 and subsequently converted back to the Cu^{I} starting material by the substrate.[20] In literature, it was often described, that one NMI molecule coordinates to the active Cu$^{I/II}$ center.[20] Proposedly, the 2nd NMI equivalent serves as base and abstracts a proton from the alcohol thereby facilitating substrate coordination by forming a Cu^{II}-alkoxide.[19-20, 66] To further elucidate the role of NMI during the catalytic cycle and to distinguish between ligand and base related effects, the reaction was monitored by our coupled *operando* EPR/UV-vis/ATR-IR spectroscopic set-up using different amounts of bpy (1.0-2.0 equivs.) and NMI (0-3.0 equivs.).[119] Some figures of **chapter 4.1** have been published in reference 119 and marked appropiately.

Figure 5A shows the activity of different catalytic systems reflected by the formation of BA in dependence on time (calculated by using the calibration plot in **Figure 4A**). The performance of $Cu^{I}OTf$ in combination with 1.0 or 2.0 equivs. bpy without NMI is very poor with only 20% and 32% conversion, respectively, after 100 min. Interestingly, the experiment using 2.0 equivs. bpy actually shows lower activity and a slightly different kinetic profile compared to 1.0 equiv. bpy which was a surprising result (**Figure 5A, grey line**). However, using 1.0 equiv. of bpy and adding NMI in molar ratios of 0.5 to 2.0 equiv. leads to a strong increase of the reaction rate. Addition of a 3rd NMI equivalent, remarkably, did not have any further significant effect.

On the other hand the sole implementation of NMI alongside $Cu^{I}OTf$ does lead to more rapid conversion of BzOH, even if only 1.0 equiv. is used, compared to the sole usage of bpy (**Figure 5B**). When raising the number of NMI equivalents from 1.0 to 3.0 a pronounced increase in reaction rate can be observed, yielding very similar reactions rates compared to the experiments using the combination of bpy and NMI. A further increase from 3.0 to 6.0 equivs. only produces marginally faster reaction rates.

This raises the questions which is the role of NMI during the catalytic cycle. Two assumptions can be made: If NMI affects the ligand sphere, an influence on the rate of Cu^{I} to Cu^{II} oxidation would be expected with increasing amount as there is additional coordination to the $Cu^{I/II}$ center. Alternatively, remaining non-coordinated NMI could act as base. In this case, it would deprotonate the alcohol and thus, facilitates the formation of a Cu^{II}-alkoxide expecting a faster reduction of Cu^{II} to Cu^{I} species.

NMI acting as a ligand and affecting the electronic and steric properties of the Cu^{I} valence state would produce distinct changes of the coordination sphere which should be evident in the *in-situ* UV-vis spectra as well as from electrochemical analyses. Hence, in the next part, the focus shall be on the formation of the *active* Cu^{I} species.

"*Which is the active Cu^{I} species*?"

From the vast number of previous studies, it is apparent that Cu^{I} salts used as complex precursors possess superior[14-16, 20, 33, 63-64] activity over Cu^{II} precursors and therefore are mainly used. Furthermore, Cu^{I} salts possessing non-coordinating counter ions show higher activity than more strongly coordinating counter ions like *e.g.* Cl^-, I^-, NO_3^- or OH^-.[16, 20] Cu^IOTf may therefore serve as an exemplary precursor for studying the coordination sphere of the Cu^I ion with respect to *in-situ* complex formation of the active species when adding the reaction components successively.

As all Cu^I species are diamagnetic due to [Ar] $3d^{10}$ electron configuration, only UV-vis spectroscopy from our current *operando* EPR/UV-vis/ATR-IR toolbox can be used to get deeper insight into the coordination sphere of the Cu^I species. The interaction between Cu^I and TEMPO in solution has been studied extensively[15, 17, 19-20, 31] and shall not be discussed in detail. Direct redox interaction of Cu^I species and TEMPO radical has not been observed.[17] Thereby, the focus in the following subchapters shall be the effect of the ligand/additives on the Cu^I coordination sphere.

First, $Cu^I(MeCN)_4OTf$ is added to MeCN under Ar atmosphere to yield a final concentration of 0.01 M. A band at approx. λ_{max}= 250 nm could be observed (**Figure 6, black line**) which is most probably related to the scaffold of the ^-OTf counter ion or weak LMCT band[120] of $Cu^I(MeCN)_4$. Cu^I complexes only yield strong absorption bands when suffieciently strong π-acceptor ligands are present.[82, 121] Another very weak absorption band could be observed at approx. λ_{max} = 375 nm which was attributed to a weak MLCT of the $Cu^I(MeCN)_4$ complex.[17, 122] Under continuous Ar flow 1.0 equiv. bpy, the same amount used by Stahl[16] and others[29, 64] is added as a solid (**Figure 6, red dotted line**). Intense and broad absorption bands in the range from approx. 300-550 nm are now dominating the spectra. Those bands clearly originate from interaction between the metal and the ligand, since the sole ligand does not yield such bands (**Figure A1**). The broad band at λ_{max}= 442 nm and a shoulder at approx. 543 nm are due to MLCT transitions of a Cu^I-bpy species.[20, 123-124] The exact nature of present species, however, is disputed, as some authors[17, 20] postulate a single coordinated $Cu^I(bpy)$ species while most others propose an equilibrium between $Cu^I(bpy)$ and $Cu^I(bpy)_2$ to occur in solution.[123, 125-126] Another broad absorption band at approx. λ_{max}= 342 nm was assigned to an intra-ligand (IL) transition shifted upon complexation to the Cu center[127-128]. Further investigations regarding the Cu^I-bpy equilibrium are discussed in the following (*vide infra*).

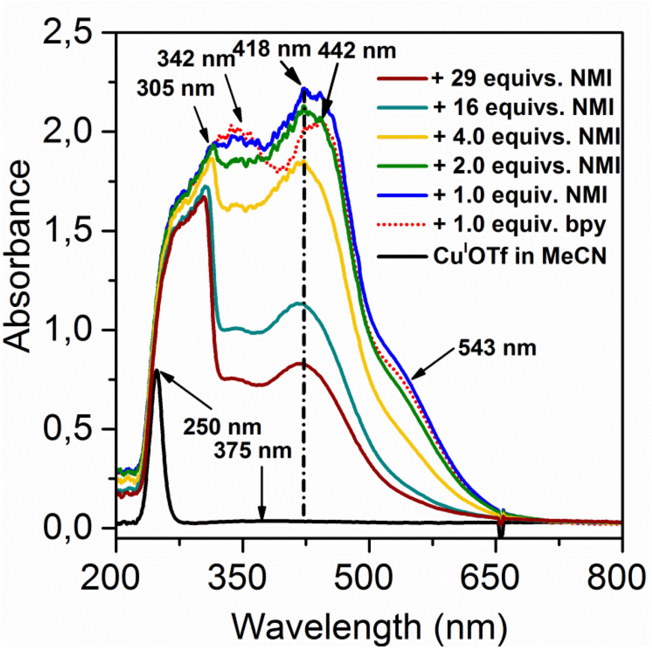

Figure 6. *In-situ* UV-vis experiments using a Cu^I concentration of 0.01 M in MeCN to elucidate the successive addition of effect of bpy and NMI upon the coordination sphere on the Cu^I center. The experiment was performed under Ar atmosphere.

In the second step NMI, previously regarded only as an additive, was added to the solution by a microliter syringe. The successive addition of NMI produces a very distinct changes to the MLCT bands in the region. Adding the 1st equiv. of NMI (**Figure 6, blue line**) leads to a slightly broadened and blue shifted MLCT band at approx. λ_{max}= 418 nm and gaining in intensity. A subtle increase in the absorption of the MLCT shoulder at 543 nm has also been noted. However, when the 2nd equiv. NMI is injected, distinct decrease is noted in bands at 342 nm, 418 nm as well as the shoulder at 543 nm. This trend can also be seen when the 4th equivalent in total (**Figure 6, yellow line**) has been added leading to a decrease in all mentioned bands. However, λ_{max} remains at approx. 418 nm and does not shift. Interestingly, a new absorption band at approx. 305 nm becomes apparent most likely stemming from the pyridine scaffold of the bpy ligand (*vide infra*). When an excess of NMI, in total, 16 equivs. and 29 equivs. has been added, significant reduction of the distinct shoulder at 543 nm is noted as well as pronounced decreasing in the MLCT band at λ_{max}=422 nm and IL band at λ_{max}=342 nm. Interestingly, the bands at 342/418/543 nm decrease simultaneously, indicating that these bands arose from bpy coordinated at the Cu^I center while no change was observed below 300 nm (*vide infra*). Bands owing to Cu^I-NMI coordination can be seen in **Figure A1**. Because of the very broad bands occurring after bpy addition it was not possible to get more in-depth information about the involved active Cu^I species using standard concentrations of 0.01 M.

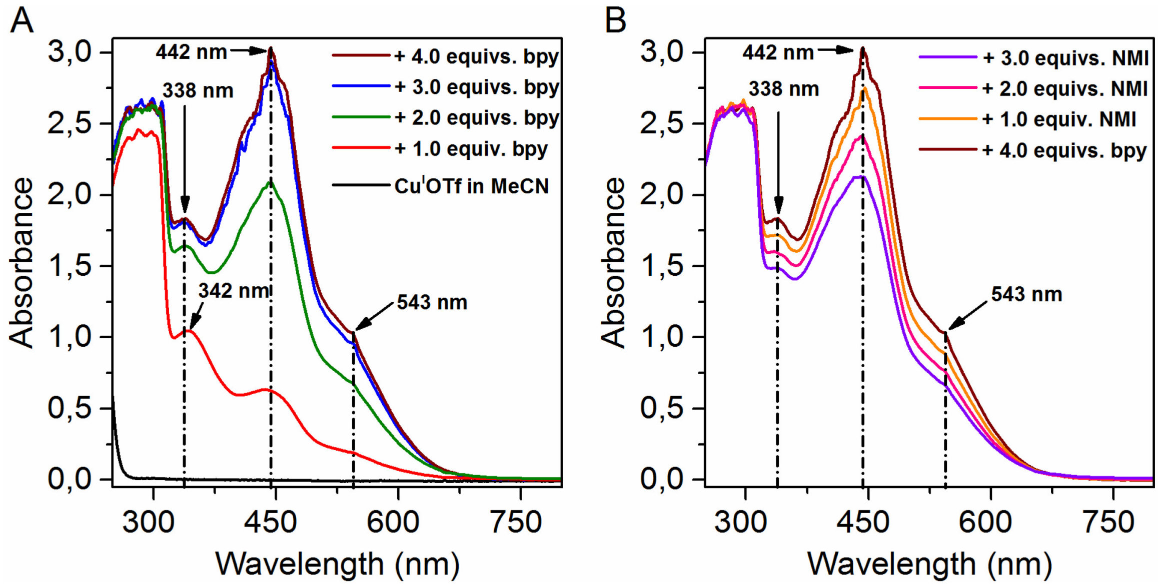

Figure 7. In-situ UV-vis experiments using a Cu^I concentration of 0.005 M in MeCN to elucidate the effect of 1.0-4.0 equivs. bpy upon the coordination sphere (**A**) and after subsequent addition of 1.0-3.0 equivs. NMI (**B**) using [Cu]=0.005 M.

Thus, *in-situ* UV-vis experiments were repeated with lower Cu concentration to get higher resolved spectra to better distinguish between the individual bands. These experiments were carried out in a 10 ml Schlenk vessel under continuous Ar flow and stirring. UV-vis spectra have been smoothed using the *Savitzky-Golay* filter method due to interfering noise.

First, the formation of the Cu^I-bpy species and its coordination sphere has been investigated in detail. For that purpose, 1.0-4.0 equivalents of bpy were added to a solution of Cu^I(MeCN)$_4$OTf in MeCN. After adding the 1st equiv. of bpy the MLCT/IL bands at λ_{max} 342 nm, 442 nm and 543 nm are now more distinctly pronounced (**Figure 7A, red line**). Below 320 nm broad bands, in particular the absorption edge at approx. 305 nm, show very high absorbances. These bands can now be clearly separated from the IL and MLCT bands of the Cu^I complex. These absorptions are most likely due to other ligand-centered transitions *e.g.* $\pi \rightarrow \pi^*$ of the bpy scaffold.[129] Interestingly, the addition of the 2nd equiv. of bpy produces considerable increase in IL/MLCT bands whereas the broad band below 320 nm only slightly increases. The band at 342 nm is slightly blue-shifted towards 338 nm (**Figure 7A, green line**). A 3rd equiv. of bpy was introduced into the solution which led to a further increase in mentioned MLCT bands, most notably at 442 nm (**Figure 7A**, **blue line**). Finally, a 4th equiv. has been added which did not produce a significant change to the bands at 338 nm and 442 nm and only subtle increase in the band at 543 nm (**Figure 7A, brown line**). Afterwards, NMI has been injected in three portions (1.0 - 3.0 equivs.) successively to that solution (**Figure 7B**). After the addition of each equivalent a distinct decrease of the

IL/MLCT bands at 342/422/543 nm (similar to **Figure 6, blue – yellow**) was observed, while no change below 320 nm was noted. In general, only minimal light absorption above 630 nm is noted meaning there is neglectable Cu^{II} formation over the course of the experiment as d-d transition bands are expected to absorb visible light in the range between 600-800 nm.[12, 83]

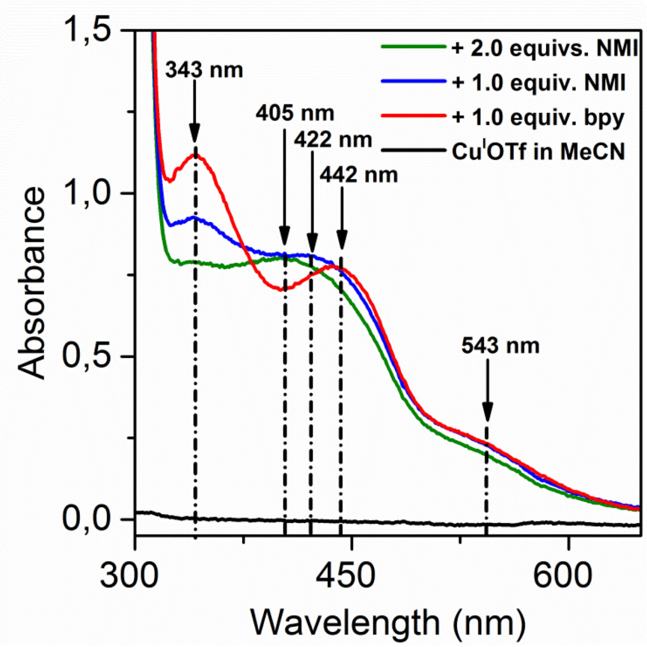

Figure 8. *In-situ* UV-vis experiments using a Cu^I concentration of 0.005 M in MeCN to elucidate the effect of NMI in detail.

Additional experiments have been performed using a 0.005 M Cu^I solution and only *one* bpy equivalent and subsequent addition of 1.0-2.0 equivalents of NMI (**Figure 8**). The aim was to study the effect of NMI on the coordination sphere but to avoid overlapping caused by the broad MLCT bands of Cu^I–bpy species when using more than 1.0 equiv. bpy. The addition of 1.0 equiv. of bpy to a solution of Cu^IOTf in MeCN produces similar, characteristic bands (**Figure 8, red**) compared to the higher concentrated experiment displayed in **Figure 7**, yet better separated. NMI injection of 1.0 equiv. leads to a decrease in the bands at 343 nm and only very minor changes in the shoulder at approx. 543 nm. However, the MLCT band at λ_{max}=442 nm broadens and blue-shifts to 422 nm (**Figure 8, blue**). The bands below 320 nm are only insignificantly affected by the presence of NMI. The second NMI equivalent again produces a distinct reduction of the band at 343 nm while a slight decrease of the shoulder at 537 nm could be noted being in agreement with the previous experiment measured at [Cu] = 0.01 M and attributed to less donation of Cu^I center towards bpy (**Figure 6, green**).[119] The λ_{max} of the MLCT band further blue-shifts from 422 nm to 405 nm (**Figure 8, green**).

These findings have significant impact on the understanding of *in-situ* formation of active Cu^I species. The complex formation of a Cu^I-bpy species can be ascertained by the evolution of strong MLCT bands and an optical change from colorless to deep brown. From **Figure 6 and 8** it is also evident, that subsequent addition of NMI leads to formation of a new $(bpy)Cu^I(NMI)_X$ complex species which can be seen *e.g.* by the increase ofthe MLCT band at 442 nm and its shoulder at 543 nm.[17, 119] Cu^I species surrounded by sterically less-demanding ligands are typically found to be either coordinated 2-, 3- and 4-fold in linear, trigonal-planar or tetrahedral geometry.[126, 130-131] This holds also true for the implemented precursor, $Cu^IOTf(MeCN)_4$,[132] or similar precursors having different counter ions[133-134], showing tetrahedral arrangement. Hence, it is important to know which are the precise Cu^I complexes present in solution before *and* after addition of NMI.

Before addition of NMI an equilibrium between $Cu^I(bpy)$ and $Cu^I(bpy)_2$ complexes seems to be reasonable. The distinct MLCT band increase beyond a ratio of L/Cu = 1 (**Figure 7A**) shows the complexation of still uncoordinated Cu^I precursor present in solution. The increasing MLCT intensity to a ratio of L/Cu = 3 might very well be explained by equilibrium effects as it was shown that an excess of bpy is required to completely shift the equilibrium from $Cu^I(bpy)$ to $Cu^I(bpy)_2$.[123] However, the predominant Cu^I species is $Cu^I(bpy)_2$ when bpy is added to Cu^I precursors.[123, 125, 135] One could argue that before addition of NMI the total amount of Cu^I species present in solution might only be single coordinated in the form of a $Cu^I(bpy)$ species. However, in this case one would expect different spectroscopic features between $Cu^I(bpy)$ and $Cu^I(bpy)_2$ complexes. The λ_{max} of the MLCT bands at 338 nm, 442 nm and 543 nm (**Figure 7A**) do not shift upon addition of more than 1.0 equiv. of bpy which points to immediate formation of the $(bpy)_2Cu^I$ complex. The stability constant $\log\beta 2$ of the $Cu^I(bpy)_2$ complex is reported in literature in the order of 13.8–14.4[125, 136] which is similar to those found for $Cu^I(phen)_2$ species.[137-138] In general, chelate ligands like bpy or phen are known to be strong ligands,[139] in particular stronger than non-chelating ligands *e.g.* MeCN or pyridine,[140] thus, further evidencing the major species present in solution to be $Cu^I(bpy)_2$.[123] Moreover, replacement of bpy by solvent molecules would be entropically disfavored owing to the chelate effect of the bpy ligand[141] suggesting an equilibrium towards the $Cu^I(bpy)_2$ complex. On the other hand, that implies when adding low amounts, *i.e.* 1.0 equiv. bpy (***cf.*** **Figure 7A**) non-coordinated Cu^IOTf should remain in solution. We assume, that the initial addition of 1.0 equiv. bpy to Cu^I precursor produces predominantly $Cu^I(bpy)_2$ besides some amount of $Cu^I(bpy)$ while non-converted Cu^I remains in solution.

When 2.0 equivs. NMI are added the equilibrium is shifted towards a (bpy)$Cu^I(NMI)_2$. This was concluded from spectroscopic results after adding NMI into Cu^I–bpy containing solutions. The band behavior, *i.e.* the decrease of MLCT bands at λ_{max}=543 nm and the blue-shift of MLCT band at λ_{max}=442 nm (**Figure 6 and 8**), suggestes that a substantial fraction of $Cu^I(bpy)_2$ is converted into another complex species. This can also be deduced from the significant decrease in the IL band at λ_{max}= 343 nm band, which only arises from coordinated bpy (**Figure A1**), after adding NMI. This effect points to displacement of bpy from the Cu^I ligand sphere. From **Figure 6** it is evident that no further changes are seen in the position of λ_{max} after adding > 2.0 equivs. . NMI. Probably, one bpy is lost during this process and replaced by NMI ligands which would explain the observed blue-shift.[119] Interestingly, as bpy is known to be a better π-acceptor ligand compared to NMI[20, 82, 142] the replacement of one bpy ligand by NMI (which in turn is a stronger σ-donor[142-143]) is expected to yield a *red-shift* of the MLCT bands. However, the interaction between CT band frequency and electronic/steric effects of the ligands on the other hand is intricate.[144] While the $Cu^I(bpy)_2$ exhibits tetrahedral geometry[136] the loss of one bpy unit and the replacement by two NMI ligands would significantly release steric strain. As seen in other examples *e.g.* $Cu^I(phen)_2$ complexes, this indeed could be responsible for a blue-shift of MLCT bands.[144-145]

Interestingly, the activity data (**Figure 5**) show increased activity within an experiment solely using 1.0 equiv. bpy compared to 2.0 equivs. This finding might also be directly related to the equilibrium between $Cu^I(bpy)_2$ and Cu^I(bpy) species as it was reported that Cu^I(bpy) is more easily oxidized than its 2-fold coordinated analogue.[123, 125] Zamudio et al. reported that the Cu^I(bpy) species is more reactive towards O_2 as those complexes are not completely chelated by bpy facilitating formation of an Cu^I(bpy)–O_2 adduct as an intermediate in the oxidation to Cu^{II}.[123, 136] This would corroborate the decrease in activity when using 2.0 equivs. bpy, since the amount of Cu^I(bpy) species is even less, in turn producing less Cu^{II} species in the first reaction step.

In comparison, in the Cu^IOTf–NMI catalytic systems, only less intense absorption bands below 300 nm are visible owing to the weaker π-acceptor capabilities of imidazoles[142] (**Figure A1**). This indicates that the blue-shift (***cf.*** **Figure 8 green**) *cannot* arise from a transition between Cu^I and NMI. It should be noted that the NMI ligands might only weakly interact with the (bpy)Cu^I complex.[119, 142, 146] When an excess of NMI is added, the majority of (bpy)$Cu^I(NMI)_2$ will most likely revert to a $Cu^I(NMI)_X$ species which exhibits no bands in the region between 300-600 nm explaining the loss in MLCT features in **Figure 6 and 7B**. One should be careful about the exact coordination number of $Cu^I(NMI)_X$ complexes as they might be below 4 based on electrochemical investigations[143, 147] and precipitates.[148] Catalytic systems utilizing only Cu^IOTf/NMI nevertheless possess high activity in the aerobic oxidation of alcohols (**Figure 5B**) being only slightly inferior to Cu^IOTf/bpy/NMI systems (**Figure 5A**). A similar catalytic system incorporating Cu^II in combination with NMI and TEMPO has also been reported very recently in literature[148] achieving high yields for both aromatic as well as aliphatic substrates.

More insight into Cu^I active sites through electrochemical analyses

The Cu^I complex formation has also been studied by *in-situ* electrochemical analyses, in particular, cyclic voltammetry (CV) (**Figure 9**).

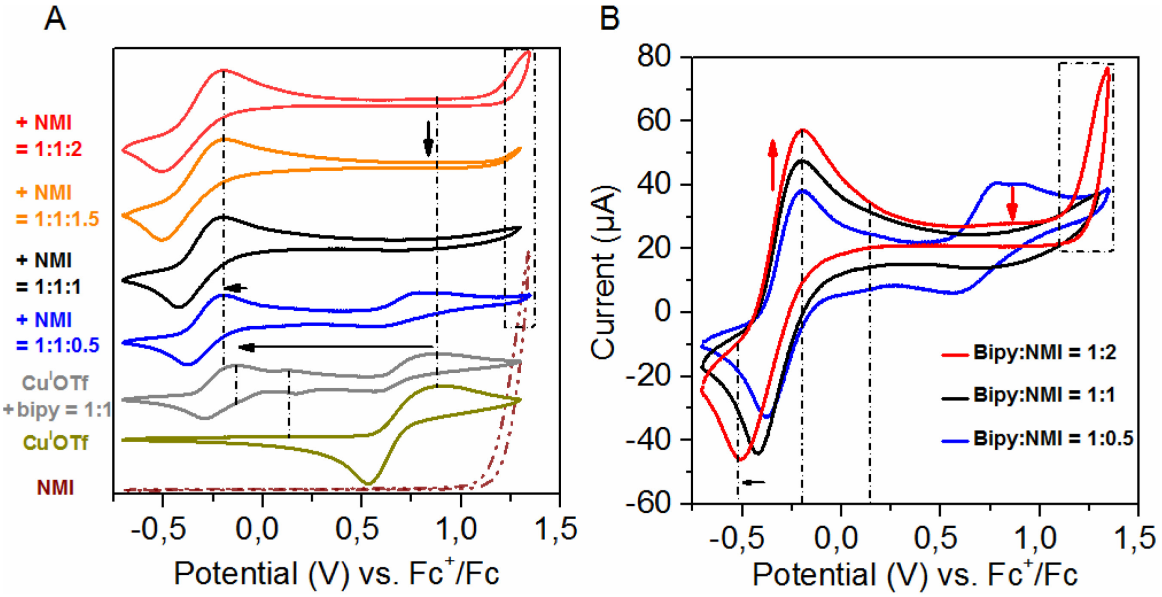

Figure 9. CV measurements on catalytic systems using Cu^IOTf with subsequent addition of bpy and NMI in steps of 0.5 equivalents compared to NMI solely measured in MeCN. The Ferrocene redox couple (Fc^+/Fc) was measured at 0.505 V (Ag/AgCl) and subtracted from the measured potentials. Adapted with permission from reference 119.

To gain more insight into the formation and redox behavior of assumed Cu^I/bpy/NMI complexes, cyclic voltammetry has been performed (**Figure 9**). Cu^IOTf in MeCN solution gives rise to one oxidation peak at approx. +0.85 V and a reduction event at approx. +0.6V attributed to the $Cu^{I/II}$ center (**Figure 9A**) can be seen. Susbequent addition of 1.0 equiv. of bpy to this solution leads to a decrease of this redox feature. However, a new broad redox event can be evidenced and is ascribed to a $Cu^I(bpy)_2$ complex, the oxidation peak occurs at approx. –0.15 V whereas the reduction peak can be seen at approx. –0.25V. These findings clearly show, that the bpy ligand significantly lowers the Cu^I redox potential making the Cu center more prone to oxidation by O_2. Intriguingly, a considerable amount of Cu^IOTf is still present in solution which points to immediate formation of a $Cu^I(bpy)_2$ complex while non-converted Cu^I remains in solution. This coincides with the appearance of a smaller redox event at approx. + 0.11 V which could very well belong to a single coordinated $Cu^I(bpy)$ complex. The addition of 0.5 equiv of NMI led to a further shift in the oxidation wave to approx. −0.19 V, showing the instantaneous formation of a new Cu species, presumably, $(bpy)Cu^I(NMI)_2$, being the major species. This is in accordance with previous findings indicating that oxidation of $Cu^I(bpy)_X$ complexes by O_2 is enhanced by NMI due to a significant decrease in its oxidation potential.[17, 20]

When increasing the amount of NMI to 1.0 equiv. the redox signal of Cu^IOTf nearly completely vanishes, suggesting the formation of the $(bpy)Cu^I(NMI)_2$ complex species to be complete. Addition of more than 1.0 equivalent of NMI (up to 2.0 equivs) leads to the appearance of a peak around 1.25 V, being very similar to the sole NMI ligand in MeCN. These observations indicate that the second NMI molecule might be bound only weakly, and hence can be electrochemically oxidized. These findings support the UV-vis results which indicate facile changes when more than 1.0 equiv. of NMI are added.[119] For the sake of comparison, the individual CVs have been overlaid in **Figure 9B**. It is evident that the measured current of the oxidation wave of presumed $(bpy)Cu^I(NMI)_2$ species at approximately −0.19 V increases and broadens with the subsequent addition of NMI, even when *more* than 1.0 equiv. of NMI are injected. The oxidation peak does not shift in the presence of increased amounts of NMI. However the reduction wave changes its position markedly, indicating irreversible electrochemical processes at the electrode. In the CV after addition of 0.5 equivs. NMI (**Figure 9B, blue line**) two other redox events – one at approx. +0.75 V and a smaller one at approx. +0.08 V – could be observed. The latter one might be an intermediate $Cu^I(bpy)$ species as the free bpy ligand does not give rise to a redox event around that position (for CV of bpy ***cf.*** **Figure A2A**). This points to formation of a $(bpy)Cu^I(NMI)_2$ complex without intermediate stages leaving significant amounts of Cu^IOTf present in solution. If all Cu^I species in solution would have been coordinated by *one single* bpy ligand, the redox event attributed to the starting material Cu^IOTf should be absent or at least significantly smaller (**Figure 9A, grey**). Interestingly, that particular redox event significantly decreases after addition of 1.0 equiv. NMI (**Figure 9, black**) and is absent when adding NMI in total of 1.5 and 2.0 equivs. of NMI (**Figure 9 orange and red**). However, the intensity of the oxidation event at –0.19 V increases up to a ratio of NMI/Cu ~ 2 meaning that the amount of Cu complex species increases. Concurrently, the oxidation event slightly broadens. These findings suggest that either a higher amount of the presumed (bpy)$Cu^I(NMI)_2$ species is present or that $Cu(NMI)_X$ species are formed in addition. It is reasonable that such species might be responsible for the rise *and* broadening in the –0.19 V oxidation event confirming our previous assumptions of multiple Cu^I complex species in solution evidenced from our UV-vis studies. Corresponding differential pulse voltammograms (DPV) corroborating the trends observed from the CVs can be found in **Figure A2B**. Comparison of the redox event of the starting material, Cu^IOTf, before and after adding 1.0 equiv. of bpy, reveals a significant portion of the starting material to remain in solution *after* addition of bpy. Reduction of that DPV feature can be seen, however, when NMI is added afterwards similar to **Figure 9B**. Moreover, an experiment using Cu^I+NMI in the absence of bpy, displays a very broad redox event centered around –0.21 V which could be responsible for the broadening of the redox features observed in **Figure 9A red line.**

Brief summary

In contrast to contemporary references which suggest the formation of one Cu^I species,[20, 28-29, 32] our UV-vis and electrochemical studies rather suggest that addition of bpy and NMI to the Cu^I precursor in solution produces several Cu^I complexes. Most likely $Cu^I(bpy)_2$, (bpy)$Cu^I(NMI)_2$ and $Cu^I(NMI)_X$ species are forming an intricate equilibrium (**Scheme 12**).

$$2\ Cu^I(MeCN)_4 + bpy \rightleftharpoons Cu^I(bpy)_2(MeCN)_2 + Cu^I(MeCN)_4$$

$$Cu^I(bpy)_2(MeCN)_2 + NMI \rightleftharpoons Cu^I(bpy)_2(NMI)_2 + 2\ MeCN$$

$$Cu^I(MeCN)_4 + NMI \rightleftharpoons Cu^I(NMI)_X + X\ MeCN$$

Scheme 12. Equilibrium depicting major Cu^I complex species when using 1.0 equiv. bpy and 2.0 equivs. NMI according to our spectroscopic and electrochemical results.

The most prevalent species before addition of NMI, $Cu^I(bpy)_2$, is converted into an NMI containing Cu^I complex after addition of NMI. However, a significant amount of the Cu^IOTf starting material remains in solution which is, however, transformed into another Cu^I complex upon subsequent addition of NMI. This suggests that $Cu^I(NMI)_X$ species do occur, too, and might also play a role as catalytic species. The interaction between one NMI ligand within the presumed (bpy)$Cu^I(NMI)_2$ complex seems to be weaker as a ratio of more than 1.0 equiv. of NMI shows a redox event which is similar to that of the free NMI ligand in solution.

"Which is the active Cu^{II} species?"

As shown previously[17, 20], the oxidation of Cu^{I} to Cu^{II} formed Cu^{II} species which can be monitored by *in-situ* UV-vis as well as EPR spectroscopy. Hence, we wondered how the nature and the amount of ligands affect oxidation and reduction steps within the aerobic alcohol oxidation.

Monitoring of active Cu^{II} sites by EPR/UV-vis/ATR-IR coupling

Upon introducting O_2 into solutions containing Cu^{I}OTf + 1.0 equiv. bpy, 2.0 equivs. NMI and 1.0 equiv. TEMPO a characteristic d-d band at λ_{max}=650 nm evolves with time (**Figure 10A**).

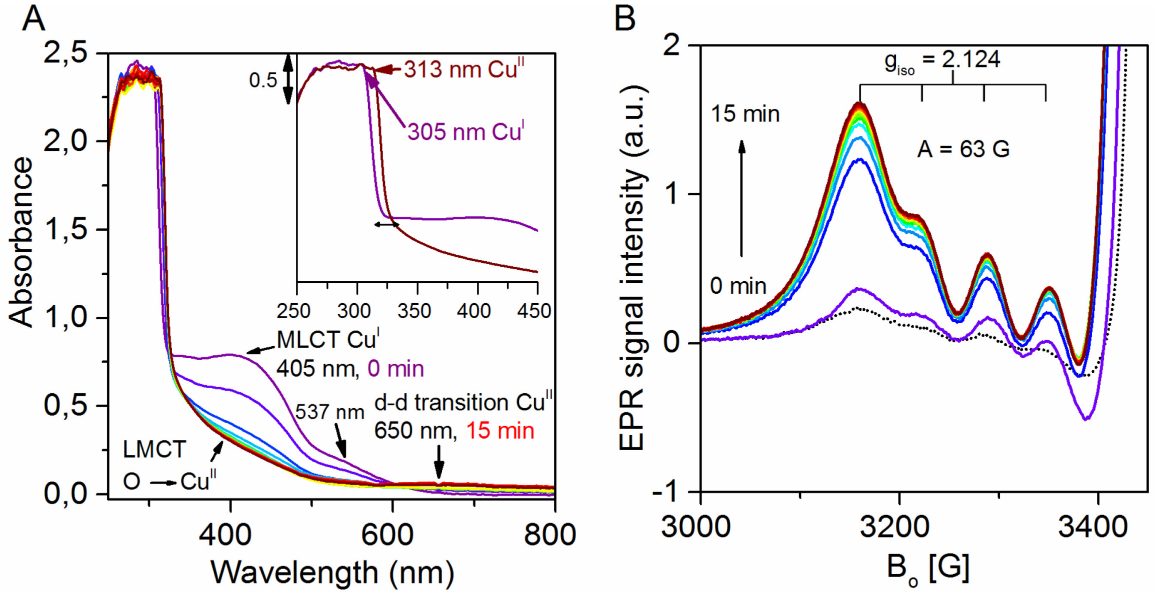

Figure 10: Exemplary Cu^{II} formation monitored by EPR (**A**) as well as UV-vis (**B**) spectroscopy in the presence of Cu^{I}OTf and 1.0 equiv. bpy, 2.0 equivs. NMI and 1.0 equiv. TEMPO ([Cu] = 0.02 M). The UV-vis spectrum shows an experiment using only [Cu] = 0.005 M. The simultaneously acquired spectra can be found in **Figure A3**. Adapted with permission from reference 119.

Simultaneously, the MLCT bands of the Cu^{I}(bpy)(NMI)$_2$ complex at λ_{max}=405 nm and the shoulder at 537 nm decrease, indicating that (bpy)Cu^{I}(NMI)$_2$ is oxidized to a (bpy)Cu^{II}(NMI)$_X$ species. A broad LMCT band[17] at λ_{max}=313 nm with a shoulder in the range between 325 and 450 nm remains after oxidation. In Cu^{II} complexes which derive from Cu^{I} precursors, broad absorptions in the range between 350 and 500 nm in general point to coordination of an O-species to the Cu^{II} center.[58] The precise species is not known and might be difficult to determine while other reaction components are present in solution. However, a Cu^{II} end-on superoxide[58] or Cu^{II} dimers[58, 149-150], *e.g.* bis-μ-hydroxy or peroxo bridged Cu^{II} dimers, are viable candidates. This might also explain why an isosbestic point is not observed, in accordance with Stahl's observations,[20] indicating that conversion of *one species into one other* is certainly not occurring (close up ***cf.*** **Figure A3**). The exact nature of these complexes will be discussed in detail later.

A similar behavior during O_2 introduction is also evident from the simultaneously measured EPR spectra in which an isotropic Cu^{II} signal is observed (**Figure 10B**). The characteristic hfs quartet of the Cu^{II} species increases with time, which arises from spin coupling of the unpaired electron with the $^{63/65}$Cu nucleus (d^9, $S = 1/2$, and $I = 3/2$). This signal is partly overlapped on the high field $m_I = -3/2$ peak by the hfs triplet ($S = 1/2$ and $I_N = 1$) of the TEMPO radical ($g_{iso} = 2.004$) as shown in more detail in **Figure 18**. The behavior of the TEMPO signal was recently investigated.[17] It broadens and narrows reversibly upon the introduction or removal of O_2 because of dipolar interaction without being engaged in a redox reaction itself. However, this hypothesis is discussed later.

A step-wise oxidation and reduction protocol was applied to explore the behavior of the active Cu^{II} species in detail. The original spectra can be found in **Figure A4** and **A5**. The Cu^{II} signal intensity is followed by monitoring the relative change of the low field peak $m_I = +3/2$ of the Cu^{II} hfs signal (**Figure A4A, A5A**) plotted with time in **Figure 11A** as well as the relative change in UV-vis absorbance measured at 650 nm (d-d transition band of Cu^{II}) (**Figure A4D)** until equilibration of the spectroscopic features **Figure 11B**. Interestingly, the rate of increase of the Cu^{II} EPR signal intensity as well as of the UV-vis absorbance is faster for the experiment using 2.0 equivs. NMI. Maximum signal intensity in presence of 2.0 equivs. of NMI is reached after approx. 10 min but only after about 13 min in the case of 1.0 equiv. of NMI. This clearly shows that oxidation of the Cu^{I} species is faster when 2.0 equivs. NMI are added to a solution of Cu^{I}OTf and 1.0 equiv. bpy in MeCN.

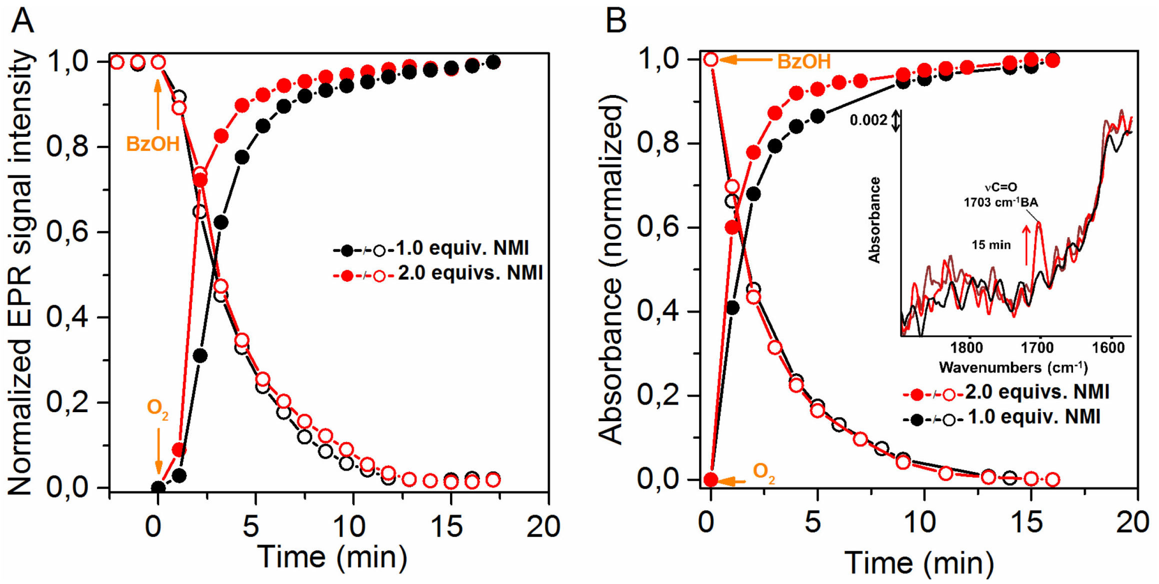

Figure 11. Progression of relative, normalized Cu^{II} intensity measured at m_I=3/2 low-field peak by EPR spectroscopy during oxidation (closed symbols) and reduction (open symbols) in presence of 1.0 or 2.0 equivs. of NMI (**A**) and corresponding UV-vis data measuring the normalized intensity of the d-d transition band at 650 nm. The inset is showing the detection of BA during the experiment using 1.0 equiv. NMI after 15 min (**B**). Adapted with permission from reference 119.

Subsequently, the reduction behavior of the formed Cu^{II} species was explored. After introducing argon (to remove excess O_2, thus preventing re-oxidation) and the addition of stoichiometric amounts of BzOH (1.0 equiv.), the Cu^{II} signal intensity decreases again because the assumed $(bpy)Cu^{II}(NMI)_2$ species is reduced to $(bpy)Cu^{I}(NMI)_2$ (**Figure A4B** and **A5B**). However, this process proceeds with virtually identical rates for solutions containing either 1.0 or 2.0 equivs. NMI, leading to complete decline of the Cu^{II} EPR signal after approx. 13 min. During reduction, distinct changes in the UV-vis features, appearance of MLCT bands of Cu^{I} and disappearance of the Cu^{II} d-d band, are also noted (**Figure A4E, A5E**). Formation of BA could be evidenced by ATR-IR spectroscopy during reduction (**Figure 11, inset**) confirming not only the reduction of Cu^{I} to Cu^{II} but also the simultaneous conversion of BzOH to the substrate during this reaction step. When O_2 is introduced again (re-oxidation of reduced Cu^{II} species) similar features, compared to those during the initial oxidation, are observed **(Figure A4C/F, A5C/F, A6)**, suggesting that the active Cu species is able to shuttle between Cu^{I} and Cu^{II} valence states. Surprisingly, the Cu^{II} reduction rate does not change when using either 1.0 or 2.0 equivs. of NMI, though a faster reduction in the presence of excess NMI would be expected when NMI acts as a base.[19-20, 66] In this case, deprotonation of the alcohol substrate would favor formation of a Cu^{II}-alkoxide species, which would speed up the conversion into BA. However, it is more convincing that a profound ligand effect plays a major role, that alters the coordination situation around the Cu^{I} species. From the investigations of the Cu^{I} species is it evident that a $(bpy)Cu^{I}(NMI)_2$

complex is formed upon addition of NMI, being the major catalytically active species alongside $Cu^I(NMI)_X$. As the oxidation of Cu^I to Cu^{II} only slowly progresses in the absence of NMI, it seems plausible that the stronger σ-donor effect of the NMI ligand compared to bpy, is responsible.[142] Previously, we found that an intricate equilibrium between several Cu^I species exists (***cf.*** **Scheme 12**). If addition of 2.0 equivalents promotes fast oxidation this might be due to three factors:

1) Additional NMI leads to formation of a higher fraction of $(bpy)Cu^I(NMI)_2$ species and hence more active species
2) $Cu^I(NMI)_X$ could be formed from the remaining Cu^IOTf in solution
3) Weak interaction between formerly proposed (bpy)Cu(NMI) species and an additional NMI molecule might boost the ability of the $Cu^I(bpy)(NMI)$ complex to get oxidized[119]

Due to the increased number of strong σ-donor ligands (*i.e.* NMI), Cu^I complexes are oxidized more easily as those ligands stabilize the Cu^{II} oxidation state.[142] This is further evidenced by the fact that ligands having stronger π-acceptor properties such as bpy[151] and MeCN[152] are known to stabilize the Cu^I valence state.[20, 121, 142]

The importance of NMI for the oxidation step shall be further highlighted by experiments involving *solely* bpy and NMI as ligands. When a solution containing Cu^I/bpy/TEMPO is exposed to O_2 for more than 100 min, conversion into a Cu^{II} species can be observed, too (**Figure 12**) in contrast to previous reports.[17] Intriguingly, kinetics seem to be quite different, compared to experiments with both bpy and NMI ligands (***cf.*** **Figure 11**) which could only be evidenced by the simultaneous coupling of *in-situ* EPR and UV-vis spectroscopy. In the UV-vis spectra two bands (MLCT and d-d band) were monitored. The MLCT shoulder at 550 nm (***cf.*** **Figure 7**) seems stable for approx. 40 min after O_2 introduction while the d-d transition band at 650 nm increases steadily with time and follows the trend of the Cu^{II} EPR signal.

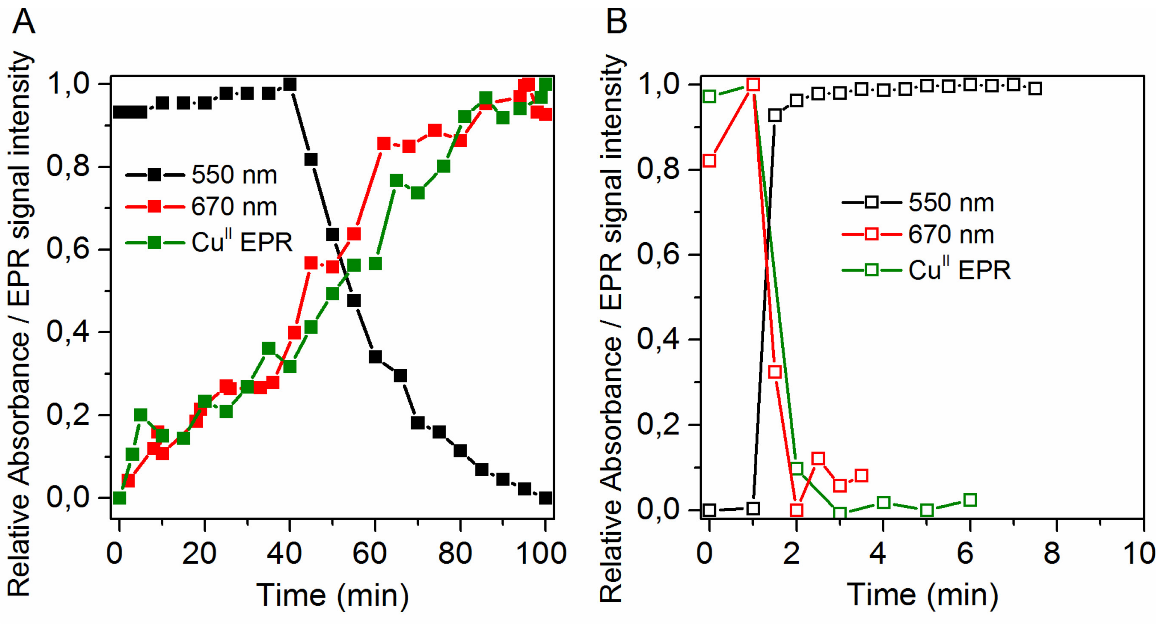

Figure 12. Progression of relative, normalized Cu^{II} intensity measured at m_I=+3/2 low-field peak by EPR spectroscopy as well as corresponding UV-vis data measuring the normalized intensity of MLCT at 550 nm and d-d transition band at 650 nm in presence of Cu^{I}OTf and 1.0 equiv. bpy during oxidation (**A**) and reduction (**B**).

Only after approx. 45 min the MLCT band drops significantly. This suggests that a two-step process takes place. It was reported, that the single coordinated Cu^I(bpy) species is more susceptible to oxidation[123, 136] than Cu^I(bpy)$_2$. Therefore, the Cu^I(bpy) species, present in solution due to equilibrium between Cu^I(bpy) and Cu^I(bpy)$_2$ (*vide supra*), is oxidized first giving rise to a steady increase in Cu^{II} signal intensity. The reason for this effect lies in the faster adduct formation of the latter resulting in (bpy)Cu^I-O$_2$ species.[17, 123, 136] The lack in MLCT band intensity decrease at the beginning might be explained by remaining Cu^I(bpy)$_2$ in solution, since those MLCT transitions mainly arise from the Cu^I(bpy)$_2$ species.[123] Only when a significant amount of this complex species is starts to get oxidized, a noticeable reduction of the MLCT band intensity can be observed. If 1.0 equiv. BzOH is added to these solutions, rapid reduction of the formed Cu^{II} species can be observed. These findings further confirm that NMI is *not necessary* for the reduction to proceed smoothly; hence, it does not act as a base contrary to earlier studies.[19-20] The fact that the oxidation proceeds faster for Cu^I(bpy) compared to Cu^I(bpy)$_2$ species would also explain the higher conversion and different reaction profiles observed during the activity screening (**Figure 5A**) when using 1.0 equiv. bpy compared to 2.0 equivs. Using more than 1.0 equiv. bpy shifts the equilibrium towards the (bpy)$_2$Cu^I species, which is harder to oxidize.[123]

On the other hand, omitting bpy and only employing NMI as a ligand leads to rapid formation of Cu^{II} species during the first 5 min (**Figure 13**). In fact, the relative rate of Cu^{II}

formation is between that of experiments with bpy+1.0 equiv. NMI and bpy+2.0 equivs. NMI (*cf.* **Figure 11**). This was expected, as NMI acts as a stronger σ-donor ligand compared to bpy, facilitating oxidation of Cu^I to Cu^{II}.[142]

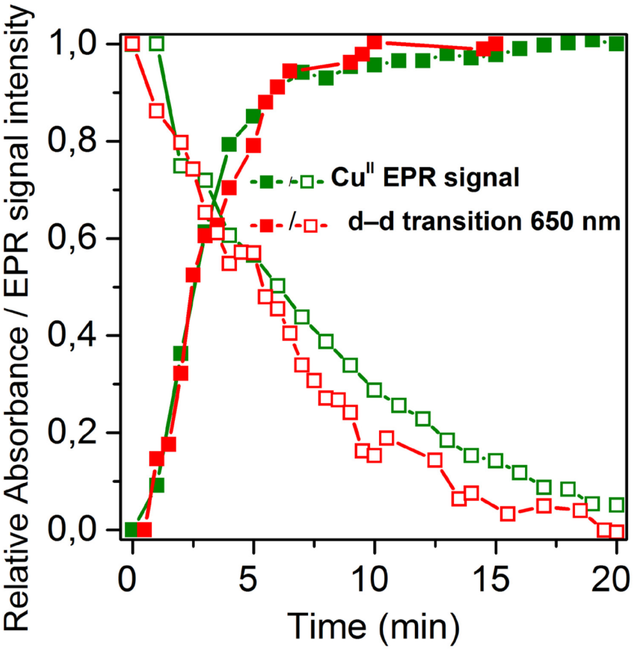

Figure 13. Progression of relative, normalized Cu^{II} intensity measured at m_I=3/2 low-field peak by EPR spectroscopy as well as corresponding UV-vis data measuring the normalized intensity of the d-d transition band at 650 nm in presence of Cu^IOTf and 3.0 equivs. NMI during oxidation (closed symbols) and reduction (open symbols).

On the other hand, the reduction of formed $Cu^{II}(NMI)_X$ species is markedly delayed. This is a direct result from the more stabilized Cu^{II} oxidation state by σ-donor ligands making reduction by BzOH slightly more difficult.

Brief summary

Summarizing this subchapter, our EPR and UV-vis studies using a step-wise approach clearly reveal that a catalytic system consisting of Cu^I/bpy and NMI as an additive shows an increased tendency for oxidation when the amount NMI is raised. This highlights the significance of NMI as a ligand. However, the reduction step seems to be unaffected by the presence of NMI which is not in accordance with NMI acting as a base. These findings could be corroborated, when bpy and NMI were solely employed as ligands with Cu^I as catalyst. In the absence of NMI, Cu^I/bpy containing systems are oxidized very slowly. On the other hand, Cu^{II} species derived from Cu^I/bpy systems can be reduced by BzOH even in the absence of NMI. This further shows that NMI does not primarily act as a base and correlates with previous findings that the rate-determining step is the oxidation/re-oxidation of the Cu^I complex when aromatic alcohols are used as substrates.[15, 18, 20]

To avoid superposition of signals from Cu^{II} and TEMPO in the EPR spectra, we carried out additional experiments with Cu^{I}OTf, 1.0 equiv. bpy and 1.0-3.0 equivs. NMI in the *absence* of TEMPO. Such a protocol allowed us to investigate the active (bpy)Cu^{II}(NMI)$_X$ species formed after oxidation in greater detail, as changes in the high-field peaks can be better differentiated. In **Figure 14** the normalized EPR spectra measured after introduction of O_2 for 30 min are displayed. A clear increase of the line-width can be observed most prominently at the two m_I=–1/2 and m_I=–3/2 Cu^{II} high-field peaks, when increasing the NMI/Cu ratio from 1 to 3. However, the two low-field components do not change significantly.

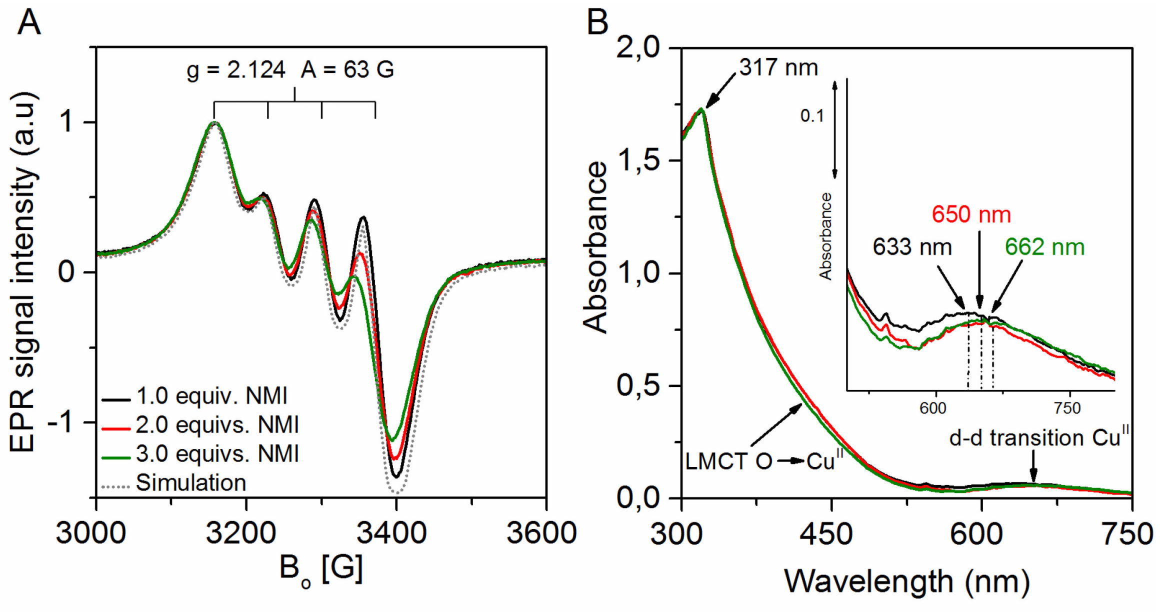

Figure 14. Normalized EPR spectra of oxidized solutions containing Cu^I(bpy) and either 1.0, 2.0 or 3.0 equivs. of NMI (**A**) and corresponding UV-vis spectra acquired simultaneously (**B**). Adapted with permission from reference 119.

Such broadening of hfs lines of transition metal complexes can be caused by a decrease in the tumbling rate, *e.g.*, by hydrogen bonding or by changes in the coordination sphere due to the coordination of sterically more demanding ligands. This was *e.g.* observed for various vanadium cluster compounds[153] and might explain the effects observed within the (bpy)Cu^{II}(NMI) system by weak interaction with additional NMI molecules within the coordination sphere.

A small red shift of the d-d transition band by approx. 30 nm from 633 to 662 nm with increasing number of NMI equivalents (1.0-3.0 equivs.) can also be seen within the simultaneously acquired UV-vis spectra. These effects can be caused by coordination of additional NMI molecules[154-157] being in accordance with the known role of imidazole-type ligands as labile ligands in naturally occurring enzymes systems.[158-161] The previously reported broad LMCT band in the around 400 nm is not significantly affected by additional NMI ligands.

Sometimes EPR spectra show a superhyperfine structure (shfs) which arise from the coupling of the unpaired electron with nuclei of neighboring atoms, in this case nitrogen. For better resolution of such shfs, *ex-situ* EPR spectra have been recorded at 240 K (**Figure 15A**). A similar effect as in the room temperature EPR spectra can be seen, even when the 2nd equivalent of NMI had been injected into the solution *after* the introduction of O$_2$. In these spectra, a slight increase of the g_{iso} value from 2.128 to 2.130 was accompanied by a slight decrease of the hfs constant from A = 65 G to A = 61 G after addition of the 2nd equivalent of NMI. These findings clearly show that the 2nd NMI molecule interacts with the (bpy)Cu^{II}(NMI) complex accompanied by slight changes of its local geometry.

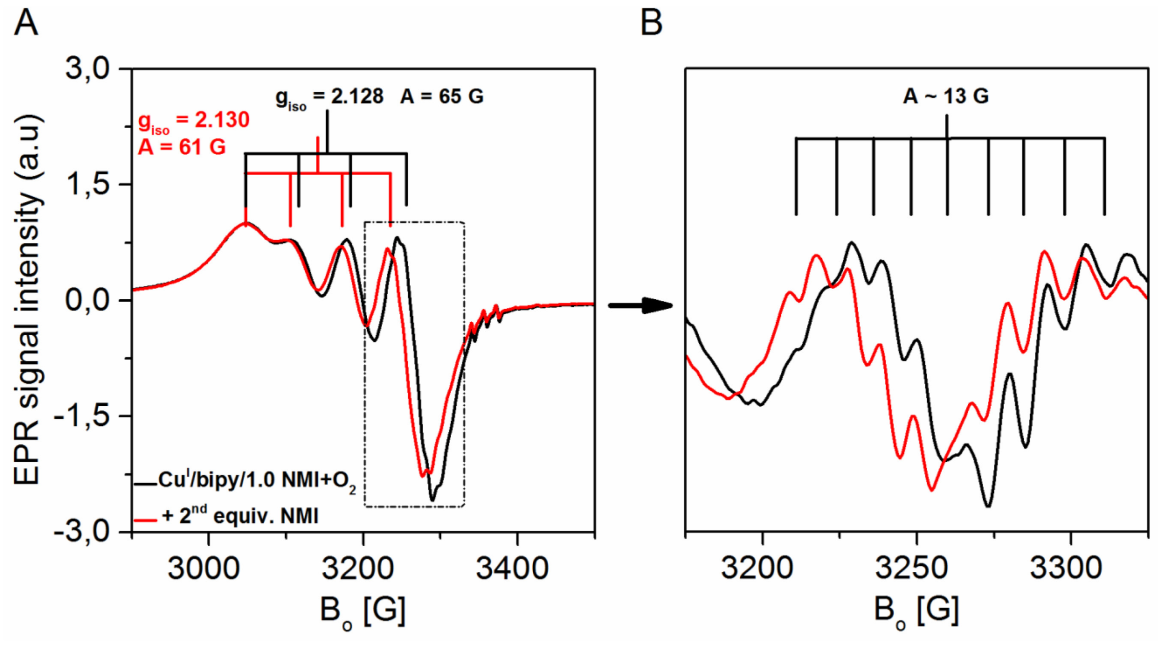

Figure 15. *In-situ* EPR measurements of a solution containing Cu^{I}OTf, 1.0 equiv. bpy and 1.0 equiv. NMI with subsequent addition of 1.0 equiv. NMI (**A**) and a part of these spectra seen in 2nd derivative (**B**). Adapted with permission from reference 119.

Since the individual transitions of the electron spin gain in intensity as the temperature decreases, better resolved shfs lines in the 2nd derivative of the EPR spectra are expected. Thus, in the 2nd derivative a shfs becomes visible displaying at least seven lines are which correspond to at least three coordinating N-ligands (**Figure 15B, black**). These features are absent at room temperature due to a higher tumbling rate. However, after injection of the 2nd NMI equivalent into the same solution, the shfs is more pronounced and additional features appear while the line-width increases simultaneously (**Figure 15B, red**). The determination of the exact number of lines is difficult. A shfs coupling constant of approx. 13 G was observed which lies in the range expected for the coupling to a ^{14}N nucleus.[162] Besides the increase in line-width, the observed broadening and asymmetry might be related to an overlap caused by the $^{63/65}$Cu^{II} isotope mixture.[142]

In summary, it is clear that the 2nd NMI equivalent interacts with the presumed (bpy)Cu^{II}(NMI) complex favoring the formation of a (bpy)Cu^{II}(NMI)$_2$ species in which at least one NMI molecule might be weaker bound and hence labile.

An additional EPR sample of (bpy)Cu^{II}(NMI)$_2$ was measured *ex-situ* at 100 K for investigating the g tensor components, since they are arranged in a specific order according to the local geometry of the Cu^{II} complex (**Figure 16**).[163]

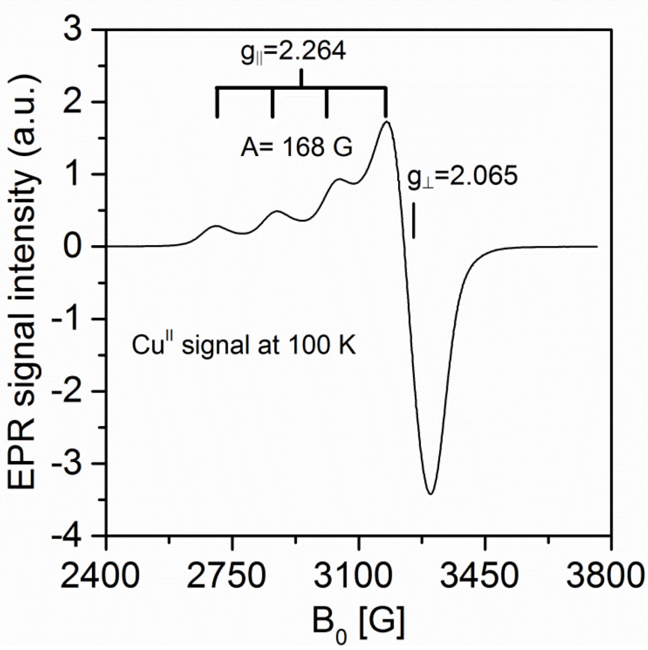

Figure 16. *Ex-situ* EPR sample of a mixture containing (bpy)Cu^I(NMI)$_2$+O$_2$ in MeCN.

A typical axial Cu^{II} signal is seen in the EPR spectra in a solution containing Cu^{I}OTf+1.0 equiv. bpy, 2.0 equivs. NMI after oxidation with O$_2$. We found values for $g_{\|}$=2.264 and for $g_{\perp}$=2.065 with a hfs coupling constant of 168 G. These values are in accordance with literature data suggesting a Cu^{II} surrounded by four strongly coordinating N donor ligands in a Jahn-Teller distorted environment.[164] The g tensor features are in the order of $g_{\|}>g_{\perp}>g_e$ which is typical for a tetragonal symmetry indicating a local geometry of the Cu^{II} ion in either octahedral or square-pyramidal arrangement.

In-situ, low-temperature IR measurements

The involvement and weak interaction of a second NMI ligand could also be affirmed by *in-situ* IR measurements at 233K (**Figure 17**). The studies were performed at lower temperatures, since we intended to monitor possible reactive intermediates such as the Cu–$O_2^{\bullet -}$ intermediate and to get better resolved spectra. Unfortunately, we did not observe bands related to any Cu^{II}–OR or other oxygen species. For these investigations, higher concentrations of the compounds were needed (0.08 M with respect to Cu^{I}OTf). In the IR spectra, a deformation vibration of the imidazole ring[165] was observed at 661 cm^{-1} in a solution containing Cu^{I}OTf, bpy and 2.0 equivs. of NMI in MeCN. This band splits into two bands centered at approx. 657 and 664 cm^{-1} as soon as O_2 was introduced into the solution causing oxidation of Cu^{I} to Cu^{II}. The band at 664 cm^{-1} is very close to the one of the free NMI ligand in MeCN whereas the band at 657 cm^{-1} corresponds to NMI coordinated to Cu^{II}. For investigating the reduction process, the solution was flushed with Ar to remove solved O_2 from the solution before adding BzOH.

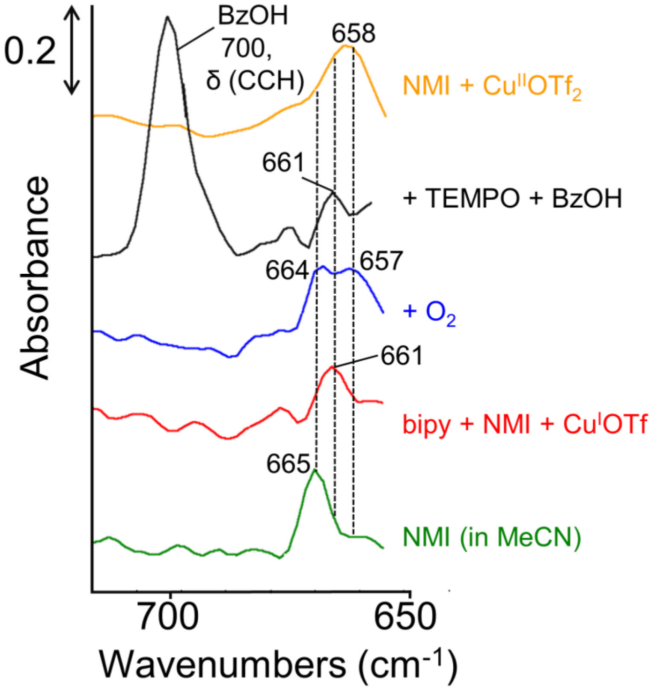

Figure 17. Sequential addition of compounds measured by *in-situ* IR at 233 K compared NMI added to a Cu^{II}OTf precursor in MeCN. Adapted with permission from reference 119.

Interestingly, when BzOH was added, no significant changes could be observed. Only after the addition of TEMPO the two bands merge into one, suggesting consumption of *coordinated* O_2 species (since the solution had been flushed with Ar) and re-coordination of NMI. This is in accordance with our assumption that NMI acts reversibly as a labile ligand.

Thus, it might be possible, that the weakly coordinated NMI molecule also serves as a proton shuttle during the coordination of the alcohol substrate.[119] On the other hand, the band at 665 cm^{-1} is so close to the band of the free ligand in solution, that there might be other processes involved, too. Complete detachment of (one) NMI molecule from the Cu^{II} center might also be possible, when *e.g.* Cu^{II} dimers are formed which possess a coordination environment of less than two NMI ligands. In **Scheme A1** a modified reaction cycle is shown highlighting the role of NMI. Furthermore in **Chapter 4.3** we took a closer look into such processes by using our new EPR/UV-vis/XANES/EXAFS/ATR-IR coupling set-up.

Changes of the TEMPO signal during the redox processes

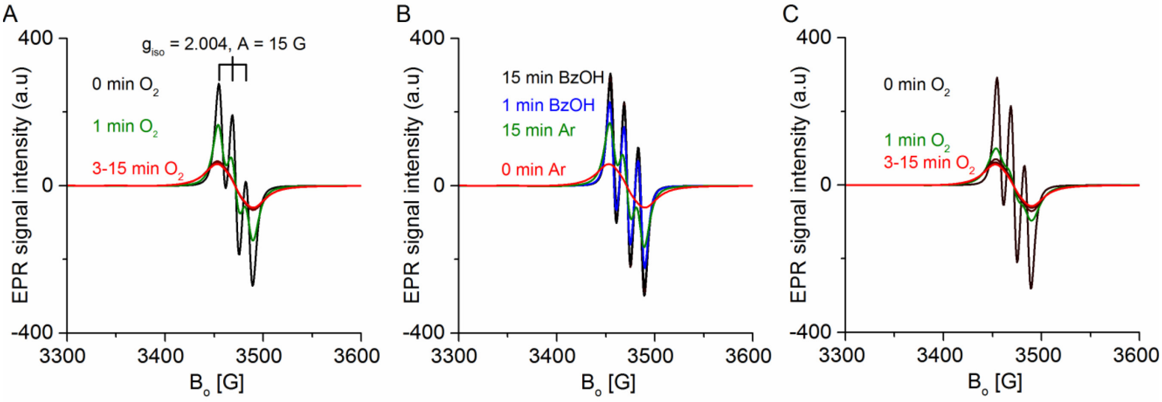

Figure 18. TEMPO Signal during **A**) oxidation of $(bpy)Cu^{I}(NMI)_2$ in presence of TEMPO during introduction of O_2 **B**) reduction of the formed Cu^{II} complex by BzOH under Ar atmosphere and **C**) during re-oxidation. Adapted with permission from reference 119.

As the behavior of the TEMPO signal has been investigated extensively in the past,[17, 19-20, 31] it shall not be the main emphasis of this thesis. Several mechanistic pathways have been proposed (*vide supra*) *e.g.* the direct involvement of TEMPO in a redox pair with $Cu^{I/II}$ [30, 72] or a pathway starting from a reduced TEMPOH species.[19-20] From our past[17] and recent investigations[119] carried out by using *in-situ* EPR spectroscopy we have evidence for a completely different pathway while there is no hint for a redox shuttle between the $Cu^{I/II}$ valence states and the TEMPO radical.

Within a solution of $(bpy)Cu^{I}(NMI)_2$ in MeCN in the absence of O_2 the characteristic hfs triplet of TEMPO can be observed. These features originate from interaction of the unpaired electron with the nuclear spin of N (I_N = 1) (**Figure 18A**), giving rise to a hfs coupling constant of A = 15 G and g_{iso} = 2.004, typical for an organic radical.[17] Shortly after the O_2 flow has been started the radical signal drops markedly. After approx. 3 min of O_2 flow equilibrium is achieved. The individual hfs lines broaden beyond detection and only one very broad signal can be detected (**Figure 18A, red**). This characteristic feature can be attributed to dipolar interaction as described previously[95] and also occurs in the absence of Cu catalysts.[17, 95] Simultaneously, a Cu^{II} signal appears and rises with time (**Figure A4A**). During Ar flushing the TEMPO signal regenerates to a certain degree (**Figure 18B, green**). However, only addition of BzOH leads to complete regeneration of the TEMPO signal, while the Cu^{II} signal decreases as it is reduced to Cu^{I} (**Figure 18B, black, A4B**)**.** Similar changes in the TEMPO signal can be seen during repeated introduction of O_2 (re-oxidation) (**Figure 18C**) compared to the initial oxidation. This raises the question:

***What kind of interaction occurs between TEMPO and the Cu^{II} species*?**

In a previous work conducted in our group the intense line broadening was explained by dipolar interaction of the TEMPO radical with a Cu^{II}-$OO^{\bullet}$ monomeric species.[17] This interaction was supposed to be weak but our new results suggest a much stronger involvement of the TEMPO radical, since Ar flushing does not fully restore the prior signal shape (**Figure 18B**). These results rather suggest that the majority of the TEMPO radical present in solution only reversibly interacts with the O_2 flushed into. This is in accordance with the results of the Stahl group[15, 18-20] that the reaction order with respect to TEMPO is zero, meaning it is independent on the TEMPO concentration. Only a fraction of the TEMPO signal interacts with some other component present in solution. The comparison of the double integrated TEMPO signals after 15 min of Ar flushing and subsequent addition of BzOH (**Figure 18B, green vs black line**) revealed an approx 11% higher signal area for the measurement *after* consumption of BzOH. Thus, that fraction of TEMPO must have reacted chemically with another compound. These findings are in accordance with the observation that during the catalytic reaction the signal intensity of the TEMPO radical remains at only 19% throughout the reaction (***cf.*** **Figure 21**).

It is highly unlikely, that a Cu^{II} superoxide is stable under these conditions[89], since similar observations are made regarding the TEMPO signal when the radical is added to the solution *e.g.* 30 min *after* initiating O_2 flow (**Figure A7**). Those Cu^{II} solutions are also active and reduced to the Cu^{I} valence state when BzOH is present; both the Cu^{II} and the TEMPO EPR signal behave in a similar manner (***cf.*** **Figure A4B and 18**).

Cu^{II} species derived from Cu^{I} precursors naturally form mononuclear Cu^{II} hydroxide[10, 149] or Cu^{II} dimeric or higher nuclear species such as *e.g.* peroxo- or bis-µ-hydroxy Cu^{II} dimers.[10, 83] It should be stressed, however, that such Cu^{II} peroxo dimers, which might be initially formed, are also not stable under such conditions[166], being readily transformed to *e.g.* bis-µ-hydroxy

Cu^{II} dimers.[20] Other Cu oxygen species such as Cu^{II} super- or hydroperoxides can only be regarded as intermediates during the oxidation processes.[10] Furthermore, in the course of those oxidation processes H_2O_2 formation can be detected[20] with the protons most likely coming from solvent molecules or other reaction components.[19, 167] It is certainly possible according to the redox potentials[168] of involved species that H_2O_2 or $^{\bullet}OH$, and $^{\bullet}OOH$ radicals - which might be produced during Fenton's like processes[10, 91] - oxidize the TEMPO radical to the corresponding oxoammonium species, TEMPO$^+$ [168-169] (**Scheme 13**). In turn, the oxoammonium species could facilitate the hemolytic cleaving of the C-H bond of the alcohol substrate with the oxoammonium being reduced back to its TEMPO radical state. This means TEMPO would cycle between its radical and oxoammonium state throughout the reaction without interacting with Cu$^{I/II}$ at all. This would also explain the fact that from EPR and UV-vis spectroscopic data no interaction between the TEMPO radical and Cu valence state I or II can be found.[17, 31-32] Finally, a TEMPO$^+$ pathway would explain the spectroscopic evidence gathered from the *in-situ* EPR measurements such as the Cu^{II} signal increase / TEMPO signal decrease during oxidation and reverse behavior during reduction.

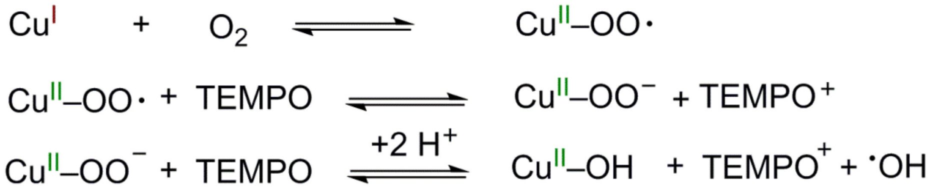

Scheme 13. Proposed interaction of Cu^{II} oxygen species and TEMPO according to our new results.

These assumptions are more convincing than the most prevalent reaction to date, Stahl's mechanism.[18-20, 31] The latter involves cleaving of Cu^{II} dimers by TEMPOH (yielding TEMPO radical) and the regeneration of TEMPOH during the substrate oxidation (***cf.*** **Scheme 8**). However, TEMPOH is not present at the beginning of the reaction and it is unlikely to form under such conditions by disproportionation.[1, 4] Although Cu^{II} reduction / BzOH oxidation was reported from Cu^{II} precursors under anerobic, stoichiometric TEMPO conditions[20, 32] it is unclear if this proceeds via a TEMPOH pathway. Moreover, the experiments conducted by the Stahl group[20] were performed using higher concentrated solutions (~6x the standard concentration [Cu]=0.01 M) and double the amount of TEMPO radical (ratio TEMPO/Cu^{I} = ~2).

Very recently Stahl et al. presented a detailed study based on EXAFS measurements and extensive DFT calculations of multiple, solid Cu^{II}-Cl complexes crystallized from TEMPO/ABNO containing solutions. Hereby, they found that the nitroxyl radicals coordinate to Cu^{II} complexes in an adduct like fashion. The Cu^{II}-nitroxyl radical bonding situation was best described to have Cu^{I} character whereas the radical has *oxoammonium-like* character. However, complete electron transfer from the radical species to the Cu^{II} ion was deemed to be impossible. Those adducts were assumed to facilitate hydride transfer from the C-H bond of the substrate alcohol to the nitroxyl radical (***cf.*** **Scheme 9**).The nitroxyl radical in turn donates an electron to Cu^{II} reducing it to Cu^{I}. Subsequently, the radical undergoes a two-electron reduction by the hydride to yield TEMPOH.[31] This *oxoammonium-like* reactivity supposedly is the key step during aerobic alcohol oxidation according to the authors while the Cu^{II} center merely serves as a template for substrate coordination. Although they propose an oxoammonium intermediate here in contrast to their previous TEMPOH-mediated mechanism, no evidence was provided that these aminoxyl radical adducts also form in solution. Furthermore, the role of formed superoxo/peroxo Cu^{II} intermediates which arise when using Cu^{I} precursors (opposed to Cu^{II} precursors) is still unclear. Those reactive oxygen species also likely interact with the TEMPO radical.[170] As it is evident from the TEMPO intensities before and after introduction of O_2 flow (**Figure 18**) that an interaction between TEMPO and the active Cu^{II} complex exists, their newly proposed cooperative pathway seems questionable. If their mechanistic pathway holds true, an interaction should only be observed in the presence of the substrate. Consequently, a decrease of the TEMPO signal would be expected as the EPR-active TEMPO radical is converted in the EPR-silent TEMPOH. However, the opposite occurs: the TEMPO radical signal increases upon addition of alcohol. Therefore, the precise mechanism remains highly uncertain and warrants further detailed investigations.

Brief summary

In this subchapter we could reveal the effects of different molar ratios of NMI on the EPR parameters of Cu^{II} complexes derived from Cu^{I}OTf/bpy/NMI. A clear increase in line-width was observed when higher molar ratios of NMI are used while the shfs is more pronounced. Low temperature investigations showed an axial EPR Cu^{II} signal which corresponds to a tetragonal distorted geometry of the individual Cu^{II} complexes. From additional IR measurements after oxidation of Cu^{I}/bpy/NMI containing solutions a band corresponding to the free NMI ligand became apparent and hence attributed to weak interaction of a second NMI molecule with the Cu^{II}/bpy/NMI complex. Additional studies regarding the Cu^{II}/TEMPO interactions were performed which showed a more intricate behavior. Some fraction of the TEMPO radical EPR signal disappears during the oxidation step which cannot be explained by a TEMPO/superoxide interaction. More likely, the TEMPO radical is oxidized TEMPO$^+$ by Cu^{II}–O$_2$ intermediate species during the oxidation step.

4.1.2. Effect of substituents in the imidazole scaffold

After investigating the effect of NMI on the Cu$^{I/II}$ species we focused on the effect of substituents of the imidazole ring on the reaction behavior. From **Figure 19** it is clear that the rate of BzOH oxidation depends crucially on the substitution pattern of the used imidazole. In **Table A1** the tested imidazole-type additives are summarized along with the reaction time and pKa values, if available.

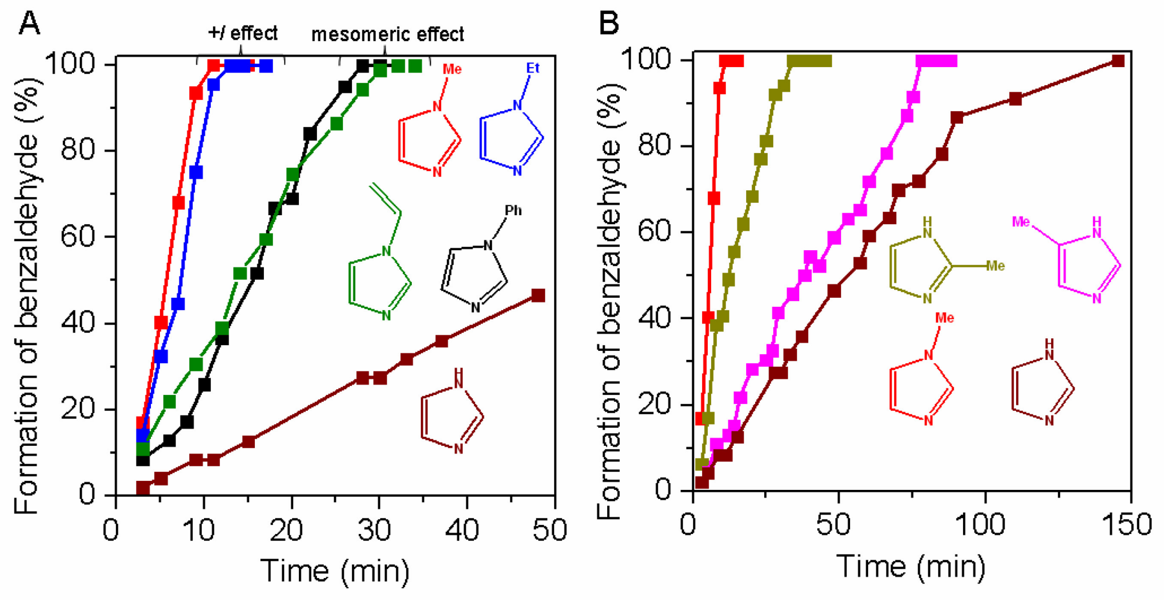

Figure 19. Formation of BA with time for various N-substituted imidazoles (**A**) and imidazoles substituted at other positions (**B**). Adapted with permission from reference 119.

Evidently, the reaction proceeds slowest with 1-H-imidazole. When the 1-H position is substituted with alkyl moieties in *e.g.* NMI or 1-ethylimidazole, a significantly faster conversion of BzOH to BA can be observed (**Figure 19A**). These findings might be related to the +*I* effect[142, 171] of the alkyl substituents which donate electron density to the active Cu^I species via the imidazole ring at the coordinating imine N, thus boosting its σ-donor ability.[142, 171] This could favor the electron transfer from Cu^I to the molecular O$_2$ during the first step of the reaction cycle, forming Cu^{II}.[17] No significant differences in the reaction rate depending on the chain length and the branching of the alkyl substituents were observed which might be related to their similar electronic properties[172] (**Table A1**). On the other hand, substituents bearing conjugated systems *e.g.* vinyl or phenyl substituents lead to slower reaction rates. This is most probably due to mesomeric effects as implementation of unsaturated substituents with *e.g.* allyl or benzyl groups (**Table A1)**, where the conjugated system is interrupted, only led to small increase of the reaction time in comparison with alkyl substituted imidazoles. This effect was attributed to less electron density donation into the imidazole ring, in turn slowing down electron transfer from Cu^{I} to the O_2 present in solution. Hence the formation of Cu^{II} in the first reaction step is slightly hindered. These effects might be caused by only weak resonance donation of substituents bearing a conjugated system *e.g.* vinyl and phenyl substituents.[173-175]

In the next step, imidazoles with an unsubstituted NH-moiety were studied to correlate the impact of the NH moiety on the reaction progress (**Figure 19B, Table A1**). Significantly lower reaction rates could be seen for all unprotected 1-H-imidazoles with that of the unsubstituted one having the slowest reaction rate (**Figure 19B, brown**). Clearly different reaction rates of 2-methylimidazole and 4(5)-methylimidazole could be due to both tau-tomeric[176] and electronic effects[177-178] as the $+I$ effect of a methyl substituent in C2 position was found to be slightly higher than in C4(5) position [142, 177] due to increased hyperconjugation.[179] The proton is able to shift easily between the imidazole N1 and N2.[176, 180]
Substituents in C4 or C5 position might cause the formation of isomers upon coordination of the imidazole to the Cu center, since proton shift is no longer possible. Therefore, the reason for the low activity of $(bpy)Cu^{I}(4(5)\text{-methylimdiazole})_2$ might stem from steric hindrance within the coordination sphere of $Cu^{I/II}$ complexes on one hand and less electron donation[179] towards the Cu^{I} species during O_2 activation on the other hand. Conversion times of BzOH to BA were found to be significantly longer for dimethyl imidazoles substituted at C1,2 and C2,4(5) positions (**Table A1**) compared to mono-substituted imidazoles, being attributed to steric factors. The faster rate for 1,2-dimethylimidazole is attributed to the protected NH-moiety, since 2,4(5)-dimethyl imidazole might be deprotonated *in-situ* and hence, can interact, with other Cu complex centers[181-185] or even form imidazolato-bridged Cu^{II} dimeric species.[186-187] This might be the main reason, why the unsubstituted 1-H imidazole shows the lowest reaction rate, since interaction with other Cu^{II} centers might hamper substrate coordination and hence, the reduction step. Since this ligand does not have any substituents, it is not possible to influence such interaction between close Cu^{II} centers, *e.g.* by electronic and steric effects from by methyl groups.[179, 188-189]

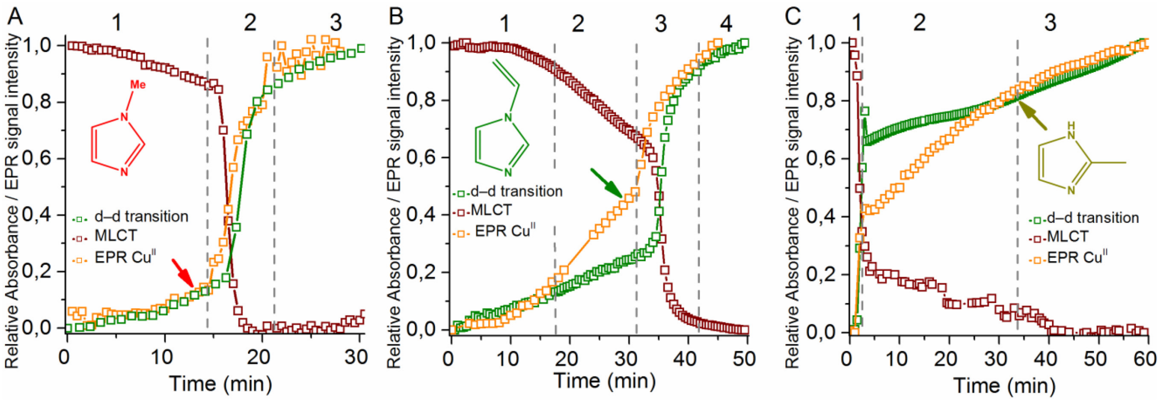

Figure 20. *In-situ* EPR spectra analyzed by monitoring the signal amplitude of the Cu^{II} low field peak m = +3/2 peak and UV-vis absorbance at 550 nm (corresponding to Cu^{I}) and 650 nm (corresponding to Cu^{II}) for NMI (**A**) 1-vinylimidazole (**B**) and 2-methylimidazole (**C**). Time of full conversion of BzOH to BA is marked with arrows.

To investigate these effects originating from alkyl and aryl substituents as well as the unprotected NH-moiety in more detail, the reaction behavior obtained from *in-situ* EPR and UV-vis measurements with time were compared, exemplarily, for NMI, 1-vinylimidazole and 2-methylimidazole (**Figure 20**), since these ligands differ significantly in their reaction rates. The EPR and UV-vis spectra can be found in **Figure A8-10**. For the sake of completeness pKa values[190] (of the conjugate base) of selected imidazoles are shown in **Table A1**. Interestingly, no direct correlation could be found between the pKa values[190] and the time required for full conversion of BzOH to BA (**Table A1**). It seems that the substitution pattern and the (un-)protected NH-moiety are more likely to affect the conversion rate.

The EPR signal amplitude of the Cu^{II} low field peak at $m_I=+3/2$ as well as the corresponding UV-vis absorbance at 550 nm (MLCT shoulder of Cu^{I}) and 650 nm (d-d transition of Cu^{II}) during the course of the reaction are depicted in **Figure 20.** For NMI three distinct phases during the reaction could be observed. During the 1st phase between 0 and approx. 13 min a slow increase of the EPR signal due to oxidation of $(bpy)Cu^{I}(NMI)_2$ to $(bpy)Cu^{II}(NMI)_2$ by O_2 can be seen at the start which is evidenced from a very slow drop of the MLCT band intensity of Cu^{I} (550 nm) and slight increase of the Cu^{II} d-d band (650 nm) in the UV-vis spectra as well as a slight increase of the Cu^{II} signal monitored by EPR (**Figures 20A and A8**). In the catalytic cycle, Cu shuttles between oxidation state I and II. The Cu^{II} species oxidizes BzOH to BA and is reduced back to Cu^{I}. Thus, as long as unconverted BzOH is still present in the solution, the Cu^{II} EPR and UV-vis signals reflect the equilibrium concentration of Cu^{II}. Consequently, this marginal increase in Cu^{II} signal intensity under these conditions could reflect unequal redox process, *i.e.* a slightly hindered reduction. Alternatively, these results could indicate slight deactivation processes (*vide infra*).

The 2nd phase between approx. 13 and 20 min is marked by a rapid decrease in the MLCT band and a fast increase in d-d transition band and EPR Cu^{II} signal intensity, respectively. This finding coincidences with the conversion of BzOH to BA after approx. 12 min. It indicates the oxidation of the remaining Cu^{I} species in solution after complete consumption of BzOH. In the 3rd stage from 20 to approx. 30 min an equilibrium concentration of Cu^{II} complexes is achieved.

A very different reaction behavior was observed when 1-vinylimidazole with a conjugated backbone was utilized as a ligand (**Figure 20B, A9**). Here, roughly four phases could be observed. In the first phase from 0 to approx. 10 min the formation of Cu^{II} species in solution is very low as evidenced from the UV-vis and EPR results. The 2nd phase follows from 10 to approx. 33 min characterized by a steady increase in d-d transition band / Cu^{II} EPR signal intensity and a drop in the MLCT band of Cu^{I}. This was unexpected, as the formation of BA was not yet complete (**Figure 20B, arrow**). The accumulation of Cu^{II} in solution might indicate that the reduction is hindered. It was proposed earlier that the ligand not only modifies the electronic properties of the $Cu^{I/II}$ species but serves also as a proton shuttle during the coordination of BzOH (**Scheme A1**).[119]
However, the slightly lower pKa (conjugated base) values of 1-vinylimidazole 6.26[191] vs NMI 7.21[190] mean that NMI would serve as a better proton shuttle due to its higher basicity. Consequently, proton transfer from the coordinated BzOH to the oxygen species and reduction of Cu^{II} to Cu^{I} should be hindered with 1-vinylimidazole. Interestingly, during the 2nd phase the EPR Cu^{II} signal rises faster compared to the intensity of the d-d transition band which was unexpected. Since the d-d transition band comprises all Cu^{II} species, it is reasonable that other Cu^{II} species are also actively participating in the reaction, *e.g.* EPR-inactive Cu^{II} dimers, indicating that some processes must occur leading to accumulation of EPR active Cu^{II} monomeric species. Tentative deactivation pathways are discussed **in chapter 4.3** and might be the reason for this effect. The 3rd phase from 33 to approx. 40 min is similar to phase 2 when using NMI. After the conversion of BzOH to BA is complete after approx. 32 min the residual Cu^{I} species are oxidized to Cu^{II}. During the last stage equilibrium concentration of Cu^{II} species is achieved.

The usage of 2-methylimidazole as a ligand gives rise to completely different reaction trend compared to 1-methylimidazole (**Figure 20C, A10**). Herein, two distinct phases and one equilibration period could be observed. During the initial phase a very steep increase of the Cu^{II} EPR signal (accompanied by a simultaneous drop of the Cu^{I} MLCT and an increase of the Cu^{II} d-d transition band) occurs within the first 3 minutes after starting O_2 introduction. Afterwards, from 3 to approx. 35 min the Cu^{II} concentration increases steadily. The rise in the signal intensity is slightly faster after 35 min until equilibrium is achieved after approx. 60 min. A direct correlation between the evolution of Cu^{II} species and the formation of BA during the reaction could not be made. However, the Cu^{II} concentration does indeed increase slightly faster after approx. 35 min after all of the BzOH has been converted to BA. The rapid increase in Cu^{II} species shortly after starting O_2 introduction was surprising and could also be observed with unsubstituted 1-H imidazole (*vide infra*) (**Figure A11**), indicating that the reduction of the formed Cu^{II} is significantly hindered. Curiously, the rise of the Cu^{II} signal intensity is distinctly different in the UV-vis and the EPR spectra, respectively. The significantly higher relative Cu^{II} percentage reflected by the UV-vis d-d transition band suggests that some Cu^{II} species might be present in EPR-inactive form, *e.g.* as Cu^{II} dimers. Thus, as mentioned before, imidazoles having an unprotected NH moiety probably interact by this moiety significantly with neighboring Cu^{II} centers. Moreover, the redox behavior of the $Cu^{I/II}$ shuttle might be influenced, too, which is discussed later.

The behavior of TEMPO during the catalytic reaction

In addition to tracking the Cu^{II} signal with time we also monitored the TEMPO radical signal by EPR spectroscopy during the course of the catalytic reaction. The relative signal intensities were obtained by double integration between 3430 and 3600 G with subsequent normalization. The relative progression when using either NMI, 1-vinylimidazole or 2-methylimidazole is depicted in **Figure 21**. In all three cases it is evident that the TEMPO signal intensity decreases rapidly for approx. 4 min after initiating O_2 flow. However, afterwards in the case of NMI and 1-vinylimidazole the signal intensity raises again to approx. 19% and 16%, respectively, until conversion to BA is complete after approx. 13 min for NMI or approx. 32 min for 1-vinylimidazole. When using 1-vinylimidazole a plateau phase is encountered during the active conversion of BzOH to BA. After the reaction is finished (marked by black arrows) the signal intensity decreases again until equilibrium is achieved. Interestingly, in the case of 1-vinylimidazole the signal intensity remains slightly elevated. The exact cause for this effect is not known and might be an artefact over the course of the measurement.

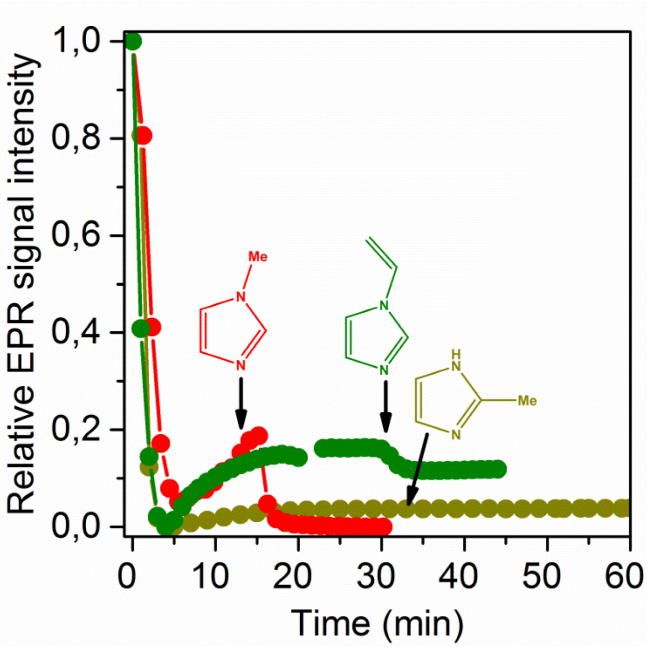

Figure 21. Relative TEMPO signal intensity with time during the catalytic conversion of BzOH to BA using either NMI (red), 1-vinylimidazole (green) or 2-methylimidazole (dark yellow) as ligands. Time of complete conversion of BzOH to BA marked with arrows.

A very different picture could be seen when 2-methylimidazole is utilized as there is very little rise in TEMPO signal intensity after the initial rapid decrease due to O_2 inlet and no correlation with the formation of BA can be observed.

When we explain the behavior of the TEMPO signal according to the pathway suggested previously,[17] it appears that during the initial phase the TEMPO radical mostly dipolarly interacts with the O_2 dosed into the system, which leads to line broadening. After the addition of BzOH, the signal intensity increases again when the Cu^{II}-$O_2^{\bullet-}$-TEMPO adduct dissociates upon BzOH consumption. As this process is continuously cycling during the catalytic reaction, the TEMPO radical signal remains nearly stable until the BA formation is complete. Afterwards the TEMPO radical again interacts with the Cu^{II}-$O_2^{\bullet-}$ intermediate leading to an increase in line width and hence a decrease in signal intensity. When 2-methylimidazole is employed as a ligand the lack of a plateau phase might be caused by three effects. On one hand the reduction of formed Cu^{II}-$O_2^{\bullet-}$ species could be hindered by electronic or steric effects (*vide infra*) exerted by the 2-methylimidazole ligand leading to dissociation of the weak Cu^{II}-$O_2^{\bullet-}$-TEMPO adduct. In turn, the TEMPO radical engages in dipolar interaction with the solved O_2 and hence only minimally interacts with the Cu^{II} oxygen species. The second reason could be the formation of less active Cu^{II} species when using imidazoles having an unprotected NH-moiety, *e.g.* by protonation and subsequent decomposition of the Cu^{II}-$O_2^{\bullet-}$ intermediate. In this case the TEMPO radical is also expected to interact primarily with the O_2 dosed into the solution. At last, EPR inactive Cu^{II} dimeric species formed by 2-methylimidazole as a bridging ligand through the deprotonated NH moiety might lead to active Cu^{II} species which govern the catalytic reaction. Of further interest is the fact that during the plateau phase (for NMI and 1-vinylimidazole) the relative percentage of the TEMPO signal intensity is only around 16-19% which mirrors Stahl et al. studies[18-20] that only a fraction of the amount of TEMPO is participating in the reaction.

Brief summary

In summary, it can be stated that the activity in the aerobic alcohol oxidation derived from the ATR-IR data was explored showing highest activity for catalytic systems consisting of Cu^{I}/bpy in addition to alkyl imidazoles (*e.g.* NMI). Imidazoles having an extension of the mesomeric system *e.g.* 1-vinyl or 1-phenyl imidazole show significantly prolonged reaction times. The longest reaction times, however, are observed for imidazoles having an unprotected NH moiety (*e.g.* 1-H imidazole). These findings are directly related to the different behavior of the Cu^{II} and TEMPO species during the conversion of BzOH to BA which is imposed by the different types of ligands nicely showing the added value of combining *in-situ* EPR and UV-vis spectroscopy. The precise ligand effects shall be investigated in the following.

Deeper insight into the redox behavior of Cu/imidazole complexes by *in-situ* EPR and UV-vis spectroscopy

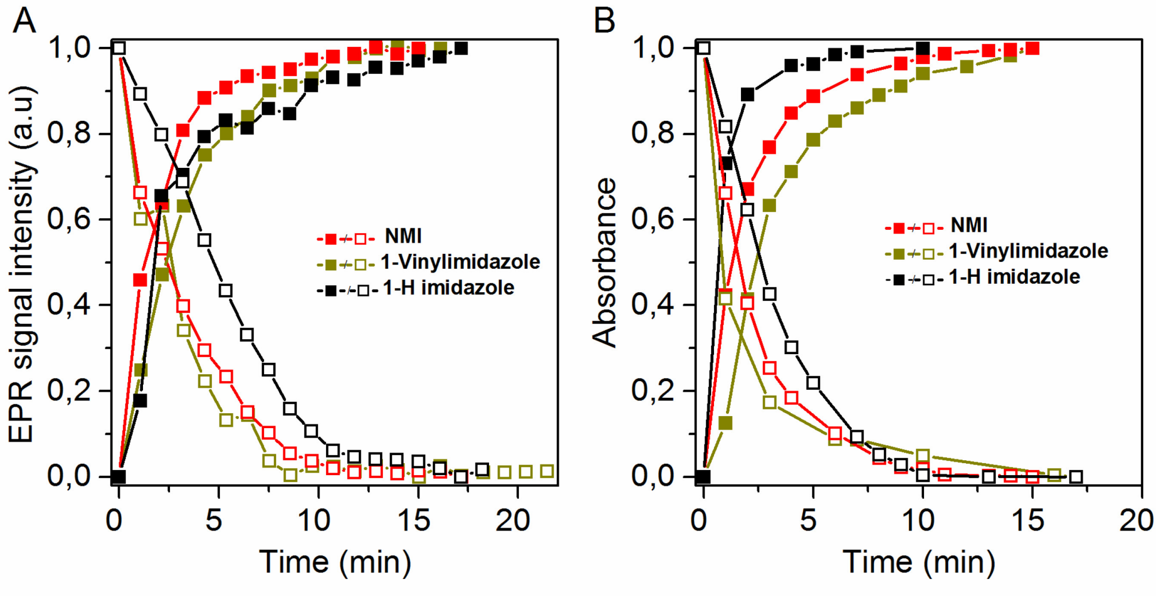

Figure 22. Oxidation of (bpy)Cu^I(IM)$_2$ by O$_2$ in the presence of TEMPO (solid lines, filled symbols) and subsequent reduction of formed (bpy)Cu^{II}(IM)$_2$ by excess BzOH (dashed lines, open symbols) in the presence of 2.0 equivs. of NMI, 1-VI or 1-H imidazole monitored by the relative change in amplitude of low field peak (m=3/2) Cu^{II} EPR signal (**A**) and the d-d transition band monitored at 650 nm (**B**). Adapted with permission from reference 119.

Since the relative equilibrium concentrations of Cu^I and Cu^{II} during the catalytic conversion of BzOH to BA are directly related to the individual Cu$^{I/II}$ redox rates, those two processes were analyzed in detail. A similar step-wise procedure was applied which was used to determine the differences between the reaction rates of various molar ratios of NMI (***cf*** **Figure 11**). For this experiment, too, the low field Cu^{II} EPR peak (m=+ 3/2) as well as the UV-vis absorbance at 650 nm (d-d transition band of Cu^{II}) were used as references. Starting with a solution of (bpy)Cu^I in MeCN containing TEMPO and 2.0 equivs. of either NMI, 1-vinyimidazole or 1-H imidazole, O$_2$ was introduced for 15 min leading to rapid oxidation. Subsequently, the solution was flushed with Ar for another 15 min to remove solved O$_2$. Finally, an excess of BzOH (20 equivs.) was added to reduce the active Cu^{II} species to the starting complex. (**Figure 22**)

Distinct differences in the redox properties between the three ligands became evident. When using 1-vinylimidazole (**Figure 22, dark yellow**) we found the oxidation of Cu^I to Cu^{II} to proceed slower compared to NMI (**Figure 22, red**) from both the EPR and the UV-vis results. The reduction on the other hand seems to occur with nearly similar rates for 1-vinylimidazole and NMI.

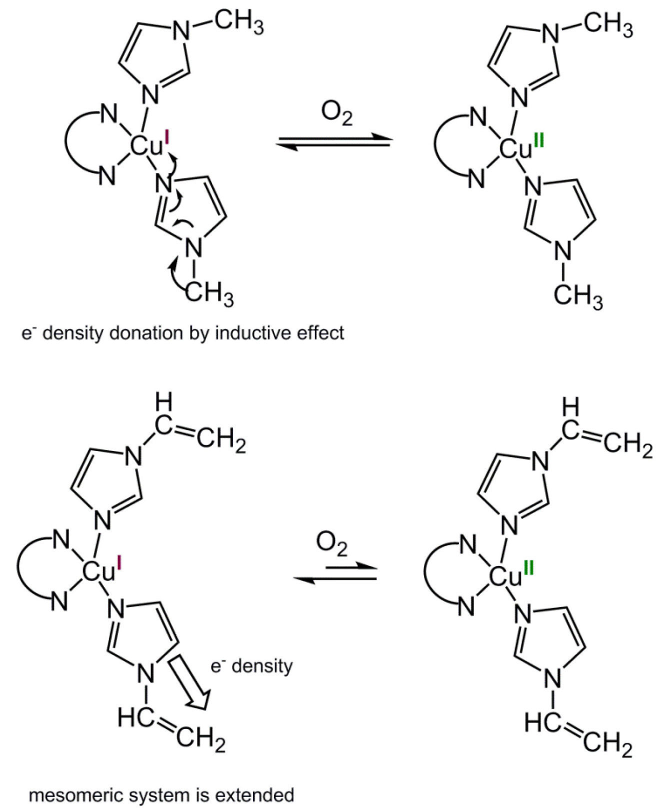

Scheme 14. Influence of the substituent in Cu/imidazole containing catalytic systems.

These findings might be related to the stronger σ-donor properties of the methyl substituent compared to the vinyl group, favoring the oxidation of Cu^I to Cu^{II} in the first reaction step, since more electron density is donated to the Cu^I valence state (**Scheme 14**).[142] This effect might explain the lower reaction rate for 1-vinylimidazole as the active Cu^{II} complex is formed slower. However, it does not explain the increasing Cu^{II} signal before the total conversion of BzOH to BA when using that ligand. Deactivation processes on the other hand might be the reason for these findings which is tentatively explained in **chapter 4.3**. In this case the ligand would act as a proton acceptor for scavenging proton sources *e.g.* BzOOH which could arise from overoxidation of BA. Those proton sources might lead to decomposition of Cu^{II} oxygen species leaving less active Cu^{II} complexes behind. Since NMI would be a better proton acceptor than 1-vinylimidazole according to their pKa values[190-191], a greater deactivation would be expected in the case of 1-vinylimidazole which holds true.

If the unsubstituted 1-H imidazole is used as a ligand, EPR results suggest that the rate of Cu^I oxidation might be between those of NMI and 1-VI. However, from the UV-vis measurements a very rapid formation of Cu^{II} is observed after only 1 min. These apparently conflicting results point to formation of EPR-silent Cu^{II} dimers, since the corresponding d-d transition band is well-established (**Figure A11B**). Magnetic interaction between neighboring

Cu^{II} complexes could also explain the higher line width and lower signal intensity in the corresponding EPR spectra (**Figure A11A**).[192] These findings could be explained by Cu^{II}-imidazolato-bridged dimers, which are well-known.[193] The formation of those species might very well be the reason for the low Cu^{II} signal in the EPR spectra and could be formed via *in-situ* deprotonation of the NH-moiety during reaction with oxygen species which is shown in **Scheme 15**.[17, 20, 185, 194]

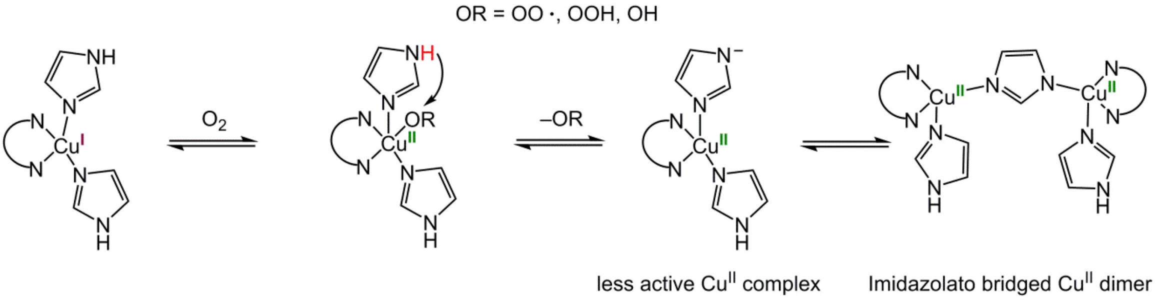

Scheme 15. Decomposition of Cu^{II} oxygen species and possible formation of imidazolato bridged Cu^{II} dimers.

Moreover, in the UV-vis spectra a broad shoulder of the LMCT related to a Cu^{II}-oxygen species[58, 101] is notably less pronounced when imidazoles with an unprotected NH-moiety are used (***cf.* Figure A11B and A26A**). This is evidence for such a decomposition route of oxygen species coordinated to the active Cu^{II} complex (*e.g.* the proposed Cu^{II}-O$_2^{\bullet -}$ intermediate[17] or Cu-OH species[19-20]) (***cf.* chapter 4.3**) as seen with other proton sources.[193, 195] On the other hand it is also fairly reasonable to suggest, that the rapid oxidation might be due to increased electron density within the imidazole ring due to hyperconjugation[188] which is in turn related to deprotonation[17, 20, 185, 194] of the NH-moiety. Interestingly, upon addition of BzOH the reduction of those Cu^{II} species is significantly hindered as observed from both, the EPR and UV-vis spectra. These findings could be attributed to the mentioned effects, too. Increased stabilization of the Cu^{II} valence state by electron density donation, arising from a left behind negative charge in N2 position, makes reduction to Cu^{I} more difficult.[142, 194, 196] The active Cu^{II} species, as already mentioned, might be decomposed leaving less active Cu^{II} complexes behind.[19-20] Moreover, interactions between neighboring Cu^{II} centers (or other components within the reaction mixture) via a deprotonated NH-moiety or hydrogen bonding in a non-deprotonated NH-moiety[172, 184-185, 197-198] might be sufficient to shield the Cu^{II} centers from access by BzOH. Such interaction could lead to less or non-active Cu^{II} species. Interestingly, from the *in-situ* EPR spectra we could observe that the reduction of

Cu^{II} species is not complete when using 1-H imidazole ligands, suggesting some remaining non-active Cu^{II} complexes in solution (**Figure A11C**).

Redox behavior of Cu/imidazole complexes studied by electrochemical analyses

Electrochemical investigations were carried out to verify our assumptions that electron density donation towards the Cu^{I} center is strongly influenced by the substituents at the imidazole scaffold in the (bpy)Cu^{I}(imidazole)$_2$ complexes, differential pulse voltammetry (DPV) has been study redox potentials of selected examples (**Figure 23**).

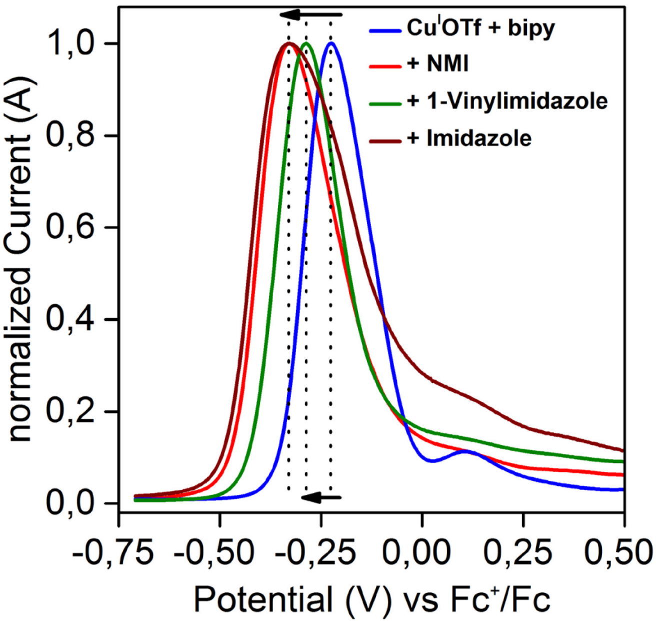

Figure 23. Normalized differential pulse voltammograms of Cu^{I}/bpy acquired in MeCN and after subsequent addition of either NMI, 1-VI or imidazole under Ar atmosphere. Adapted with permission from reference 119.

Since less electron density is donated by the vinyl substituent, a slightly higher potential should be expected for (bpy)Cu^{I}(1-vinylimidazole)$_2$ compared to (bpy)Cu^{I}(NMI)$_2$. On the other hand the redox potentials of (bpy)Cu^{I}(1-H imidazole)$_2$ and (bpy)Cu^{I}(NMI)$_2$ should be in similar range, since the observed increase of the Cu^{II} features from the *in-situ* EPR and UV-vis measurements during the oxidation step is comparable. Cu^{I}OTf and 1.0 equiv. of bpy within an O_2-free MeCN solution shows a redox event at -0.22 V [Fc^{+}/Fc] due to the formed (bpy)$_2$$Cu^{I}$ complex (**Figure 23**). A smaller, distinct redox event could be seen at approx. +0.11 V (***cf.* Figure 9, A2A**) which was earlier ascribed to a Cu^{I} center coordinated by only one bpy ligand. Upon addition of 1.0 equiv. of NMI, the peak shift to -0.33 V

[Fc$^+$/Fc] due to immediate formation of the (bpy)Cu^I(NMI)$_2$ complex while the redox event at +0.11 V disappears. A very similar redox event can be observed when 1.0 equiv. of 1-H imidazole is added to a Cu^I/bpy containing MeCN solution. However, very broad tailing is observed. This likely reflects the previous results of characteristic interactions *e.g.* by hydrogen bonding[172, 184] or through formation of imidazolate-bridged Cu^{II} dimers,[186-187] neighboring complexes when an unprotected NH moiety is present. These findings are similar to the observed broad signals seen in the *in-situ* EPR spectra (***cf.* Figure A11**). In contrast, upon adding 1.0 equiv. of 1-vinylimidazole, the redox features is shifted only to -0.28 V [Fc$^+$/Fc] corroborating the direct electronic effect of the vinyl compared to a methyl substituent.[199-201] The slightly higher potential of (bpy)Cu^I(1-vinylimidazole)$_2$ compared to (bpy)Cu^I(NMI)$_2$ is consequently related to its lower ability to promote Cu^I oxidation. Our findings suggests that the electron donating ability of the vinyl group might be weaker than the +*I* effect of the methyl group of NMI and thus, proves our *in-situ* EPR and UV-vis results obtained from the activity screening as well as step-wise oxidation/reduction studies.

Brief summary

In-situ EPR and UV-vis spectroscopy as well as additional cyclovoltammetry enabled us to study the redox behavior of complexes of the type Cu^I/bpy/Im$_2$, whereas Im in this case denominates NMI, 1-vinylimidazole or 1-H imidazole. During step-wise oxidation and reduction steps, we were able to determine the detrimental effect of the vinyl group on the oxidation step, since less electron density is donated towards the Cu^I center. On the other hand, the hampering effect of the unprotected NH-moiety upon the reduction rate was related to formation of less active Cu^{II} complexes and/or Cu^{II} imidazolato bridged dimers. These findings were corroborated by cyclovoltammetry showing a lower redox potential in the case of Cu/bpy/NMI complexes compared to Cu/bpy/1-vinylimidazole and very broad signals when 1-H imidazole is used. This led us to conclude that at least three types of imidazole-type ligands exist favoring either both redox steps or only one particular partial reaction. These effects are directly related to the catalytic performance of Cu complexes composed of those ligands, since they determine the amount of active Cu^{II} species present during the catalytic turnover of BzOH to BA:

4.2. Catalytic system formed *in-situ* from CuOTf, bpy and / or substituted pyridines

Zhang et al. implemented 4-dimethylaminopyridine (4-DMAP) as the sole ligand/additive in combination with Cu^I and Cu^{II} precursors in the oxidation of alcohols to carbonyl compounds using similar reaction conditions as Stahl et al.[16] but with H_2O as the *sole* solvent.[14] Those conditions were not used before, since mixtures of *e.g.* 2:1 $MeCN/H_2O$ were reported to decrease the catalytic activity signifantly.[14, 19] The authors proposed a variety of mononuclear and more complex dimeric and tetranuclear Cu^{II} complexes as active catalyst species that have been precipitated from the aqueous reaction solutions.[14, 33] It is not known, if such Cu^{II} complexes are formed in MeCN, too, and if their structural arrangement is retained during the reaction; hence, if those complexes represent the active catalyst. Beyond that, to the best of our knowledge, systematic investigations *e.g.* regarding the substituents at the pyridine scaffold and its influence on reaction rates within aerobic alcohol oxidation have not been performed so far.

The aim of this chapter is to analyze the influence of differently substituted pyridines (**Table A2**) on redox properties and catalytic performance of *in-situ* formed active Cu complexes by *operando* EPR/UV-vis/ATR-IR spectroscopy. We chose selected examples of different classes of pyridine-type ligands, *i.e.* unsubstituted pyridine, $–NR_2$ substituted pyridines (*ortho* position (2-AmP, 2-DMAP), *meta* position (3-AmP), *para* position (4-AmP, 4-DMAP, 4-pyrrolidinopyridine, 4-piperidinopyridine)) as well as non-NR_2 substituted pyridines (4-MeO-pyridine, 4-aminomethylpyridine) and N,N-dimethylanilline. For the sake of comparison, similar reaction conditions concerning the solvent, concentration of Cu precursor and molar ratios of ligands/additives as in **chapter 4.1** were used.

4.2.1. Comparison of Cu/pyridine-type and Cu/bpy/pyridine-type mixed-ligand systems

Catalytic performance determined by *operando*-ATR-IR spectroscopy

The catalytic activity of *in-situ* formed complexes constituting of Cu^{I}OTf/TEMPO/bpy with addition of either 4-DMAP or 4-AmP in different molar ratios was studied (**Figure 24**).

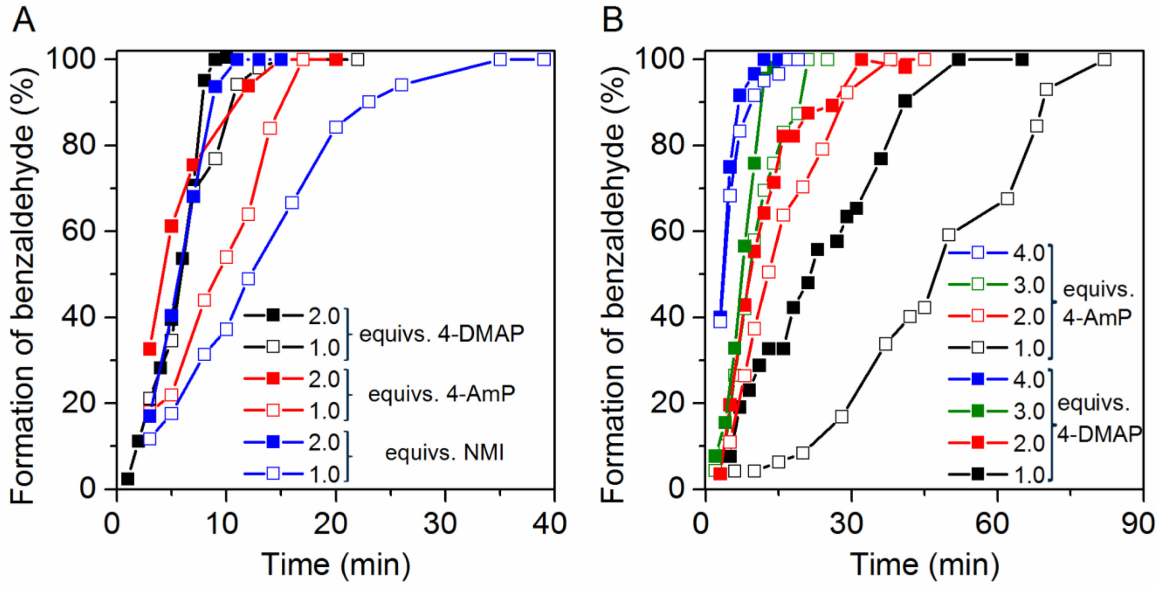

Figure 24 Formation of BA monitored with time for the Cu^{I}OTf/bpy/TEMPO catalytic system with different molar ratios of 4-DMAP, 4-AmP, and NMI (**A**) and in absence of bpy (**B**).

These ligands were implemented, since potential σ–donors are known to enhance Cu catalyzed redox processes.[202-203] Furthermore, these ligands provide the opportunity to determine the effect of the methyl substituents (NH_2 vs. NMe_2 moiety) on the catalytic performance. For comparison, results from our investigations using the Stahl et al. Cu^I/TEMPO/bpy/NMI system[16] were included in **Figure 24A**. In the second part, experiments in the absence of bpy with different molar L/Cu ratios (L = 4-DMAP or 4-AmP) have been conducted to investigate the sole impact of these ligands on the catalytic performance (**Figure 24B**).

In the catalytic system containing Cu^I/TEMPO alongside bpy, implementation of either 2.0 equivalents of 4-DMAP or NMI led to the highest activity and similar reaction rates (**Figure 24A**) reaching full conversion of BzOH to BA after about 9 to 10 min. Interestingly, implementation of only 1.0 equivalent 4-DMAP showed significantly higher activity compared to NMI. In the catalytic system containing 4-AmP, BA formation is slower compared to NMI or 4-DMAP (in the case of 2.0 equivs.). However; the reaction rate with

1.0 equiv. of 4-AmP lies in between those obtained for 4-DMAP and NMI. Cu^I/TEMPO/L systems, without bpy, show significant dependence of the BA formation rates on the molar L/Cu ratios (**Figure 24B**). Highest rates with 4-DMAP and 4-AmP are found for L/Cu = 4. Curiously, those rates are still lower compared to the corresponding systems with bpy and L/Cu = 2 (4-DMAP/4-AmP) (**Figure 24A**). Full conversion in the 4-DMAP/Cu = 4:1 system was found after 12 min, but only 9 min are required in mixed ligand systems (4-DMAP/bpy/Cu = 2:1:1). These findings and prior studies of similar Cu/N_X complexes[164, 202] lead us to the tentative assumption that at least four coordinating N donor ligands are needed for an efficient catalytic performance (*vide infra*).[202] BA formation rates, in general, are lower with 4-AmP compared to 4-DMAP. Complete conversion with 4.0 equiv. of 4-AmP was only obtained after approx. 16 min. The reason for this might be an additional +*I* effect of the two methyl substituents of the *para* N-moiety in 4-DMAP. Possible side reactions, *e.g.* the reaction of BA with 4-AmP ligands to imines can be excluded, since no related imine bands have been observed in the IR spectra. This points to active involvement of the NH_2 moiety lone pair (**Scheme 15**) which would be needed for the formation of the corresponding imines. Taking into account the strong σ-donors properties[204-205] of 4-DMAP and 4-AmP due to resonance effects of the *para* N-moiety lone pair (electron density donation into the pyridine ring, +*M* effect) towards the coordinating imine nitrogen, oxidation of Cu^I to Cu^{II} is expected to be favored (**Scheme 16**).

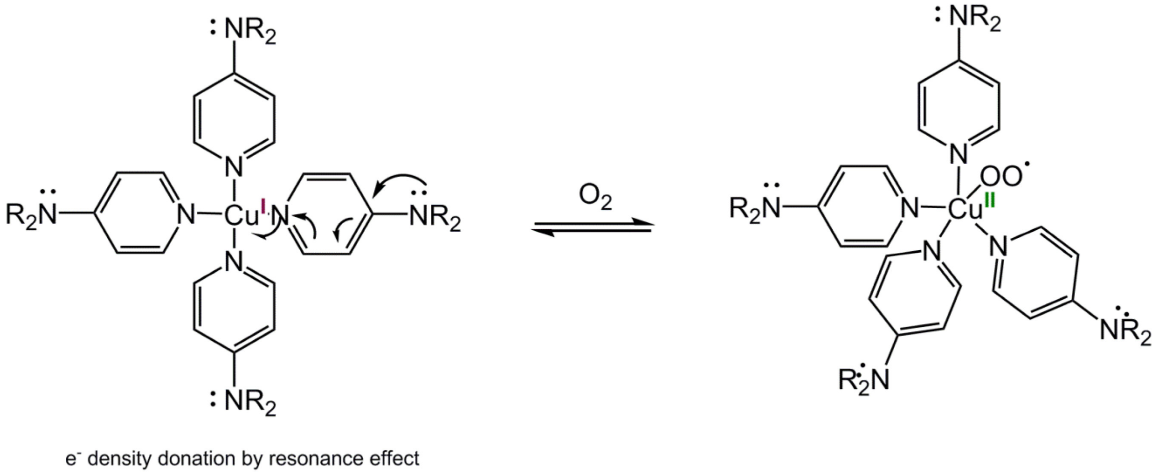

Scheme 16. Resonance donation of σ-donor ligands exemplarily depicted for Cu/NR_2-substituted pyridine complexes.

The assumption, that resonance donation towards the Cu active site plays a crucial role in enhancing the catalytic reactivity, was proven by implementing 3-AmP as a ligand. In this case, resonance electron donation is expected to be less, since the NH_2 group is in *meta* position.[206] As expected, with 3-AmP the reaction rate decreased considerably and only 70 % formation of BA was achieved after 5h (**Figure A12**). Interestingly, only traces of BA were found by implementation of 2-DMAP and 2-AmP with a NMe_2 or a NH_2 moiety in *ortho* position (**Table A2**) supposed to exhibit similar electronic effects compared to *para* position.[206] We attributed this to chelating effects in which both the imine nitrogen and the amine nitrogen of the NH_2 moiety in *ortho* position coordinate to Cu^I center eventually preventing access of O_2 and/or the substrate to Cu centers.[207]

Pyridine and N,N-dimethylaniline, being scaffolds of 4-DMAP, were also tested, but only very low BA yields could be obtained (**Table A2,** Entries 1 and 16). Similar findings were observed for 4-aminomethylpyridine which formed a precipitate shortly after beginning O_2 dosing. (**Table A2**, Entry 14) Due to this, those additives are not discussed in detail in the following. On the contrary, 4-pyrrolidinopyridine as well as 4-piperidinopyridine led to high yields attributed to their strong +*M* effects of the NR_2 moiety despite having sterically more demanding substituents (**Table A2,** Entries 7-8). Substituents in *para* position other than the $–NR_2$ moiety *e.g.* –OMe moiety (**Table A2**, Entry 10) lead to only approx. 10% conversion after 90 min further demonstrating the significance of the proper substitution pattern.

Thus, screening of differently substituted pyridines revealed highest catalytic activity for pyridine-type ligands having an $–NR_2$ substituent in *para* position, likely due to resonance effects.[204]

Formation and characterization of the active Cu^{II} species

For bpy/imidazole-type containing systems described in the previous chapter, oxidation of Cu^I to $(bpy)(NMI)_2Cu^{II}O\text{-}O^{-\bullet}$ proceeds after introducing O_2 into solutions of Cu^IOTf, bpy and NMI.[17, 119] Similar to those experiments, we begin analyzing the *in-situ* formation of active $Cu^{I/II}$ complexes by using 4-DMAP exemplarily. Afterwards, the catalytic reaction of those complexes with BzOH in the presence of TEMPO is explored.

Addition of 4-DMAP step-wise to a solution of Cu^IOTf in MeCN while introducing O_2 leads to prompt appearance of an isotropic signal of Cu^{II} in the EPR spectra, split into four hyperfine structure (hfs) lines similar *e.g.* to the active $(bpy)Cu^{II}(NMI)_2$ species in Stahl's system (**Figure 10B**).[17, 119] EPR spectra simulation revealed values of g_{iso}=2.119 and A=78 G typical for a mononuclear Cu^{II} complex (**Figure A13A**).[164, 202] Additionally, a well-resolved superhyperfine structure (shfs) from the coupling of the Cu electron spin with the nuclear spin of nitrogen $I_N=1$ of the 4-DMAP ligand is observed on the $m_I= – 3/2$ high field peak indicating coordination of this ligand to the Cu^{II} center. From the 2nd derivative spectra (**Figure A 13B**) splitting into 9 lines with a coupling constant of $A_N=14$ G is evident. This indicates, in agreement with literature data, that *four* 4-DMAP ligands coordinate to the active Cu^{II} center.[164, 202, 208-210] Such a well pronounced shfs at room temperature has not been observed in Stahl's system[16] (*vide supra*) nor when bpy is used in addition to 4-DMAP (*cf.* **Figure 31**). This is most likely caused by a slower tumbling rate of those complexes due to the rigidity of the bpy ligand leading to intense line broadening.[153, 211] The Cu^{II} signal intensity increases up to a molar ratio of 3.0 after addition of 4-DMAP, suggesting complete conversion of the $Cu^{I}OTf$ precursor to Cu^{II} species (**Figure 25A**). Interestingly, the shfs pattern is already well-established after adding only 1.0 equiv. of 4-DMAP. This pattern itself does not change with further addition suggesting that a distinct $Cu^{I}(4\text{-DMAP})_4$ complex is formed, even when only 1.0 equiv. of ligand is added, which might be immediately transformed into the corresponding Cu^{II} species upon introduction of O_2. Complete replacement of coordinating solvent molecules of the $Cu^{I}(MeCN)_4OTf$ precursor by four 4-DMAP ligands at relatively low 4-DMAP concentration might be driven by high complex stabilization of $Cu^{II}(4\text{-DMAP})_4$ species.[202, 212] Such process is reasonable, since addition of 4-DMAP to a $Cu^{II}OTf_2$ precursor yields very different results (*vide infra*).

Since $Cu^{I}OTf$ is oxidized only very slowly in the absence of strong N-donor ligands *e.g.* 4-DMAP or NMI[17, 119] uncoordinated Cu^{I} species remain in solution when less than 4.0 equivs. 4-DMAP are added. Interestingly, addition of the 4th equiv. of 4-DMAP did not lead to changes within the EPR spectrum which was unexpected. These findings suggest that either remaining Cu^{I} species are not readily oxidized and/or that some EPR-inactive Cu^{II} dimers are formed. However, this implicates a certain amount of uncoordinated 4-DMAP to be present in solution after oxidation, since those Cu^{II} dimers are believed to carry less than four 4-DMAP ligands.[202] A hint for this suggestion has been obtained from ATR-IR measurements (*vide infra*).

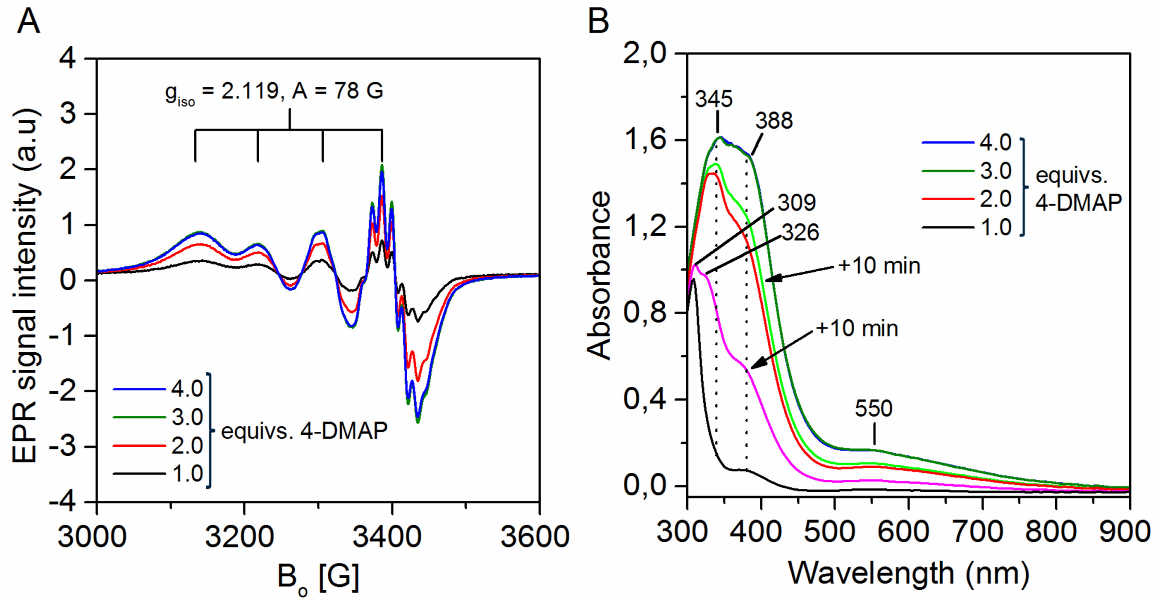

Figure 25. *In-situ* EPR spectra recorded after addition of 1.0-4.0 equivs. of 4-DMAP to a solution of Cu^IOTf in MeCN while introducing O_2 (**A**). Simultaneously obtained UV-vis spectra(**B**).

Corresponding UV-vis spectra support the findings derived from EPR spectra (**Figure 25B**). The UV-vis spectrum of Cu^IOTf and 1.0 equiv. of 4-DMAP shows a sharp band around 309 nm arising from a metal-to-ligand charge-transfer (MLCT) transition which should mainly stem from Cu^IOTf[17, 119] since this might be still the dominating species at this stage (**Figure 25B**). Continuous introduction of O_2 led to a gradually increasing band at approx. 326 nm with a shoulder at approx. 388 nm, which has been assigned to charge transfer within a $Cu^{II}(4\text{-DMAP})_4$ complex.[14, 202, 213] A corresponding d-d transition band of Cu^{II} was observed at approx. 550 nm.[202] When the 2nd and 3rd equiv. of 4-DMAP are added, a sharp and sudden increase of the CT/d-d band of $Cu^{II}(4\text{-DMAP})_4$ species can be seen, while the spectra do not change upon adding the 4th equiv. of 4-DMAP, being in excellent agreement with the EPR results (**Figure 25A**).

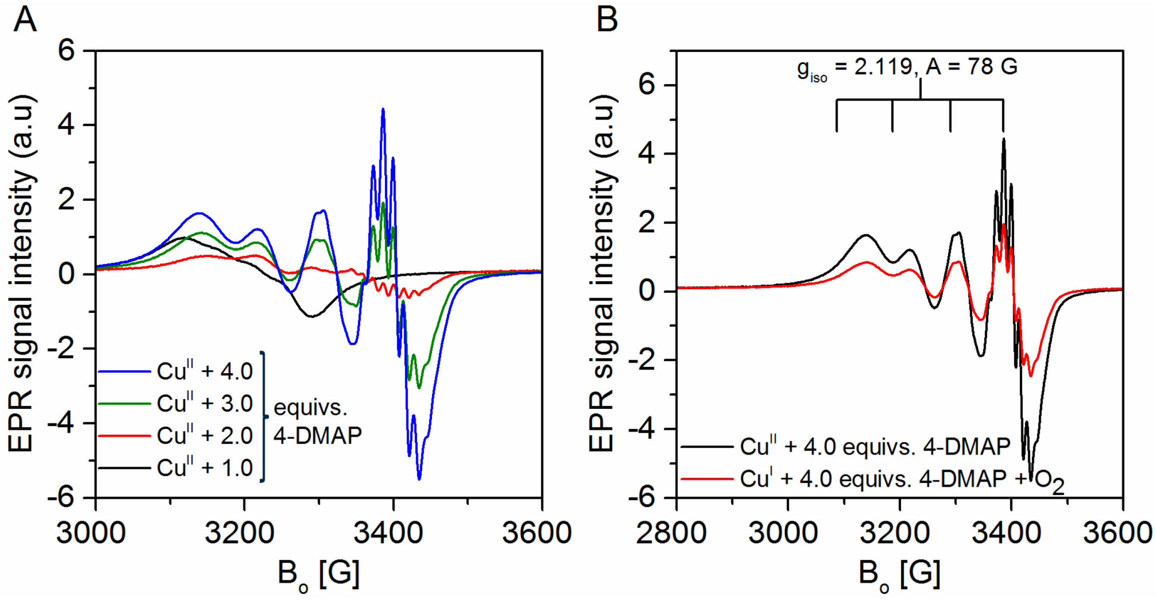

Figure 26. EPR spectra recorded when adding 4-DMAP to a Cu^{II}OTf$_2$ precursor in MeCN (**A**) and comparison of absolute EPR spectra measured after adding 4-DMAP to either Cu^{I}OTf (+O$_2$) or Cu^{II}OTf$_2$ as precursors in MeCN (**B**).

Since Cu^{II} precursors were reported to be catalytically active, too, we wanted to verify, if similar results can be obtained with Cu^{II}OTf$_2$ (**Figure 26A**). The Cu^{II} signal shape and its calculated EPR parameters after addition of 3.0/4.0 equivs. of 4-DMAP to the Cu^{II}OTf precursor are very similar to the corresponding Cu^{I}OTf (+ O$_2$) spectra evidencing formation of Cu^{II}(4-DMAP)$_4$ species in both cases (**Figure 26B**). Remarkably, when only 1.0 or 2.0 equivs. of 4-DMAP are added to the Cu^{II}OTf$_2$ precursor, EPR signals with different g$_{iso}$ and A$_{iso}$ are obtained. These findings suggest formation of mononuclear Cu^{II}(4-DMAP)$_X$ intermediates with x<4 in the case of the Cu^{II} precursor. Those intermediates are eventually converted into the final Cu^{II}(4-DMAP)$_4$ complex when additional 4-DMAP is present.[202] Furthermore, in contrast to the experiment using the Cu^{I}OTf precursor + O$_2$, addition of a 4th equiv. of 4-DMAP to the Cu^{II}OTf$_2$ containing solution leads to a significant increase in intensity (**Figure 26A**). This could be corroborated by simultaneously acquired UV-vis spectra (**Figure A14**) showing a blue-shifted d-d transition band from approx. λ_{max} 780 nm to approx. 550 nm when increasing the amount of 4-DMAP from 0 up to 4.0 equivalents. Moreover, lower absorbance in the range between 400-500 nm is observed (***cf.* Figure 25B**) which could indicate to the absence of O-species coordinated to the Cu^{II} center. Those are known to cause LMCT bands in this spectral region (***cf.* Figure 14B**)[58, 149] and their absence is expected when using the Cu^{II}OTf$_2$ precursor.

These findings confirm our assumptions, that some EPR-silent Cu$^{I/II}$ complexes are formed which are coordinated by less than four 4-DMAP ligands, when starting with Cu^{I}OTf as Cu precursor. These effects become even more apparent when the *absolute* EPR spectra of $Cu^{II}(4\text{-DMAP})_4$ complexes originating from different Cu precursors are compared (**Figure 26B**). The integrated area of the spectrum from the $Cu^{I}(4\text{-DMAP})_4 + O_2$ experiment equals to only approx. 47% of the area calculated for the system of the Cu^{II} precursor with 4-DMAP, confirming *significant* formation of EPR silent $Cu^{I/II}$ species. However, it is not clear, if the proposed dinuclear[19-20, 33, 214] or even tetranuclear Cu species[14, 33, 214] as active sites (mainly based on X-ray structure analysis of solid complexes precipitated from reaction solutions) exhibit the *same* structure within solutions. It is at least questionable, if the structure of such *in-situ* formed Cu complexes are retained during the reaction. From our *in-situ* spectroscopic results, at the moment, we are not able to further distinguish between those EPR inactive Cu^{II} species under reaction conditions. However, based on literature, formation of EPR silent dinuclear Cu^{II} species seems to be the most reasonable.[202, 215] Currently, it is unknown if such species play a major role in the catalytic cycle. Further investigations are needed in this case (*vide infra*).

Compared to the Cu/bpy/NMI system,[17, 19] rigorous studies regarding the geometry of the Cu^{II} site in the Cu/4-DMAP catalytic system have not yet been performed. For this purpose, EPR spectra of the $Cu^{II}(4\text{-DMAP})_4$ complexes formed from $Cu^{I}OTf$ ($+O_2$) and $Cu^{II}OTf_2$ were recorded in frozen solution at 90 K (**Figure 27**). The EPR spectra in both cases show signals with axial symmetry and g tensor components in the order of $g_\parallel > g_\perp > g_e$. In this case, resolution of shfs splitting is prevented by line broadening which results from dipol-dipol interaction between the Cu^{II} complexes promoted by MeCN as a dipolar solvent.[211]

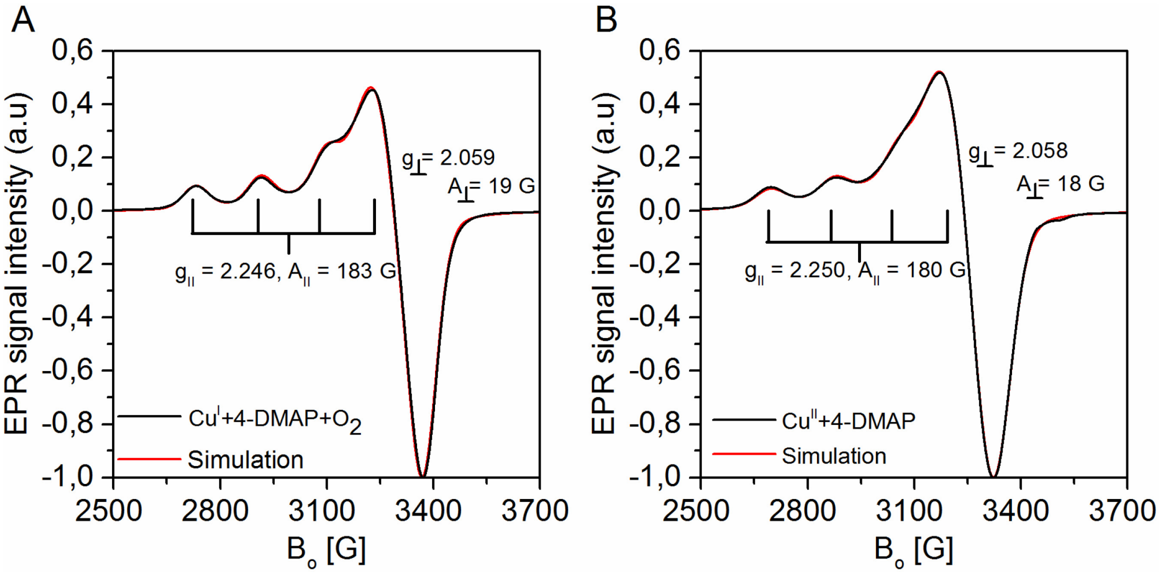

Figure 27. EPR spectra of $Cu^{II}(4\text{-DMAP})_4$ formed using $Cu^{I}OTf$ ($+O_2$) (**A**) and $Cu^{II}OTf_2$ recorded at 90 K (**B**).

The parameters g and A of complexes originating from both Cu precursors (calculated by spectra simulation) are close to those reported for similar $Cu^{II}L_4$ complexes having four N-donor ligands (**Table 2**).[164, 202, 208-210] In general, these values suggest either a distorted square-pyramidal or a tetragonally distorted octahedral geometry of Cu^{II} complexes.[216-217] These findings are in agreement with X-ray single crystal analysis of $Cu^{II}(DMAP)_4(BF_4)_2$ complexes showing Cu^{II} centers in tetragonal symmetry having two weaker bound ligands occupying axial positions.[202] In the present case, those axial positions could very well be occupied by the solvent, MeCN (originating from a Cu^{II} precursor). In the case of the $Cu^{I}OTf$ precursor those positions might be coordinated with MeCN and one oxygen species, *e.g.* coordinated $O_2^{-\bullet}$, as previously proposed,[17, 119] due to oxygen activation during the first reaction step.

Table 2. Calculated EPR parameters of different $Cu^{II}N_4$ complexes derived from different $Cu^{I/II}$ precursors.

Complex	$g_{\parallel}$	$A_{\parallel}$	$g_{\perp}$	$A_{\perp}$	Reference
$Cu^{II}(4\text{-}DMAP)_4$ from $Cu^{I}OTf$	2.246	183 G	2.059	19 G	present work
$Cu^{II}(4\text{-}DMAP)_4$ from $Cu^{II}OTf_2$	2.249	180 G	2.058	18 G	present work
$Cu^{II}(pyridine)_4$ from $Cu^{I}Cl$	2.250	175 G	2.050	n. d.[a]	Praliaud et al.[218]
$Cu^{II}(4\text{-}DMAP)_4$	2.240	180 G	2.040	n. d.[a]	Koning et al.[202]

[a] n.d.=not determined

To gain more insight into the complex formation and behavior of the active $Cu^{II}(4\text{-}DMAP)_4$ species formed from the Cu^{I} precursor, additional *in-situ* ATR-IR spectroscopic studies were performed at 233 K (to yield well-defined bands). We started the experiment by introducing O_2 into a solution containing $Cu^{I}OTf$ and 3.0 equivs. of 4-DMAP (**Figure 28**). In the spectrum of the sole 4-DMAP ligand in MeCN a band at 1602 cm^{-1} can be seen which stems from the $\nu(C{=}C)$ stretching vibration of the pyridine ring.[212, 219-223] After adding $Cu^{I}OTf$ to this solution, a blue-shift to 1613 cm^{-1} is observed for this band, since coordination of 4-DMAP via the imine nitrogen[219-220] strengthens this bond due to electron donation to the Cu^{I} center. Upon introducing O_2 this band is split into two features: one at 1602 cm^{-1} likely results from uncoordinated 4-DMAP. The other more prominent band at 1622 cm^{-1} is attributed to the Cu^{II}(4-DMAP)$_4$ complex, since a very similar band can be seen from Cu^{II}Otf$_2$/MeCN solutions containing 3.0 equivalents of 4-DMAP. The blue shift from 1613 cm^{-1} (Cu^{I}) to 1621 cm^{-1} (Cu^{II}) after the oxidation might be caused by the strengthening of the Cu^{II}-N bond, since Cu^{II} is a harder lewis acid compared to the Cu^{I} ion donating less electron density to the imine nitrogen.[224] A similar blue shift could be observed in the range between 1525 and 1544 cm^{-1} where additional C=C, Ph-N and C=N vibrations are known to occur.[212, 219]

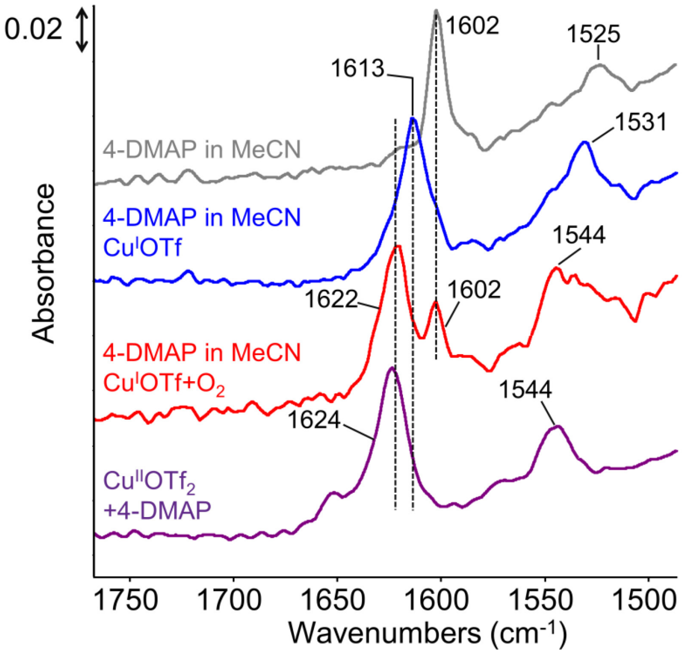

Figure 28. *In-situ* ATR-IR spectra measured at 233 K of 4-DMAP in MeCN (**grey**), after addition of Cu^{I}OTf while introducing Ar (**blue**), and subsequent introduction of O_2 (**red**). The spectrum of 4-DMAP added to a Cu^{II} precursor (Cu^{II}OTf$_2$) in MeCN (**purple**) was added for comparison.

The ATR-IR spectra (**Figure 28,** grey and blue line) suggest that after adding Cu^{I}OTf to a 4-DMAP containing solution the complete amount of 4-DMAP coordinates to the Cu^{I} center forming the (active) Cu^{I}(4-DMAP)$_4$ species.[202, 225] On the other hand, the corresponding Cu^{II}(4-DMAP)$_4$ complex is formed, when using a Cu^{II}OTf$_2$ precursor (**purple**). However, oxidation of Cu^{I}(4-DMAP)$_4$ to the respective Cu^{II} species by introduction of O_2 leaves obviously uncoordinated 4-DMAP behind, besides the Cu^{II}(4-DMAP)$_4$ complex (**red**). This might occur, when Cu^{II} dimeric species are formed which are coordinated by less than four 4-DMAP ligands. It may also be possible, that some 4-DMAP ligands of the newly formed $Cu^{II}(4\text{-DMAP})_4$ complex are just weakly interacting, *e.g.* by occupying apical positions,[119, 156] giving rise to these IR features, also observed in the case of the Cu^{I}/bpy/NMI system (**Figure 17**).[119] Based on these results, we cannot make a definite statement on the nature of such species; however, combining *in-situ* EPR and ATR-IR data there is sufficient evidence to propose that the formation of Cu^{II} dimers causes those effects.

Brief summary

Rigorous investigations regarding the nature and formation of the active Cu^{II} species revealed a $Cu^{II}(4\text{-DMAP})_4$ complex as the most probable active center. However, from the comparison with the $Cu^{II}OTf_2$ precursor it is evident, that a significant portion (approx. 50%) of EPR-inactive Cu^{II} species are formed, most likely Cu^{II} dimers. Those complexes are likely coordinated by less than four 4-DMAP ligands giving rise to bands of the *free* ligand from the *in-situ* IR spectra.

Behavior of the active Cu complex during reaction

One major catalytically active species, the mononuclear CuL_4 complex, has been identified in the previous section, so we monitored its behavior during the catalytic reaction by simultaneous *operando* EPR/UV-vis/ATR-IR spectroscopy. Since the highest activity was achieved by using 4-DMAP and 4-AmP as ligands, detailed studies about their corresponding Cu complexes during the reaction have been conducted.

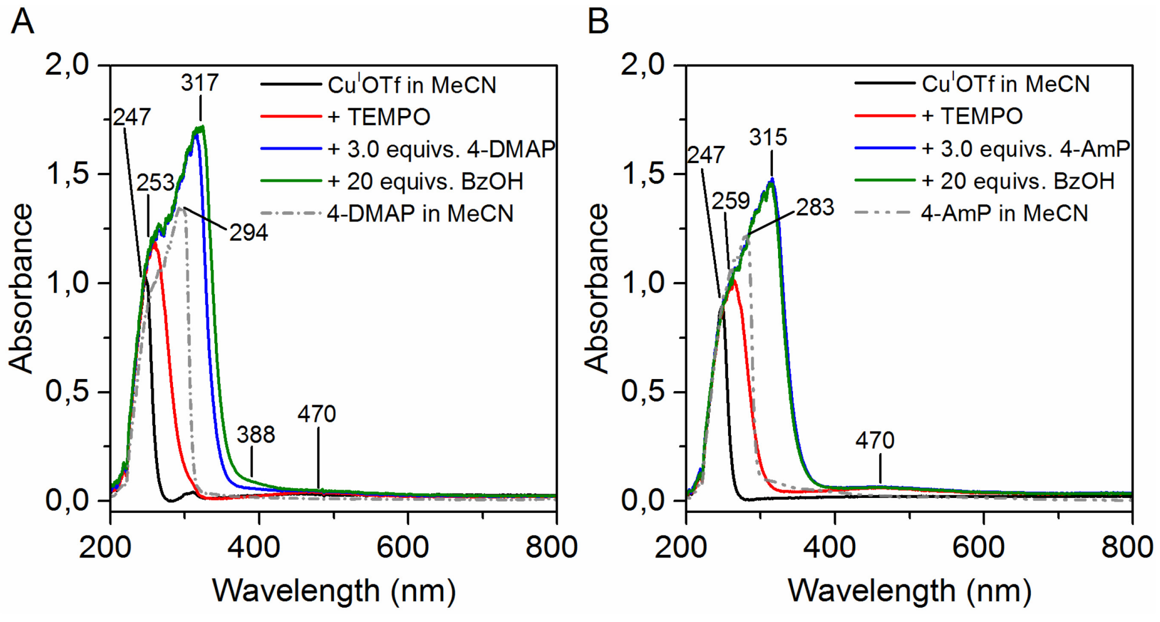

Figure 29. UV-vis spectra of $Cu^{I}OTf$ in MeCN under Ar (**black**) and after subsequent addition of components (**A**) when using 4-DMAP or (**B**) in the case of 4-AmP. Broken lines show spectra of only 4-DMAP and 4-AmP in MeCN.

Cu^IOTf in MeCN under inert atmosphere only produces a sharp band at 247 nm due to a CT transition of Cu^I with the solvent (**Figure 29, black**). Adding TEMPO to this solution leads to overlap of bands since the sole TEMPO radical also gives rise to a broad feature around 250 nm. 4-DMAP or 4-AmP added to those Cu^IOTf/TEMPO solutions produce new bands attributed to MLCT transitions[124, 213] at 317 nm and 315 nm, respectively, with shoulders at 253 or 259 nm indicating coordination of those ligands to the Cu^I center. These shoulders most likely arise from π-π* transitions of the aromatic ring[124, 218, 226] which are also seen in the spectra of the sole 4-DMAP and 4-AmP ligand in MeCN(dashed lines in **Figure 29**). The *in-situ* formed Cu^I/4-DMAP complexes in MeCN solution are colorless. Addition of BzOH led to no significant changes of the MLCT bands around 315/317 nm, indicating that the Cu^I complexes with 4-DMAP and 4-AmP interact with BzOH only very weakly. The introduction of O_2 into those solutions, exemplarily shown for the Cu^IOTf/TEMPO/4-DMAP/BzOH system (**Figure 30**), leads to continuous broadening of the band at approx. 317 nm shifting to 350 nm, while a new band around 550 nm emerges (**Figure 30A**). As previously described, these bands are related to CT and d-d transition bands, respectively, of a mononuclear $Cu^{II}(4\text{-DMAP})_4$ species[202] most likely in tetragonal distorted geometry.[227] This could be corroborated from the *in-situ* EPR spectra in **Figure 30B** showing the same isotropic signal of Cu^{II} as mentioned before (***cf.*** **Figure 25**). In the high-field range ($m_I = -3/2$) this Cu^{II} signal is partly overlayed by the signal of the TEMPO radical. Using 4-AmP instead of 4-DMAP displays similar spectral features (**Figure A15**).

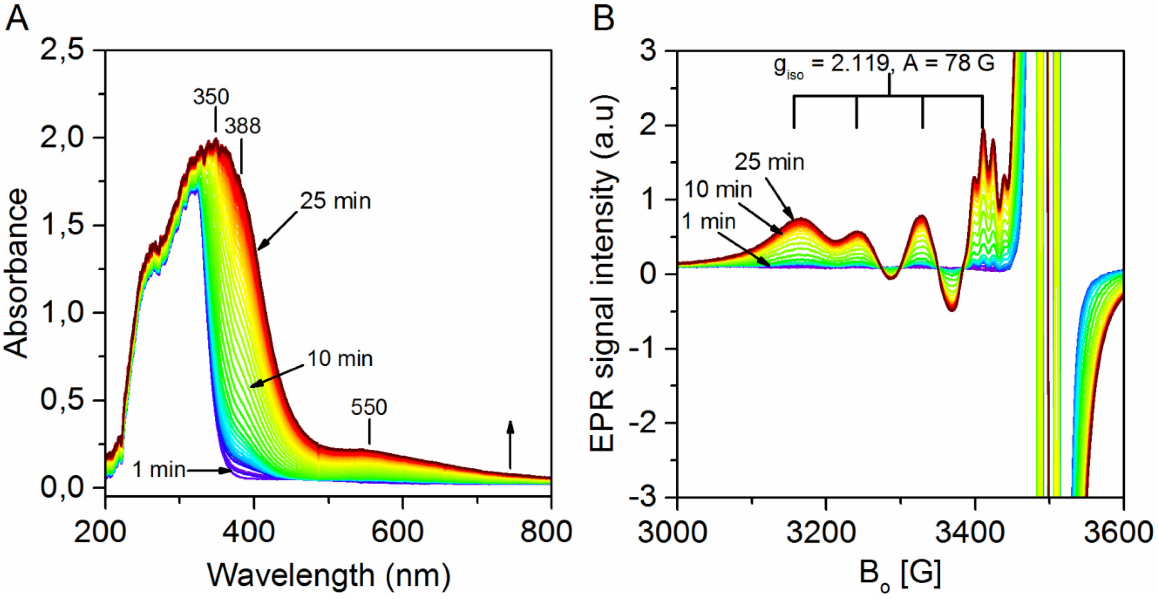

Figure 30 *In-situ* UV-vis (**A**) and EPR spectra (**B**) monitored with time during the catalytic conversion of BzOH to BA using Cu^IOTf/TEMPO and 3.0 equivs. of 4-DMAP.

Interestingly, a markedly different behavior was found when a mixed-ligand system (bpy in addition to 4-DMAP) was used (**Figure 31)**. From the *in-situ* UV-vis spectra (**Figure 31A**), the MLCT transitions of the *in-situ* formed Cu^{I} complex are dominated by the Cu^{I}-bpy coordination due to its stronger π-acceptor properties[82, 151] appearing at approx. 450 nm with a shoulder at approx. 528 nm.[119] This was also clearly evident from the brown color of these solutions. Coordination of 4-DMAP to the Cu^{I} center was evidenced from an increase of mentioned broad MLCT bands in the range between 400 and 550 nm similar to the investigated (bpy)Cu^{I}(NMI)$_2$ complex (**Figure A16**).[119] Those features decrease upon introducing O_2 into the reaction solution, and CT and d-d transitions bands of the corresponding (bpy)Cu^{II}(4-DMAP)$_2$ complex at 335 nm and 650 nm, respectively, become evident. From the simultaneously acquired EPR spectra (**Figure 31B**) an isotropic Cu^{II} signal can be observed. The g_{iso} and A_{iso} values slightly differ from those with only 4-DMAP but are similar to those found for (bpy)Cu^{II}(NMI)$_2$ complexes (***cf.* Figure 10 & 14**)[17, 119] The shfs splitting from the coordinating nitrogen is not resolved in this case, due to the decreased tumbling rate with attached bpy ligand (***cf.* Figure 14**).[153, 211]

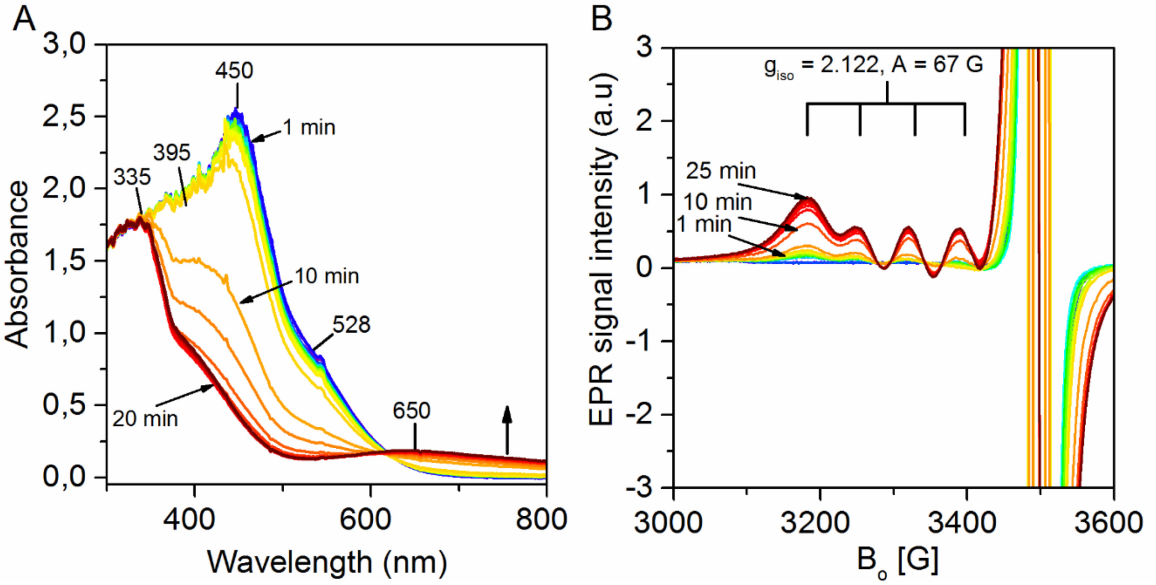

Figure 31. *In-situ* UV-vis (**A**) and EPR spectra (**B**) monitored with time during catalytic covnersion of BzOH to BA using Cu^{I}OTf/TEMPO + 1.0 equiv. bpy + 2.0 equivs.4-DMAP.

Normalized EPR intensities derived from the Cu^{II} low field peak (m_I = +3/2) and from the double integrated TEMPO signal with time are shown in **Figure 32**. The behavior of the d-d transition bands with time taken from the *in-situ* UV-vis spectra is very similar (**Figure A17**). During the reaction the behavior of the Cu^{II} signal shows four approximate phases: 1) sharp increase of the Cu^{II} EPR signal after introducing O_2 and hence starting the catalytic reaction, 2) a slowed down increase to approx. 7-8 min, 3) a fast increase and 4) finally saturation of the Cu^{II} signal. When using bpy, phase 3 is fastest and starts already approx. 9 min after BzOH is completely consumed (***cf.* Figure 24A**). Afterwards the catalytic Cu^{I}/Cu^{II} cycle is stopped and remaining O_2 leads to formation of Cu^{II} until equilibrium is achieved. Curiously, upon sole usage of 4-DMAP/4-AmP, phase 3 starts before conversion of BzOH to BA is completed. The rate of Cu^{I} oxidation *during the catalytic reaction*, especially in phase 3, follows the order of bpy/4-DMAP >> 4-DMAP > 4-AmP, being in agreement with the observed trend BA formation rate (***cf.* Figure 24**).

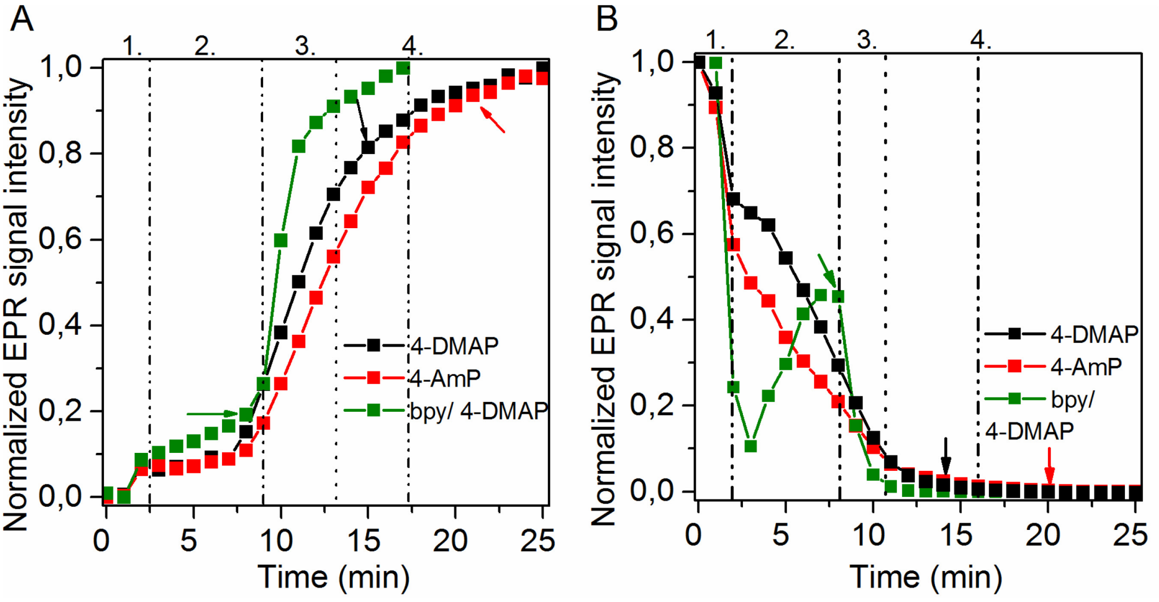

Figure 32. Normalized EPR Cu^{II} signal intensity at low field ($m_I = +3/2$) (**A**) and the TEMPO signal obtained after double integration (**B**) for Cu^{I}OTf/TEMPO/3.0 equivs. 4-DMAP (**black**), Cu^{I}OTf/TEMPO/1.0 equiv. bpy/2.0 equivs. 4-DMAP (**blue**) and Cu^{I}OTf/TEMPO/3.0 equivs. 4-AmP (**red**) with time. Time of complete conversion of BzOH to BA has been indicated with arrows.

The trend of the TEMPO signal (**Figure 32B**) does not completely follow the trend of the Cu^{II} low field peak. However, in this case, too, roughly four phases can be distinguished. In phase 1 a significant drop is observed within 2-3 min after starting O_2 introduction which is more pronounced in the experiment with bpy/4-DMAP compared to only 4-DMAP or 4-AmP. This parallels to phase 1 of the Cu^{II} signal. Afterwards, the signal intensity decreases more slowly in the case of the sole ligands, paralleling stage 2/3 in the corresponding Cu^{II} plot. This proceeds until complete oxidation of Cu^{I} to Cu^{II} is achieved after approx. 18 min. Using 4-AmP instead of 4-DMAP leads to a faster decrease in the TEMPO signal between 3 and 10 minutes (**Figure 32B**, red line).

A different TEMPO signal behavior has been observed in the case of bpy/4-DMAP (**Figure 32B**, green line). During the first 3 min of O_2 introduction the TEMPO signal shows a faster decrease compared to sole utilization of 4-DMAP or 4-AmP. Afterwards, the TEMPO signal increases, which is contrary to the other two experiments. When the conversion of BzOH to BA is nearly complete after approx. 8 min, the signal intensity begins to drop again sharply. These findings indicate clearly different redox rates of the active $Cu^{I/II}$ shuttle in mixed-ligand systems compared to the sole usage 4-DMAP/4-AmP.

As shown in **chapter 4.1**, $(bpy)Cu^{I}(Imidazole)_2$ complexes (Imidazole *here*: differently substituted imidazoles) displayed highest conversion rates of BzOH to BA when the rates of the two main steps of the catalytic cycle are similar. Those processes are the oxidation of Cu^{I} by O_2 to the presumed active $(bpy)Cu^{II}(Imidazole)_2$-$O_2^{-\bullet}$ intermediate, which is capable of oxidizing the substrate, and reduction of such species to Cu^{I} by BzOH (regeneration of the starting complex). This holds true in the case of NMI.[119] In this case, an active Cu^{II}-O-$O^{-\bullet}$–TEMPO adduct was assumed, in which dipolar interaction of the TEMPO radical with the Cu^{II}–O-$O^{-\bullet}$ intermediate led to reversible line broadening and loss of the TEMPO EPR signal, which increased again during oxidation of the BzOH substrate since the Cu^{II}-O-$O^{-\bullet}$ intermediate was reduced. After full conversion of BzOH was achieved, the TEMPO signal dropped again, since the Cu^{II}-O-$O^{-\bullet}$–TEMPO intermediate was recreated (***cf.* Scheme 8**) since no substrate is available to temporarily break up this adduct.[17]

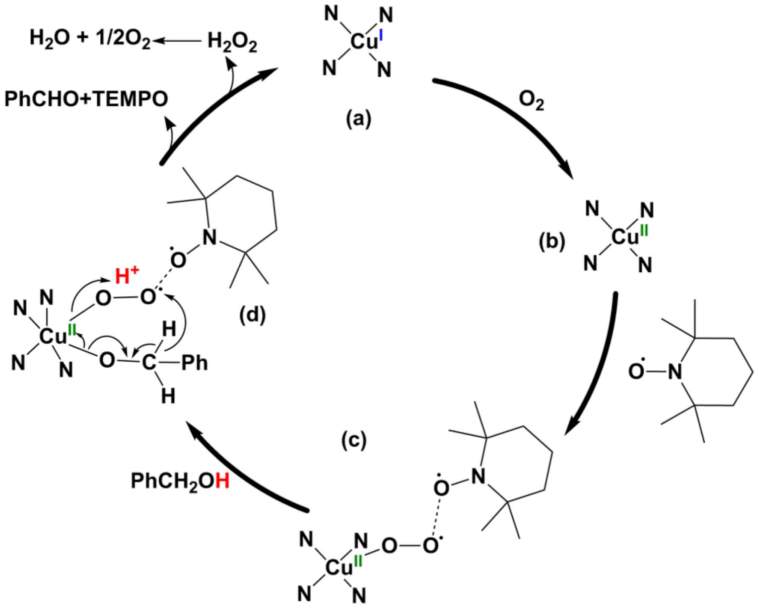

Scheme 17. Proposed reaction cycle when using pyridine-type ligands in the catalytic system $Cu^{I}OTf$/TEMPO/N (N = *e.g.* 4-DMAP, 4-AmP).

Based on the previous results[17, 119] a very similar reaction scheme is proposed for the Cu/4-DMAP catalytic system (**Scheme 17**). The effects seen in the Cu/4-DMAP and Cu/4-AmP systems suggest a much higher rate of oxidation (**a→b**) compared to the reduction step (**d→a**) within the Cu^{I}/Cu^{II} shuttle. This suggests, that a higher equilibrium concentration of the Cu^{II}-O-$O^{-\bullet}$ intermediate (**c**) must be present during the catalytic cycle which led to the observed rise of the Cu^{II} and decrease of the TEMPO signal by dipolar interaction at the start of the catalytic reaction (**Figure 32**, phase 1). Since 4-DMAP and 4-AmP are known as strong σ-donor ligands, the resulting Cu^{II}-O-$O^{-\bullet}$-TEMPO adduct (**c**) might be weaker than with less electron donating or even withdrawing ligands and the TEMPO radical might preferably interact with excess molecular O_2 in the reaction solution.[95, 119] This could explain the slow decrease of the TEMPO signal in the presence of 4-DMAP and 4-AmP (phase 2/3 in **Figure 32B**) and also the fact that the Cu^{II} concentration only increases gradually in phase 3 (**Figure 32A**), before full conversion of BzOH is complete. When bpy is used in combination with 4-DMAP, reduction of Cu^{II} by BzOH seems to be faster compared to 4-DMAP or 4-AmP alone and hence the TEMPO signal intensity increases in phase 2 and 3 (**Figure 32B**) due to continuous $Cu^{I/II}$ turnover. This may favor transition state (**d**) leading to less interaction with the Cu^{II}-O-$O^{-\bullet}$ species.

Due to the very similar features seen in the EPR spectra when using either a Cu^{I} or a Cu^{II} precursor (***cf.* Figure 26B**), it should be checked if a Cu^{II} precursor leads to similar catalytic activity towards the oxidation of BzOH, since preliminary investigations suggested activity in catalytic systems using 4-DMAP as ligands.[14, 33] For this reason we employed 4-DMAP in combination with $Cu^{II}OTf_2$ as Cu precursor and compared the catalytic activity of that system with the previously discussed $Cu^{I}OTf$/4-DMAP system in the catalytic conversion of BzOH to BA (**Figure 33**).

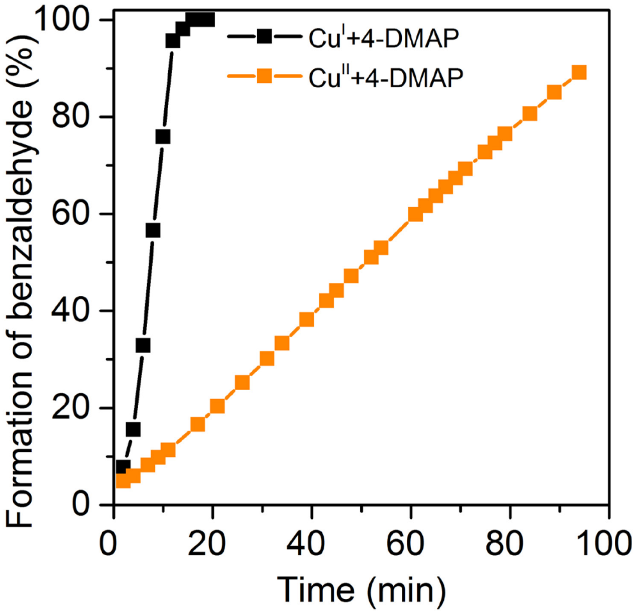

Figure 33. Formation of BA with time in catalytic systems using either $Cu^{II}OTf$/TEMPO or $Cu^{I}OTf$/TEMPO in combination with 3.0 equivs. 4-DMAP.

Based on the catalytic tests derived from *in-situ* IR spectra a much slower reaction rate is observed when using Cu^{II}/4-DMAP compared to Cu^{I}/4-DMAP. However, it is still higher compared to that of *e.g.* (bpy)$Cu^{II}(NMI)_2$, derived from Cu^{II} precursors, which only showed limited catalytic activity.[17] Most probably, two reasons are responsible for the lower activity of the $Cu^{II}OTf_2$/4-DMAP system: First, significant stabilization of the Cu^{II} oxidation state by the 4-DMAP ligands hinders the reduction of the Cu^{II} species by BzOH at the beginning of the reaction, as only Cu^{II} centers are present at that stage. Another reason might the reported finding[19-20] that Cu^{II} precursors are in general less active, when employed as catalysts, since they lack a pre-formed base to start the catalytic cycle by forming the corresponding alkoxide with the substrate.[19]

Brief summary

In this subchapter, we tested the catalytic performance of different Cu complexes formed from $Cu^{I}OTf$ and pyridine-type ligands. We observed the highest catalytic activity for systems consisting of Cu^{I}/4-NR_2-pyridines and Cu^{I}/bpy/4-NR_2-pyridines. A significantly different reaction behavior was observed when using Cu^{I} precursors in combination with 4-NR_2-pyridines alone or with bpy in a mixed-ligand system. In mixed-ligand systems the equilibrium Cu^{II} concentration during the catalytic reaction is low and correlates with the conversion of the substrate to the product. However, when pyridine-type ligands are used alone, the rate of Cu^{II} during the reaction is higher and does not correspond with the conversion rate of BzOH. These findings point to different progression in the fundamental catalytic steps, namely the oxidation of Cu^{I} to Cu^{II} and the reduction of Cu^{II} to Cu^{I}. Our hypothesis concerning the active Cu^{I}/Cu^{II} shuttle is, that, when using 4-DMAP or 4-AmP as sole ligands, the oxidation rate might be much faster than the reduction rate. This will be explored in the next subchapter. Interestingly, $Cu^{II}OTf_2$ used as precursor, although spectroscopically very similar to the active Cu^{II} complex derived from the Cu^{I} precursor, displays lower catalytic activity which is attributed to missing –OR species coordinated to the Cu center.

4.2.2. Effect of pyridine-type ligands on the redox behavior of the Cu$^{I/II}$ shuttle

Step-wise oxidation and reduction

To study the redox behavior of the Cu$^{I/II}$ shuttle in detail, we used different *in-situ* formed Cu^{I} complexes. To Cu^{I}OTf in MeCN either 3.0 equivs. of 4-DMAP or 4-AmP alone, and in a mixed-ligand system 1.0 equiv. bpy and 1.0 equiv. 4-DMAP were added to correlate the individual redox processes with the catalytic performance of those systems. For this purpose, Cu^{I}OTf was first oxidized in presence of these ligands and TEMPO. Afterwards, the resulting Cu^{II} species were reduced by adding BzOH to these solutions. Changes of the Cu^{II} EPR signal intensity and the absorption at 650 nm (d-d transition) in the UV-vis spectra were analyzed during the oxidation and the subsequent reduction process.

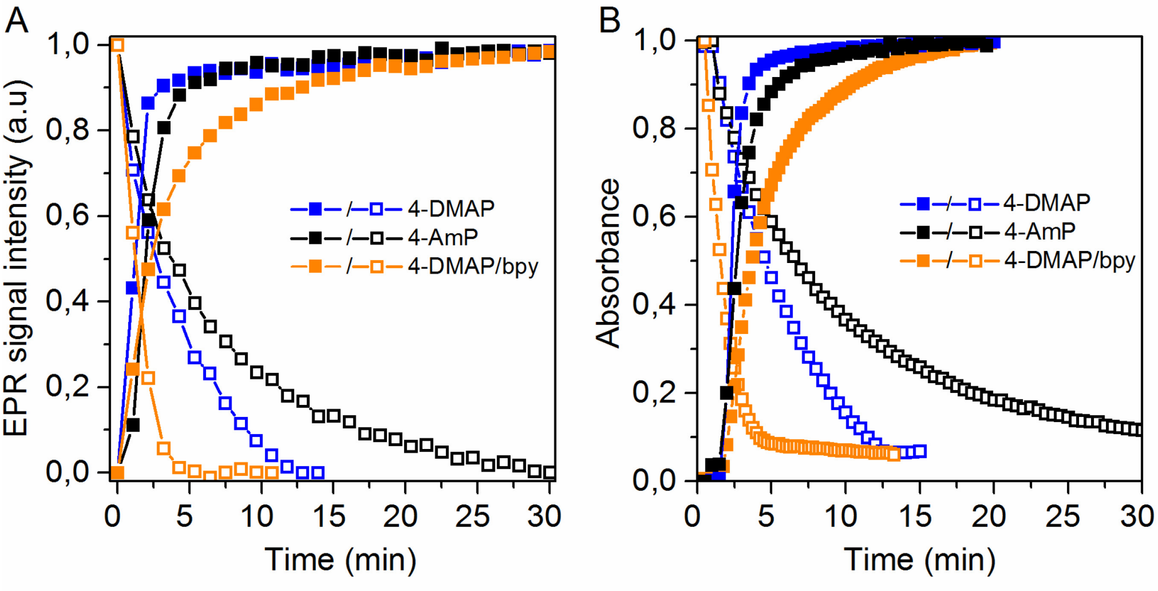

Figure 34. Normalized progression of Cu^{II} EPR low-field signal intensity (A) and simultaneously acquired d-d band intensity from the UV-vis spectra (B) measured during step-wise oxidation (**closed symbols**) and reduction (**open symbols**) of either Cu^{I}OTf/TEMPO + 3.0 equivs. 4-DMAP, + 3.0 equivs. 4-AmP or 1.0 equiv. bpy + 1.0 equiv.-DMAP.

During oxidation, the Cu^{II} EPR signal increases very fast when only 4-DMAP or 4-AmP (**Figure 34,** closed symbols) were used. This is attributed to electron density donation from the pyridine ligand towards the Cu^{I} center favoring its oxidation. Such an effect is enhanced by strong σ-donor ligands *e.g. para* N-substituted pyridines in comparison to bpy.[228-229] Thus, replacing two coordinating N-ligands of 4-DMAP by bpy should lead to a slower oxidation, since bpy is a weaker σ-donor but a stronger π–acceptor ligand.[82] This could be nicely corroborated by *in-situ* EPR results of the Cu^{II} signal (**Figure 34A**) as well as the simultaneously acquired UV-vis spectra showing similar behavior of the d-d transition band (**Figure 34B**).

When BzOH is added to those solutions a significant decrease of the Cu^{II} EPR signal is observed accompanied by a change of color from light green to colorless in the case of 4-DMAP or 4-AmP and from light green to brown when using the mixed-ligand system 4-DMAP/bpy. This clearly evidences the reduction of the active Cu^{II} complex and re-forming the starting complex. In the mixed-ligand system the reduction proceeds fastest being complete after approx. 8 min, in contrast to about 13 min when bpy is absent thus confirming that *para* N-substituted pyridines as strong σ-donors stabilize the resulting Cu^{II} complexes which provokes slower reduction.[230-232] On the other hand, bpy compared to 4-DMAP or 4-AmP is known as a stronger π-acceptor ligand, thus stabilizing the Cu^{I} valence state over Cu^{II}.[20, 82] These properties would explain both the hindered oxidation rate as well as the improved reduction rate when using mixed-ligand systems incorporating both bpy and a strong σ-donor ligand. Astonishingly, the reduction rate is significantly prolonged in the case of 4-AmP. In this case the conversion of Cu^{II} to Cu^{I} is only complete after approx. 30 min. These findings might be attributed to dipolar interaction/hydrogen bonding between the NH_2 moiety[233-234] of 4-AmP and neighboring Cu^{II} centers or other constituents of the reaction solution (*e.g.* free ligands, BzOH) which was previously found to occur for 1*H*-imidazoles with an unprotected NH moiety.[119] This could be an explanation for the observed higher catalytic performance of the 4-DMAP compared to the 4-AmP system (**Figure 24**) and the different behavior of the Cu^{II} and TEMPO EPR signals during the catalytic conversion of BzOH to BA (***cf.* Figure 32**). The Cu^{II} formation during phases 1-3 is quite similar for both 4-DMAP and 4-AmP before full conversion of BzOH is achieved. In the case of the TEMPO signal the decrease in signal intensity during phase 2-3 is faster when using 4-AmP, which suggests that the reduction step is even more hindered compared to 4-DMAP and could be shown by our results from the step-wise redox studies (**Figure 34, black line**). This could only arise from the unprotected NH_2-moeity since both *para* N-substituted pyridines are strong σ-donor ligands.

Those findings strongly suggest electronic effects of the ligands on the $Cu^{I/II}$ centers which affect their redox properties and, thus, their catalytic activity. Especially, the facilitated oxidation of Cu^{I} to Cu^{II} by *para* N-substituted pyridines was intriguing. Consequently, we investigated those effects in detail by extending our studies on various substituted pyridines possessing either *+M*, *+I* or *- I* effects (**Table A2**). The position of the substituents was also varied to better differentiate between mesomeric effects. Therefore, $Cu^{I}OTf$ was oxidized by introducing O_2 for 30 min in the presence of pyridine-type ligands, as well as, N,N-dimethylaniline and monitored by *in-situ* EPR. Since the TEMPO radical was absent, semi-quantitative determination of the Cu^{II} EPR signal could be carried out by avoiding interference of TEMPO and Cu^{II} signals. The Cu^{II} signal intensity was obtained by double integration of the total spectrum and used to monitor the different ability to promote Cu^{I} oxidation. It could be shown, that pyridines with an N-moiety in *para* position led to a significantly faster Cu^{II} formation compared to pyridines having an N-moiety in *meta* or *ortho* position (**Figure 35A**) or no substituent at all. This further evidences the participation of the lone pair of the $–NR_2$ moiety in donating electron density to the Cu active site, thus explaining why no imine formation is observed in the case of 4-AmP (since it is actively involved). Those *para* N-substituted pyridines are able to promote Cu^{I} oxidation independent from the steric backbone of the substituents as long as the NH_2 moiety is protected by methyl groups yielding similar results, $NH_2 << NMe_2 \sim N(CH_2)_4 \sim N(CH_2)_5$ as observed in the normalized Cu^{II} signal with time (**Figure 35B**).These findings nicely correlate with the catalytic behavior of systems *e.g.* incorporating 4-pyrrolidinopyridine or 4-piperidinopyridine, having even slightly higher reaction rates compared to 4-DMAP (**Table A2,** entries 7-8). Similar effects could be evidenced in the Cu^{II}-mediated oxidative coupling of phenols.[203] This might be due to +*I* effects of the methyl substituents.

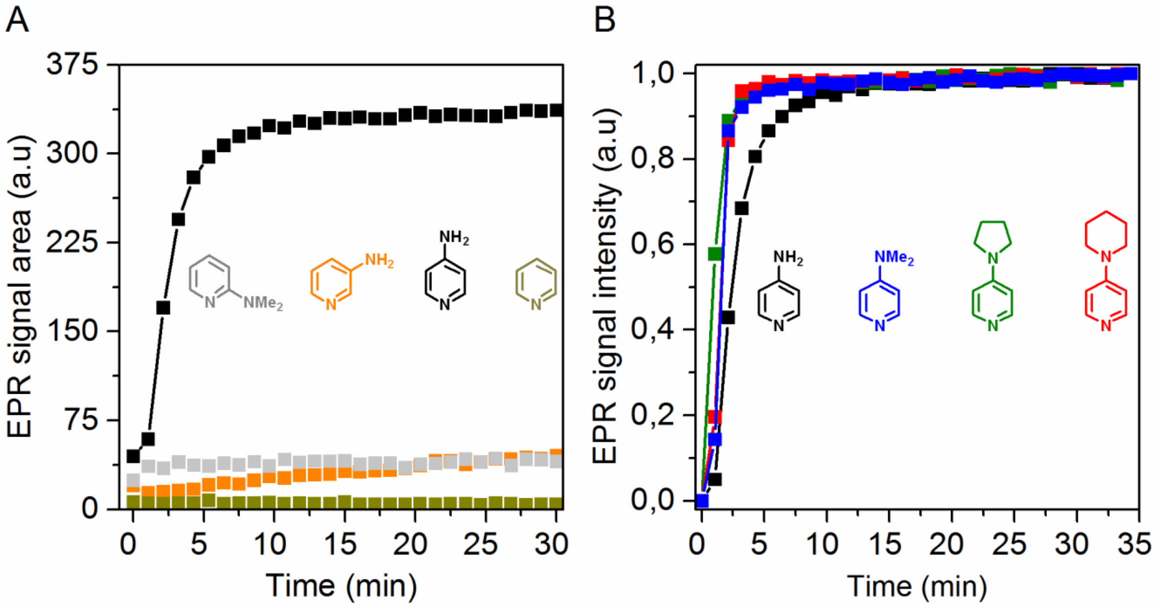

Figure 35. Comparison of EPR Cu^{II} signal intensity (obtained by double integration) with time during oxidation of $Cu^{I}OTf$ in the presence of various pyridine-type ligands (**A**) and relative increase (normalized Cu^{II} signal intensity) using differently *para*-substituted pyridines (**B**).

However, only a slow increase in Cu^{II} signal intensity and marginal Cu^{II} formation could be evidenced for *meta*-and *ortho* N-substituted pyridines *e.g.* 3-AmP or 2-AmP, respectively

(**Figure 35A**). This is related to less electron donation in *meta* position. *Ortho* N-substituted pyridines might exhibit a chelating effect at the Cu^I center preventing oxidation by shielding Cu^I from access to O_2. Those findings could explain the significantly lower rates of BA formation when using these ligands (***cf.* Figure A12, Table A2**). All other tested pyridines with moieties differing from NR_2 only led to a slight formation of Cu^{II}, independent from their effects (+*I*, -*I* or +*M*) (**Table A2**, Entries 9-15). The scaffolds of 4-DMAP, pyridine and N,N-dimethylaniline, also did not show significant oxidation of Cu^I during the monitored time-span (**Table A2**, Entries 1 and 16). This correlates well with their very low activity within the catalytic reaction. Interestingly, the catalytic activity and the ability to facilitate Cu^I oxidation within catalytic systems containing pyridine-type ligands seems to be correlated to the basicity of the ligand. Ligands having highest pK_a values (of the conjugated acid) displayed the highest reaction rates in the conversion of BzOH to BA (**Table A2**, Entries 5-8). Remarkably, compared to 4-AmP, slight Cu^{II} formation has been observed when employing 4-aminomethylpyridine as a ligand (**Table A2**, Entry 14). This might be attributed to the absence of resonance donation of the $-NH_2$ moiety into the aromatic system since it is interrupted by one CH_2 unit.[204] This fact could also explain the low catalytic activity in that case. On the other hand, blue-greenish precipitate containing Cu^{II} species was observed when using 4-aminomethylpyridine shortly after introducing O_2. Similar effects were observed for 1*H*-imidazole[119] which points to interaction with other $Cu^{I/II}$ centers via both the amine and the imine nitrogen leading to Cu^{II}-containing aggregates.

Electrochemical analyses

To corroborate discussed EPR results regarding the ability to promote Cu^I oxidation, the redox behavior of different *in-situ* formed $Cu^I(L)_X$ complexes was studied for selected ligands by cyclovoltammetry (CV) (**Figure 36**). Cu^IOTf in MeCN produces one $Cu^{I/II}$ redox pair possessing an oxidation wave at approx. +0.7 V [Fc^+/Fc] (**Figure 36, black line**) and a reduction event at approx. +0.4 V [Fc^+/Fc]. When 3.0 equivs. of pyridine are added subsequently, broadening of those features is observed and both peaks shift to lower potentials (**Figure 36, orange line**). In this case, the oxidation wave is measured at approx. +0.8 V whereas the reduction wave is measured at approx. –0.4 V. Addition of 20 equivs. of pyridine gives rise to a distinct and well-defined oxidation signal at approx. +0.4 V [Fc^+/Fc] (**Figure 36, blue line**). Those findings suggest complexation of the total amount of Cu^I by pyridine to yield probably a $Cu^I(pyridine)_4$ species.[235] Pyridine is known to form only weak complexes with Cu^I, which undergo rapid ligand exchange with MeCN. Therefore, higher concentrations of pyridine are necessary to form stable Cu^I complexes.[124] Adding 3.0 equivs. of 4-DMAP to a solution of Cu^{I}OTf in acetonitrile leads to appearance of an oxidation wave at approx. –0.1 V [Fc$^+$/Fc] attributed to the Cu^I(4-DMAP)$_4$ species (**Figure 36, red line**). The reduction feature nearly completely disappeared indicating irreversible electrode processes. A second small oxidation wave is observed at approx. +0.9 V [Fc$^+$/Fc] which might stem from Cu^{I}OTf as the stoichiometry 4-DMAP/Cu = 3 might not be sufficient to completely convert the starting material into the desired 4-DMAP complex. When 3.0 equivs. 3-AmP are added to the Cu^{I}OTf precursor, two broad oxidation waves at approx. +0.4 V and +0.9 V [Fc$^+$/Fc] become apparent (**Figure 36, pink line**) which we assign to a Cu^I(3-AmP)x species and to non-converted Cu^{I}OTf remaining in solution, respectively. The reduction peak is also absent in this case, indicating similar irreversible oxidation processes.

These findings clearly show, that the oxidation potential of corresponding Cu^I complexes shifts in the order of pyridine > 3-AmP > 4-DMAP affirming the results seen in **Figure 35**. Moreover, from the CV results it could be shown that 4-DMAP forms more stable Cu^I complexes compared to *e.g.* pyridine since in the latter case an excess of ligand is necessary to yield well-defined redox peaks.

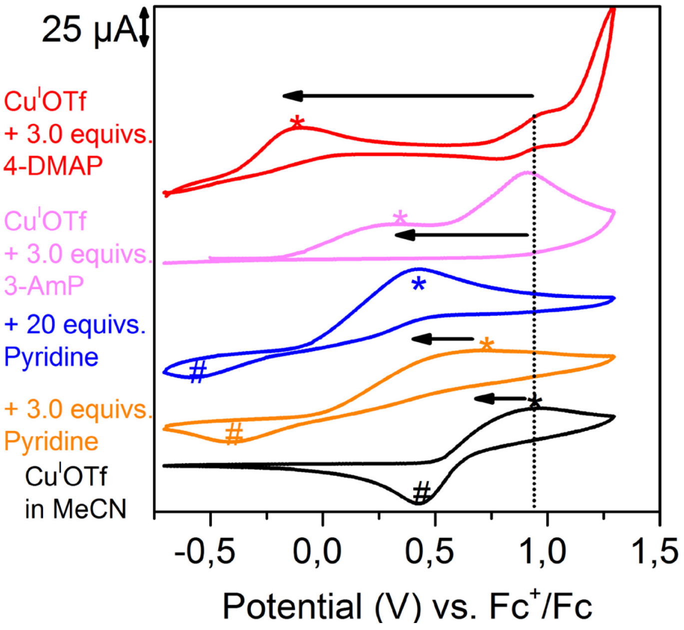

Figure 36. Cyclovoltammetry (CV) of selected, *in-situ* formed Cu/L complexes (L=Pyridine, 3-AmP, 4-DMAP) compared to the starting material Cu^{I}OTf in MeCN (oxidation and reduction events are marked with asterisks and hashes, respectively).

Brief summary

We could provide strong evidence for the assumption that the main factor for high catalytic activity in systems using Cu/pyridine-type ligands is the Cu^{I} oxidation, the first step of the catalytic cycle.[17, 20, 119] We found, that this ability is directly related to electron density donation of N-substituents in the *para* position to the imine nitrogen of the pyridine ring. These findings nicely correlate with the observed order of 4-DMAP > 4-AmP >> 3-AmP > 2-AmP in the catalytic conversion of BzOH to BA. On the other hand, the low catalytic activity of pyridine ligands containing *meta* or *ortho* substituents, *e.g.* 3-AmP, 2-AmP and 2-DMAP, is linked to the fact, that oxidation of Cu^{I} to Cu^{II}, in the first step of the catalytic cycle, is significantly hindered. Interestingly, our findings could be corroborated by additional electrochemical investigations.

Our approach of separating the oxidation and the reduction step led us to two different ligand-related effects. In Cu^{I} systems with 4-DMAP or 4-AmP as the sole ligand the oxidation step is significantly favored. Contrary, with bpy and 4-DMAP in mixed-ligand systems the reduction step is favored due to enhanced π-acceptor properties of the bpy ligand. Since the oxidation step seems to be primarily influenced by pyridine-type ligands, studies focusing on this particular reaction step were repeated with the possibility of semi-quantitative analyses. In the course of these investigations it was clearly evident that only *para* substituted $–NR_2$ pyridines lead to significant formation of Cu^{II} which was independent from the R-backbone as long as R is not hydrogen atom. Those findings could be confirmed by recording cyclovoltammograms of solutions containing differently substituted pyridines showing lowest redox potentials for complexes comprised of Cu^{I}/4-DMAP.

4.3. Deeper insight into active sites: *Operando* XANES/EXAFS/EPR/UV-vis/ATR-IR

From our 3-in-1 coupled spectroscopic studies of the aerobic alcohol oxidation, several issues regarding the nature of *in-situ* formed (bpy)$Cu^{I/II}$(NMI)$_2$ species, their structural arrangement and their redox behavior during the catalytic conversion of BzOH to BA remain unclear. With the current EPR/UV-vis/ATR-IR coupling we are not able to discriminate between the nature of coordinating ligands or determine the distances between the next neighbours of the Cu centers.
Hence, the most important questions are:

Are Cu^{II} dimers or Cu^{II} species of higher nuclearity formed during the reaction?

Are Cu^{II} bis-μ-hydroxy dimers formed as proposed by other groups?[20, 148] In the case they are formed: How is their molar ratio and activity ccompared to the mononuclear Cu^{II} species, which have been proven beyond doubt[17, 19-20, 28, 119] to cycle during the reaction? Furthermore, the precise coordination sphere as well as geometry of the active Cu^{I} and Cu^{II} centers is still unknown and *in liquid phase* can only be investigated by X-ray absorption techniques.

Therefore a new coupling technique, EPR/UV-vis/ATR-IR/XAS, was built to answer those questions and get deeper insight into the catalytic pathways. From the XANES part of the spectrum the formal valence state of Cu and its general coordination environment can be derived. EXAFS analyses allow us to determine the distances and angles of the next neighbors of the Cu centers. By maintaining the other spectroscopic techniques, *i.e.* EPR, UV-vis and ATR-IR, parameters such as the catalytic activity and the behavior of EPR-active Cu^{II} species can be interrelated with the structural data of the active Cu complexes. Thereby, clear structure-reactivity relationships can be established.
There are, however, several obstacles in the development and implementation of such a set-up. First, a reactor had to be developed capable of transmitting X-rays while being implemented within the EPR resonator, *i.e.* enabling the tuning of the EPR cavity and recording of EPR spectra. A second issue concerns the possibility of mounting an EPR spectrometer at a specific synchrotron beamline. The latter has been accomplished by using a portable EPR spectrometer the EMXnano by Bruker. The EPR cavity of that spectrometer was replaced by a custom made resonator. Furthermore, the electronic mainboard in the back of the spectrometer had to be rearranged (***cf.*** **Figure 2**) for clearing the X-ray beam path. In general, with this set-up, recording of XANES/EXAFS spectra was only possible in

transmission mode.

The first issue, the development of a suitable reactor, proved to be challenging. Two criteria must be fulfilled: On one hand the EPR cavity and the reaction tube must allow the X-ray beam to pass through. Simultaneously, such reactor must be stable and capable of allowing circulation of the reaction solution. On the other hand, the volume of the reaction tube has to be limited, since larger volumes of the polar solvent would lead to dielectric loss of MW energy. This could be accomplished by using a reaction tube composed of polyimide (Kapton®) having a very small inner diameter, similar to the tubular mid-section of the reactor used for the EPR/UV-vis/ATR-IR coupling. Polyimide is a polymer transmissive towards X-rays and able to withstand high mechanical stress while still maintaining flexibility. To further stabilize this Kapton® tube, an outer quartz glass reactor was used as a jacket. As quartz glass reduces the intensity of X-radiation[236] the quartz glass tube itself had to be modified accordingly. For this purpose, two small holes, in the front and in the back were drilled into the quartz glass reactor. This was necessary to expose the polyimide tube to the X-ray beam passing through the reaction solution onto the detector (**Figure 37**).

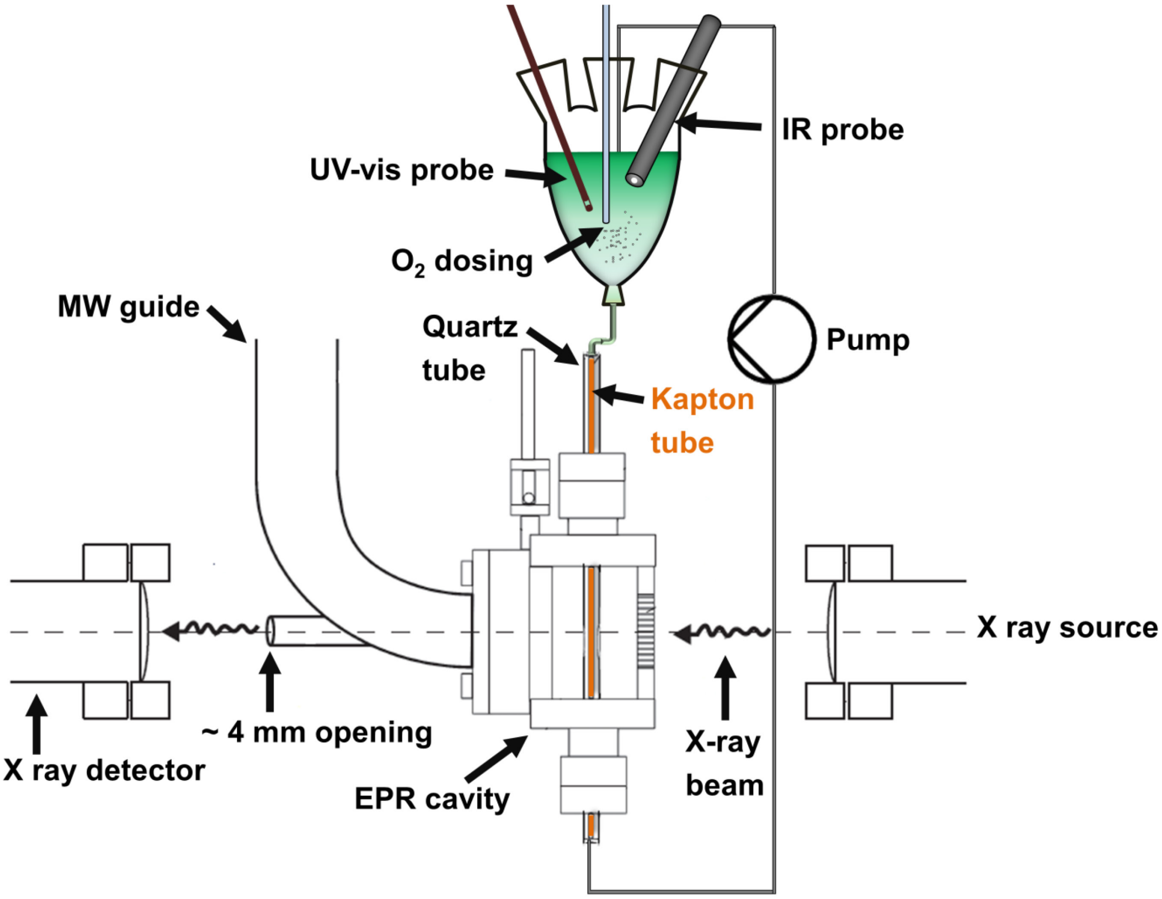

Figure 37. Technical drawing depicting the combined *operando* EPR/UV-vis/ATR-IR/XAS set-up within the X-ray beam path at the ROCK beamline at synchrotron SOLEIL in France.

As EPR cavity, a custom-made half-wave resonator was used equipped with a grid in the front and an opening in the back allowing the X-ray beam to pass through the set-up. The fiber-optical probes for UV-vis and ATR-IR measurements are located in a reservoir on top of the EPR reactor connected to a circulation device.

Finally, this set-up was assembled at the Quick-EXAFS ROCK beamline at SOLEIL synchrotron facility. This beamline was chosen, since it is renowned for the acquisition of XAS spectra down to the millisecond range.

4.3.1. Kinetic profiling of Cu^I/Cu^{II} species

By using this set-up, we used a protocol similar to that described in **chapter 4.1.1**. A higher Cu concentration of 0.025 M was necessary to yield high quality XANES/EXAFS spectra. However, it was found by UV-vis measurements that those solutions are comparable to the standard concentration ([Cu] =0.01 M) which was used in the experiments without XAS.

In a first stage, the solution containing 0.025 M [Cu], 1.0 equiv. bpy, 2.0 equivs. NMI and 1.0 equiv. TEMPO in MeCN has been prepared in the glove box and added to the reactor under inert atmosphere. Afterwards, O_2 introduction was started at a rate of 25 ml/min. The formation of the $(bpy)Cu^I(NMI)_2$ complex was evidenced in the UV-vis spectra by the characteristic MLCT band at approx. λ_{max} = 405 nm displaying the typical shoulder at approx. 537 nm (**Figure 38A, purple**).[17] At the same time, only the TEMPO radical signal could be observed in the EPR spectra, since Cu^{II} was not as expected at this stage (**Figure A18**).[17] A very small Cu^{II} signal can be seen, caused by remaining O_2 in the solution despite Ar purging (**Figure 38B, purple**).

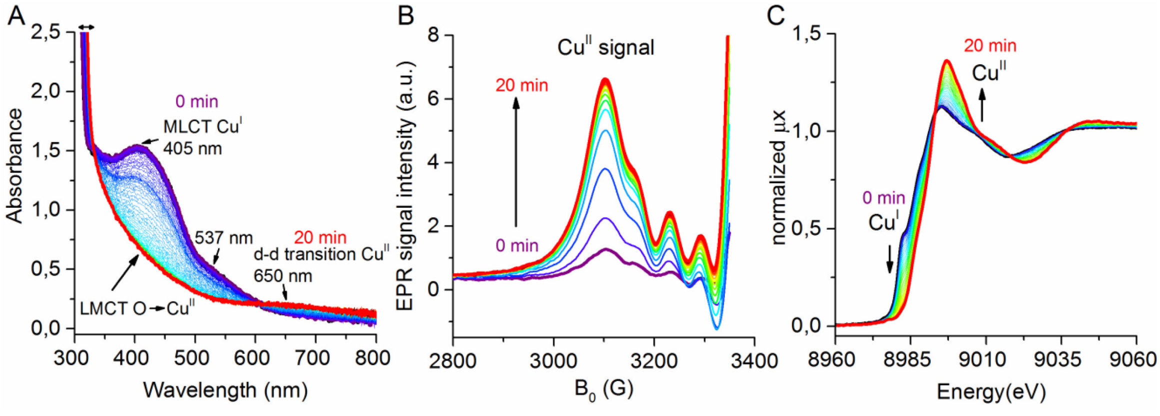

Figure 38. Progression of EPR (**a**), UV-vis (**b**) and XANES spectra (**c**) of a Cu^IOTf, 1.0 equiv. bpy, 2.0 equivs. NMI and 1.0 equiv. TEMPO containing MeCN solution while introducing O_2.

In the corresponding XANES spectra of that solution a shoulder is resolved in the rising edge at 8983.0 eV. An absorption maximum at 8995.2 eV assigned to the 1s→4p transition of Cu^I confirms the predominant Cu^I stage (**Figure 38C**).[237] These findings clearly show that the *in-situ* formed Cu^I is not oxidized solely by TEMPO as proposed before.[29, 238-239] Oxidation of Cu^I to Cu^{II} could be noted directly after starting the introduction of O_2. This was evidenced by a fast increasing Cu^{II} EPR signal displaying the typical hfs structure observed before. (**Figure 38B**).[17, 119] From the UV-vis spectra the disappearance of the MLCT band of Cu^I could be observed while simultaneously a d-d transition band of Cu^{II} at approx. λ_{max} =637 nm as well as an LMCT absorption in the range between 350 and 450 nm emerges.[83] Moreover, the Cu^I shoulder at 8983.0 eV observed in XANES spectra completely disappeared and the absorption maximum shifted to higher energies (8997.2 eV). Concurrently, a rise in the white line and the emergence of a new very weak pre-edge feature at 8978 eV is noted (**Figure 38C, red line**). This particular feature can be assigned to a forbidden 1s ➔ 3d transition of Cu^{II} ions gaining intensity due to 3d+4p orbital mixing occurring in non–centrosymmetric transition metal ions. [240-241]

For detailed kinetic studies investigating the behavior of the $Cu^{I/II}$ shuttle with time, BzOH was subsequently in four portions of 5.0 equivs instead of one portion of 20 equivs. and all four spectroscopic techniques were applied simultaneously. UV-vis and XAS spectra can be found in **Figures A19** and **A21** clearly showing the appearance of the distinct features of Cu^I when BzOH is added to the oxidized reaction solution. Reappearance of the Cu^{II} characteristics are noted, when BzOH has been consumed, since continuous O_2 introduction leads to re-oxidation of the Cu^I species in the absence of a reducing agent. Interestingly, isosbestic points could not be observed during the four additions of BzOH in the UV-vis spectra (**Figure A19A-G, A20**) suggesting the involvement of more than two Cu species during the consequent redox cycles. The lack of an isosbestic point has been described before by Stahl et al.[20] and was also observed in the course of our previous investigations (***cf.*** **Figure A3**). Moreover, λ_{max} of the d-d transition band of Cu^{II} continuously red-shifts during the successive redox cycles from approx. 650 to 670 nm (**Figure A19**).

For the identification of individual components contributing to the sum of the spectra and their concentrations profiles, the XAS and UV-vis data sets (during the four repeated redox cycles) were analyzed using the Multivariate Curve Resolution Alternating Least Squares fitting method (MCR-ALS) **(Figure 39A–D)**.[242-243] Three discreet Cu species were sufficient to explain the variance within the UV-vis and XAS spectra: two mononuclear species (*1 x* Cu^I, *1 x* Cu^{II}) and one Cu^{II} dimer, being derived from EXAFS and UV-vis analyses, could be distinguished (**Figure 39A and B, A22-23, Table A3**). It was found that after the initial oxidation two Cu^{II} species are formed immediately, in the ratios of approx. 60%

monomeric Cu^{II} and 40% dimeric Cu^{II} (**Figure 39C and D**) remaining stable at this level. Upon addition of the first dose of BzOH, the feature of both Cu^{II} species disappear in the UV-vis and XAS spectra and the features of Cu^{I} reappears and rises to its maximum remaining at this level for 1 min before decreasing again, since O_2 is continuously introduced into the reaction solution. Interestingly, this Cu^{I} species is virtually identical to the starting species (**Figure A24**) further validating our extraction processes by MCR-ALS analyses. Furthermore, it is very interesting to note, that those two distinct Cu^{II} species are reduced to the same Cu^{I} species exhibiting virtually identical conversion rates (**Figure 39C and D**).

From the EXAFS analysis of the local geometry of the three Cu species, it could be revealed that the Cu^{I} species is tetra-coordinated in accordance with our proposed $(bpy)Cu^{I}(NMI)_2$ complex and both Cu^{II} species display backscattering patterns of a penta-coordinated environment (**Table A3**). The monomeric Cu^{II} species can be sufficiently explained by either a $(bpy)Cu^{II}(NMI)(MeCN)$ or $(bpy)Cu^{II}(NMI)_2$ complex. On the other hand, the dimeric Cu^{II} species was revealed to possess a second Cu-Cu shell at a distance of 2.91Å (**Table A3**). This is in accordance with a bis-μ-hydroxy N_3Cu^{II} dimer (reported to have a Cu-Cu distance of 2.93Å)[244] being proposed by Stahl et al. before as a resting species.[19-20] We therefore assign the scattering from the dinuclear species to the bis-μ-hydroxy Cu^{II} dimer, $[(bpy)Cu^{II}(NMI)\mu\text{-}OH]_2$.

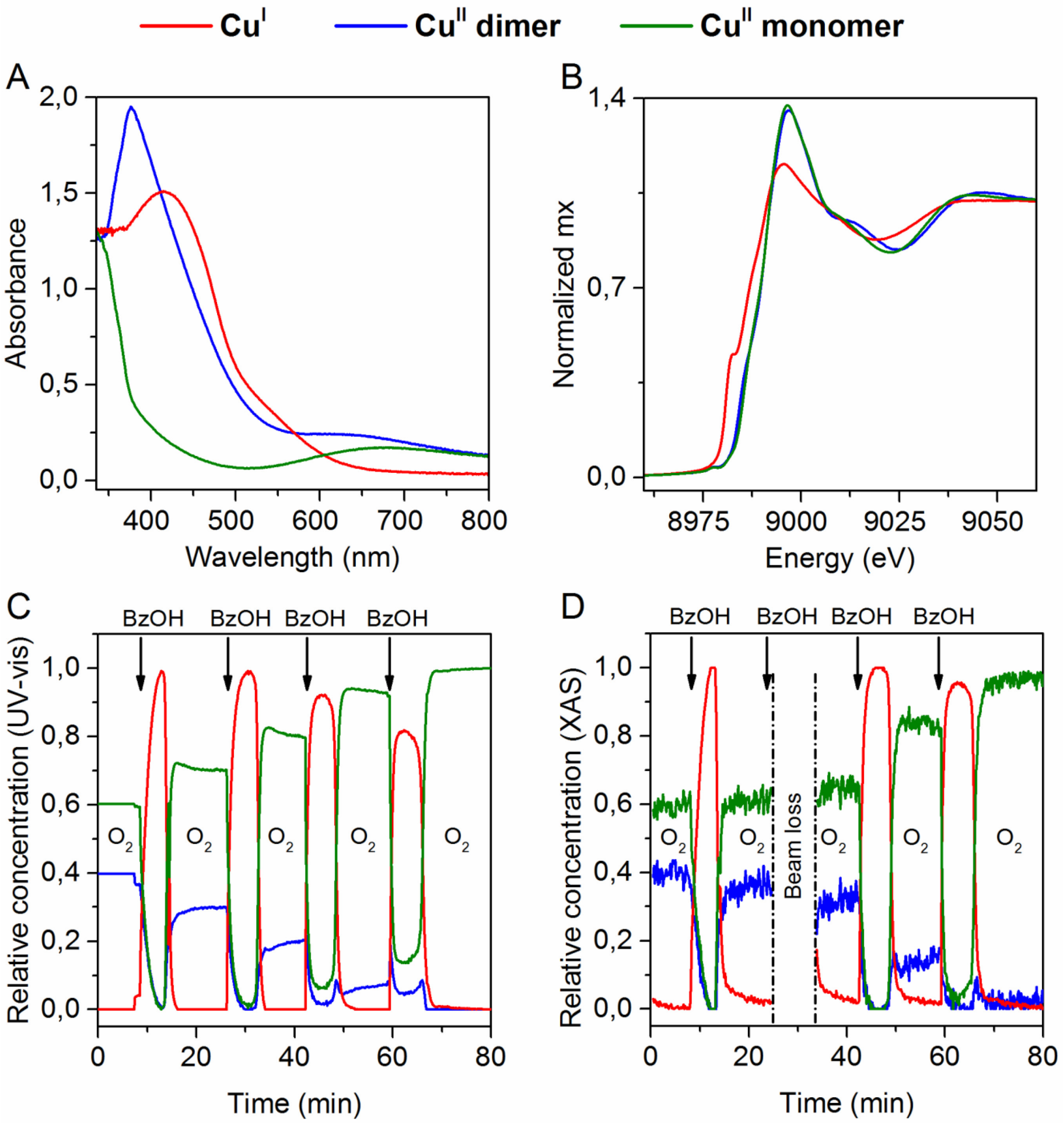

Figure 39. Extracted Cu$^{I/II}$ species using MCR-ALS of UV-vis (**A**) and XAS (**B**) spectra. Concentration profiles of those species for the corresponding UV-vis (**C**) as well as XAS (**D**) methods.

Previously, Stahl et al. proposed different peroxo-bridged Cu^{II} dimers or even oxo-bridged Cu^{III} dimers to occur as intermediate species during the catalytic reaction.[20] However, such peroxo Cu^{II} species typically have longer Cu-Cu distances (more than 3Å);[11-12] moreover features suggesting a Cu^{III} valence state have not been found in the course of our investigations.

Since the bis-μ-hydroxy Cu^{II} dimer displays an equilibrium with the corresponding Cu^{II}-OH monomers (proposed to be the major active Cu^{II} species by some authors)[19-20, 28] it is very plausible that both Cu^{II} components, extracted from the UV-vis/XAS analyses, are reduced to the same Cu^I monomer complex upon BzOH addition. From the previous low temperature EPR studies (**Figure 16**) we observed an EPR spectrum exhibiting $g_{\|}>g_{\perp}>g_e$ features suggesting tetragonally-distorted geometry[163] of those EPR active Cu^{II} monomers. Combining these results with the present EXAFS analyses (**Figure A22-23, Table A3**) revealing a penta-coordinated Cu^{II} monomer, a local structure of a square-pyramidal Cu^{II} monomeric center seems plausible. This has also been reported very recently for Cu^{II} ions in MeCN.[245] During the course of additional three redox cycles both Cu^{II} species re-emerge during the oxidation step and are subsequently reduced to the same Cu^{I} species again (**Figure 39 C and D**).

However, two effects have been observed. First, the ratio of the Cu^{II} species changes after each BzOH addition and sequent re-oxidation steps. With time the Cu^{II} dimers disappear and only the Cu^{II} monomer appears to be the catalytically active species. (**Figure 39C and D**).This might indicate that formed bis-μ-hydroxy Cu^{II} dimers are not stable in MeCN solutions, especially when other reaction constituents *e.g.* ligands, TEMPO, BzOH and BA are simultaneously present.[19, 246] Moreover, increasing concentration of H_2O in the reaction solution would *promote* the formation of OH-bridged Cu^{II} dimers.[19] Thus, the formation of H_2O as a byproduct cannot be a factor for the *cleaving* of those species. Since the Cu^{II} nuclei in these dimers are separated by only 2.91Å, they should exhibit strong exchange interaction depending on the bridging angle[247], *e.g.* antiferromagnetic or ferromagnetic coupling, forming either $S = 0$ and $S = 3$ spin systems, respectively.[83, 248]

However, EPR studies (**Figure 16**) and references[17, 19-20] do not observe a distinct forbidden $g_{1/2}$ ($\Delta m = \pm 2$) transition (which can be observed in $Cu_2(bpy)_2(\mu\text{-}OH)_2$ dimers depending on the used ligands[249]) thus suggesting the present bis-μ-hydroxy Cu^{II} dimers to be antiferromagnetically coupled, hence EPR *silent*. From the comparison of the EPR signal intensities (double integrals) of the $(bpy)Cu^{II}(NMI)_2$ complexes derived either from a $Cu^{I}OTf$ or a $Cu^{II}OTf_2$ precursor using the same concentration ([Cu]=0.025 M) (**Figure A25 black and blue line**), it is evident that the former comprises only 52% of the total Cu^{II} amount compared with the $Cu^{II}OTf_2$ precursor. As both UV-vis and XAS spectroscopy indicate complete oxidation of Cu^{I} to Cu^{II} (**Figure 39 C and D**), this means that approx. 48% of Cu^{I} must be oxidized to an EPR silent Cu^{II} species, which might be the bis-μ-hydroxy Cu^{II} dimer derived from the EXAFS analysis. These finding roughly agree with the results of the MCR-ALS analysis, in which approx. 40% of the total copper in the pre-oxidized $Cu^{I}OTf$/bpy/NMI solution were found as Cu^{II} dimer (**Figure 39 C and D**).

The formation of an EPR-silent Cu^{II} dimer upon oxidation of the $Cu^{I}OTf$/bpy/NMI solution has also been confirmed indirectly. When benzoic acid (BzOOH) was added to such a solution, an almost twofold increase of the Cu^{II} EPR signal intensity was observed (**Figure A25, black and red line**). This is due to the cleaving of the EPR-silent Cu^{II} dimer and formation of an EPR-active mononuclear Cu^{II} complex**.** This is described in detail in **chapter 4.3.2.**

Thus, the vanishing of those EPR silent Cu^{II} dimers during the reaction should give rise to EPR active Cu^{II} monomers. However, a *steady increase* in the Cu^{II} EPR signal should occur, which is not observed. The total EPR Cu^{II} signal remains at a similar level during the four consecutive redox cycles compared to the initial oxidation of Cu^{I} to Cu^{II} (**Figure A26**). At the present stage, we must conclude the formation of an EPR silent Cu^{II} monomer which does not contribute to the total Cu^{II} EPR signal intensity. The only possible candidate would be an antiferromagnetically coupled Cu^{II}-TEMPO adduct. Such kind of complexes have already been postulated recently.[31, 250] Moreover, we found direct EPR evidence for the strong interaction between TEMPO and monomeric Cu^{II} complexes formed in pre-oxidized solutions containing Cu^{I}OTf/bpy/NMI. When TEMPO is added to these solutions after flushing with Ar (to remove excess O_2), the Cu^{II} hfs signal broadens and looses intensity (**Figure A27, blue and red line**), while the TEMPO signal intensity drops simultaneously, compared to the TEMPO spectrum under the same conditions, but in the absence of the Cu catalyst (**Figure A27, red and black line**).
An alternative explanation could be a pseudo Jahn-Teller effect of the Cu^{II} species, which according to recent literature could also yield Cu^{II}-OH monomeric species, which are EPR silent.[251]

The presence of Cu^{II} dimeric species during the reaction raises the question of a new reaction mechanism, since the Brückner pathway clearly requires an end-on oxygen radical species coordinated at the Cu^{II} center which interacts with the TEMPO radical. It should be stressed, that at the moment, we do not have sufficient spectroscopic evidence to clearly substantiate a pathway involving Cu^{II} dimers. Stahl's pathway[20] incorporating Cu^{II} dimeric species, however, is not likely, due to the conflicting behavior of the EPR Cu^{II} and TEMPO signals as investigated previously (**cf. Figure 18***)*.[17] A mechanistic proposal can be found in **Scheme 18**.

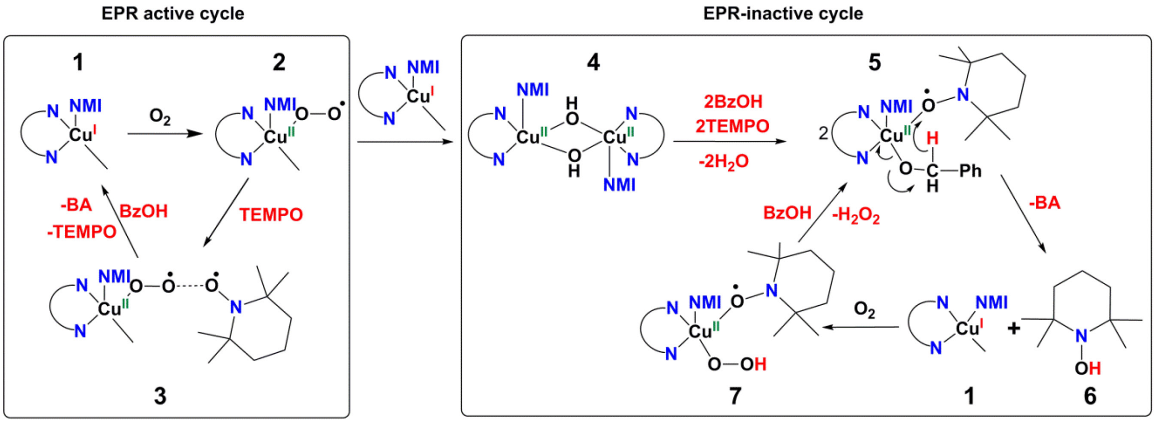

Scheme 18. Proposed reaction mechanism of the Cu/TEMPO catalyzed aerobic alcohol oxidation involving Cu^{II} monomeric species in an EPR active and Cu^{II} dimers in an EPR inactive cycle.

In this mechanistic proposal, besides the Cu^{II}–$OO^{\bullet}$–TEMPO (**3**) pathway, an initially formed Cu^{II} superoxide (**2**) reacts with another Cu^{I} starting complex (**1**) to yield the bis-μ-hydroxy Cu^{II} dimer (**4**) by passing an instable peroxo-bridged Cu^{II} intermediate. Dimer **4** is cleaved by reaction with the substrate and TEMPO to form species **5**. That complex releases the product and forms the EPR silent Cu^{I} and TEMPOH species. Stahl et al proposed that the interaction of complex **1** with TEMPOH (**6**) in the presence of O_2 leads to formation of a monomeric Cu^{II}-OH species as well as TEMPO radical.[20] This would lead to an increase of both the Cu^{II} and TEMPO EPR signal, which was not observed. Therefore, we propose that complexe **1** interacts with **6** in the presence of O_2 to result in complex **7**. Very recently, similar Cu^{II}–TEMPO adducts, in which the oxygen atom of the TEMPO radical coordinates to the Cu^{II} center in end-on η^1 fashion, were found to be intermediates during aerobic alcohol oxidation.[31, 250] Since the MCR-ALS analyses only revealed three Cu species, small changes in the coordination sphere such as replacement of one NMI or solvent molecule by by the TEMPO radical, might not be distinguishable.

4.3.2. Deactivation within Cu^{I}/bpy/NMI catalytic systems

Another effect has been observed by investigation of the corresponding ATR-IR spectra collected during the experiment (**Figure 40A**). The slope during the linear course of BA formation continuously decreases (in total approx. 40%) over the subsequent addition of four BzOH portions in the order of $k_1>k_2>k_3>k_4$ suggesting deactivation of the Cu$^{I/II}$ catalyst system. Interestingly, the percentage of decrease in reaction rate (0.025 vs 0.015 mmol/min) is comparable to the vanishing of the Cu^{II} dimeric species, which decreased from 40% after the initial oxidation of Cu^{I} to Cu^{II} to virtually zero after addition of the last BzOH portion. Simultaneously, the amount of non-reducible Cu^{II} species increases throughout the reaction as evidenced from the EPR spectra (**Figure 40B**), since the Cu^{II} EPR signal does not completely vanish upon BzOH addition.

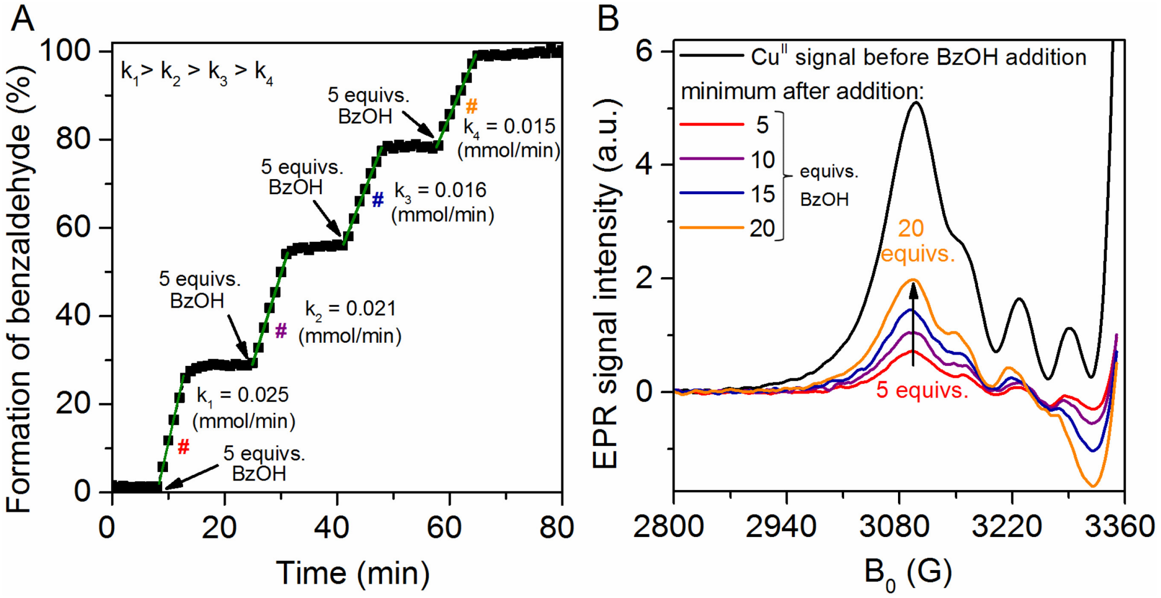

Figure 40. (**A**)Formation of benzaldehyde with time during the four subsequent addition of BzOH to a solution of (bpy)Cu^{I}(NMI)$_2$/TEMPO in MeCN. (**B**) The minimum of the Cu^{II} EPR signal after the subsequent additions of BzOH is marked with corresponding hashes in A.

It was assumed before that catalyst deactivation might occur due to excess amount of H_2O favoring the formation of the bis-μ-hydroxy Cu^{II} dimer,[19] however, this is not the case, since the Cu^{II} dimeric species vanishes. However, Brønsted acids have also been proposed as main suspects responsible for deactivation.[19, 252] Therefore, we conducted catalytic tests with the addition of proton sources in addition to Cu^{I}/bipy/NMI at the beginning of the reaction (**Figure 41**).When only 1.0 equiv. of BzOOH or NMIHOTf (the weak, conjugate acid of NMI and the Cu^{I}OTf precursor anion) were added, the catalytic activity was significantly inhibited. NMIHOTf was used, since it was suggested by Stahl et al. that this compound might lead to catalyst deactivation, when NMI acts as a base and accepts a proton.[19] From the formation of BA with time it is very clear that the presence of proton sources, regardless of their nature, have a detrimental effect on the reaction rate. No significant differences between the rates of NMIHOTf and BzOOH were observed. Both experiments show around 20% conversion after 200 min in contrast to the experiment in absence of a proton source which displays full conversion after approx. 14 min. We assume that such effects are responsible for the continuous decrease in the linear reaction rate. Since NMI works *at most* as a proton shuttle and not as a base as shown previously (***cf.* Scheme A1**), the accumulation of NMIHOTf during the catalytic reaction seems unlikely.

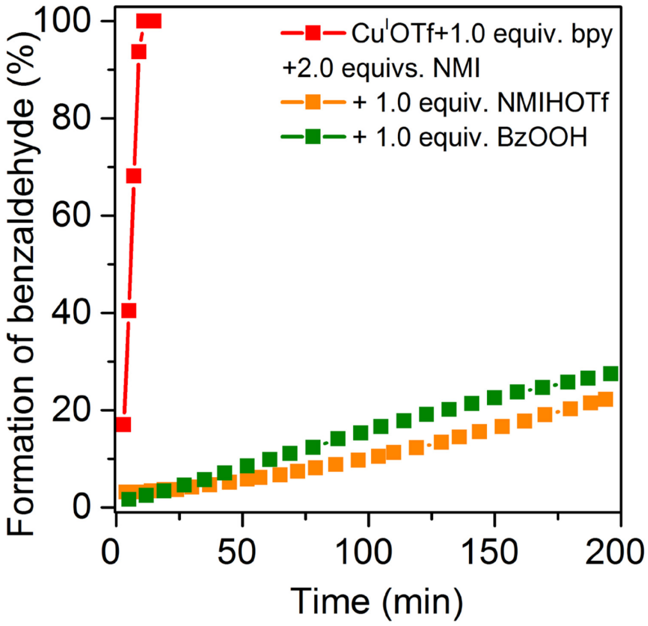

Figure 41. Formation of BA with time during catalytic reaction containing $Cu^{I}OTf$+1.0 equiv. bpy + 2.0 equivs. NMI + BzOH and with addition of either 1.0 equiv. NMIHOTf or 1.0 equiv. BzOOH.

Hence, formation of benzoic acid by over-oxidation of benzaldehyde seems the more likely culprit in the present case.[252] However, direct evidence for benzoic acid formation could not be found, as neither the $\nu C{=}O$ of carboxylic acids nor the distinct $\nu_{as}COO^{-}$ of the corresponding carboxylate was visible. This might be related to the very *small amount* of benzoic acid which is formed during the reaction, being too low to be detected by *in-situ* IR. Addition of proton sources might lead to catalyst deactivation via protonation of Cu^{II}-OR monomeric or dimeric species, since the *pre-formed base* is lost.[19] Thus, less reducible Cu^{II} species are formed, that remain despite addition of BzOH as seen from **Figure 39C-D** in the 3rd and 4th cycle. This would explain, the behavior of the Cu^{II} EPR signal throughout the reaction (**Figure 40B**), since less-reducible Cu^{II} monomers are formed which persist during the reduction step. Because the decrease in reaction rates is also associated with the disappearance of Cu^{II} dimers, we assume the small amount of benzoic acid, which is generated throughout the reaction, might attack *both* Cu^{II} species. This could be another reason for observed Cu^{II} dimer cleaving besides Cu^{II}-TEMPO adduct formation mentioned in **chapter 4.3.1**. Probable deactivation pathways are depicted in **Scheme 19** showing protonation of different Cu^{II}-OR species by benzoic acid. From the XAS data, in particular EXAFS, those small effects *e.g.* the loss of a coordinated OOH, $OO^{-\bullet}$ or OH^{-} species might not be distinguishable, since those ligands are replaced by the MeCN solvent, which is an N donor having similar backscattering patterns due to similar atomic orbital structure. Thus, it is not surprising, that **Figure 39** does *not* display multiple Cu^{II} monomeric species. However, from **Figure 39C and D** we indeed observe a small amount of remaining Cu^{II} species (mainly monomeric) at the end of the 3rd and 4th redox cycle in the UV-vis as well as XAS concentration profiles. This effect can also be seen in the progression of the Cu^{I} species with time, which does not reach 100% during the 3rd and 4th redox cycles.

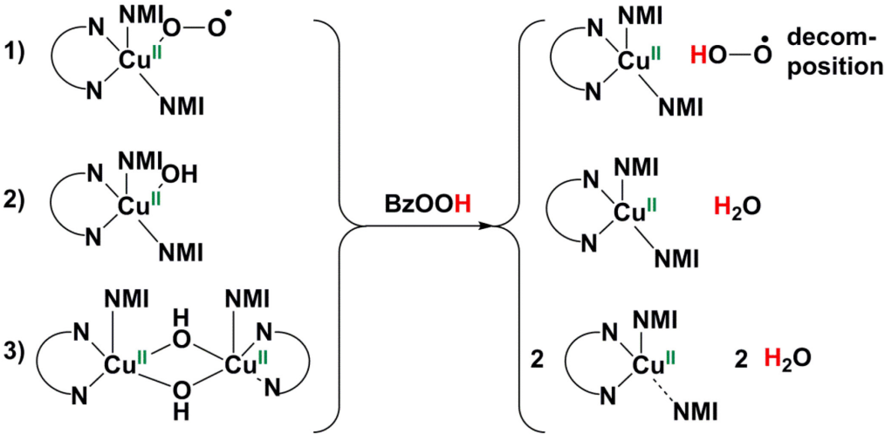

Scheme 19. Possible deactivation mechanisms within Cu/TEMPO catalyzed aerobic alcohol oxidation when a proton source (in this case benzoic acid) is present.

In the *in-situ* UV-vis spectra these effects are visible from a distinct decrease in the LMCT shoulder originating from several possible O→Cu^{II} transitions[58, 101, 150] since there is continuous decrease of this feature throughout the course of the four redox cycles (**Figure A19**). This is also accompanied by a red-shift of the λ_{max} of the d-d transition band from approx. 650 to approx. 670 nm (**Figure A19**) evidencing our assumptions of possible decomposition of oxygen species and replacement by other ligands leading to less active Cu^{II} species and hence reduction of catalytic activity.

This was further explored by studying the effects of different proton sources (BzOOH, NMIHOTf and 1-H-imidazole) on the UV-vis as well as EPR features (**Figure A28**). The *in-*

situ UV-vis spectra (**Figure A28A**) clearly show absence of assumed LMCT feature, when 1.0 equiv. BzOOH or NMIHOTf are added to a solution of Cu^{I}/bpy/NMI in MeCN under O_2 dosing. In the case of 1-H-imidazole, this feature is reduced significantly, while the d-d transition band appears blue-shifted compared to the experiment using NMI. Interestingly, the addition of BzOOH leads to a *red-shift* of the d-d transition, being more pronounced compared to using NMIHOTf. Such a red-shift is also observed in the UV-vis spectra of our catalytic experiments (**Figure A19**) providing further evidence for the involvement of BzOOH in the decomposition of active Cu^{II} species. Coordination of benzoate to the Cu^{II} center could very well be the reason for such a red-shift.[252] In the corresponding, absolute EPR spectra (**Figure A28B**) addition of BzOOH or NMIHOTf shows increased (approx. 55% higher) Cu^{II} signal intensity and slightly different EPR parameters compared to the experiment without proton sources similar to **Figure A25**. If the decrease in the LMCT feature from the UV-vis spectra is also taken into account, we assume that the presence of acids in the reaction system clearly leads to splitting of Cu^{II} dimers.

If 1-H-imidazole is used as a ligand, the EPR spectra show significantly reduced Cu^{II} signal intensity, which is approx. 39% smaller compared to the experiment using NMI. In the wake of the UV-vis results, we also propose, that initially formed Cu^{II}-O species are decomposed by deprotonation of the NH moiety as mentioned before (**Scheme 15**). However, the EPR results rather suggest, that Cu^{II} dimers are not cleaved. Instead, presumably, the formation of imidazolate bridged Cu^{II} dimers is favored via the deprotonated NH moiety.[186, 253] This would explain the lower Cu^{II} EPR signal intensity, since those dimers are likely EPR-inactive,[187] while the d-d transition remains well-pronounced, suggesting a significant amount of Cu^{II} species to be present in the reaction solution.

5. CONCLUSIONS AND OUTLOOK

In the course of this thesis coupled *operando* spectroscopic methods have been successfully applied to elucidate mechanistic aspects within the Cu/Tempo catalyzed aerobic alcohol oxidation.

Investigating the catalytic system Cu^I/Bpy/NMI it was found from UV-vis and electrochemical investigations that an active (bpy)Cu^I(NMI)$_2$ complex is formed, clearly showing that two NMI are involved in coordinating to the Cu^I species. Moreover, evidence for the formation of *several* active as well as less-active Cu^I species is presented. Step-wise addition of components provided deeper insight into the complex formation. When bpy is added first, appearance of Cu^I(bpy)$_2$ as major species is evidenced which show low activity compared to the (bpy)Cu^I(NMI)$_2$ complexes. Subsequent addition of NMI was found to lead to immediate formation of (bpy)Cu^I(NMI)$_2$ species possessing highest catalytic activity. However, besides (bpy)Cu^I(NMI)$_2$ other complexes are formed, too, showing catalytic activitiy. .

Detailed step-wise investigations were carried out regarding the oxidation and reduction behavior of Cu^I/bpy catalytic systems having different molar ratios of NMI. Using our coupled *in-situ* technique approach it could be proved that systems with 2.0 equivs. NMI show a faster oxidation rate compared to 1.0 equiv., probably facilitating formation of proposed intermediate Cu^{II}–O$_2^{\bullet-}$ species. These findings correlate well with observed reactivity of those systems as Cu^I/bpy/2.0 equivs. NMI was found to be the most active system. Interestingly, the rate of reduction was independent from the NMI ratios which was unexpected, since NMI was regarded as a base.

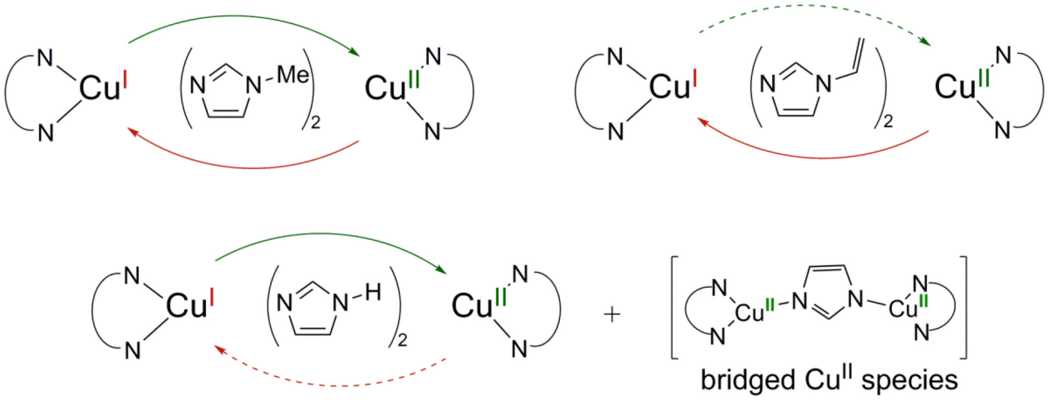

Scheme 20. Influence of differently substituted imidazoles at on the Rate of Cu^I oxidation (green) and Cu^{II} reduction (red).

The tremendeous importance of NMI as a ligand in terms of modulation of the coordination sphere of Cu^{II} centers could be discovered from *in-situ* UV-vis and EPR investigations. Motivated by these results, differently substituted imidazoles were utilized and compared according to their redox qualities using the same step-wise protocol as before. It was found that 1-R substituents exhibiting *+I* properties show superior oxidation rates compared to *+M* substituents while R = H (imidazole) showed fast oxidation but significantly prolonged reduction rates (**Scheme 20**). Interestingly, by comparison of UV-vis and EPR spectroscopic results, it could be shown, that 1-*H* imidazoles lead to significant formation of EPR-silent Cu^{II} species attributed to Cu^{II} imidazolate bridged dimers. These results in turn are in accordance with catalytic tests implementing differently substituted imidazoles which clearly showed increased performance of *+I* substituents in comparison to *+M* containing moieties or unprotected 1-*H*-imidazoles. The catalytic conversion of BzOH to BA is influenced by the nature of the used imidazole ligands. Three distinct types could be identified according to those *+I* and *+M* effects, as well as the effect of the unprotected NH moiety, respectively, which control the amount of (in)active Cu^{II} species present during the catalytic cycle. This is directly related to observed oxidation/reduction steps, which are hampered in some cases (**Scheme 20, dotted lines**).

Investigations of catalytic systems which include pyridine-type ligands, in particular, 4-DMAP revealed that the catalytic activity is strongly dependent on molar ratios of 4-DMAP. Icreasing activity was observed up to a ratio of L/Cu ~ 4, suggesting at least four coordinating N ligands on the Cu center. This could be further substantiated when two N ligands are substituted by bpy observing same ratio dependency. Consequently, Cu^{II} complex formation was studied by *in-situ* and *ex-situ* EPR techniques.Thereby, we could reveal the $Cu^{II}(4\text{-DMAP})_4$ complex as the most plausible species, having a tetragonally distorted geometry. Interestingly, 4-DMAP showed higher activity within the oxidation of alcohols as its structurally related compound, 4-AmP. This is attributed to electronic effects governed by R= NMe_2. Thus, it could be proven, by using a similar step-wise procedure, that both, the oxidation and reduction rates, are faster when 4-DMAP is used. Those unexpected results were attributed to *+I* effects of the methyl substituents as well as hydrogen bonding in the case of R=NH_2. As confirmed by varying the nature as well as position of the substituent R at the pyridine scaffold the catalytic activity is nearly exclusively limited to pyridine derivatives having an -NR_2 substituent in *para* position (**Scheme 21**). When methyl substituents are present the oxidation of Cu^I to Cu^{II} is enhanced regardless of the number of carbons bound to NR_2 moiety in the order $NH_2 << NMe_2 \sim N(CH_2)_4 \sim N(CH_2)_5$. These findings could be further corroborated by electrochemical investigations showing a decrease in redox potential for a Cu^I/4-DMAP complex compared to Cu^I/pyridine. Furthermore, it could be shown that in mixed ligand systems (bpy/4-DMAP) the oxidation and reduction rates are more balanced and hence the catalytic activity was superior to sole usage of 4-DMAP (**Scheme 21**). Sole usage of *para* substituted NR_2 pyridines as ligands led either rapid oxidation due to enhanced σ–donor properties and hindered reduction, while the *meta* substituted 3-AmP only only showed slow oxidation of Cu^I to Cu^{II} with time.

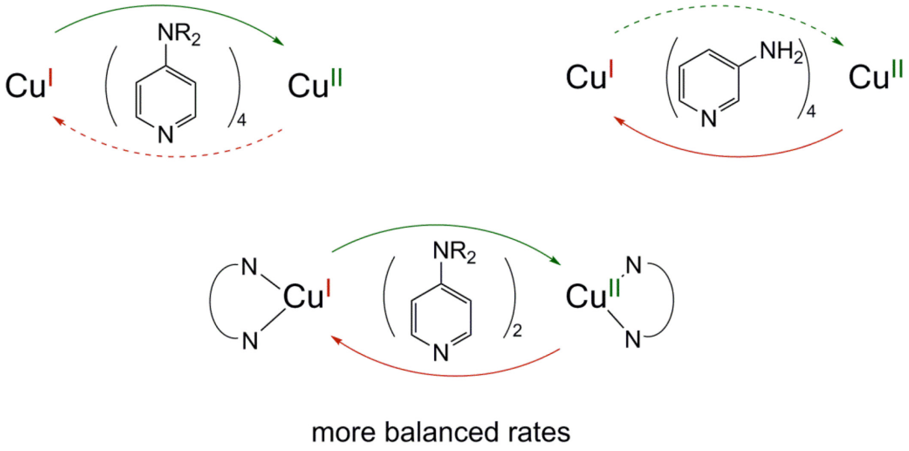

Scheme 21. Influence of differently N-substituted pyridines, in presence/ absence of bpy, on the rate of Cu^I oxidation (green) and Cu^{II} reduction (red).

The newly developed EPR/UV-vis/ATR-IR/XANES/EXAFS coupling was utilized to investigate the catalytic system, Cu^I/bpy/NMI. XANES/EXAFS analyses of the starting solution, containing $(bpy)Cu^I(NMI)_2$ complexes, confirmed the four-fold coordination in tetrahedral geometry. By subsequent oxidation remarkably two distinct Cu^{II} species are produced. One is a monomeric species attributed to $(bpy)Cu^{II}(NMI)_2$–OR. The other species exhibits a Cu-Cu distance of ~ 2.91 Å, which points to a bis-μ-hydroxy bridged Cu^{II} dimer. Interestingly, both Cu^{II} species exhibit five-fold coordination with distorted square-pyramidal symmetry being the most likely configuration as further evidenced by EPR spectroscopy. Addition of BzOH leads to decrease of both Cu^{II} species and re-formation of one Cu^I complex. This suggests that both Cu^{II} species are active and converted to the same Cu^I species. The ratio of those two species changes with subsequent oxidation and reduction cycles, since the dimer nearly completely vanishes (*i.e.* splits) and the monomer governs sole catalytic activity towards the end. Those Cu^{II} dimers are EPR silent, since the EPR spectra lack any features of an S = 3 spin system. The Cu^{II} monomeric species resulting from the cleaving of the Cu^{II} dimers are also likely EPR silent, which was tentatively attributed to Cu^{II}-TEMPO adduct formation. The linear course of the BA reaction rates during four repeated redox cycles decreased slightly in the order of $k_1 > k_2 > k_3 > k_4$. Those findings have not been reported before, and we attributed them to deactivation processes during the reaction as *e.g.* overoxidation of BA to BzOOH, which can provoke the decomposition of active (bpy)$Cu^{II}(NMI)_2$–OR or Cu^{II}-$(OH)_2$-Cu^{II} species. As experimentally confirmed, the BA formation is effectively suppressed when adding only 1.0 equiv. of BzOOH to the active catalyst solution containing (bpy)$Cu^{I}(NMI)_2$ and BzOH. Hence, a new catalytic cycle was proposed based on those findings incorporating both monomeric and dimeric Cu^{II} species.

In summary, it could be shown that *operando* coupled spectroscopic techniques, in particular, the EPR/UV-vis/ATR-IR coupling and the newly developed EPR/UV-vis/ATR-IR/XANES/EXAFS technique are versatile and important tools for elucidating mechanistic pathways. In the present example of the Cu/TEMPO catalyzed aerobic alcohol oxidation, significant ligand/additive effects were observed and structural information of involved $Cu^{I/II}$ species could be gathered and subsequently interpreted within the context of contemporary and past literature. Several issues, however, are still unclear or still not properly understood.

It might be wise to use the newly developed 4-in-1 coupling to investigate *e.g.* the pristine interaction between the TEMPO radical and $Cu^{I/II}$ complex species in more detail. Moreover, when using the Cu/4-DMAP catalytic system additional studies are required *e.g.* for elucidating the exact nature of the EPR-silent $Cu^{I/II}$ species which are formed during the oxidation and reduction processes similar to the presented application of the EPR/UV-vis/ATR-IR/XANES/EXAFS coupling onto Stahl's system.

Even more, that particular method coupling offers new possibilities for unravelling multiple mechanistic aspects in the broad field of biochemistry (*e.g.* monitoring the actives sites of enzymes) and biomimetic catalyst design. Furthermore, from our extensive studies regarding the oxidation and reduction behavior depending on used ligands, benefits could be derived for the tailoring of ligands. Specifically designed ligands might combine several and more balanced electronic and steric effects, hence leading to more active catalytic systems.

6. REFERENCES

1. Tojo, G.; Fernandez, M., *Oxidations of Alcohols to Aldehydes and Ketones*. Springer, New York, **2006**.
2. Norman, R. O. C., *Principles of Organic Synthesis*. CRC Press: **2017**; Chapter 19.
3. Das, O.; Paine, T. K., *Dalton Trans.* **2012,** *41*, 11476.
4. Tojo, G.; Fernandez, M., *Oxidation of Primary Alcohols to Carboxylic Acids*. 1st ed.; Springer, New York, **2007**.
5. Thomas, J. M.; Raja, R., *Annu. Rev. Mater. Sci.* **2005,** *35*, 315-350.
6. Stahl, S. S.; Alsters, P. L., *Liquid Phase Aerobic Oxidation Catalysis: Industrial Applications and Academic Perspectives*. Wiley, **2016**.
7. Cao, Q.; Dornan, L. M.; Rogan, L.; Hughes, N. L.; Muldoon, M. J., *Chem. Commun.* **2014,** *50*, 4524.
8. Campbell, A. N.; Stahl, S. S., *Acc. Chem. Res.* **2012,** *45*, 851.
9. Elstner, E. F., *Annu Rev Plant Biol.* **1982,** *33*, 73.
10. Elwell, C. E.; Gagnon, N. L.; Neisen, B. D.; Dhar, D.; Spaeth, A. D.; Yee, G. M.; Tolman, W. B., *Chem. Rev.* **2017,** *117*, 2059.
11. Lewis, E. A.; Tolman, W. B., *Chem. Rev.* **2004,** *104*, 1047.
12. Mirica, L. M.; Ottenwaelder, X.; Stack, T. D. P., *Chem. Rev.* **2004,** *104*, 1013.
13. Schultz, M. J.; Sigman, M. S., *Tetrahedron* **2006,** *62*, 8227.
14. Zhang, G.; Yang, C.; Liu, E.; Li, L.; Golen, J. A.; Rheingold, A. L., *RSC Adv.* **2014,** *4*, 61907.
15. Steves, J. E.; Stahl, S. S., *J. Am. Chem. Soc.* **2013,** *135*, 15742.
16. Hoover, J. M.; Stahl, S. S., *J. Am. Chem. Soc.* **2011,** *133*, 16901.
17. Rabeah, J.; Bentrup, U.; Stößer, R.; Brückner, A., *Angew Chem Int Ed Engl.* **2015,** *54*, 11791.
18. Ryland, B. L.; Stahl, S. S., *Angew Chem Int Ed Engl.* **2014,** *53*, 8824.
19. Hoover, J. M.; Ryland, B. L.; Stahl, S. S., *ACS Catal.* **2013,** *3*, 2599.
20. Hoover, J. M.; Ryland, B. L.; Stahl, S. S., *J. Am. Chem. Soc.* **2013,** *135*, 2357.
21. W., B.; J., G. C., *Recl. Trav. Chim. Pays-Bas* **1966,** *85*, 221.
22. W., B.; J., G. C., *Recl. Trav. Chim. Pays-Bas* **1966,** *85*, 257.
23. W., B.; J., G. C., *Recl. Trav. Chim. Pays-Bas* **1966,** *85*, 242.
24. Vélez, R. P.; Ellmers, I.; Huang, H.; Bentrup, U.; Schünemann, V.; Grünert, W.; Brückner, A., *J. Catal.* **2014,** *316*, 103.
25. Brückner, A., *Chem. Commun.* **2005,** 13, 1761.
26. Brückner, A.; Kondratenko, E., *Catal. Today* **2006,** *113*, 16.
27. Grabow, K.; Bentrup, U., *ACS Catal.* **2014,** *4*, 2153.

28. Ryland, B. L.; McCann, S. D.; Brunold, T. C.; Stahl, S. S., *J. Am. Chem. Soc.* **2014,** *136*, 12166.

29. Gamez, P.; Arends, I. W. C. E.; Sheldon, R. A.; Reedijk, J.,. *Adv. Synth. Catal.* **2004,** *346*, 805.

30. Semmelhack, M. F.; Schmid, C. R.; Cortes, D. A.; Chou, C. S., *J. Am. Chem. Soc.* **1984,** *106*, 3374.

31. Walroth, R. C.; Miles, K. C.; Lukens, J. T.; MacMillan, S. N.; Stahl, S. S.; Lancaster, K. M., *J. Am. Chem. Soc.* **2017,** *139*, 13507.

32. Kumpulainen, E. T. T.; Koskinen, A. M. P., *Chem.-Eur. J.* **2009,** *15*, 10901.

33. Liu, E.; Zhang, Y. Z.; Li, L.; Yang, C.; Fettinger, J. C.; Zhang, G., *Polyhedron* **2015,** *99*, 223.

34. Ciriminna, R.; Pandarus, V.; Béland, F.; Xu, Y.-J.; Pagliaro, M., *Org. Process Res. Dev.* **2015,** *19*, 1554.

35. Fetizon, M.; Balogh, V.; Golfier, M., *The Journal of organic chemistry* **1971,** *36*, 1339.

36. De Graauw, C.; Peters, J.; Van Bekkum, H.; Huskens, J., *Synthesis* **1994,** *1994*, 1007.

37. Karoui, H.; Moigne, F. L.; Ouari, O.; Tordo, P., Nitroxide Radicals: Properties, Synthesis and Applications. In *Stable Radicals*, Hicks, R. G., Ed. **2010**.

38. Hicks, R. G., *Org. Biomol. Chem.* **2007,** *5*, 1321.

39. Frémy, E., *Ann. Chim. Phys.* **1845,** *15*.

40. G., K. R.; Eric, K.; Thomas, M., *Concept Magn. Reson.* **1992,** *4*, 145.

41. Teuber, H. J.; Jellinek, G.,. *Naturwissenschaften* **1951,** *38*, 259.

42. Lebedev, O. L.; Kazarnovskii, S. N., *Zhur. Obshch. Khim.* **1960,** *30*, 1631.

43. Souza, M. V. N. D., *Mini-Rev. Org. Chem.* **2006,** *3*, 155.

44. Golubev, V. A.; Rozantsev, É. G.; Neiman, M. B., *Bull. Acad. Sci. USSR, Div. Chem. Sci.* **1965,** *14*, 1898.

45. Lucio Anelli, P.; Biffi, C.; Montanari, F.; Quici, S., *J. Org. Chem* **1987,** *52*, 2559.

46. Gerken, J. B.; Stahl, S. S., *ACS Cent. Sci.* **2015,** *1*, 234.

47. Armstrong David, A.; Huie Robert, E.; Lymar, S.; Koppenol Willem, H.; Merényi, G.; Neta, P.; Stanbury David, M.; Steenken, S.; Wardman, P., Standard electrode potentials involving radicals in aqueous solution: inorganic radicals. In *BioInorganic Reaction Mechanisms*, **2013**, Vol. *9*, p 59.

48. Hodgson, J. L.; Namazian, M.; Bottle, S. E.; Coote, M. L., *J. Phys. Chem. A* **2007,** *111*, 13595.

49. Liu, R.; Liang, X.; Dong, C.; Hu, X., Transition-Metal-Free: *J. Am. Chem. Soc.* **2004,** *126*, 4112.

50. Martell, A. E.; Sawyer, D. T., Oxygen Complexes and Oxygen Activation by Transition Metals. **1988**, pp. 129 ff.

51. Kumar, D.; Thiel, W.; de Visser, S. P., *J. Am. Chem. Soc.* **2011,** *133*, 3869.

52. Whittaker, M. M.; Whittaker, J. W., *Biophys. J.* **1993,** *64*, 762.

53. Kroneck, P. M. H.; Vortisch, V.; Hemmerich, P., *Eur J Biochem* **1980,** *109*, 603.

54. Chaudhuri, P.; Hess, M.; Flörke, U.; Wieghardt, K.,. *Angew Chem Int Ed Engl.* **1998,** *37*, 2217.

55. Solomon, E. I.; Heppner, D. E.; Johnston, E. M.; Ginsbach, J. W.; Cirera, J.; Qayyum, M.; Kieber-Emmons, M. T.; Kjaergaard, C. H.; Hadt, R. G.; Tian, L., *Chem. Rev.* **2014,** *114*, 3659.

56. Festa, R. A.; Thiele, D. J., *Curr Biol* **2011,** *21*, 877.

57. Wang, Y.; DuBois, J. L.; Hedman, B.; Hodgson, K. O.; Stack, T. D. P., *Science* **1998,** *279*, 537.

58. Gamez, P.; Koval, I. A.; Reedijk, J., *Dalton Trans.* **2004,** 24, 4079.

59. Avigad, G.; Amaral, D.; Asensio, C.; Horecker, B. L., *J. Biol. Chem.* **1962,** *237*, 2736.

60. Whittaker, J. W., *Galactose oxidase.* In *Advances in Protein Chemistry*, Academic Press: **2002**, Vol. 60, pp. 1-49.

61. Brackman, W., *Nature* **1966,** *211*, 818.

62. Tretyakov, V. P.; Chudaev, V. V.; Zimtseva, G. P., *Ukr. Khim. Zh. (Russ. Ed.)* **1985,** *51*, 942.

63. Betzemeier, B.; Cavazzini, M.; Quici, S.; Knochel, P., *Tetrahedron Lett.* **2000,** *41*, 4343.

64. Ragagnin, G.; Betzemeier, B.; Quici, S.; Knochel, P., *Tetrahedron* **2002,** *58*, 3985.

65. Semmelhack, M. F.; Schmid, C. R.; Cortés, D. A., *Tetrahedron Lett.* **1986,** *27*, 1119.

66. Gamez, P.; Arends, I. W. C. E.; Reedijk, J.; Sheldon, R. A., *Chem. Commun.* **2003,** 2414.

67. Sheldon, R. A.; Arends, I. W. C. E.; ten Brink, G. J.; Dijksman, A., *Acc. Chem. Res.* **2002,** *35*, 774.

68. Hill, N. J.; Hoover, J. M.; Stahl, S. S., *J. Chem. Educ.* **2013,** *90*, 102.

69. Steves, J. E.; Stahl, S. S., *J. Org. Chem.* **2015**, *80*, 11184.

70. Greene, J. F.; Hoover, J. M.; Mannel, D. S.; Root, T. W.; Stahl, S. S., *Org. Process Res. Dev.* **2013,** *17*, 1247.

71. Hoover, J. M.; Steves, J. E.; Stahl, S. S., *Nat. Protoc.* **2012,** *7*, 1161.

72. Dijksman, A.; Arends, I. W. C. E.; Sheldon, R. A., *Org. Biomol. Chem.* **2003,** *1*, 3232.

73. Semmelhack, M. F.; Chou, C. S.; Cortes, D. A., *J. Am. Chem. Soc.* **1983,** *105*, 4492.

74. Semmelhack, M. F.; Schmid, C. R., *J. Am. Chem. Soc.* **1983,** *105*, 6732.

75. Yuan, B.; He, R.; Shen, W.; Huang, C.; Li, M., *J. Org. Chem.* **2015,** *80*, 6553.

76. Liu, H.; Ramella, D.; Yu, P.; Luan, Y., *RSC Adv.* **2017,** *7*, 22353.

77. M., R. B.; Xuan, J.; J., W. C.; H., N. N.; J., M. M.; Virgil, P., *J. Polym. Sci. Pol. Chem.,* **2009,** *47*, 5606.

78. Dance, J. M.; Gambardella, M. T. D. P.; Santos, R. H. D. A.; Medina, E.; Manrique, F. G.; Palacios, M. S., *Inorg. Chim. Acta* **1989,** *162*, 239.

79. Cramer, C. J.; Tolman, W. B., *Acc. Chem. Res.* **2007,** *40*, 601.

80. Cooper, D.; Plane, R. A., *Inorg. Chem.***1966,** *5*, 2209.

81. Masui, H.; Lever, A. B. P.; Auburn, P. R., *Inorg. Chem.* **1991,** *30*, 2402.

82. Mueller, E.; Piquet, C.; Bernardinelli, G.; Williams, A. F., *Inorg. Chem.* **1988,** *27*, 849..

83. Kitajima, N.; Moro-oka, Y., *Chem. Rev.* **1994,** *94*, 737.

84. Addison, A. W.; Rao, T. N.; Reedijk, J.; van Rijn, J.; Verschoor, G. C., *J. Chem. Soc., Dalton Trans.* **1984,** 7, 1349.

85. Kivelson, D.; Neiman, R., *J. Chem. Phys.* **1961,** *35*, 149.

86. Ji-Cai, F.; Zhi-Cai, S.; Jun, L.; Xiu-Hong, L.; Yang, L., *J. Phys. Org. Chem.* **2008,** *21*, 945.

87. Bandini, M.; Tragni, M., *Org. Biomol. Chem.* **2009,** *7*, 1501.

88. Donoghue, P. J.; Gupta, A. K.; Boyce, D. W.; Cramer, C. J.; Tolman, W. B., *J. Am. Chem. Soc.* **2010,** *132*, 15869.

89. Iovan, D. A.; Wrobel, A. T.; McClelland, A. A.; Scharf, A. B.; Edouard, G. A.; Betley, T. A., *Chem. Commun.* **2017,** *53*, 10306.

90. Mahroof-Tahir, M.; Murthy, N. N.; Karlin, K. D.; Blackburn, N. J.; Shaikh, S. N.; Zubieta, J., *Inorg. Chem.* **1992,** *31*, 3001.

91. Biswas, S.; Dutta, A.; Debnath, M.; Dolai, M.; Das, K. K.; Ali, M., *Dalton Trans.* **2013,** *42*, 13210.

92. Deng, K.; Yang, J.; Zhu, Q., *J. Chem. Phys.* **2000,** *113*, 7867.

93. Gong, Y.; Zhou, M.; Tian, S. X.; Yang, J., *J. Phys. Chem. A.* **2007,** *111*, 6127.

94. Li, S.; Cheng, L.; Wu, Q.; Zhang, Q.; Yang, J.; Liu, J., *Catalysts* **2017,** *7*, 264.

95. Alberto, M.; Francesca, O. M.; Waldemar, A.; Anatoly, B.; Steffen, J.; J., T. N., *Helv. Chim. Acta* **2006,** *89*, 2441.

96. Bañares, M. A., *Catal. Today* **2005,** *100*, 71.

97. Bañares, M. A.; Wachs, I. E., *J. Raman Spectrosc.* **2002,** *33*, 359.

98. Das, S.; Addis, D.; Knöpke, L. R.; Bentrup, U.; Junge, K.; Brückner, A.; Beller, M., *Angew. Chem., Int. Ed.* **2011,** *50*, 9180.

99. Prakash, C. R.; Raja, S., *Mini-Rev. Med. Chem.* **2012,** *12*, 98.

100. Mellmann, D.; Barsch, E.; Bauer, M.; Grabow, K.; Boddien, A.; Kammer, A.; Sponholz, P.; Bentrup, U.; Jackstell, R.; Junge, H.; Laurenczy, G.; Ludwig, R.; Beller, M., *Chem. Eur. J* **2014,** *20*, 13589.

101. Tromp, M.; van Strijdonck, G. P.; van Berkel, S. S.; van den Hoogenband, A.; Feiters, M. C.; de Bruin, B.; Fiddy, S. G.; van der Eerden, A. M.; van Bokhoven, J. A.; van Leeuwen, P. W., *Organometallics* **2010,** *29*, 3085.

102. Tromp, M. *Developments of time-resolved XAFS spectroscopy techniques-applications in homogeneous catalysis*. Universiteit Utrecht, *PhD thesis*, **2004**.

103. Tromp, M.; Sietsma, J. R. A.; van Bokhoven, J. A.; van Strijdonck, G. P. F.; van Haaren, R. J.; van der Eerden, A. M. J.; van Leeuwen, P. W. N. M.; Koningsberger, D. C., *Chem. Commun.* **2003,** 1, 128.

104. Briois, V.; Fontaine, C. L.; Belin, S.; Barthe, L.; Th, M.; Pinty, V.; Carcy, A.; Girardot, R.; Fonda, E., *J. Phys. Conf. Ser.* **2016,** *712*, 012149.

105. Rabeah, J.; Adomeit, S.; Brückner, A. *Probe setup for combined EPR and XAS measurements*. Vol. PCT/EP2018/053047, **2018**.

106. Lesage, C.; Dervers, E.; Legens, C.; Fernandes, G.; Roudenko, O.; Briois, V., *Catal. Today* **2018,** *submitted.*

107. Ravel, B.; Newville, M., *J. Synchrotron Radiat.* **2005,** *12*, 537.

108. Newville, M., *J. Synchrotron Radiat.* **2001,** *8*, 322.

109. Clegg, W.; Nicholson, J. R.; Collison, D.; Garner, C. D., *Acta Crystallogr. C* **1988,** *44*, 453.

110. Jain, R.; Gibson, T. J.; Mashuta, M. S.; Buchanan, R. M.; Grapperhaus, C. A., *Dalton Trans.* **2016,** *45*, 18356.

111. Wannarit, N.; Pakawatchai, C.; Mutikainen, I.; Costa, R.; Moreira, I. d. P. R.; Youngme, S.; Illas, F., *Phys. Chem. Chem. Phys.* **2013,** *15*, 1966.

112. Martini, A.; Borfecchia, E.; Lomachenko, K. A.; Pankin, I. A.; Negri, C.; Berlier, G.; Beato, P.; Falsig, H.; Bordiga, S.; Lamberti, C.,. *Chem. Sci.* **2017,** *8*, 6836.

113. Rochet, A.; Baubet, B.; Moizan, V.; Pichon, C.; Briois, V., *C. R. Chim.* **2016,** *19*, 1337.

114. Cassinelli, W. H.; Martins, L.; Passos, A. R.; Pulcinelli, S. H.; Santilli, C. V.; Rochet, A.; Briois, V., *Catal. Today* **2014,** *229*, 114.

115. Voronov, A.; Urakawa, A.; Beek, W. v.; Tsakoumis, N. E.; Emerich, H.; Rønning, M., *Anal. Chim. Acta* **2014,** *840*, 20.

116. Garrido, M.; Rius, F. X.; Larrechi, M. S., *Anal. Bioanal. Chem.* **2008,** *390*, 2059.

117. de Juan, A.; Jaumot, J.; Tauler, R., *Anal. Methods* **2014,** *6*, 4964.

118. Jaumot, J.; de Juan, A.; Tauler, R., *Chemom. Intell. Lab. Syst.* **2015,** *140*, 1.

119. Adomeit, S.; Rabeah, J.; Surkus, A. E.; Bentrup, U.; Brückner, A., *Inorg. Chem.* **2017,** *56*, 684.

120. Carlsson, B.; Wettermark, G., *Z. Naturforsch. A* **1976,** *31*, 297.

121. James, B. R.; Williams, R. J. P., *J. Chem. Soc.,* **1961,** *0*, 2007.

122. Johnson, D. K.; Stevenson, M. J.; Almadidy, Z. A.; Jenkins, S. E.; Wilcox, D. E.; Grossoehme, N. E., *Dalton Trans.* **2015,** *44*, 16494.

123. Zamudio, W.; García, A.-M.; Spodine, E., *Transit. Met. Chem.* **1983,** *8*, 69.

124. Kitagawa, S.; Munakata, M.; Higashie, A., *Inorg. Chim. Acta* **1982,** *59*, 219.

125. Zamudio, W.; García, A. M., *Transit. Met. Chem.* **1986,** *11*, 422.

126. Kitagawa, S.; Munakata, M., *Inorg, Chem.* **1981,** *20*, 2261.

127. Yokoyama, Y.; Nakatani, K., *Photon-Working Switches*. Springer Japan, **2017**.

128. Williams, R. J. P., *J. Chem. Soc.* **1955,** 0, 137.

129. Weizman, H.; Tor, Y., *J. Am. Chem. Soc.* **2001,** *123*, 3375.

130. Rubino, J. T.; Franz, K. J., *J. Inorg. Biochem.* **2012,** *107*, 129.

131. Burke, P. J.; McMillin, D. R.; Robinson, W. R., *Inorg. Chem.* **1980,** *19*, 1211.

132. Salomon, R. G., *Copper(I) Trifluoromethanesulfonate*. In *Encyclopedia of Reagents for Organic Synthesis*, Wiley, **2005**.

133. Black, J. R.; Levason, W.; Webster, M., *Acta Crystallogr. C* **1995,** *51*, 623.

134. Jones, P. G.; Crespo, O., *Acta Crystallogr. C* **1998,** *54*, 18.

135. Pecht, I.; Anbar, M., *J. Chem. Soc. A* **1968,** *0*, 1902.

136. Sykes, A. G., *Advances in Inorganic Chemistry*, Elsevier Science, **1990**, 34, pp. 30 ff.

137. Proskurnin, M. A.; Chernysh, V. V.; Pakhomova, S. V.; Kononets, M. Y.; Smirnova, A. P.; Nedosekin, D. A., *Anal. Sci.* **2002,** *17*, i1169.

138. Pakhomova, S. V.; Proskurnin, M.; V. Chernysh, V.; Kononets, M.; K. Ivanova, E., **2001**, *56*, 910.

139. Rappoport, Z.; Marek, I., *The Chemistry of Organocopper Compounds*. Wiley, **2010**, pp. 289 ff.

140. Ishii, T.; Tsuboi, S.; Sakane, G.; Yamashita, M.; Breedlove, B. K., *Dalton Trans.* **2009,** 4, 680.

141. Atkinson, G.; Bauman Jr, J., *Inorg. Chem.* **1963,** *2*, 64.

142. Andersson Trojer, M.; Movahedi, A.; Blanck, H.; Nyden, M., *J. Chem.* **2013,** *2013*, 23.

143. Li, N. C.; White, J. M.; Doody, E., *J. Am. Chem. Soc.* **1954,** *76*, 6219.

144. Armaroli, N.; Accorsi, G.; Cardinali, F.; Listorti, A., In *Photochemistry and Photophysics of Coordination Compounds I*, Springer, **2007**, pp 69 ff..

145. Armaroli, N., *Chem. Soc. Rev* **2001,** *30*, 113.

146. Crichton, R. R., *Biological Inorganic Chemistry: An Introduction*. Elsevier Science, **2007**, pp.22-24.

147. Güntensperger, M.; Zuberbühler, A. D., *Helv. Chim. Acta* **1977,** *60*, 2584.

148. Liu, Z.; Shen, Z.; Zhang, N.; Zhong, W.; Liu, X., *Catal. Lett.* **2018**, 2709.

149. Yasuo, I.; Yasuomi, N.; Yuzo, N.; Sigeo, K., *Bull. Chem. Soc. Jpn.* **1973,** *46*, 3728.

150. Karlin, K. D.; Hayes, J. C.; Gultneh, Y.; Cruse, R. W.; McKown, J. W.; Hutchinson, J. P.; Zubieta, J., *J. Am. Chem. Soc.* **1984,** *106*, 2121.

151. Kwik, W. L.; Ang, K. P.; Chen, G., *J. Inorg. Nucl. Chem.* **1980,** *42*, 303.

152. Li, G.; Liu, L.; Wang, J.; Li, Q.-s.; Xie, Y.; King, R. B., *Transit. Met. Chem.* **2013,** *38*, 617.

153. Jabor, J. K.; Stösser, R.; Feist, M.; Neubauer, P.; Meisel, M., *Inorg. Chemi.* **2008,** *47*, 9293.

154. Frank, P.; Benfatto, M.; Hedman, B.; Hodgson, K. O., *Inorg. Chemi.* **2012,** *51*, 2086.

155. Shiga, D.; Hamano, Y.; Kamei, M.; Funahashi, Y.; Masuda, H.; Sakaguchi, M.; Ogura, T.; Tanaka, T., *J. Biol. Inorg. Chem.* **2012,** *17*, 1025.

156. Gampp, H.; Sigel, H.; Zuberbuehler, A. D., *Inorg. Chem.***1982,** *21*, 1190.

157. Robert A. Schoonheydt, F. V., Rita Baerts, Jan B. Uytterhoeven, *Clay Clay Miner.* **1979,** *27*, 269.

158. Slocik, J. M.; Ward, M. S.; Somayajula, K. V.; Shepherd, R. E., *Transit. Met. Chem.* **2001,** *26*, 351.

159. Colbran, S. B.; Paddon-Row, M. N., *J J. Biol. Inorg. Chem.* **2003,** *8*, 855.

160. Ralle, M.; Verkhovskaya, M. L.; Morgan, J. E.; Verkhovsky, M. I.; Wikström, M.; Blackburn, N. J., *Biochemistry* **1999,** *38*, 7185.

161. Costa, H. S.; Santos, H.; Turner, D. L.; Xavier, A. V., *Eur. J. Biochem.* **1992,** *208*, 427.

162. H., K. P. M.; Volker, V.; Peter, H., *Eur. J. Biochem.* **1980,** *109*, 603.

163. Hathaway, B. J.; Billing, D. E., *Coord. Chem. Rev.* **1970,** *5*, 143.

164. Reedijk, J., *Transit. Met. Chem.* **1981,** *6*, 195.

165. Mesu, J. G.; Visser, T.; Soulimani, F.; Weckhuysen, B. M., *Vib. Spectrosc.* **2005,** *39*, 114.

166. Patricia, L.; Kristina, K.; Alexander, H.; Thomas, S.; Isabella, S.; Anne, T.; Claudia, W.; Roland, S.; Kai, S.; Matthias, B.; Maximilian, D.; Ivana, I.-B.; Sonja, H.-P., *Chem. Eur. J.* **2017,** *23*, 12171.

167. Comba, P.; Haaf, C.; Helmle, S.; Karlin, K. D.; Pandian, S.; Waleska, A., *Inorg. Chem.* **2012,** *51*, 2841.

168. Krishna, M. C.; Grahame, D. A.; Samuni, A.; Mitchell, J. B.; Russo, A., *Proc. Natl. Acad. Sci. U.S.A.* **1992,** *89*, 5537.

169. Takeshita, K.; Okazaki, S.; Itoda, A., *Anal. Chem.* **2013,** *85*, 6833.

170. Samuni, A.; Goldstein, S.; Russo, A.; Mitchell, J. B.; Krishna, M. C.; Neta, P., *J. Am. Chem. Soc.* **2002,** *124*, 8719.

171. Andersson, M.; Hedin, J.; Johansson, P.; Nordström, J.; Nydén, M., *J. Phys. Chem. A* **2010,** *114*, 13146.

172. Welleman, J. A.; Hulsbergen, F. B.; Verbiest, J.; Reedijk, J., *J. Inorg. Nucl. Chem.* **1978,** *40*, 143.

173. Katritzky, A. R.; Ramsden, C. A.; Joule, J. A.; Zhdankin, V. V., 3.4 - *Reactivity of Five-membered Rings with Two or More Heteroatoms.* In *Handbook of Heterocyclic Chemistry (3rd Edition)*, Elsevier, Amsterdam, **2010,** pp. 473-604.

174. Pagni, R., *Modern Physical Organic Chemistry* (Eric V. Anslyn and Dennis A. Dougherty). *J. Chem. Educ.* **2006,** *83*, p. 387.

175. Bean, G. P., *The Synthesis of 1H-Pyrroles.* In *Chemistry of Heterocyclic Compounds*, Wiley,: **2008**, pp. 105-294.

176. Worth, G. A.; King, P. M.; Richards, W. G., *Biochim. Biophys. Acta, Gen. Subj.* **1989,** *993*, 134.

177. Reddy, G. S.; Hobgood, R. T.; Goldstein, J. H., *J. Am. Chem. Soc.* **1962,** *84*, 336.

178. Paiva, A. C. M.; Juliano, L.; Boschcov, P., *J. Am. Chem. Soc.* **1976,** *98*, 7645.

179. Hofmann, K., *Imidazole and Its Derivatives.* Wiley, **2009**, *1*, pp.13-15.

180. Green, H.; Day, A. R., *J. Am. Chem. Soc.* **1942,** *64*, 1167.

181. Mohr, P.; Scheler, W.; Schumann, H.; Müller, K., *Eur. J. Biochem.* **1967,** *3*, 158.

182. Kadish, K. M.; Smith, K. M.; Guilard, R., *The Porphyrin Handbook: Electron transfer.* Elsevier, **2000**, *8*, pp. 54 ff. and 117 ff.

183. Russo, N.; Salahub, D. R.; Witko, M.; Division, N. A. T. O. S. A., *Metal-Ligand Interactions: Molecular, Nano-, Micro-, and Macro-systems in Complex Environments.* Springer Netherlands, **2003**, pp. 26 ff.

184. Tondreau, G. A.; Sweigart, D. A., *Inorg. Chem.* **1984,** *23*, 1060.

185. Mohajer, D.; Karimipour, G.; Bagherzadeh, M., *New J. Chem.* **2004,** *28*, 740.

186. Zongwan, M.; Degang, F.; Qinwei, H.; Wenxia, T.; Kaibei, Y., *Polyhedron* **1993,** *12*, 1465.

187. Jancso, A.; Torok, I.; Korecz, L.; Rockenbauer, A.; Gajda, T., *J. Chem. Soc., Dalton Trans.* **2002,** 13, 2601.

188. Katritzky, A. R.; Ramsden, C. A.; Joule, J. A.; Zhdankin, V. V., *Handbook of Heterocyclic Chemistry*. Elsevier Science, **2010**, pp. 486-492.

189. Wang, W.; Wang, S.; Xie, X.; lv, Y.; Ramani, V., *Int. J. Hydrog. Energy* **2014,** *39*, 14355.

190. Lenarcik, B.; Ojczenasz, P., *J. Heterocyclic Chem.* **2002,** *39*, 287.

191. Tarley, C. R. T.; Corazza, M. Z.; Somera, B. F.; Segatelli, M. G., *J. Colloid Interface Sci.* **2015,** *450*, 254.

192. Bales, B. L.; Meyer, M.; Smith, S.; Peric, M., *J. Phys. Chem. A* **2009,** *113*, 4930.

193. Strothkamp, K. G.; Lippard, S. J., *Acc. Chem. Res.* **1982,** *15*, 318.

194. Ali-Torres, J.; Rodriguez-Santiago, L.; Sodupe, M., *Phys. Chem. Chem. Phys.* **2011,** *13*, 7852.

195. Ji, H.-F.; Zhang, H.-Y., *Chin. J. Chem.* **2006,** *24*, 822.

196. Sundberg, R. J.; Martin, R. B., *Chem. Rev.* **1974,** *74*, 471.

197. Bauman, J. E.; Wang, J. C., *Inorg. Chem.* **1964,** *3*, 368.

198. Török, I.; Surdy, P.; Rockenbauer, A.; Korecz Jr, L.; Anthony A. Koolhaas, G. J.; Gajda, T., *J. Inorg. Biochem.* **1998,** *71*, 7.

199. Hathcock, D.; Morris, J.; Madden, J.; Slattery, S. J., *Chem Educ.* **1997,** *2*, 1.

200. Reimann, S.; Ehlers, P.; Petrosyan, A.; Kohse, S.; Spannenberg, A.; Surkus, A. E.; Ghochikyan, T. V.; Saghyan, A. S.; Lochbrunner, S.; Kühn, O.; Ludwig, R.; Langer, P., *Adv. Synth. Catal.* **2014,** *356*, 1987.

201. L'Her, M.; Pondaven, A., *104 - Electrochemistry of Phthalocyanines A2* - In *The Porphyrin Handbook*, Smith, K. M.; Guilard, R., Eds. Academic Press, Amsterdam, **2003**, pp. 117-169.

202. Koning, C. E.; Challa, G.; Hulsbergen, F. B.; Reedijk, J., *J. Mol. Catal.* **1986,** *34*, 355.

203. Verlaan, J. P. J.; Alferink, P. J. T.; Challa, G., *J. Mol. Catal.* **1984,** *24*, 235.

204. Jantzi, K. L.; Wiltrakis, S.; Wolf, L.; Weber, A.; Cardinal, J.; Krieter, K., *J. Chem. Educ.* **2011,** *88*, 328.

205. Roberto, D.; Ugo, R.; Bruni, S.; Cariati, E.; Cariati, F.; Fantucci, P.; Invernizzi, I.; Quici, S.; Ledoux, I.; Zyss, J., *Organometallics* **2000,** *19*, 1775.

206. Cartier, J. P.; Sandorfy, C., *Can. J. Chem.* **1963,** *41*, 2759.

207. Wada, A.; Honda, Y.; Yamaguchi, S.; Nagatomo, S.; Kitagawa, T.; Jitsukawa, K.; Masuda, H., *Inorg. Chem.* **2004,** *43*, 5725.

208. Libus, W.; Hoffmann, S. K.; Kluczkowski, M.; Twardowska, H., *Inorg. Chem.* **1980,** *19*, 1625.

209. Scholl, H. J.; Huettermann, J., *J. Phys. Chem. A* **1992,** *96*, 9684.

210. Romanowski, S. M. d. M.; Tormena, F.; Santos, V. A. d.; Hermann, M. d. F.; Mangrich, A. S., *J. Braz. Chem. Soc.* **2004,** *15*, 897.

211. Rabeah, J.; Dimitrov, A.; Surkus, A.-E.; Jiao, H.; Baumann, W.; Stößer, R.; Radnik, J.; Bentrup, U.; Brückner, A., *Organometallics* **2014,** *33*, 4905.

212. Dilip, C. S.; Manikandan, K.; Subahashini, D. R.; Thiruneelakandan, R., *J. Chem.* **2013,** *2013*, 16.

213. Simon, J. A.; Palke, W. E.; Ford, P. C., *Inorg. Chem.* **1996,** *35*, 6413.

214. Zhang, G.; Proni, G.; Zhao, S.; Constable, E. C.; Housecroft, C. E.; Neuburger, M.; Zampese, J. A., *Dalton Trans.* **2014,** *43*, 12313.

215. Koning, C. E.; Eshuis, J. J. W.; Viersen, F. J.; Challa, G., *React. Funct. Polym.* **1986,** *4*, 293.

216. Hathaway, B. J. *A new look at the stereochemistry and electronic properties of complexes of the copper(II) ion* In Complex Chemistry. Structure and Bonding, Springer Berlin Heidelberg, **1984**, vol. 57, pp. 55-118.

217. Brown, S. J.; Stephan, D. W.; Mascharak, P. K., *J. Am. Chem. Soc.* **1988,** *110*, 1996.

218. Praliaud, H.; Kodratoff, Y.; Coudurier, G.; Mathieu, M. V., *Spectrochim. Acta A* **1974,** *30*, 1389.

219. Sundaraganesan, N.; Kalaichelvan, S.; Meganathan, C.; Joshua, B. D.; Cornard, J., *Spectrochim. Acta A* **2008,** *71*, 898.

220. Ferrer, E. G.; Baeza, N.; Naso, L. G.; Castellano, E. E.; Piro, O. E.; Williams, P. A. M., *J. Trace Elem. Med. Biol.* **2010,** *24*, 20.

221. Goldstein, M.; Mooney, E. F.; Anderson, A.; Gebbie, H. A., *Spectrochim. Acta* **1965,** *21*, 105.

222. Wilmshurst, J. K.; Bernstein, H. J., *Can. J. Chem.* **1957,** *35*, 1183.

223. Long, D. A.; Murfin, F. S.; Thomas, E. L., *J. Chem. Soc. Faraday Trans.* **1963,** *59*, 12.

224. Long, D. A., *Infrared and Raman characteristic group frequencies. Tables and charts* George Socrates, Wiley, Chichester, 3rd Edition, **2001**, in *Journal of Raman Spectroscopy* **2004,** *35*, 905.

225. Persson, I.; Penner-Hahn, J. E.; Hodgson, K. O., *Inorg. Chem.* **1993,** *32*, 2497.

226. Wang, L.; Sun, D. P., *Mater. Sci. Forum* **2011,** *688*, 296.

227. Ahmed, A.; Lal, R. A., *Arab. J. Chem.* **2017,** *10*, S901.

228. Mo, W.; Xiong, H.; Li, T.; Guo, X.; Li, G., *J. Mol. Catal. A Chem.* **2006,** *247*, 227.

229. Bonnet, S.; Collin, J.-P.; Gruber, N.; Sauvage, J.-P.; Schofield, E. R., *Dalton Trans* **2003,** 24, 4654.

230. Cadranel, A.; Oviedo, P. S.; Alborés, P.; Baraldo, L. M.; Guldi, D. M.; Hodak, J. H., *Inorg. Chem.* **2018**, *57*, 3042.

231. Pitto-Barry, A.; Lupan, A.; Zegke, M.; Swift, T.; Attia, A. A. A.; Lord, R. M.; Barry, N. P. E., *Dalton Trans.* **2017,** *46*, 15676.

232. Bart, S. C.; Chłopek, K.; Bill, E.; Bouwkamp, M. W.; Lobkovsky, E.; Neese, F.; Wieghardt, K.; Chirik, P. J., *J. Am. Chem. Soc.* **2006,** *128*, 13901.

233. Lah, N.; Koller, J.; Giester, G.; Segedin, P.; Leban, I., *New J. Chem.* **2002,** *26*, 933.

234. van Albada, G. A.; Komaei, S. A.; Kooijman, H.; Spek, A. L.; Reedijk, J., *Inorg. Chim. Acta* **1999,** *287*, 226.

235. Lewin, A. H.; Michl, R. J.; Ganis, P.; Lepore, U.; Avitabile, G., *J. Chem. Soc. Chem. Comm.* **1971,** 21, 1400.

236. Hoffman, A.; Debefve, L.; Bendjeriou-Sedjerari, A.; Ouldchikh, S.; Bare, S. R.; Basset, J.-M.; Gates, B., *Rev. Sci. Instrum.* **2016,** *87*, 073108.

237. Walroth, R. C.; Uebler, J. W. H.; Lancaster, K. M., *Chem. Commun.* **2015,** *51*, 9864.

238. Han, B.; Yang, X.-L.; Wang, C.; Bai, Y.-W.; Pan, T.-C.; Chen, X.; Yu, W., *J. Org. Chem.* **2012,** *77*, 1136.

239. Sheldon, R. A., *Catal. Today* **2015,** *247*, 4.

240. Woolery, G. L.; Powers, L.; Winkler, M.; Solomon, E. I.; Lerch, K.; Spiro, T. G., *Biochim. Biophys. Acta, Protein Struct. Mol. Enzymol.* **1984,** *788*, 155.

241. Asato, E.; Hashimoto, S.; Matsumoto, N.; Kida, S.,. *J. Chem. Soc., Dalton Trans.* **1990,** 6, 1741.

242. Tauler, R., *Chemom. Intell. Lab. Syst.* **1995,** *30*, 133.

243. de Juan, A.; Tauler, R., *Anal. Chim. Acta* **2003,** *500*, 195.

244. Kitajima, N.; Fujisawa, K.; Fujimoto, C.; Morooka, Y.; Hashimoto, S.; Kitagawa, T.; Toriumi, K.; Tatsumi, K.; Nakamura, A., *J. Am. Chem. Soc.* **1992,** *114*, 1277.

245. D'Angelo, P.; Migliorati, V., *J. Phys. Chem. B* **2015,** *119*, 4061.

246. Zurita, D.; Gautier-Luneau, I.; Ménage, S.; Pierre, J.-L.; Saint-Aman, E., *J. Biol. Inorg. Chem.* **1997,** *2*, 46.

247. Atanasov, M.; Angelov, S.; Mayer, I., *J. Mol. Struc.-Theochem.* **1989,** *187*, 23.

248. Burk, P. L.; Osborn, J. A.; Youinou, M. T.; Agnus, Y.; Louis, R.; Weiss, R., *J. Am. Chem. Soc.* **1981,** *103*, 1273.

249. Castro, I.; Faus, J.; Julve, M.; Bois, C.; Real, J. A.; Lloret, F., *J. Chem. Soc., Dalton Trans.* **1992,** 1, 47.

250. Iron, M. A.; Szpilman, A. M., *Chem. Eur. J.* **2017,** *23*, 1368.

251. Godiksen, A.; Stappen, F. N.; Vennestrøm, P. N.; Giordanino, F.; Rasmussen, S. B.; Lundegaard, L. F.; Mossin, S., *J. Phys. Chem. C* **2014,** *118*, 23126.

252. Steinhoff, B. A.; Guzei, I. A.; Stahl, S. S., *J. Am. Chem. Soc.* **2004,** *126*, 11268.

253. Bhirud, R. G.; Srivastava, T. S., *J. Inorg. Biochem.* **1990,** *40*, 331.

254. Rossini, E.; Netz, R. R.; Knapp, E.-W., *J. Chem. Theory Comput.* **2016,** *12*, 3360.

255. Caballero, N. A.; Melendez, F. J.; Muñoz-Caro, C.; Niño, A., *Biophys. Chem.* **2006,** *124*, 155.

256. Speer, D. V., *The Chemistry and Physical Properties of Densely Charged Pyridinium Compounds.* University of California, Berkeley, **1989**.

257. Ülikool, T., *Organic Reactivity*, Tartu State University, **1986**, vol. 23.

258. Speight, J., *Lange's Handbook of Chemistry, 70th Anniversary Edition*, McGraw-Hill Companies, Incorporated, 16th ed. **2004**, p. 295.

259. Alvarez-Builla, J.; Vaquero, J. J.; Barluenga, J., *Modern Heterocyclic Chemistry, 4 Volume Set.* Wiley, **2011**, p.1468.

260. Shaw, S. A., *Development of chiral pyridine catalysts: applications in kinetic resolution and asymmetric quaternary carbon synthesis*, PhD thesis, University of Michigan, **2005**, p. 8.

261. Bansal, R. K., *Heterocyclic Chemistry*, New Age International Limited, **1999**, p. 219.

262. Ishikawa, T., *Superbases for Organic Synthesis: Guanidines, Amidines, Phosphazenes and Related Organocatalysts*, Wiley, **2009**, p. 251.

7. APPENDIX

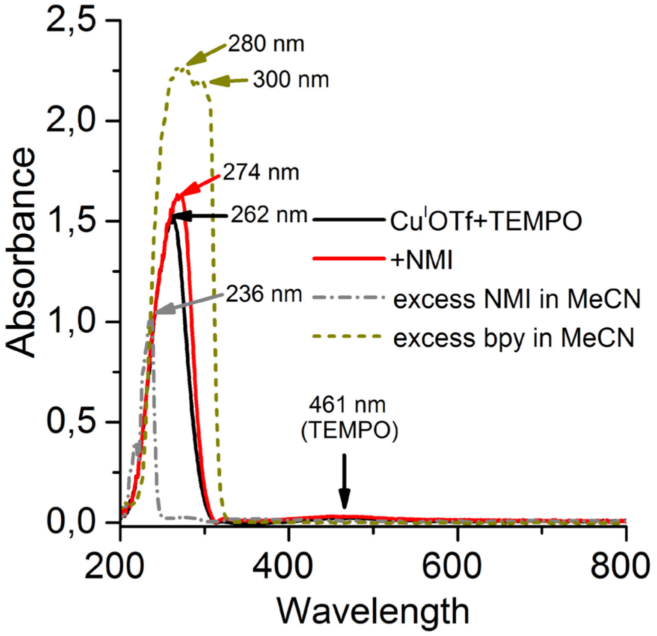

Figure A 1. Changes in UV-vis spectra of a MeCN solution containing Cu^IOTf/TEMPO (black) after addition of NMI (red) compared to an excess of the ligand solely in MeCN.

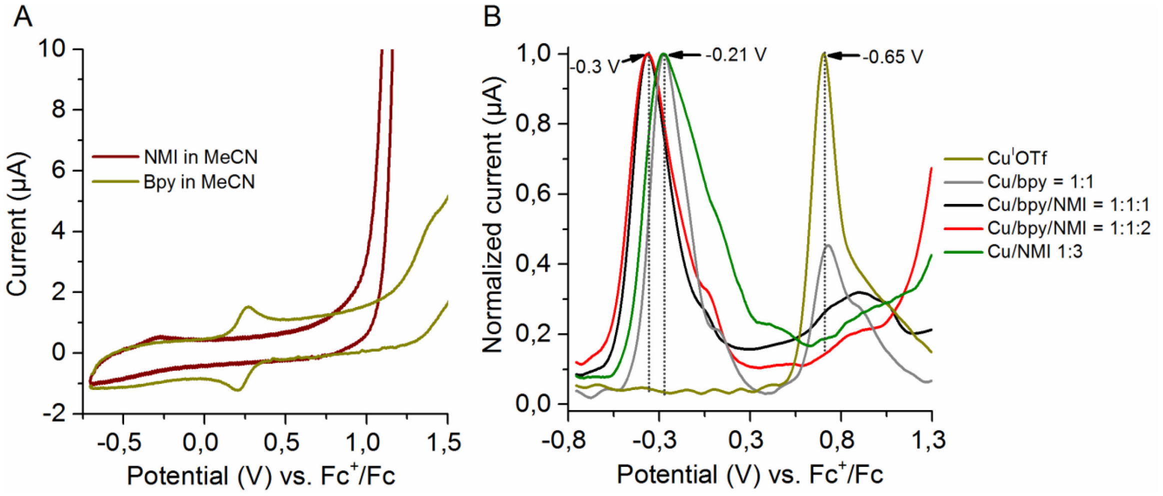

Figure A 2. CV of NMI and bpy solely in MeCN (A). DPVs of Cu^IOTf in MeCN with subsequent addition of bpy and NMI compared to Cu/NMI=1:3 (B).

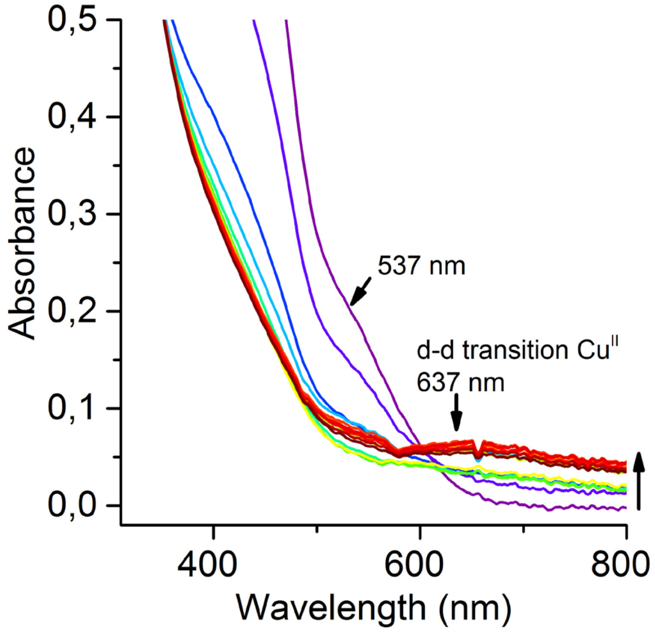

Figure A 3. Oxidation of Cu^IOTf + 1.0 equiv. bpy + 2.0 equivs. NMI+1.0 equiv. TEMPO using [Cu] = 0.005 M. Close-up of **Figure 10**.

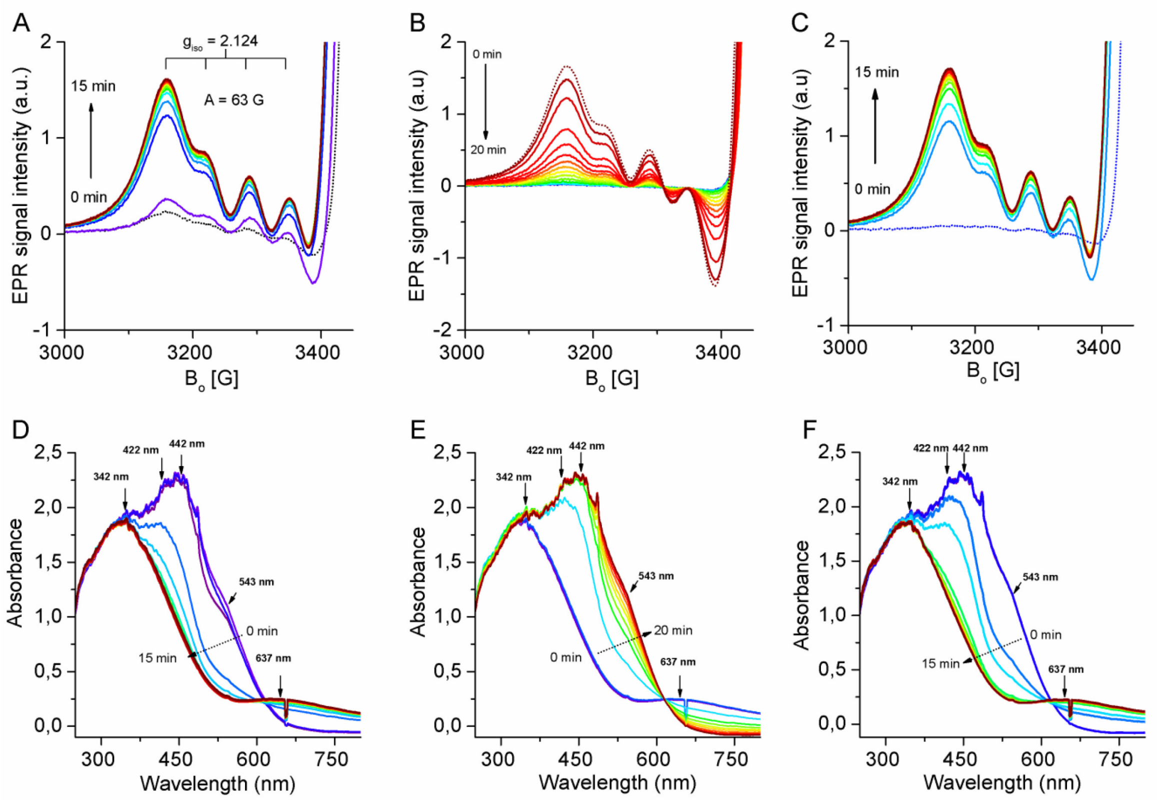

Figure A 4. Cu^IOTf (0.02 M) + 1.0 equiv. bpy + 2.0 equivs. NMI+1.0 equiv. TEMPO. The behavior of the EPR Cu^{II} signal during oxidation (A), reduction (B) and subsequent re-oxidation (C).Corresponding UV-vis spectra are shown during oxidation (D), reduction (E) and re-oxidation (F). Adapted from reference 119.

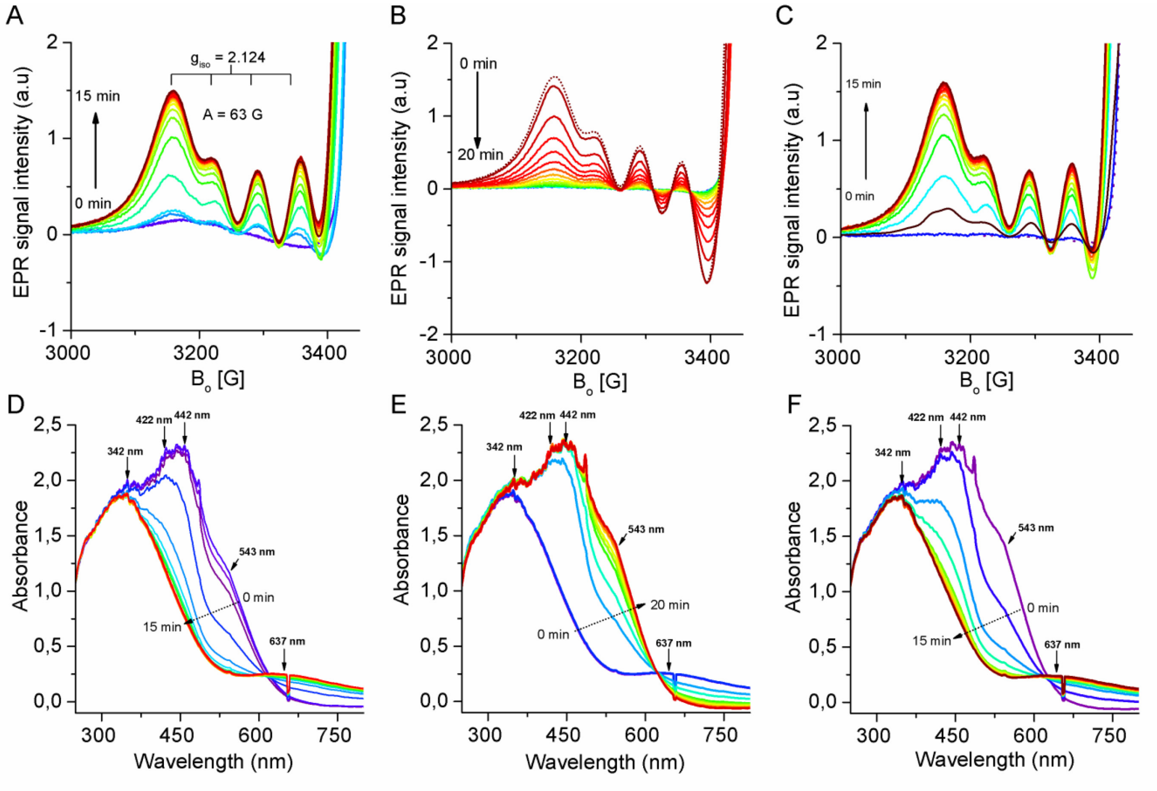

Figure A 5. Cu^{I}OTf (0.02 M) + 1.0 equiv. bpy + 1.0 equivs. NMI+1.0 equiv. TEMPO. The behavior of the EPR Cu^{II} signal during oxidation (A), reduction (B) and subsequent re-oxidation (C).Corresponding UV-vis spectra are shown during oxidation (D), reduction (E) and re-oxidation (F). Adapted from reference 119.

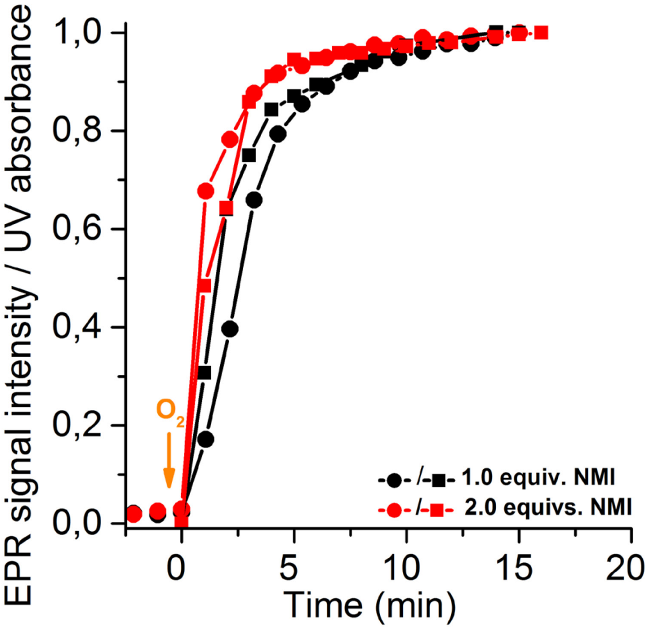

Figure A 6. Normalized EPR Cu^{II} signal intensity (dots) and Normalized UV-vis absorbance at 650 nm (squares) of the re-oxidaton of a catalytic system containing Cu^{I}OTf(0.02 M)+1.0 equiv. bpy+ 1.0 equiv. TEMPO+ 1.0 equiv. BzOH after and either 1.0 (black) or 2.0 equivs. NMI (red). Adapted from reference 119.

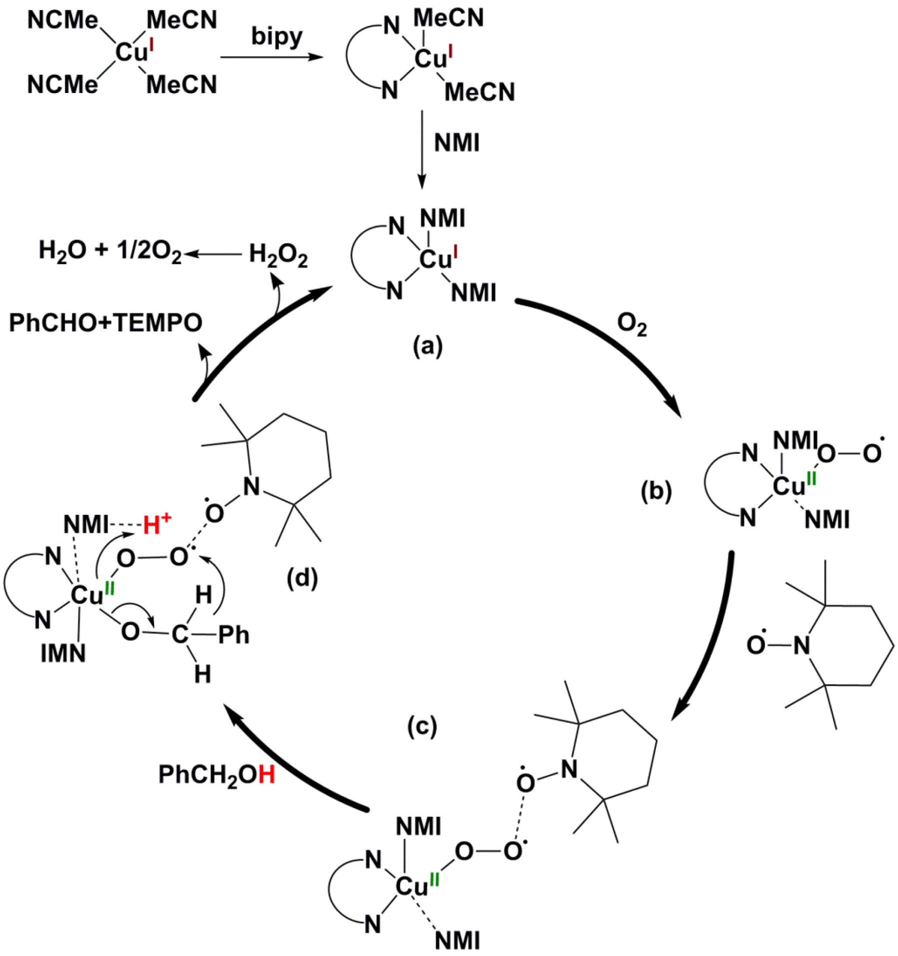

Scheme A 1. Modified reaction scheme according to the Brückner pathway[17] incorporating the effect of the NMI additive. Adapted from reference 119.

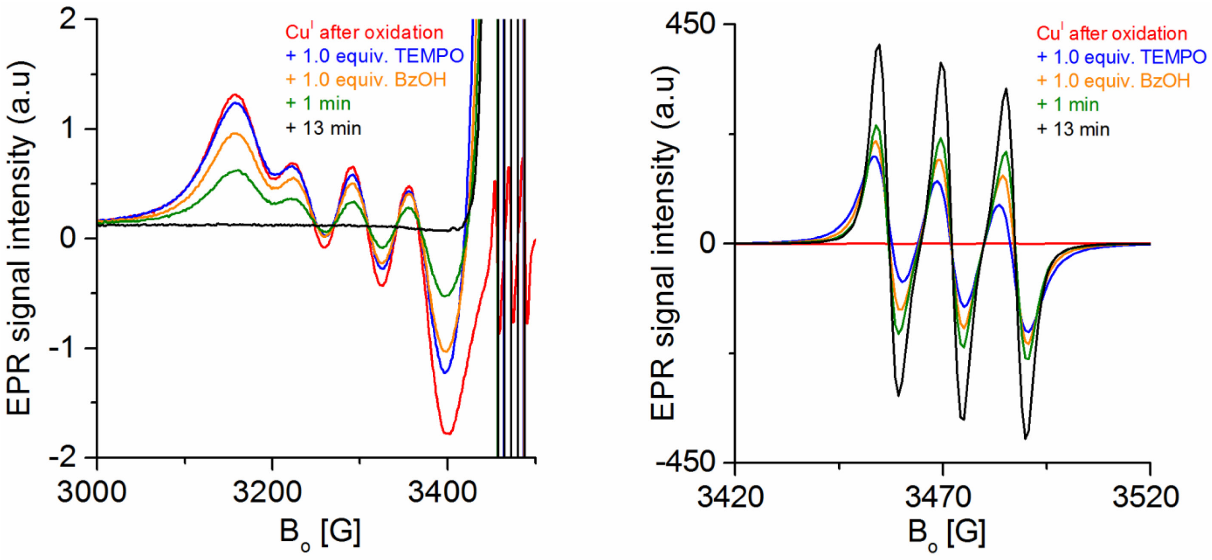

Figure A 7. Cu^{II} EPR signal (produced from $Cu^{I}OTf$ [0.02M]+1.0 equiv. bpy+1.0 equiv. NMI+O_2) under Ar and subsequent addition of 1.0 equiv. TEMPO and BzOH (A) and corresponding TEMPO EPR signal.

Table A 1. Reaction time for various (substituted) imidazoles used as ligands/additives within Cu/TEMPO catalyzed aerobic alcohol oxidation. pKa values taken from Lenarcik et al. [190] Adapted from reference 119.

Entry	Imidazole derivative	pKa value[190] (conjugated acid)	Structure	Time needed for complete conversion of BzOH to BA
1	1-methylimidazole	7.21	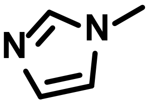	11 min
2	1-ethylimidazole	7.26	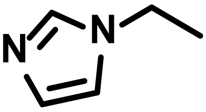	13 min
3	1-*n*-propylimidazole	7.22	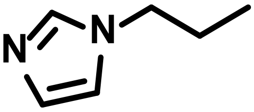	13 min
4	1-*i*-propylimidazole	–	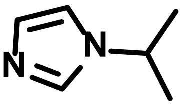	13 min
5	1-*n*-butylimidazole	7.21	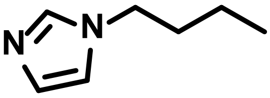	13 min
6	1-allylimidazole	–	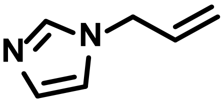	15 min
7	1-benzylimidazole	–	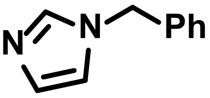	15 min
8	1-vinylimidazole	6.26[191]	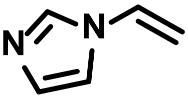	30 min

9	1-phenylimidazole	–	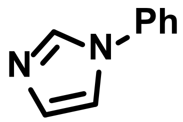	28 min
10	2-methylimidazole	7.85	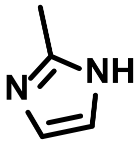	34 min
11	4(5)-methylimidazole	7.80	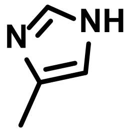	78 min
12	1,2-dimethylimidazole	8.21	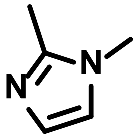	41 min
13	2,4(5)-dimethylimidazole	8.50	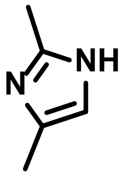	58 min
14	1-*H*-imidazole	6.95	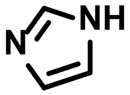	145 min

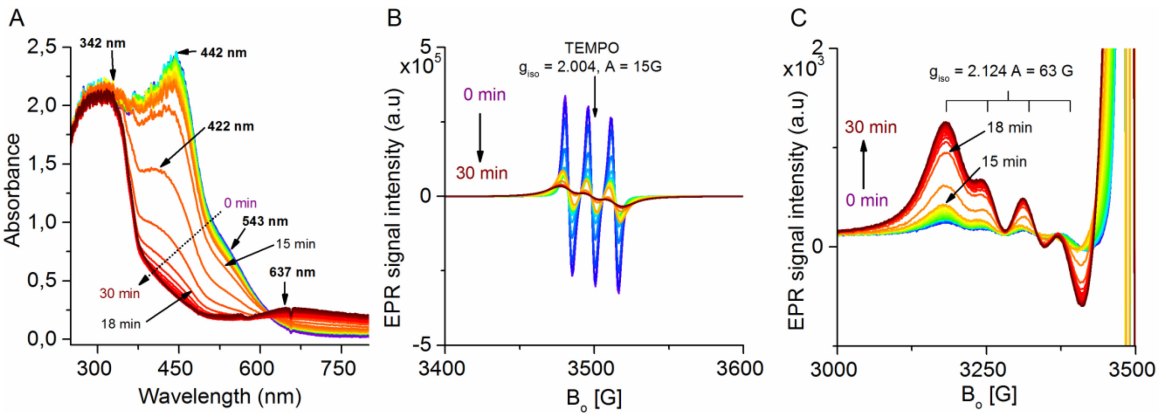

Figure A 8. Behavior of UV-vis (A) and EPR TEMPO (B) and Cu^{II} (C) features during Cu/TEMPO catalyzed aerobic alcohol oxidation using 1.0 equiv. bpy and 2.0 equivs. NMI.

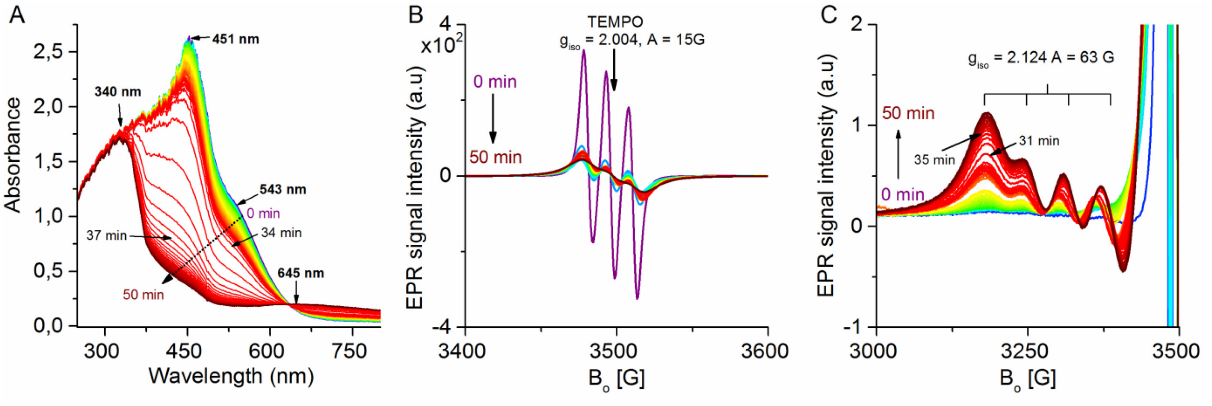

Figure A 9. Behavior of UV-vis (A) and EPR TEMPO (B) and Cu^{II} (C) features during Cu/TEMPO catalyzed aerobic alcohol oxidation using 1.0 equiv. bpy and 2.0 equivs.1-Vinylimidazole. Please note: Lower EPR signal intensity compared to the experiments using NMI and 2-methylimidazole (**Figure A8 and A10**) is due to a change in the EPR recording software but does not change the relative progression of signals.👌☺

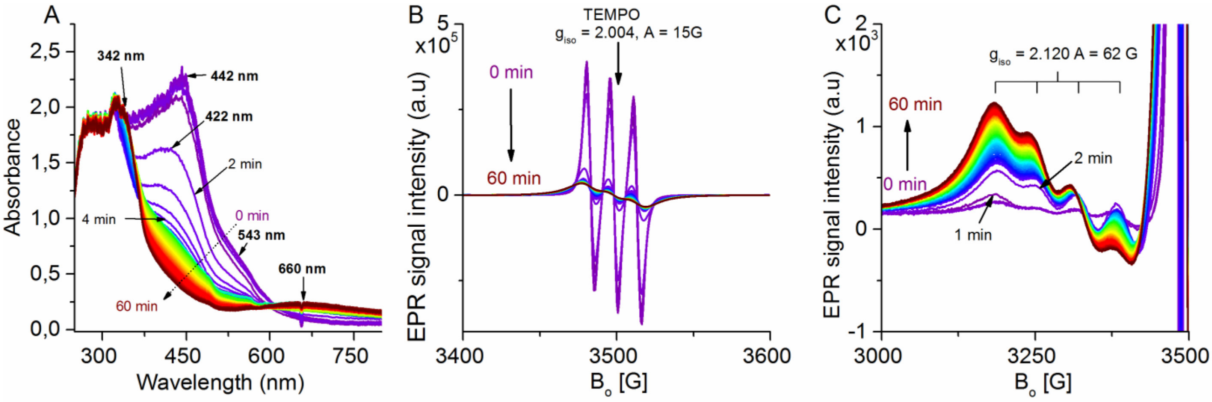

Figure A 10. Behavior of UV-vis (A) and EPR TEMPO (B) and Cu^{II} (C) features during Cu/TEMPO catalyzed aerobic alcohol oxidation using 1.0 equiv. bpy and 2.0 equivs.2-Methylimidazole.

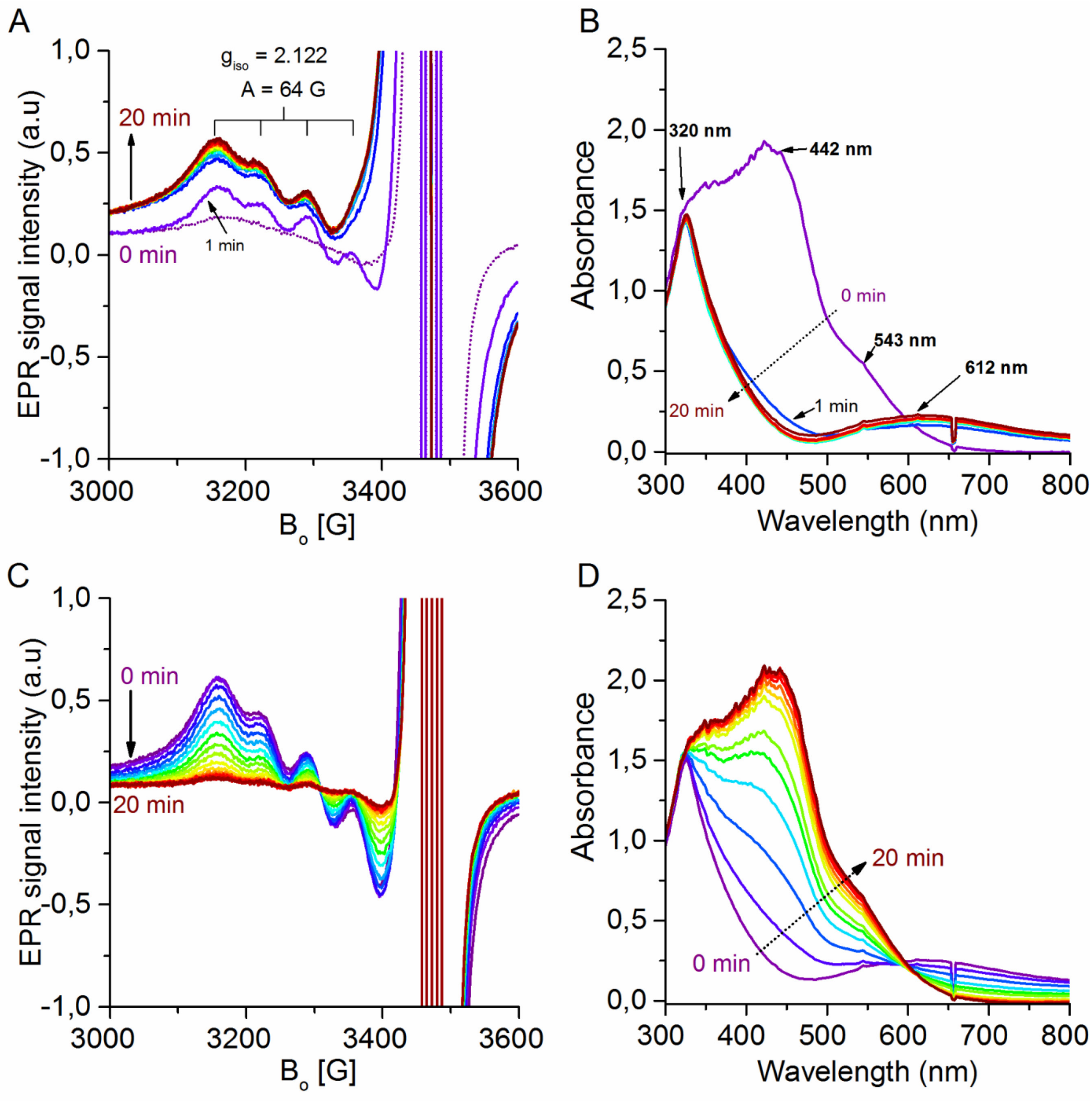

Figure A 11. Oxidation of a catalytic system containing Cu + 1.0 equiv. bpy and 2.0 equivs. 1-H-imidazole monitored by EPR (A) and UV-vis spectroscopy (B). Subsequent reduction by 20 equivs. BzOH monitored by EPR (C) and UV-vis (D). Adapted from reference 119.

Table A 2. Formation of BA after reaction of 30 min for various pyridine derivatives used as ligands/additives within Cu/TEMPO catalyzed aerobic alcohol oxidation. pKa values and the area of the Cu^{II} EPR signal after introducing O_2 into solutions containing Cu^{I}OTf and 3.0 equivs. of mentioned pyridine derivatives are given. ND = not detected, * after 90 min; additionally traces of benzoic acid were found.

Entry.	Pyridine derivative	Structure	pKa value (conjugated acid)	Formation of BA after 30 min	EPR Cu^{II} signal area after 30 min of O_2 flushing (a.u.)
1	Pyridine	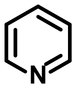	5.25[254]	trace	trace
2	2-Aminopyridine	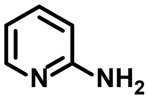	6.86[255]	trace	trace
3	2-Dimethylaminopyridine	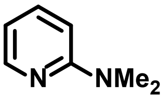	–	trace	trace
4	3-Aminopyridine	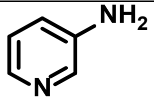	5.98[255]	trace	45.5
5	4-Aminopyridine	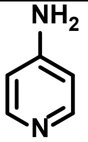	9.17[255]	100%	336.7
6	4-Dimethylaminopyridine	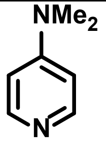	9.71[256]	100%	340.2
7	4-Pyrrolidinopyridine	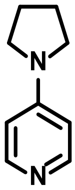	9.70[254]	100%	351.6
8	4-Piperidinopyridine	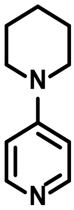	9.60[257]	100%	352.9
9	4-Hydroxypyridine	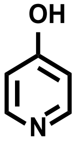	3.23[258]	–	10.2
10	4-Methoxypyridine	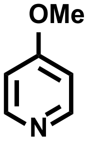	6.60[259]	10%*	trace

11	4-Phenoxypyridine	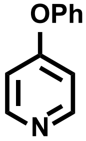	6.25[260]	–	21.4
12	4-*tert*-butylpyridine	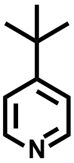	6.06[256]	–	36.6
13	4-Phenylpyridine	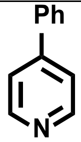	5.50[261]	–	trace
14	4-Aminomethylpyridine	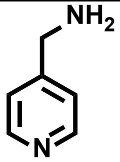	–	ND	39.5
15	4-Trifluoromethylpyridine	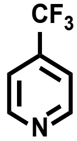	–	–	trace
16	N,N-Dimethylaniline	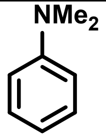	5.10[262]	ND	trace

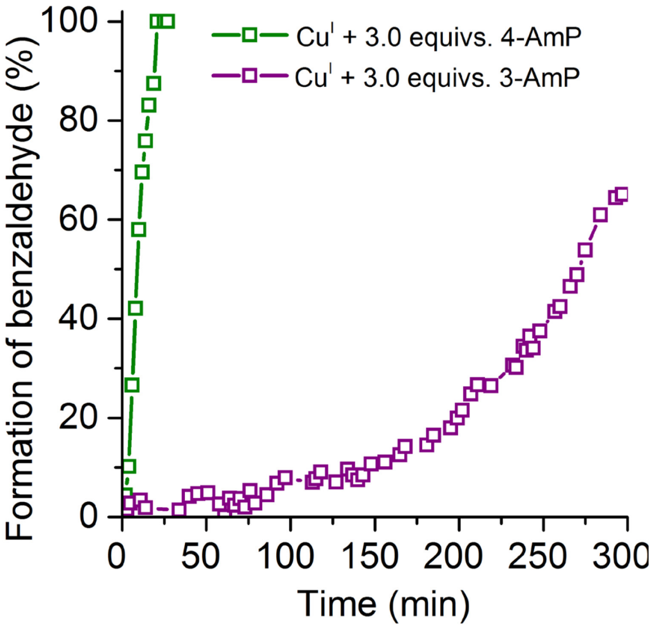

Figure A 12. Conversion of BzOH to BA using a catalytic system containing Cu^{I}OTf, 1.0 equiv.TEMPO and either 3.0 equivs. of 3-AmP or 4-AmP.

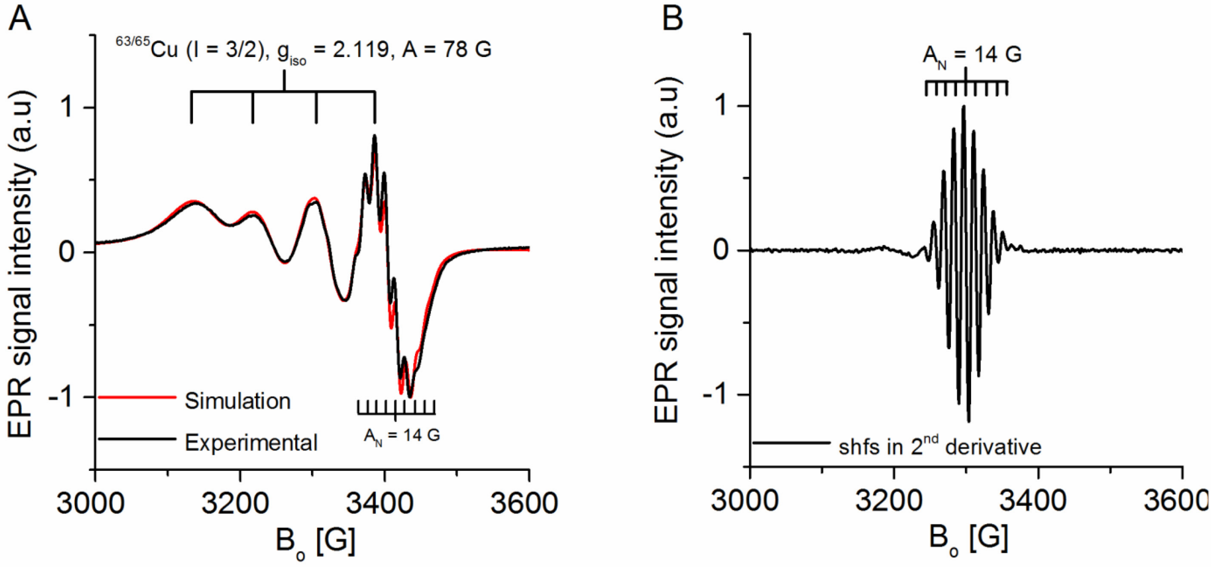

Figure A 13. Experimental and simulated EPR Cu^{II} signal spectra of an experiment using Cu^{I}OTf/4-DMAP after introducing O_2 (A) and 2nd derivative of a similar experiment starting from a CuIOTf precursor showing the shfs of the Cu^{II} m_I=-3/2 high field peak.

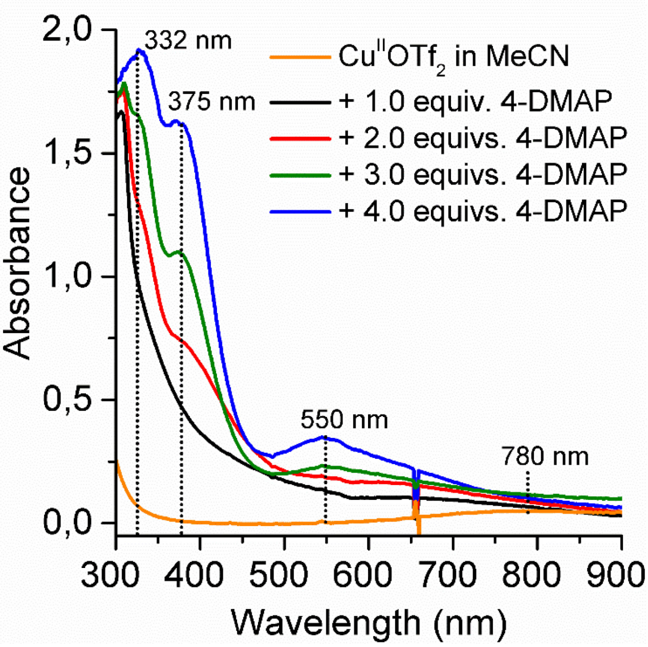

Figure A 14. Addition of 4-DMAP to the Cu^{II}OTf$_2$ precursor in MeCN in ratios from 0 to 4.0 equivs.

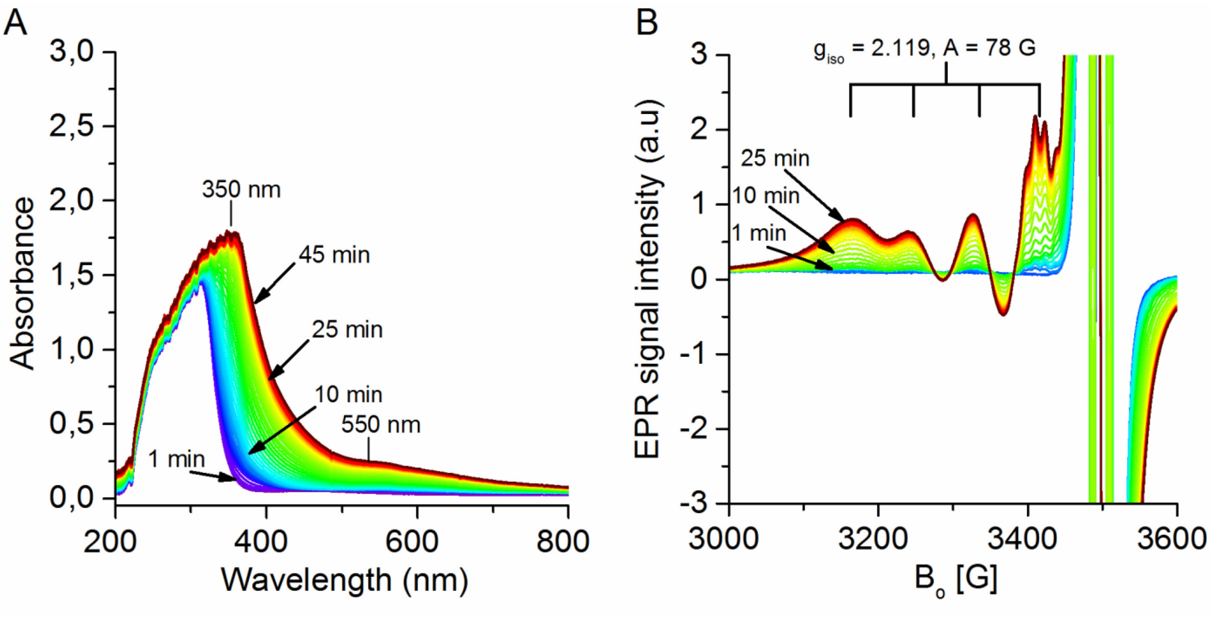

Figure A 15. UV-vis and corresponding EPR spectra of the catalytic conversion of BzOH to BA using a Cu^{I}OTf/TEMPO and 3.0 equivs. 4-AmP system.

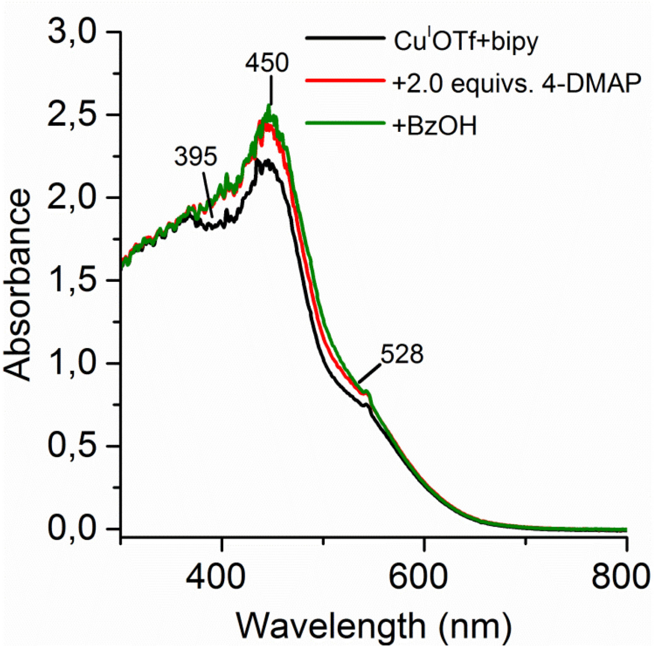

Figure A 16. Subsequent addition of 2.0 equivs. 4-DMAP and BzOH to a solution of Cu^{I}OTf in MeCN.

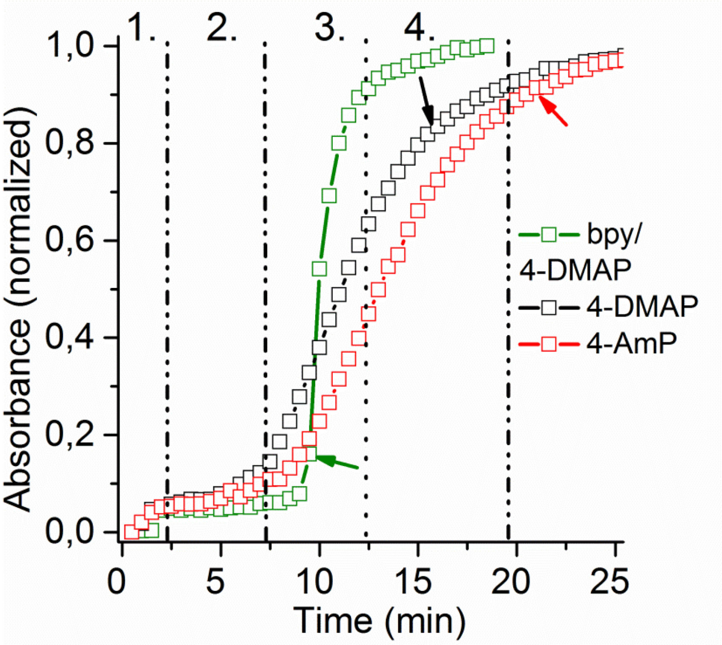

Figure A 17. Behavior of the d-d transition band during the catalytic reaction of BzOH to BA using Cu^IOTf/TEMPO in the presence of either bpy/2.0 equivs. 4-DMAP or 3.0 equivs. 4-AmP or 3.0 equivs. 4-DMAP.

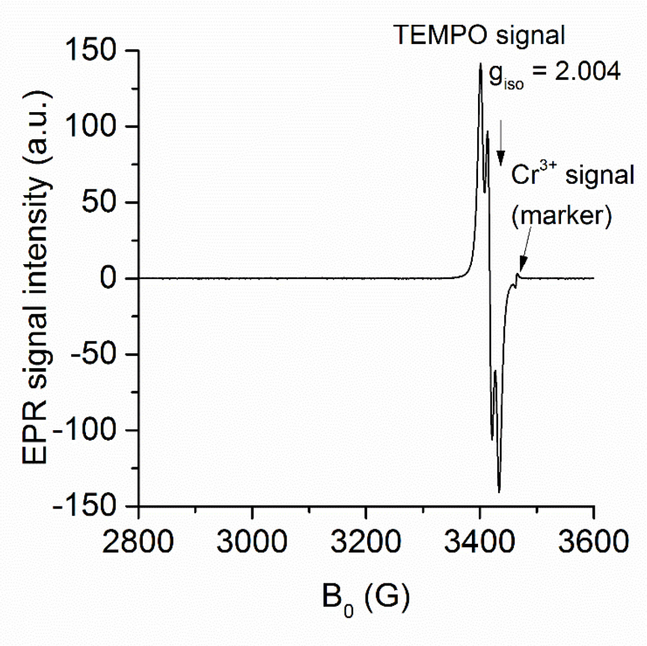

Figure A 18. TEMPO signal of reaction solution containing Cu^IOTf (0.025 M), 1.0 equiv. TEMPO, 1.0 equiv. bpy and 2.0 equivs. NMI before introducing O_2.

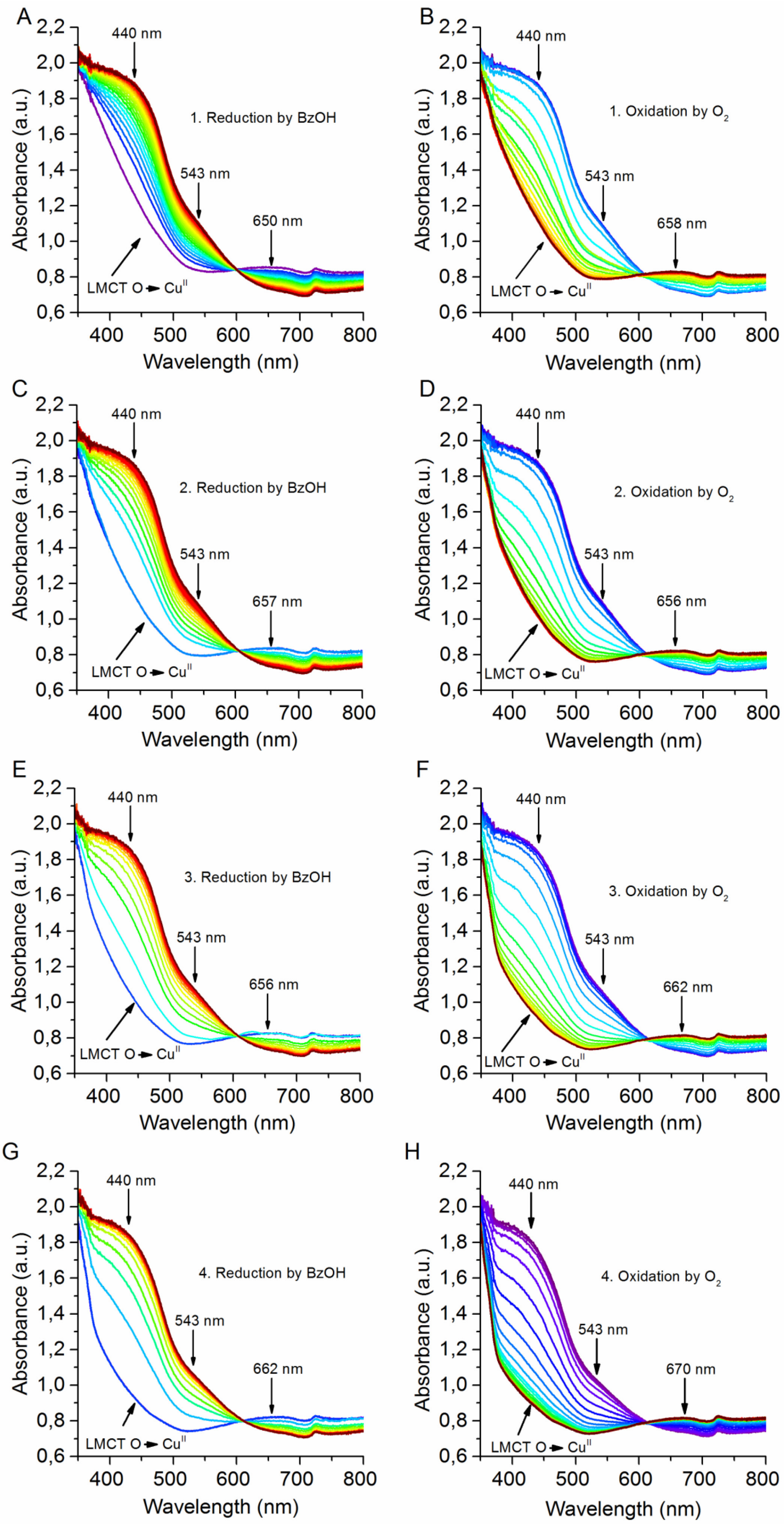

Figure A 19. *In-situ* UV-vis spectra recorded during the four consecutive redox cycles monitored with the newly developed 4-in-1 coupling.

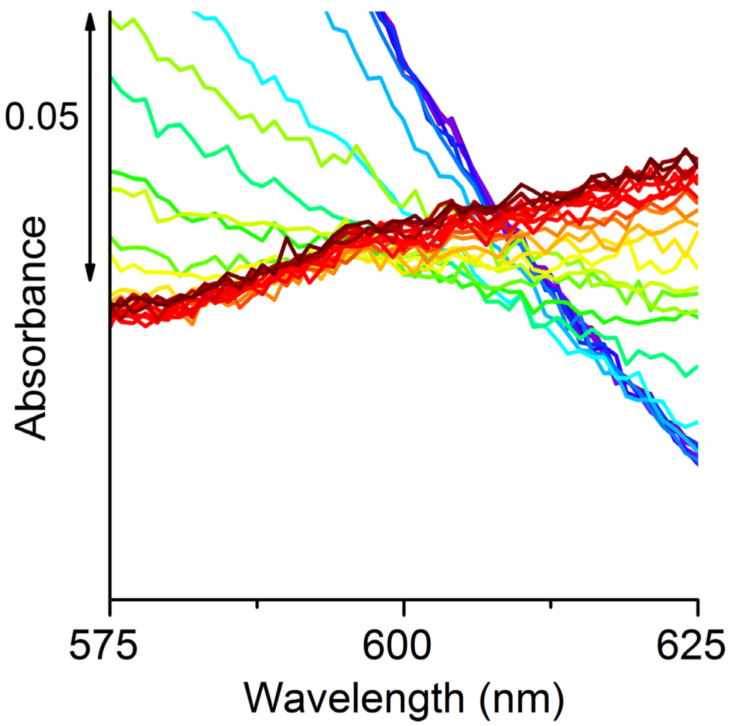

Figure A 20. Close-up of Figure A19B showing no isosbestic point during reduction of Cu/bpy/NMI/TEMPO catalytic system oxidation and first subsequent reduction by BzOH.

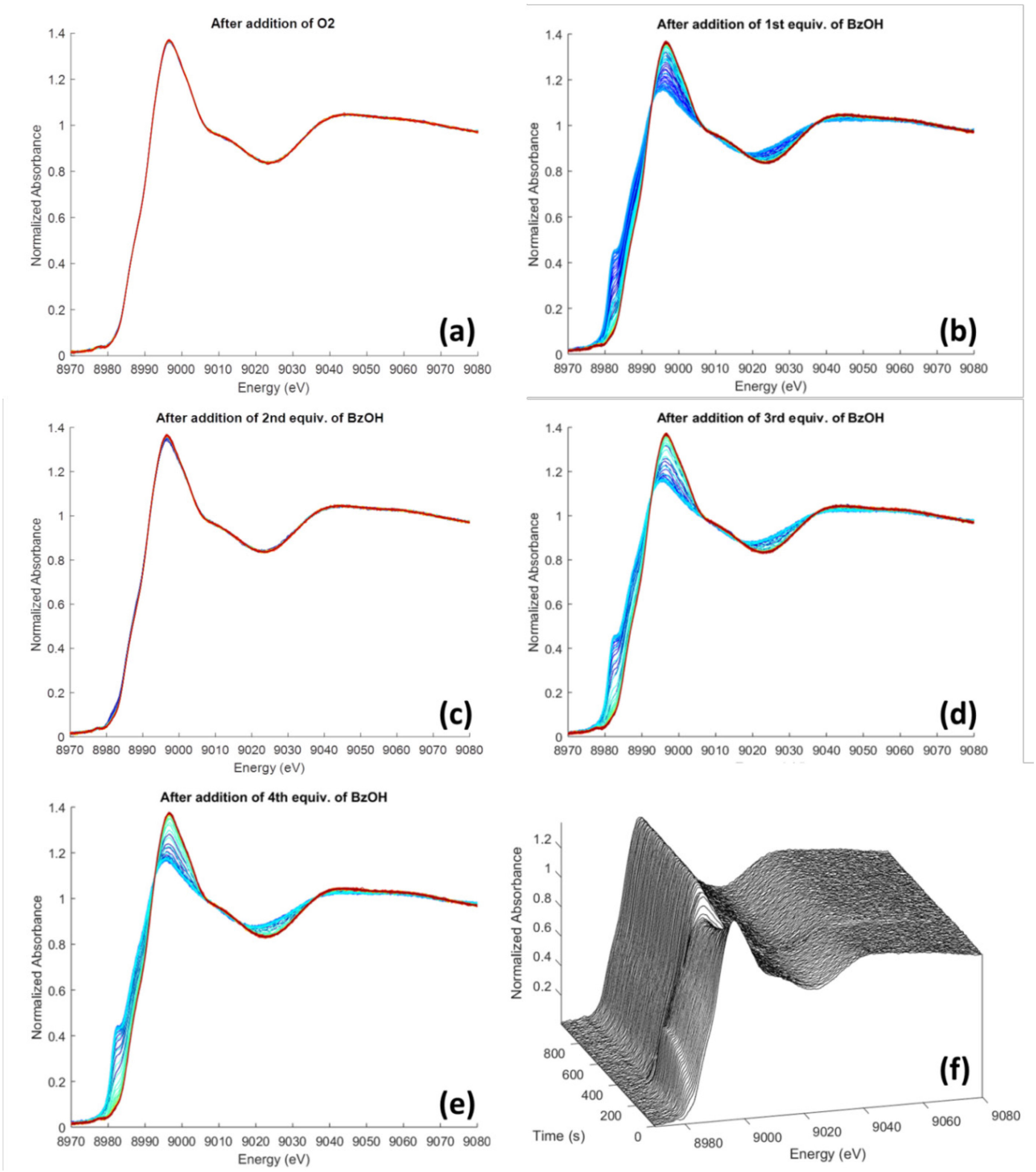

Figure A 21. Experimental XAS spectra recorded simultaneously with the UV-vis spectra in Figure A18 (a) after addition of O_2 for 20 min, (b)-(e) after subsequent addition of 4 portions of 5 equiv. of BzOH, (f) 3D time UV-vis plot for the addition of the 1st equiv. of BzOH. In plot (c) the data recorded just after addition of BzOH are missing due to radiation shutdown, only data near to the steady-state when all the BzOH was reduced have been collected.

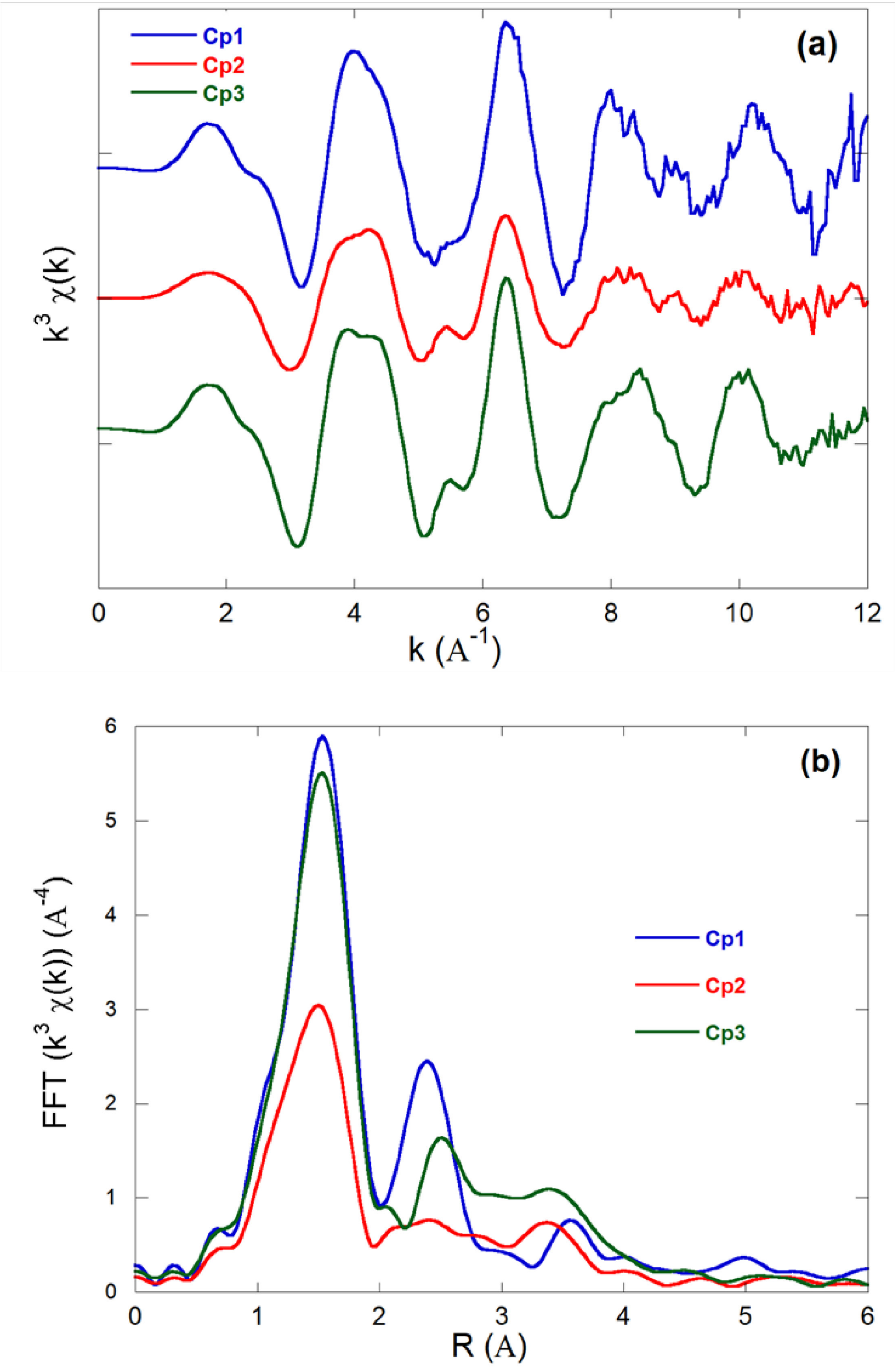

Figure A 22. EXAFS spectra associated with the mononuclear Cu^{I} (red, component 2), the mononuclear Cu^{II} (green, component 3) and the dinuclear Cu^{II} (blue, component 1) pure components derived by MCR-ALS (a), corresponding Fourier transformation of the EXAFS spectra presented before (b).

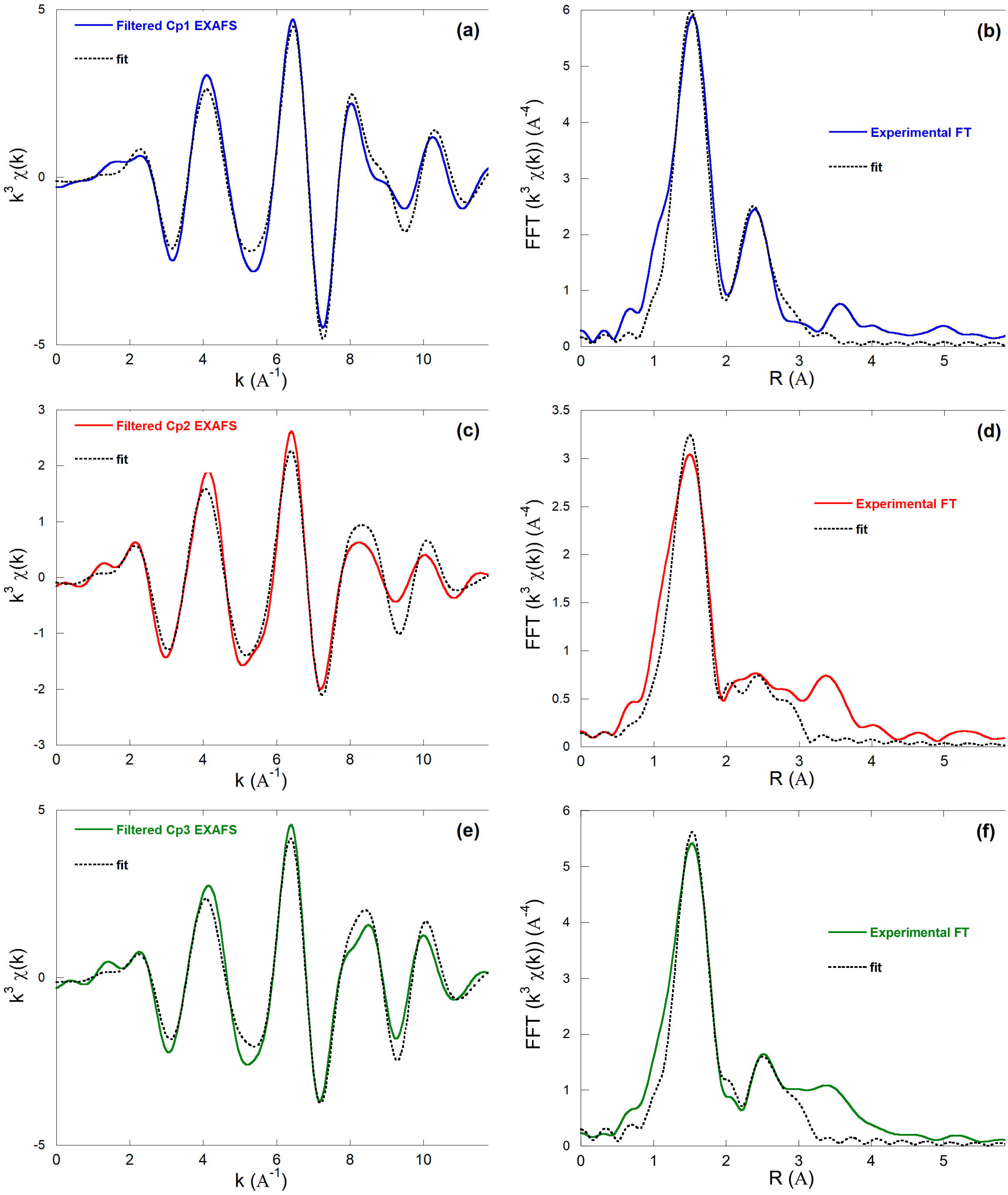

Figure A 23. Filtered EXAFS spectra (a,c,e) associated with the mononuclear Cu^{I} (red, component 2), the mononuclear Cu^{II} (green, component 3) and the dinuclear Cu^{II} (blue, component 1) pure components derived by MCR-ALS, and corresponding Fourier transformation of the EXAFS spectra (b, d, f).

Table A 3. Structural parameters obtained by fitting the EXAFS Spectra in Figure A20.

Component	N[a]	Backscatterer [a]	R (Å) [c]	$\sigma^2\ 10^{-3}$(Å^2) [d]	R_f (%) [e] Red-χ^2
Cp1	2	O	1.92 ± 0.02	2.15± 1.2	
	2	N	2.01 ± 0.03	2.15 ± 1.2	2.27%
	1	N	2.45 ± 0.07	1.65 ± 3.1	667
	4	C	2.80 ± 0.05	1.65 ± 3.1	
	1	Cu	2.91 ± 0.04	3.70 ± 3.5	
Cp2	4	N	1.98 ± 0.01	7.16 ± 1.3	
	2	C	2.87 ± 0.06	20.7 ± 15.0	2.00%
	4	C	3.00 ± 0.06	20.7 ± 15.0	494
	4	MS	3.02 ± 0.04	85.9 ± 400	
	1	C	3.17 ± 0.04	4.85 ± 5.5	
	3	MS	3.18 ± 0.04	4.85 ± 5.5	
	8	MS	3.19 ± 0.04	85.9 ± 400	
Cp3	5	N	1.99 ± 0.02	3.99 ± 1.4	
	2	C	2.84 ± 0.06	14.0. ± 11.3	2.13%
	6	C	2.97 ± 0.06	14.0 ± 11.3	4460
	12	MS	3.11 ± 0.15	4.4 ± 14.6	
	4	MS	3.12 ± 0.15	4.4 ± 14.6	
	1	C	3.23 ± 0.10	2.88 ± 11.3	
	3	MS	3.24 ± 0.10	2.88 ± 11.3	

[a] Coordination numbers were fixed during simulations.

[b] O = single scattering by oxygen, N = single scattering by nitrogen, single scattering by carbon, MS= multiple scattering paths.

[c] R = distance between Cu and the backscatterer

[d] σ = Debye Waller factor

[e] Definition of reduced χ^2 and r-factor (Rf) metrics are defined by the IXS standards and criteria committee (http://ixs.iit.edu/subcommittee_reports/sc/err-rep.pdf).

Component 1 is satisfactorily reproduced considering a cationic dinuclear Cu^{II} unit with a five-fold coordination made of 4 nearest neighbours (2 O at 1.92 Å + 2 N at 2.01 Å) and a more distant neighbour at 2.45 Å and a Cu-Cu bond length at 2.91 Å. Oxygen atoms at 1.92 Å are related to μ-OH groups bridging the Cu centers as found in similar dinuclear Cu^{II} compounds.[111] Nitrogen atoms at 2.01 Å might stem from either one bpy or two NMI ligands, in agreement with the presence of the second nearest carbon neighbours belonging to those moieties but the lack of MS contributions does not allow to be more conclusive. Distances of 2.31 - 2.66 Å are usually found for axial ligands in dinuclear Cu^{II} complexes with distorted square pyramidal geometry.[111] Accordingly, the ligand at 2.45 Å could be N from NMI, the distance of which is slightly longer than usual (around 2.0 Å) due to steric hindrance in the axial position. Regarding the composition of the pristine solution, component 1 in **Table A3** is assigned to a $[(bpy)NMICu^{II}\mu\text{-}OH]_2$ complex.

Component 2 is satisfactorily reproduced with a 4-fold coordination for Cu taking into account SS and MS paths for a (bpy)Cu^{I}(NMI)(L) with L being *e.g.* MeCN or NMI model.

Component 3 can be described by a (bpy)Cu^{II}(NMI)$_2$(CH$_3$CN) model with 5-fold coordinated Cu taking SS and MS into account. Due to limited number of independent points in the data, we are not able to split the fit for the 5-fold first coordination shell for Component 3 into 4 equatorial + 1 axial distances. It has to be mentioned that the contribution of acetonitrile in our EXAFS fits is limited to the SS and MS paths of a linear "N-C" unit. Therefore any ligand composed of similar light elements as N and C with a linear coordination to Cu could also fit the data, in particular O$_2$.

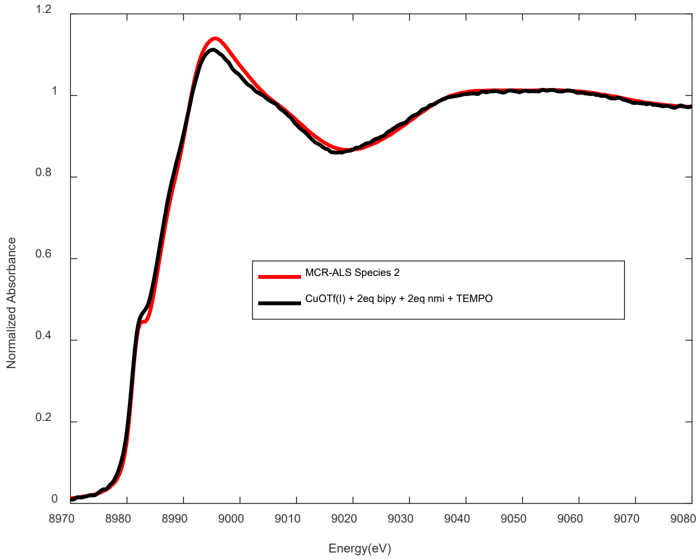

Figure A 24. XANES spectrum of the individual species, mononuclear Cu^{I}, derived from MCR-ALS (red) and the experimental spectrum recorded for the (bpy)Cu^{I}(NMI)$_2$ complex prepared in the glove box by adding 1.0 equiv. bpy, 2.0 equivs. NMI and 1.0 equiv. TEMPO to a solution of Cu^{I}OTf in MeCN.

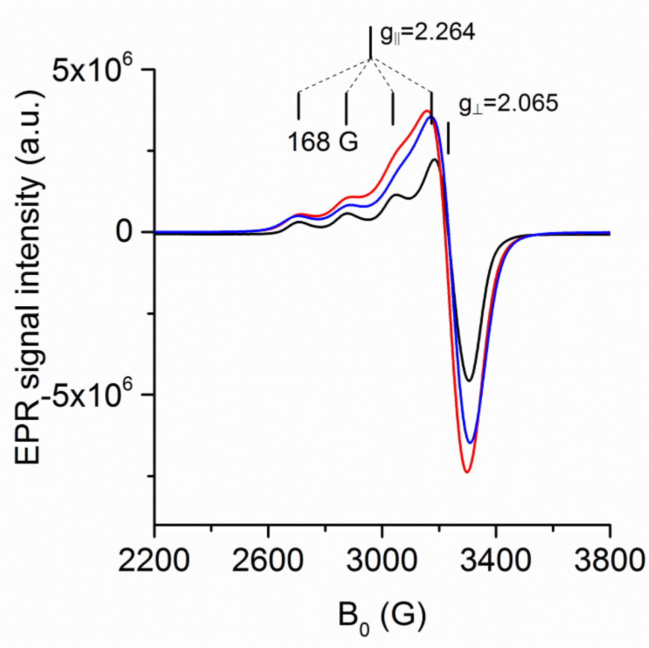

Figure A 25. EPR spectra measured at 100 K of a solution containing 0.025 M $Cu^{I}OTf$, 1.0 equiv. bpy and 2.0 equivs. NMI in MeCN after oxidation by O_2 (black) after subsequent addition of 5.0 equivs. BzOOH (red) compared to a solution of 0.025 M $Cu^{II}(OTf)_2$, 1.0 equiv. bpy and 2.0 equivs. NMI in MeCN (blue).

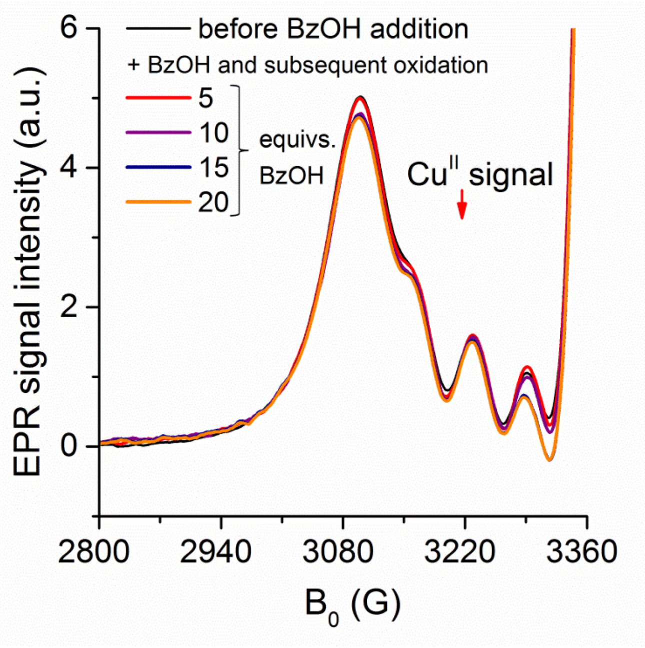

Figure A 26. Maximum of the Cu^{II} EPR signal after subsequent oxidation following addition of either 5, 10, 15 or 20 equivs. of BzOH.

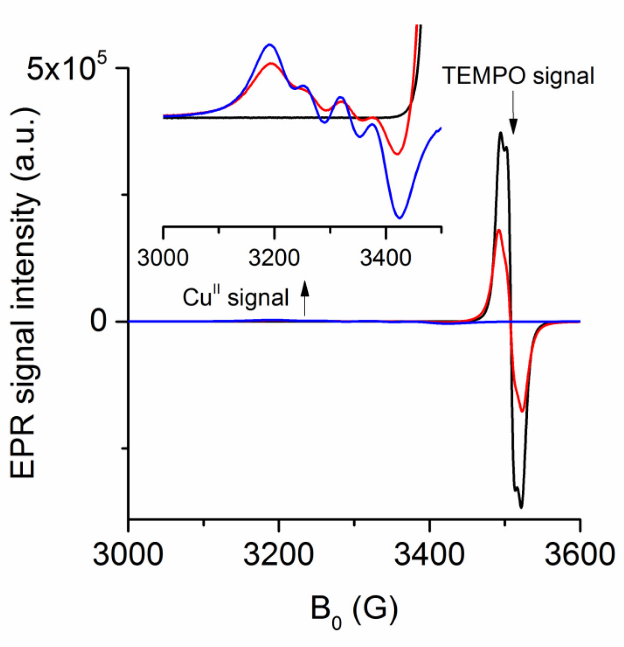

Figure A 27. EPR spectra of a 0.025 M MeCN solution of TEMPO (black) compared to Cu^{I}OTf, 1.0 equiv. bpy and 2.0 equivs. NMI after oxidation by O_2, in the presence (red) and absence of TEMPO (blue) measured at 293 K under Ar.

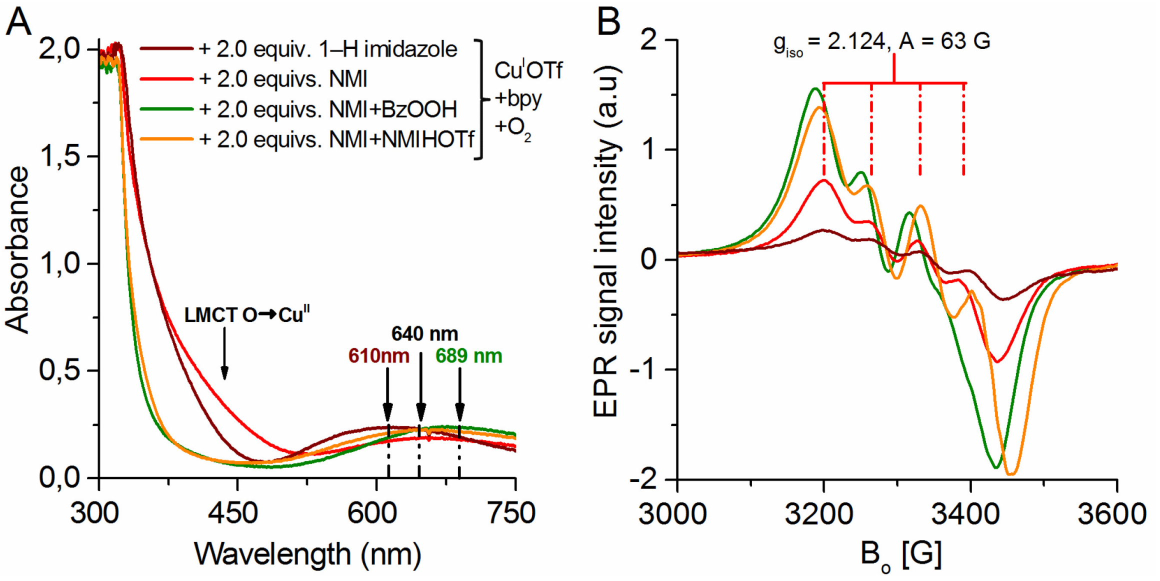

Figure A 28. *In situ* UV-vis (**A**) and corresponding EPR (**B**) spectra of Cu^{I}OTf+1.0 equiv. bpy + either 2.0 equivs. 1-H imidazole, NMI or NMI + 1.0 equiv. BzOOH as well as NMI + 1.0 equiv. NMIHOTf.

CURRICULUM VITAE

General information

Sven Adomeit, M.Sc.

born in Hamburg on the 21st October 1988, *Federal Republic of Germany*.

Academic career

PhD

02/2015 – 01/2019	Leibniz Institute for Catalysis at the University of Rostock (LIKAT) Department: Catalytic *in-situ* studies by Prof. Dr. Angelika Brückner Topic: "Structure-reactivity relationships in Cu/TEMPO catalyzed aerobic alcohol oxidation Mechanistic assessment by (coupled) *operando* spectroscopic tools" supervised by Prof. Dr. Angelika Brückner.
07/2017	Summer School "Catalysis and Organometallic Chemistry" at Würzburg University.
03/2017 and 02/2016	EXAFS/XANES measurements at SOLEIL synchrotron facility in Saint-Aubin, France.
10/2015	EXAFS/XANES measurements at ESRF synchrotron facility in Grenoble, France.

University education

10/2012 – 09/2014	Master of Science (Chemistry), Rostock University.

Topic: “Synthesis of arylidene and alkylidene succinates via base–free catalytic Wittig reaction“ supervised by Dr. habil. Thomas Werner, Organocatalysis department at LIKAT.

10/2008 – 09/2012 Bachelor of Science (Chemistry), Rostock University.

Topic: “Influence of different salts on solution properties of biogenic carbonates“ supervised by Prof. Dr. Michael Böttcher, Biogechemistry department at Leibniz Institute for Baltic Sea research Warnemünde (IOW).

School education

09/1999 – 06/2008 Abitur, Elsa-Brändström-Schule Elmshorn, Germany.

Scientific contributions

Parts of this thesis have been published:

Publications and patents related to this thesis

1. Adomeit, S.; Rabeah, J.; Surkus, A. E.; Bentrup, U.; Brückner, A., Effects of Imidazole-Type Ligands in Cu^I/TEMPO-Mediated Aerobic Alcohol Oxidation. *Inorg. Chem.* **2017**, *56*, 684-691.
2. Rabeah, J.; Adomeit, S.; Brückner, A. Vol. PCT/EP2018/053047 **2018**.
3. Adomeit, S.; Rabeah, J; Bentrup, U.; Surkus, A.-E.; Brückner, A., Impact of pyridine-based ligands on redox properties and activity of CuL_4/TEMPO catalysts in aerobic alcohol oxidation assessed by *operando* EPR/ATR–IR/UV–vis spectroscopy. **2019**, in preparation.
4. Rabeah, J.; Briois, V.; Adomeit, S.; La Fontaine, C.; Bentrup, U.; Brückner, A., Multivariate analysis of coupled operando EPR/XANES/EXAFS/UV–vis/ATR–IR spectroscopy: A new dimension for mechanistic studies of catalytic gas-liquid phase reactions. **2019**, in preparation.

Additional publications

1. Schirmer, M.-L.; Adomeit, S.; Werner, T., First Base-Free Catalytic Wittig Reaction. *Org.Lett.* **2015**, *17*, 3078-3081.
2. Schirmer, M.-L.; Adomeit, S.; Spannenberg, A.; Werner, T., Novel Base-Free Catalytic Wittig Reaction for the Synthesis of Highly Functionalized Alkenes. *Chem. Eur. J.* **2016**, *22*, 2458-2465.
3. Hinrichsen, S.; Kindjajev, A.; Adomeit, S.; Krahmer, J.; Näther, C.; Tuczek, F., Molybdenum(0) Dinitrogen Complexes Supported by Pentadentate Tetrapodal Phosphine Ligands: Structure, Synthesis, and Reactivity toward Acids. *Inorg. Chem.* **2016**, *55*, 8712-8722.
4. Sherborne, G. J.; Adomeit, S.; Menzel, R.; Rabeah, J.; Brückner, A.; Fielding, M. R.; Willans, C. E.; Nguyen, B. N., Origins of high catalyst loading in copper(I)-catalysed Ullmann–Goldberg C–N coupling reactions. *Chem. Sci.* **2017**, *8*, 7203-7210.
5. Xingchao D.*; Adomeit, S.*; Rabeah, J.; Kreyenschulte, C.; Brückner, A.; Wang, H. and Shi, F., Sustainable co-synthesis of glycolic acid, formamides and formates from 1,3-dihydroxyacetone by a single atom Cu/Al2O3 catalyst. *Angew. Chem. Int. Ed.* **2018**, accepted, DOI: 10.1002/anie.201814050 and 10.1002/ange.201814050.

Contributions at conferences

Oral presentations

1) "Simultaneous *operando* EPR/UV-vis/ATR–IR spectroscopy: A unique tool for tracing mechanisms of catalytic gas–liquid phase reactions" S. Adomeit, J. Rabeah, A.–E. Surkus, U. Bentrup, A. Brückner. *49. Jahrestreffen Deutscher Katalytiker*, March 16th – 18th **2016**, Weimar, Germany.
2) "*Operando* IR/UV-vis spectroscopic studies of Mn–catalyzed Transfer hydrogenation" S. Adomeit, U. Bentrup, J. Neumann, H. Jiao, K. Junge, A. Brückner. Summer School *"Catalysis and Organometallic Chemistry"* Würzburg University, July 24th – 28th **2017**, Würzburg, Germany.
3) **Keynote lecture** "Mechanism of Homogeneous Catalytic Alcohol Oxidation Explored by a Coupled Multitechnique *Operando* Approach" S. Adomeit, J. Rabeah, U. Bentrup, A. Brückner. *8th World Congress on Oxidation Catalysis*, September 3rd – 9th **2017**, Cracow, Poland.

Poster presentations

1) "Phosphine Catalyzed Coupling of Maleates and Aldehydes – An Organocatalytic Route to Arylidene & Alkylidene Succinates" S. Adomeit, M.-L. Schirmer, J. Modenbach, C. Grimmer, M. Hoffmann, T. Werner. *11th European Workshop on Phosphorus Chemistry*. March 24th – 26th **2014**, Sofia, Bulgaria.
2) "Phosphine Catalyzed Coupling of Maleates and Aldehydes – An Organocatalytic Route to Arylidene & Alkylidene Succinates" S. Adomeit, M.-L. Schirmer, J. Modenbach, C. Grimmer, M. Hoffmann, T. Werner. *Leibniz WissenschaftsCampus Phosphorforschung*. August 20th **2014**, Warnemünde, Germany.
3) "Microwave-Assisted Catalytic Wittig Reaction" S. Adomeit, M. Hoffmann, T. Werner. *ORCHEM 2014*. September 15th – 17th **2014**, Weimar, Germany.
4) "Effects of N-containing additives in the Cu^I/TEMPO mediated aerobic alcohol oxidation" S. Adomeit, J. Rabeah, A.–E. Surkus, U. Bentrup, A. Brückner. 18. *Norddeutsches Doktorandenkolloquium*. September 7th – 8th **2015**, Goslar, Germany.
5) "*Operando* ATR–IR/UV-vis spectroscopic study of transfer hydrogenation catalyzed by $[Mn^I(dpa)(CO)_3]Br$ pincer complex" S. Adomeit, U. Bentrup, J. Neumann, K. Junge, A. Brückner. *50. Jahrestreffen Deutscher Katalytiker*. March 15th – 17th **2017**, Weimar, Germany.

6) “*Operando* IR/UV-vis spectroscopic studies of Mn–catalyzed Transfer hydrogenation“ S. Adomeit, U. Bentrup, J. Neumann, H. Jiao, K. Junge, A. Brückner. Summer School *“Catalysis and Organometallic Chemistry“* Würzburg University, July 24th – 28th **2017**, Würzburg, Germany.
7) “New Frontiers in Liquid-Phase Reactions: *Operando* EPR/UV-vis/IR meets X-Ray Absorption Spectroscopy“ S. Adomeit, J. Rabeah, V. Briois, C. La Fontaine, U. Bentrup, A. Brückner. *HanseSymposium*. November 7th – 8th **2018**, Rostock, Germany.